THE ELECTRICAL PROPERTIES OF TRANSPARENT CONDUCTING OXIDE COMPOSITES

Daniel Slocombe
Cardiff University

A thesis submitted to Cardiff University
for the degree of Doctor of Philosophy

June 2012

DECLARATION

This work has not been accepted in substance for any degree and is not concurrently submitted in candidature for any degree.

Signed ……………………………...…(candidate) Date …………...…

STATEMENT 1

This thesis is being submitted in partial fulfilment of the requirements for the degree of PhD.

Signed ……………………………...…(candidate) Date …………...…

STATEMENT 2

This thesis is the result of my own independent work/investigation, except where otherwise stated. Other sources are acknowledged by explicit references.

Signed ……………………………...…(candidate) Date …………...…

STATEMENT 3

I hereby give consent for my thesis, if accepted, to be available for photocopying and for inter-library loan, and for the title and summary to be made available to outside organisations.

Signed ……………………………...…(candidate) Date …………...…

ABSTRACT

The electrical properties of composites containing antimony tin oxide (ATO) coated mica platelets are investigated. High frequency measurement techniques are employed to measure properties at spot microwave frequencies and over a broad microwave frequency range 100 MHz – 8.5 GHz. A novel cavity resonator configuration is developed and constructed to measure samples of arbitrary shape; the technique is then extended to measurements with a large ‘split’ present in the cavity allowing unprecedented access to TM_{010} fields and the sample under test. Higher order modes (namely the TM_{210} mode) are used as a reference to refine the measurement technique and account for ambient temperature fluctuations. To demonstrate the advantages of the split cavity, ATO powder is irradiated in the cavity and a change in conductivity is observed in real time as the electrons are excited into the conduction band.

Broadband measurements of absorption in composites of transparent conducting oxide (TCO) coated particles show that absorption peaks exist in the microwave frequency region. When samples are annealed at higher temperatures the frequency of the absorption peak increases; corresponding to an increase in electron mobility in the TCO layer. When the mobility is increased beyond some critical value, the absorption peak begins to *decrease* in frequency. Electromagnetic modelling of the layered particles confirms this behaviour, which has not been predicted or observed previously in the literature.

The electromagnetic absorption characteristics of composites of small conducting particles are investigated. A comprehensive model of absorption mechanisms in magnetic and electric fields for a range of particle conductivity and radii is developed. Analytic solutions for the electric and magnetic dipole absorption of small conducting spheres with isotropic electrical conductivity are derived and applied to the specific example of absorption in response to microwave irradiation at the ISM (i.e. industrial, scientific and medical) standard frequency of 2.45 GHz. Simple principles are thereby presented for the efficient heating of small conducting particles in microwave electric and magnetic fields.

ACKNOWLEDGEMENTS

I would like to offer my most sincere thanks to my supervisor, Professor Adrian Porch for giving me the opportunity to pursue a path so rewarding. I am grateful for his counsel and he has my lasting admiration.

I am very grateful to Professor David Barrow and Dr Richard Perks for their guidance and support and I would like to thank Professor Peter P. Edwards and Professor Michael Pepper for their exciting and fruitful collaboration.

I acknowledge the financial support of Merck KGaA and Cardiff University and the kindness and generosity of my industrial supervisors Dr Reinhold Rueger and Dr Rod Riddle.

Thank you also to my friends and colleagues David Rowe, Dr Jack Naylon, Dr Aslam Sulaimalebbe and Alex Morgan, whose enlightening conversation has informed and enthused.

Finally, I would like to give my deepest thanks to my parents, Juliet and Stephen, my parents-in-law Thomas and Megan and my wife Caroline, whose unfaltering support and encouragement have been invaluable.

CONTENTS

1 INTRODUCTION & THESIS SUMMARY

The principal aim of this thesis is the investigation of the electrical properties of conducting pigments provided by Merck KGaA. These pigments are generally micron-sized mica particles coated with a transparent conducting oxide (TCO) and are conventionally dispersed in a polymer matrix at varying volume fractions to form composite structures. To measure the electrical properties of composites and powder materials is not easy since one cannot simply attach terminals as in the measurement of bulk materials. We therefore turn to high frequency techniques, which are capable of measuring composites and powders of conducting particles, but are also capable of measuring non-conducting particles.

This thesis therefore has three main themes; 1) the development and use of high frequency measurement techniques for the application to Merck pigments, 2) the investigation of the fundamental electrical properties of TCOs, and 3) the study of the complex electrical behaviour of composites.

A thorough exploration of these themes is carried out in a number of permutations. Chapter 2 develops and uses high frequency techniques to measure composites of TCOs, chapter 3 investigates composites of TCOs theoretically, chapter 4 examines electromagnetic absorption in composites of conducting particles for the optimization of heating applications and Annex A forms a study of the fundamental optical and electrical properties of TCOs and considers the practical application of thin-film solar cells.

We now give an overview of each chapter and a summary of the aims and major original contributions of the work.

Chapter 2: *Microwave Cavities for the Measurement of Dielectric Materials*

The objective of chapter 2 is to review microwave cavity resonator measurement techniques, to extend the method and exploit these powerful tools to investigate Merck pigments and dielectric materials in general.

After a discussion of cavity resonator principles and design methodology, a cylindrical cavity is constructed in a novel ‘split’ configuration for use in the TM_{010} mode. The TM_{010} mode forms a highly uniform electric field in the centre of the cavity, which minimizes depolarization in cylindrical samples. We demonstrate theoretically that for a cylindrical water sample at 2.45GHz, a non-depolarizing configuration can increase power dissipation by a factor of 1600 over the depolarizing sample. A scheme is set out in which the material properties of cylindrical samples can be inferred based upon the frequency shift and bandwidth change in the resonant cavity upon sample insertion. A quick and easy calibration technique is developed in which a precision engineered vanadium-coated steel sphere is inserted into the cavity and from the well-defined dipole moment formed by the sphere; calibration values associated with the cavity are obtained. This is an innovative approach, and the method becomes invaluable when taking measurements at arbitrary split width.

The presence of a split in the cavity in the same plane as the axis of revolution is an original concept. Similar approaches have been used in the TE_{011} mode where the split is half way along the length of the cylinder and forms an industrial standard of measurement (JIS R 1641 [1]). In this work the TM_{010} mode is able to survive the presence of the axial split because no wall currents traverse the split boundaries; wall currents run parallel to the split. We therefore maintain a high Q factor of above 8000 for the enclosed cavity and importantly, above 7000 even for a split width of 8mm.

The ability to take measurements at large split widths allows unprecedented access to samples in the highly uniform field of the TM_{010} mode and the simple calibration method using metal spheres means that measurements can be taken at arbitrary split width.

Measurements of TCO powders are taken at increased split widths and it is found that results remain accurate to within 0.5% for a 2mm split and even for widths of

8mm are well below 4% compared with results from the enclosed cavity configuration (i.e. no split present).

Higher order modes are investigated in the cavity for novel functions in resonant perturbation techniques. We consider the TM_{210} mode as a reference mode to complement TM_{010} measurements. The TM_{210} mode exists at 5.327 GHz in the cavity constructed here and it is shown that the frequency ratio of the two modes is fixed by $f_{010} / f_{210} = 0.468$. It is demonstrated experimentally that the TM_{210} mode is unaffected by the presence of any samples inserted axially into the cavity. Crucially, we therefore have a means by which we can infer an *unperturbed* frequency even when the sample is in place. There are two major practical implications of this fact; firstly that we no longer have to take an unperturbed reference measurement before the sample is inserted in order to invert the measurement; and secondly, any shift in frequency of this mode is not due to the sample, but is due to the influences of the environment. Using this fact we can account for changes in ambient temperature and separate out any external effects. We find that we can track temperature changes down to mK accuracy. Both of these facts are demonstrated experimentally.

A major advantage of the split cavity is the unprecedented access to the sample under test in the uniform field of the TM_{010} mode. As a demonstration of this, an exciting new result is presented in which a TCO powder is stimulated by an ultraviolet (UV) lamp. A significant change in conductivity is measured in real time as the UV light excites electrons into the conduction band. For powders of antimony doped tin oxide, we observe significant responses at UV wavelengths of 254nm and 365nm.

Summary of major original contributions of chapter 2:

- A novel ‘split’ cavity is presented which gives unprecedented access to a sample under test in highly uniform TM_{010} fields. This is facilitated by a dynamic calibration technique allowing measurements to be taken at arbitrary split widths.

- We present a demonstration of the use of the TM_{210} mode as a reference since it is unaffected by the presence of the sample. This allows measurements to be taken without having to remove the sample and corrections made for ambient temperature shifts down to mK accuracy.

- Advantages of the split cavity are demonstrated by stimulating a TCO powder using an ultraviolet (UV) lamp. A significant change in conductivity is measured in real time. For powders of antimony doped tin oxide, we observe significant responses at UV wavelengths of 254nm and 365nm.

Chapter 3: *Composites of Conducting Particles and TCOs at Microwave Frequencies*

The principal objective of Chapter 3 is to develop a comprehensive theoretical model of the electrical properties of TCO coated particles at high and low concentrations and conductivities. We aim to treat polarization at high and low frequencies and describe percolation and relaxation mechanisms in composites before verifying our conclusions experimentally.

We begin by reviewing the development of mixing laws, effective medium approximations and statistical approaches to the modelling of randomly structured media. We highlight the limitations and uncertainties of these approaches. After introducing the concept of relaxation in core-shell structured particles we examine interpretations in the context of Merck pigments. Electromagnetic modelling based upon the polarization of individual particles and using the Clausius Mossotti formulation [2] is carried out and modifications to account for internal structure of the particles are shown to give illuminating results.

We observe that the conductivity of the conducting layer is proportional to the frequency of maximum absorption in composites. We also observe that as the ratio of the volumes of inner core the entire particle increases (i.e. the inner core increases in size), the absorption peak is reduced in frequency. These behaviours are known in the literature and the frequency of the absorption peak is considered to be proportional to the DC conductivity of homogeneous and core-shell structures [3,4].

Time domain analysis of the Lorentz model of an oscillating system consolidates our understanding of the mechanisms of dielectric relaxation and percolation. To investigate the alleged 'universal' behaviour of composites at the percolation threshold, we first look at random resistor-capacitor networks (RRCN). RRCNs are studied by solving large networks and analyzing the frequency dependence in the so-called 'emergent' power law region. Results from the literature are reproduced which show that the gradient of the fractional power law region of the frequency dependent conductivity corresponds to the proportion of capacitive elements in the network. These findings are supported in the literature by experimental results for the case of a porous lead zirconium titanate (PZT) pellet impregnated with water [5]. We take broadband conductivity measurements of composites of TCO coated particles and find that the power law behaviour prediction consistently underestimates the proportion of the capacitive phase in the mixture. Since the RRCN model is only applicable if a scaling behaviour is satisfied in which the aspect ratio of capacitive and resistive elements is equal we conclude that it is not a suitable approach to modelling Merck TCO composites. The model would work for a cubic arrangement of alternatively capacitive and resistive cubes, which the PZT case is clearly closer to than composites of Merck pigments.

The merits of measuring composites of conducting particle at high frequencies are shown by a direct comparison of sheet resistance measurements at DC and 2.8GHz at a range of particle volume concentrations. The DC measurements show a clear first order phase transition to the conducting state as the percolation threshold is reached, but the high frequency measurements demonstrate no such transition. Indeed, the percolation threshold remains 'invisible' to the microwave measurement technique, which simply continues to measure the quantity of conducting particle present. The question of over what frequency range this is valid is investigated by taking broadband measurements of composites through the percolation threshold. A relaxation peak of maximum absorption is observed for non-percolating samples, but as the percolation threshold is reached, the 'lower leg' of the absorption peak rises.

This low frequency dispersion shows that the effect of percolation is visible below the characteristic relaxation frequency, but above this frequency the absorption is unaffected. High frequency measurements are invariant through the percolation threshold above the relaxation frequency.

A comprehensive electromagnetic model is developed of the polarizing, layered ellipsoidal particle used in Merck composites. The model is based upon the Clausius Mossotti model used earlier in the chapter, but modifying the polarisability to account for the layered oblate spheroidal structure allows us to relate directly to the behaviour of Merck composites.

To investigate the effects of carrier mobility in the TCO layer, Merck pigment samples are annealed at increasing temperatures corresponding to increasing electron mobility values. Upon broad band measurement (100MHz-8.5GHz) we observe that the absorption peaks previously observed increase in frequency corresponding to the increase in mobility. But importantly, as the mobility is increased past some critical value, the frequency of the absorption peak is *decreased*. This result is contrary to well established theory of absorption in conducting particles since absorption peak frequency is generally considered to be proportional to DC conductivity [3,4].

To explain this behaviour we use the simple Drude model of the degenerate free electron gas to model a frequency dependent imaginary permittivity in the TCO layer. We find that for an increasing value of mobility, there is indeed a critical point at which increasing the mobility further (and therefore the DC conductivity) causes the frequency of the absorption peak to be *reduced*. This result has not previously been predicted or observed in the literature.

The theoretical prediction of this behaviour employs well established theory to yield a surprising result and is a convincing argument for the existence of this phenomenon, but to validate the experimental behaviour observed in these samples future work must eliminate the possibility of contributions from material degradation.

Summary of major original contributions of chapter 3:

- Broadband conductivity measurements of composites of TCO coated particles show that the power law behaviour prediction consistently underestimates the proportion of the capacitive phase in the mixture. We conclude that the necessary scaling behaviour exhibited in random resistor-capacitor networks and in the experimental case of PZT [5] is not satisfied by Merck TCO composites

- We demonstrate the measurement of composite materials through the percolation threshold and confirm that the percolation threshold remains ‘invisible’ to the microwave measurement technique.

- We present broadband measurements of the transition though the percolation threshold in which the development of low frequency dispersion is clearly observed. This result confirms that high frequency measurements are invariant through the percolation threshold above the relaxation frequency.

- Broadband measurements are presented in which the absorption peak increases in frequency with increasing mobility, but begins to *decrease* when some critical value of mobility is reached. Modelling of the system confirms the result which is contrary to well established theory of absorption in conducting particles. This result has not previously been predicted or observed in the literature.

Chapter 4: *Microwave Absorption in Composites of Small Conducting Particles*

The objective of chapter 4 is to investigate the electromagnetic absorption characteristics of composites of small conducting particles. We aim to develop a comprehensive model of absorption mechanisms in magnetic and electric fields for a range of particle conductivity and radii. A direct comparison of electric and magnetic absorption will then expose the conditions under which each is preferable.

Analytic solutions for the electric and magnetic dipole absorption of small conducting spheres (i.e. of particle radii much less than the wavelength of the incident radiation) with isotropic electrical conductivity are developed and applied to the specific example of absorption in response to microwave irradiation, at the ISM (i.e. industrial, scientific and medical) standard frequency of 2.45 GHz.

Knowledge of the absorption characteristics is increasingly important in many areas of scientific research and industry. Small conducting particles often feature as additives to act as catalysts or to simply augment the microwave heating characteristics of a material, though applications are wide ranging and include the enhancement of chemical and biological reactions [6], microwave absorbing screens and coatings [7], full sintering of metal particles [8] and targeted stimulus of biological functions [9].

By consideration of a full electromagnetic model of dipole absorption in conducting particles we account for the relationship of electric and magnetic dipole heating to the particle size, conductivity and magnetic properties. We establish the following simple principles for the optimisation of microwave absorption in conducting particles:

1) Magnetic absorption dominates electric absorption over a wide range of particle radii.
2) Optimum magnetic absorption is set by the ratio of mean particle radius a to the skin depth δ (specifically, by the condition $a = 2.41\delta$. Computational studies in the literature estimate this value as $a \approx 2.5\delta$ [10]).
3) For weakly conducting samples, electric dipole absorption dominates, and is maximised when the conductivity is approximately $\sigma \approx 3\omega\varepsilon_0 \approx 0.4$ S/m, independent of particle radius.
4) The absorption of sub-micron particles is small in both magnetic and electric fields. However, if the particles are magnetic, then magnetic

dipole losses are dramatically enhanced compared to their values for non-magnetic particles below the Curie point.

Summary of major original contributions of chapter 4:

- Optimization of electromagnetic absorption may be achieved by following the original principles developed here. For instance, since for non-magnetic particles, optimum absorption is achieved when $a = 2.41\delta$ this means that for particles of any conductivity, optimised magnetic absorption (and hence microwave heating by magnetic induction) can be achieved by simple selection of the mean particle size.

- Conventional approaches to explaining absorption by conducting particles by microwaves use effective medium approximations and statistical approaches [11]. In this work, by considering absorption in individual particles we have highlighted guiding principles for the efficient heating of conducting particles, which are supported by results in the literature [12].

Annex A: Transparent Conducting Oxides in Thin-Film Solar Cells

Additional to the main body of this thesis, Annex A conducts a theoretical investigation of the origin of the mutual properties of optical transparency and electrical conductivity in TCOs. We aim to develop a model of the fundamental properties of carrier concentration and carrier mobility and apply this to the practical example of the performance of TCOs in thin-film solar cells.

High optical transparency and high electrical conductivity are the key performance indicators of TCOs and nowhere is this more keenly felt than in thin-film solar cells. In TCOs, above the Mott Insulator-Conductor Transition, one may increase dopant levels in order to increase the conductivity (though this is may be offset by an associated reduction in mobility). However, as the carrier density is increased, so the optical transparency is diminished. We therefore have a trade-off between transparency and conductivity as a function of carrier density.

We must therefore look towards higher mobilities in order to maximize conductivity and transparency. We propose that in any given TCO system, higher mobilities may be reached by moving closer to the Mott critical density [13].

We model the optical and electrical power transmission through TCO layers in thin-film solar cells as a function of both the electron carrier density, n, and its mobility, μ. The electrical and optical properties of the TCO layer are described by the simple Drude model of the degenerate free electron gas and the concomitant electromagnetic absorption due to skin-depth effects is calculated.

An empirical model of ionized impurity scattering in indium tin oxide (ITO) at high carrier densities [14] allows direct comparison of the μ-n relationship in real TCO layers to the total power absorption in such layers in thin-film solar devices. We determine that decreasing the electron density from 2.6×10^{21} cm^{-3} to 2×10^{21} cm^{-3} in such an ITO layer above the Mott critical density can decrease the total power absorption in the layer by a large amount (around 8% relative to the minimum theoretical absorption).

Summary of major original contributions of Annex A:

- This original work was presented in reference [**Error! Bookmark not defined.**]. We have proposed that producers of TCOs must search closer to the Mott conductor-insulator transition for high-performance materials, where the low carrier density but high mobility is well suited to use in thin-film solar devices.

- We model the optical and electrical power transmission through TCO layers in thin-film solar cells as a function of both the electron carrier density, n, and its mobility, μ. Using an empirical model of real ITO we determine that decreasing the electron density from 2.6×10^{21} cm^{-3} to 2×10^{21} cm^{-3} in such an ITO layer above the Mott critical density can decrease the total power absorption in the layer by a large amount (around 8% relative to the minimum theoretical absorption). This highly significant result will allow optimization of the performance of a given TCO material in thin-film solar cells.

2 MICROWAVE CAVITIES FOR THE MEASUREMENT OF DIELECTRIC MATERIALS

2.1 INTRODUCTION

Microwave resonators provide robust and versatile methods for non-contact and non-destructive measurement of complex materials. Resonators can be constructed at relatively low cost and can yield real-time dynamic measurements of the electrical properties of substances. Resonators take many forms, each of which suited to different tasks of measurement, but all using the same basic principle of extracting information about a sample by the way in which it interacts with the electromagnetic field and how it perturbs the resonance. A resonant measurement technique which is particularly accommodating for samples of arbitrary shape is the cavity perturbation method. This method allows samples to be placed directly into the centre of the cavity, which in the TM_{010} mode is a region of highly uniform electric field. In this way it is possible to isolate the response due to electric field and measure the electrical properties of substances such as dielectric powders.

After a thorough examination of the theory of cavity resonators and the state of the art, this chapter goes on to present a design for a cavity resonator optimised for the measurement of dielectric powders, and with the potential to measure other samples of arbitrary shape. Following this, a novel configuration is developed in which the TM_{010} mode wall currents traverse no boundaries and a ‘split’ may be introduced to give further access to the sample under test. Such a split is highly useful, since extensive access allows parallel monitoring or stimulus of the sample under test by other means. This may mean stimulating the sample by heat, or light; or monitoring the progress of a chemical reaction in parallel using optical as well as electrical means.

The split cavity is investigated at large split widths and its characteristics and potential are discussed. The method is shown to be a dynamic one with easy calibration of the cavity at arbitrary split widths using metal spheres. The cavity maintains a high Q factor; above 7000 even for split widths of 8mm. Measurements of a cylindrical dielectric sample are carried out at increasing split widths to test the robustness of the method. The method is found to work well, but the calibration is not universal for cylindrical samples. This is because the electric fields are no longer uniform at the split for large widths; furthermore this effect is non-linear since the presence of a dielectric sample further distorts the field.

Higher order modes in the cavity are investigated and once more their characteristics and potential are discussed. The TM_{210} mode in particular is marked as a useful mode with interesting applications as a reference, since it is unperturbed by the presence of dielectric samples and maintains a constant relationship with the TM_{010} mode when both are unperturbed. This means that an unperturbed frequency for the TM_{010} mode can be inferred from the TM_{210} mode even when a sample is in place. Furthermore, the TM_{210} mode may be used to track temperature shifts in the cavity to a high degree of accuracy, and the ability of the resonator to resolve mK shifts in temperature is demonstrated. The cavity is measured over a period of 12 hours and as the ambient temperature of the laboratory fluctuates and the ability of higher order modes to track the TM_{010} mode is assessed.

Finally, the split cavity is exploited to measure transparent conducting oxide (TCO) samples under ultraviolet irradiation. A change in conductivity of the TCO is observed as electrons are excited into the conduction band and the TM_{010} mode is perturbed.

2.2 CAVITY RESONATORS: BACKGROUND

2.2.1 Cavity Resonator Fields

The cavity resonator is a useful tool for accurate measurements of microwave dielectric properties. Figure 2.0a) shows the simple cylindrical form of the TM_{010} cavity into which samples are inserted axially and 2.0b) shows the split cavity (with radius 4.6cm and height 4cm) developed in this work.

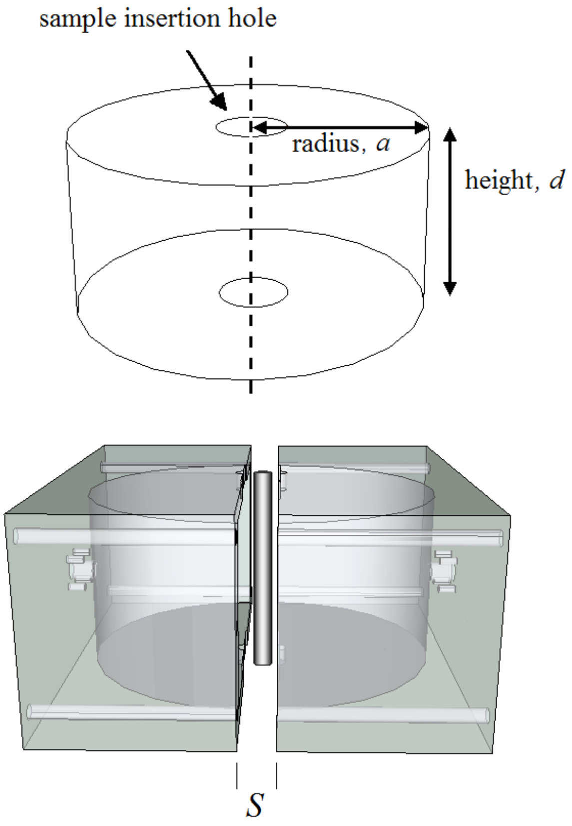

Figure 2.0 – a) The cylindrical cavity resonator (samples are inserted axially) and b) the split configuration realised in this work.

This section aims to provide some of the background theory of the electromagnetic fields and pertinent characteristics of a cylindrical cavity resonator (for a full derivation of cavity fields see [15]). Starting with Maxwell's equations, the fields of a travelling wave can be established in cylindrical coordinates. Necessary boundary conditions are then enforced for propagation in a circular waveguide. Finally, conditions for resonance are imposed by terminating the circular waveguide with conducting end-walls and an expression for resonant frequency is presented.

In a waveguide free of sources, Maxwell's equations may be written as

$$\nabla \times \overline{E} = -j\omega\mu\overline{H} \quad \textbf{(1)}$$

$$\nabla \times \overline{H} = j\omega\varepsilon\overline{E} \quad \textbf{(2)}$$

where ***E*** is the vector electric field, ***H*** is the vector magnetic field, ω is the angular frequency, μ is the permeability and ε is the permittivity.

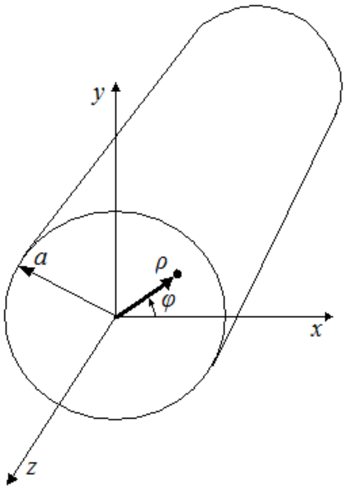

Figure 2.1 – Cylindrical coordinate system

Solving for the curl of ***E*** and ***H*** in cylindrical coordinates we can then resolve for the transverse fields in terms of the z component. Since for TM modes $H_z = 0$, we solve the wave equation for E_z

$$\nabla^2 E_z + k^2 E_z = 0 \quad (3)$$

where $k = \omega\sqrt{\mu\varepsilon}$.

We find a solution of the form

$$e_z(\rho,\phi) = (A\sin(n\phi) + B\cos(n\phi))J_n(k_c\rho) \qquad (4)$$

Where *A* and *B* are arbitrary amplitude constants and $k_c^2 = k^2 - \beta^2$. J_n denotes a Bessel function of the first kind and the integer *n* is introduced since the solution to e_z must be periodic in φ.

The circular component of the *E* field in the TM mode is sinusoidal in form; however, the component radially outwards takes the form of a Bessel function. Boundary conditions dictate that at $\rho = a$, the electric field component E_z must equal zero. So for $E_z(\rho,\phi) = 0$ at $\rho = a$ (where *a* is cavity radius), we must have $J_n(k_c a) = 0$, meaning $k_c = \frac{p_{nm}}{a}$, where p_{nm} is the *m*th root of $J_n(x)$. The propagation constant of the TM_{nm} mode is now

$$\beta_{nm} = \sqrt{k^2 - k_c^2} = \sqrt{k^2 - \left(\frac{p_{nm}}{a}\right)^2} \qquad (5)$$

The above equations describe the electromagnetic fields in a cylindrical waveguide and therefore satisfy the necessary boundary conditions at the conducting walls where $\rho = a$. To apply these equations to the cylindrical cavity resonator we apply the final boundary conditions that $E_\varphi = 0$ and $E_\rho = 0$ at the end walls where $z = 0$ and $z = d$ (where *d* is cavity height). To satisfy these conditions we have $\beta_{nm} d = l\pi$ for $l = 1,2,3,\ldots$ implying that the length of the waveguide must be an integer number of half-wavelengths.

From equation (5) $\beta_{nm} = \frac{l\pi}{d} = \sqrt{k^2 - \left(\frac{p_{nm}}{a}\right)^2}$, $k = \sqrt{\left(\frac{l\pi}{d}\right)^2 + \left(\frac{p_{nm}}{a}\right)^2}$

The resonant frequency of the cavity may now be defined as

$$f_{nml} = \frac{ck_{nml}}{2\pi} = \frac{c}{2\pi}\sqrt{\left(\frac{l\pi}{d}\right)^2 + \left(\frac{p_{nm}}{a}\right)^2} \tag{6}$$

2.2.2 Finite Element Modelling

Finite Element Modelling (FEM) is a useful tool for modelling field distributions in complex structures. Discretising the spatial dimensions of the system to finite elements allows us to solve field equations across the entire domain subject to certain boundary conditions. A comprehensive study of the method can be found in [16]. FEM lends itself to resonant electromagnetic problems of this nature and provides a useful means of optimising the design of the cavity resonator, which can be validated analytically. The FEM package COMSOL will be used in this work.

The model is constructed in two dimensions and given an axial symmetry such that the model domain describes the cylinder of the cavity. Modelling in two dimensions will improve the accuracy of the model, and exploits the symmetry of the problem. For structures without such symmetry, 3D, more complex models are required at a cost of higher computational demand and lower mesh resolution. The governing electromagnetic equations are specified in the transverse magnetic (TM) waves mode of the COMSOL RF-module and are based upon the following wave equation [17],

$$\nabla \times \left(\left(\varepsilon_r - \frac{j\sigma}{\omega\varepsilon_0} \right)^{-1} \nabla \times \overline{H} \right) - \mu_r k_0^2 \overline{H} = 0 \tag{7}$$

which can be simplified to a scalar equation for TM waves since the magnetic fields have only a φ component.

The model is discretised by creating a mesh, which allocates points in space and connects them by forming triangular or quadrilateral elements (in two dimensions) as specified by the user. The accuracy of the results produced in FEM can be directly associated with the quality of the mesh that the problem is solved on. Meshing algorithms can have difficulties meshing complex structures and sharp edges which can cause singularities in the solution. Also, to mesh complex structures effectively requires finer and more numerous elements (especially in three dimensions) making the solution more computationally demanding. The result is that for accuracy in the solution the structure of the model must be as simple as possible with sufficiently fine elements around regions of high field variation. For these reasons, where possible, the cavity model is a two dimensional mesh that is extruded about its axis for rotational symmetry. In this way we ensure the most accurate solution for this already relatively simple geometry.

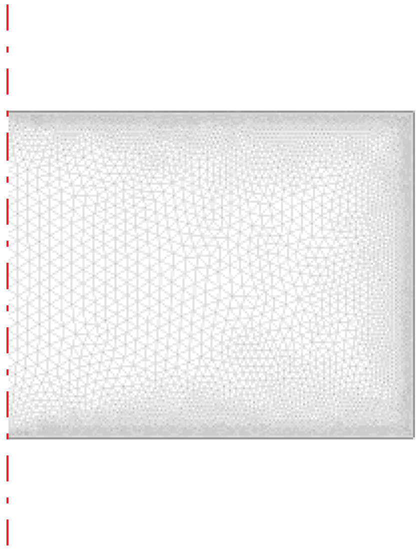

Figure 2.2 – Axisymmetric mesh of cavity structure (axis of symmetry to the left)

The domain within the cavity is set to be air (ε_r = 1) and the boundary condition $n \times \overline{E} = 0$ is enforced on the conducting walls of the cavity such that no electric field exists parallel to the surface.

With the structure, mesh and physics of the model now defined, we turn to solving the problem. In contrast to the analytical approach, where modes of resonance are defined by integer multiples of half-wavelengths and roots of Bessel functions, the FEM approach solves the governing electromagnetic equations for a number of eigenvalues given by $\lambda = -j\omega + \delta$, where the imaginary part ω represents the eigenfrequency and the real part δ represents the damping factor. The damping factor is directly related to the quality factor by Q = ω / δ, and so for highly damped systems, the Q factor is low. The desired mode of resonance will reside at one of the resulting eigenfrequencies. The solver used is the direct linear system solver (UMFPACK).

For initial dimensions of d = 4cm and a = 5cm we obtain an eigenfrequency of 2.294851 GHz and the following TM_{010} electric field distribution, where red indicates high field strength.

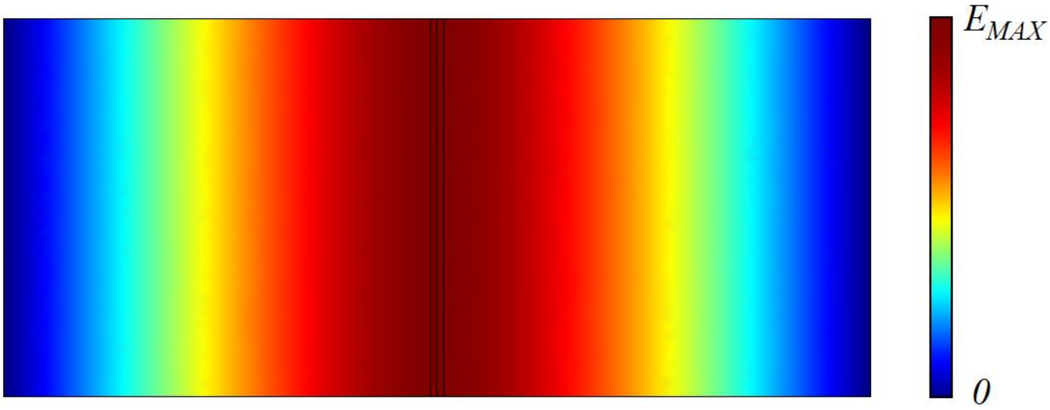

Figure 2.3 – Normalised TM_{010} electric field distribution with high field strength (red) in centre

2.2.3 Cavity Resonator Analysis

The cavity resonator may be represented as an impedance to which electromagnetic energy is coupled either capacitively (to the electric field by an open circuit transmission line) or inductively (to the magnetic field by a short circuit transmission line). Figure 2.4Figure 2.4 – Equivalent circuit for an inductively coupled resonator. m1 and m2 are mutual inductances and Z0 is the characteristic impedance of the coupling lines. shows the equivalent circuit for an inductively coupled resonator. In practice, coupling loops are used. Their mutual inductance is determined by geometrical factors alone.

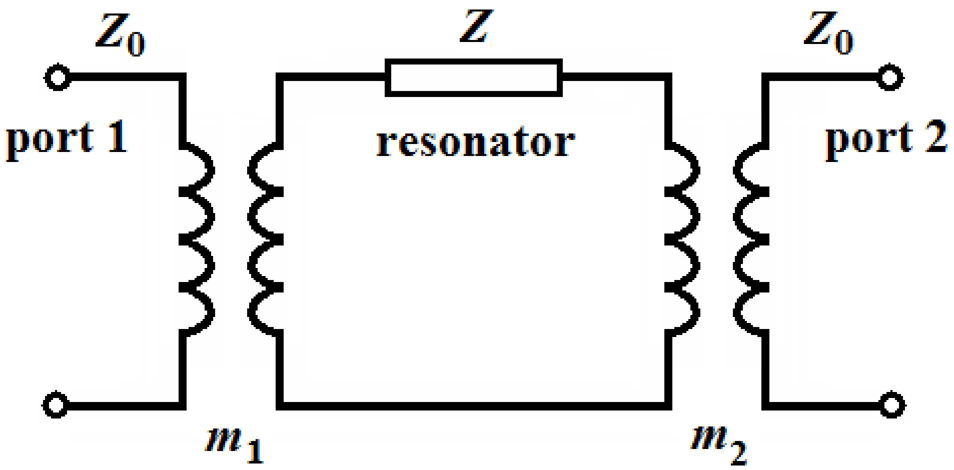

Figure 2.4 – Equivalent circuit for an inductively coupled resonator. m_1 and m_2 are mutual inductances and Z_0 is the characteristic impedance of the coupling lines.

A resonant system is defined by its resonant frequency and bandwidth (the width of the frequency band at the half-power point). The quality factor, or Q factor, is a measure of the 'sharpness' of the resonance, and is related to the bandwidth BW by Q = *f* / BW, where *f* is the frequency of resonance. If the resonator impedance *Z* is modelled as a series LRC circuit, we may exploit transfer matrices to determine a transfer function for the system in the high Q_U limit (where Q_U is the unloaded Quality factor, which describes the resonator alone and does not include the loading effects of the coupling circuit). For the voltage transmission coefficient we have [18]

$$S_{21}(f) = \frac{2\sqrt{g_1 g_2}}{1 + g_1 + g_2 + 2jQ_U \dfrac{f - f_0}{f_0}}$$

where g_1 and g_2 are the dimensionless coupling coefficients and f_0 is the resonant frequency. g_1 and g_2 are defined by

$$g_{n=1,2} = \frac{\omega_0^2 m_n^2}{Z_0 R} = \frac{\omega_0 m_n^2 Q_0}{L}$$

where Z_0 is the characteristic impedance of the coupling lines (usually 50Ω).

For the power transmission coefficient, we take

$$P(f) = |S_{21}|^2 = \frac{4g_1g_2}{(1+g_1+g_2)^2 + 4Q_U^2\left(\frac{f-f_0}{f_0}\right)^2}$$

At resonance, $\left(\frac{f-f_0}{f_0}\right) \to 0$, and we have a peak power, $P_0 = \left(\frac{2g}{1+2g}\right)^2$ for symmetric coupling. If

$$Q_L = Q_0\left(1-\sqrt{P_0}\right) \tag{8}$$

we have
$$P(f) = \frac{P_0}{1+4Q_L^2\left(\frac{f-f_0}{f_0}\right)^2}$$

where Q_L is the loaded quality factor, which accounts for the loading effect of the coupling circuit.

The resonance power transmission $P(f)$ described above forms a Lorentzian lineshape. Fitting the resonant peak to the Lorentzian form allows us to extract parameters such as resonant frequency f_0 and loaded Quality factor Q_L (which may then be unloaded to remove the effects of coupling using equation (8). These parameters are then used to measure materials by perturbation analysis, which is discussed further in section 2.3.3.

2.2.4 Cavity Design Considerations

Care taken during the design of a resonant cavity can help to ensure its effective operation. The immediate concerns are size and resonant frequency, but as we shall see in this section many more subtleties are pivotal in achieving optimum performance and ensuring that the cavity is fit for purpose.

The cavity is designed to operate in the TM_{010} mode, though subsequently we may exploit higher order modes. The TM_{010} mode will create a uniform electric field in the centre of the cavity into which a sample can be inserted to measure the electrical properties. This mode is ideal for measuring electrical properties in the region of the cavity axis; however we must be aware of other modes operating in the cavity and the effect of the presence of these modes.

The method of interpreting measurements from resonance involves measuring the frequency shift and bandwidth change of the perturbed mode. Analysis of the resonant circuit shows that this resonance forms a Lorentzian lineshape in the frequency domain, but the presence of other modes in the vicinity of the mode being measured will distort the lineshape from the ideal Lorentzian causing any measurements to be inaccurate. For this reason, we require the TM_{010} mode to be isolated from other frequencies. This must be taken into account when specifying the dimensions of the cavity for the required resonant frequency.

Samples are to be inserted into the cavity along the axis at the point of high field intensity. It is therefore necessary to have holes in the top and bottom plates wide enough to accommodate sample tubes, but small enough to avoid disturbing the electromagnetic fields too much. The holes will distort the uniform electric fields in the centre of the cavity, though this effect can be offset by increasing the height of the cavity. The distortion effect is then proportionally reduced when compared to the length of sample placed in the electric field. We note that extending the cavity height will change the resonant frequency, but also may introduce more resonant modes into the frequency region of the TM_{010} mode. Given that a number of modes will be present in the cavity, the design must allow us to couple directly to the appropriate fields i.e. the fields that contribute to the electric field in which measurement takes place.

Having developed an analytical method and a FEM method for analysis of the resonant cavity it is now possible to investigate some of the issues of design that were discussed in the previous section. Optimisation of the design at this stage will prevent problems with the cavity during operation and ensure that maximum efficiency is achieved.

When determining the cavity dimensions for operation at a desired frequency, it is possible to produce a mode chart which details all possible modes and their frequencies.

Since for TM modes
$$f_{nml} = \frac{ck_{nml}}{2\pi} = \frac{c}{2\pi}\sqrt{\left(\frac{l\pi}{d}\right)^2 + \left(\frac{p_{nm}}{a}\right)^2},$$

and for TE modes
$$f_{nml} = \frac{ck_{nml}}{2\pi} = \frac{c}{2\pi}\sqrt{\left(\frac{l\pi}{d}\right)^2 + \left(\frac{p'_{nm}}{a}\right)^2},$$

the first eleven modes of a mode chart for a cylindrical cavity resonator chart are as follows:

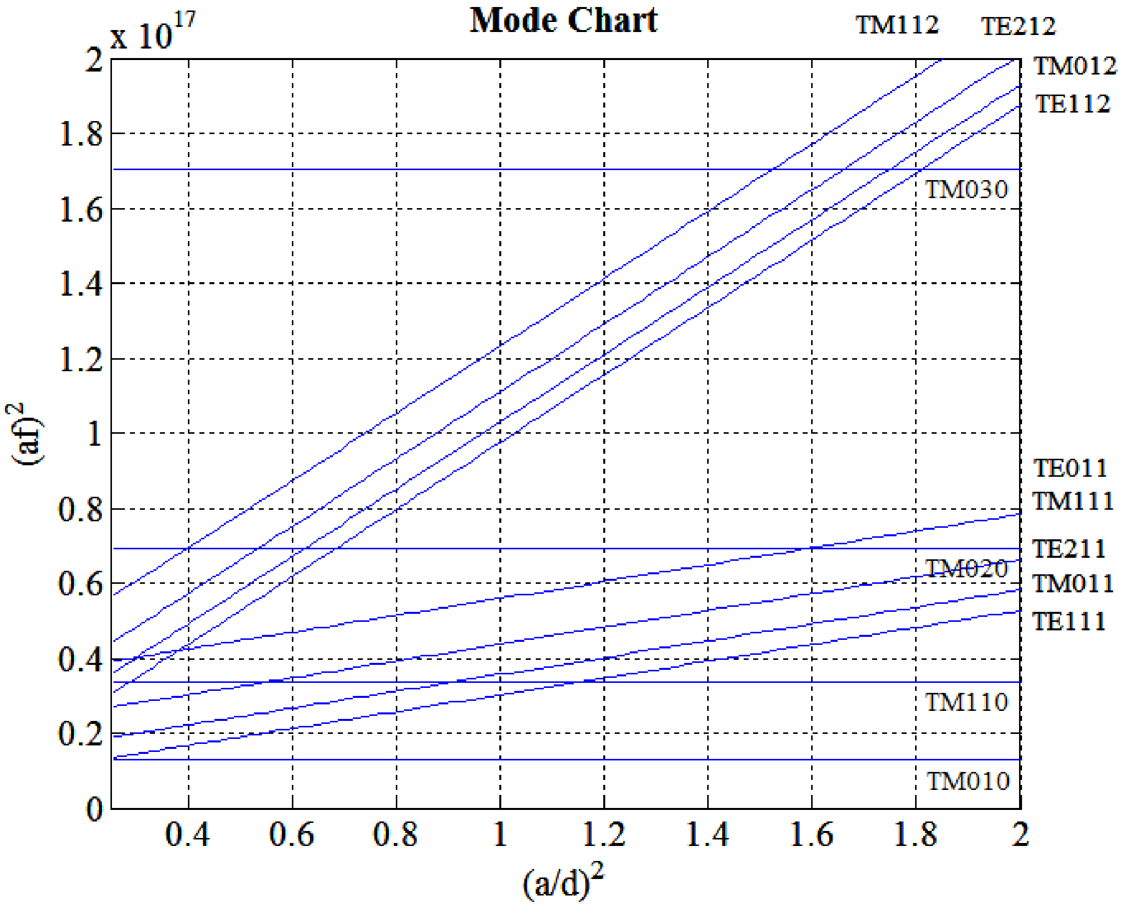

Figure 2.5 – Mode chart for cylindrical cavity resonator

The ordinate axis $(af)^2$, of the mode chart is normalised with the value of the radius a

and so the graph becomes invariant as dimensions are scaled. The mode chart is therefore extremely useful for seeing which modes are in operation for any given cavity size. Note that the horizontal lines describe modes which are affected only by the cavity radius and not by the cavity height; these include all TM_{mn0} modes.

Taking the cavity described in previous sections as an example we see that for d = 4cm and a = 4.6cm, $(a/d)^2$ = 1.3225. The mode chart shows that the TM_{010} mode which is required for measurement is clear of any other interfering modes. The chart shows that the TM_{010} mode is clear of other frequencies by over 1 GHz as demonstrated in the following table. In the next section (2.3), a cylindrical cavity is constructed with radius a = 4.6cm and height d = 4cm, such that the TM_{010} mode is clear of other modes and suitable for the high frequency measurements subsequently described in this work.

Mode	***f* GHz**
TM_{010}	2.4946
TM_{110}	3.9748
TE_{111}	4.2060
TM_{011}	4.5019
TE_{211}	4.9070
TM_{210}	5.3274
TE_{011}	5.4629
TM_{111}	5.4629
TM_{020}	5.7258
TE_{112}	7.7344
TM_{012}	7.8993
TM_{030}	8.9766

Table 1 – Resonant modes and corresponding frequencies for cavity with for *d* = 4cm and *a* = 4.6cm.

Note that though a cavity of these dimensions is clear of modes conflicting with TM_{010}, if *d* increases relative to *a* (or if *a* decreases relative to *d*), the cavity may enter a region affected by unwanted modes. This becomes important for high accuracy measurements in the TM_{010} mode, but we shall see that in order to exploit higher order modes, distortion by other local modes is a small sacrifice for the increased functionality.

The distortion of the uniform electric fields at the centre of the cavity as mentioned above is remedied by the relatively large height of the resonator compared to the small aperture through which samples will be inserted. This aperture is expected to be no more than 5mm in diameter.

With some room for manoeuvre we are able to tune the cavity to bring it into line with commonly used microwave frequencies. With a cavity height *d* = 4cm it is found that for TM_{010} resonance at 2.45GHz, the cavity radius must be 4.68cm.

Using the TM_{010} mode for dielectric measurement has major advantages such as minimal sample depolarisation high electric and magnetic field separation and high field uniformity along the axis. Though the cavity described here is designed to isolate the TM_{010} mode and, for high accuracy, keep the resonant peak free from the distorting effect of other modes, in subsequent sections higher order modes will be used to provide further data. Indeed, other modes are used to provide temperature data, multiple frequency dielectric data and even reference points for automatic calibration using the TM_{210} mode.

2.2.5 An abridged historical development of the Cavity Resonator

Resonant perturbation techniques have been used for many years. In 1945, Maclean et al. published a paper describing the reactance theorem for a resonator [19], which was closely followed by methods for cavity perturbation measurements [20] following the approach of Works, Dakin and Boggs, which were developed in parallel with Horner et al. [21,22]. In subsequent years, the method was extended and refined, for example, to include correction factors for the presence of sample insertion holes [23] and microwave perturbation methods became prolific and versatile techniques used in many areas of scientific enquiry. Early examples include the measurement of electron density in plasma columns [24,25]. Precise analytical field solutions were developed for TM_{010} cavities with cylindrical samples inserted along the axis. Transcendental equations were also developed to include the effect of the presence of sample-holding tubes [26]. The work of Kobayashi [27], Krupka [28], and Kajfez [29] continued to provide innovative approaches to measurement using this versatile technique, even forgoing the requirement to have full resonant structures by using quarter-cut image resonators [30] and half-cut image resonators [31].

In 1988, Kent et al. [32] set out an approach using a split resonant cavity to measure the complex permittivity of dielectric plates non-destructively. Using the TE_{011} mode, the cylindrical cavity was split half way along the length of the cylinder and dielectric plates were inserted. As the method was developed, the highly complex fringing fields in this configuration were solved rigorously using the Ritz-Galerkin method since analytical modelling of such evanescent fields is notoriously difficult. This proved to be a particularly useful technique and became a Japanese Industrial Standard (JIS R 1641) for the measurement of dielectric plates [27].

The benchmark was set in microwave cavity perturbation techniques with the publication in 1993 of three papers by Klein et al. [33,34,35]. These papers set out the principles, experimental scheme and applications of the techniques described and formed the basis for further development in the area of resonant microwave measurements. Today, the possibilities for applications of these versatile techniques seem countless. Recent publications continue to increase the accuracy of such measurements and examine novel techniques, for example employing higher-order modes [36], using microwave cavity technologies in the processing of materials [37] and even for measurement of the quantum hall effect [38].

2.3 The TM_{010} Split Cavity

In this section we develop a split TM_{010} cavity resonator. In contrast to the split cavity encountered in the previous section, which forms Japanese Industrial Standard, JIS-R-1641 for measurement of dielectric plates, the TM_{010} split cavity has the split in a different plane. The TE_{011} mode cavity has a split in the plane half way along, and perpendicular to the length of the cylinder. The TM_{010} cavity split is in the same plane as the sample insertion hole axis and is shown in Figure 2.9. A comprehensive discussion of the merits of such a configuration is deferred to subsequent sections, but accurate measurements may be taken with a large gap present. This benefit is utilised in the TE_{011} mode to measure plate samples, but using the TM_{010} mode we may measure samples of arbitrary shape in the highly uniform electric field, with unprecedented access to the sample under test.

A cylindrical cavity operating in the TM_{010} mode provides a highly uniform electric field at its centre. The radial electric field forms a Bessel function of the first kind and a sample can be inserted axially into the point of highest field strength. The frequency of operation of this mode is given by

$$f = \frac{ck_\rho}{2\pi} \qquad k_\rho = \frac{p_{01}}{a} \tag{9}$$

where c is the speed of light in free space, p_{01} = 2.4048 is the first root of the zeroth order Bessel function of the first kind $J_0(x)$ and a is the radius of the cavity. Note that the frequency of the resonant mode is determined by the radius of the cavity alone, since there are no variations of either the electric or magnetic fields along the z axis in this mode.

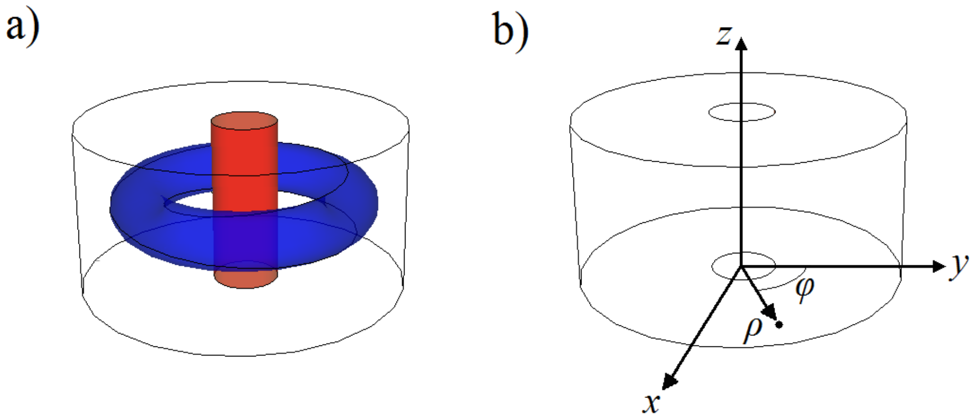

Figure 2.6 - a) Schematic of cavity fields in the TM_{010} mode showing the electric (cylinder) and transverse magnetic (toroid) fields. b) Cylindrical coordinate system for the cavity resonator.

The length of the cavity does not affect the frequency of resonance for this mode, but a longer cavity leads to mode degeneracy, which cause uncertainties in measurements. For the TM_{010} mode, the highly uniform electric field in the centre of the cavity and the axial insertion of the sample provide a configuration that may be considered to be in the quasi-static regime, vastly simplifying the analysis and leading to a more robust experimental arrangement. As will be seen in subsequent sections, the maximum Q for any of the TM_{0n0} modes occurs when the cavity length d equals the radius a.

2.3.1 Sample depolarization

In a cavity perturbation measurement using the TM_{010} mode, the inserted sample should be parallel to the *E*-field to avoid depolarization. The sample may then be a long, thin cylindrical sample, or a thin flat sample, both inserted along the axis. Indeed, as long as the sample passes through the cavity completely, and the sample volume is known, the (uniform) cross-section may be arbitrary. Since the parallel electric field is continuous at a material boundary, this configuration exhibits the smallest amount of sample depolarisation and so leads to the maximum attainable electric dipole moment of the sample. This is necessary for the sample to provide the maximum possible shift in resonant frequency and decrease in Q factor for the measurement of its complex permittivity using the cavity perturbation technique.

This behaviour is easily illustrated by calculating the power dissipated in a cylindrical sample of water at 2.45 GHz (the frequency of microwave ovens), firstly parallel to the electric field, then perpendicular to the field.

For a long, thin sample *parallel* to the *E*-field as in Figure 2.7a), the internal field is roughly equal to the applied field, $E \approx E_0$

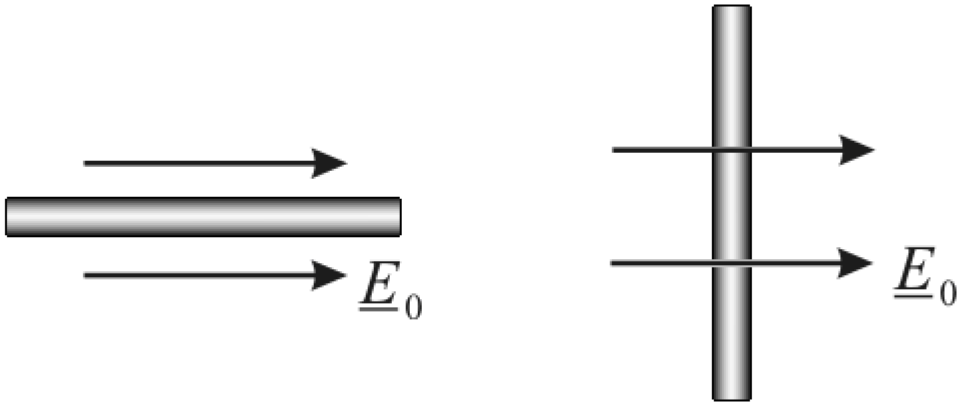

Figure 2.7 – a) Cylindrical sample in parallel, non-depolarising configuration, and b) Cylindrical sample in perpendicular, depolarising configuration.

For the power dissipated in the sample with parallel configuration we have

$$\langle W \rangle_{parallel} = \tfrac{1}{2}\,\omega\varepsilon''\varepsilon_0 E_0^2 V_s$$

where ε_0 is the permittivity of free space, ε'' is the imaginary permittivity of the sample, ω is the angular frequency of the applied electric field and V_s is the volume of the sample.

In a dielectric, permittivity is a measure of the polarisation of the sample to an incident electric field. This is a mechanism of energy storage, but in an oscillating electric field the losses incurred may be quantified by an imaginary permittivity. The complex permittivity of a sample therefore gives details of energy storage (real part ε') and loss (imaginary part ε''). We have a complex permittivity, $\varepsilon^* = \varepsilon' - j\,\varepsilon''$, the imaginary part of which quantifies the loss mechanisms present and may be used to determine power dissipation (i.e. heating) in the sample.

For a sample which is *perpendicular* to the applied field as in Figure 2.7b), the internal field is reduced due to depolarisation giving [39]

$$E \approx \frac{2E_0}{1+\varepsilon^*} \approx \frac{2E_0}{\varepsilon' + 1 - j\varepsilon''}$$

and for the power dissipated in the sample with perpendicular configuration we have

$$\langle W \rangle_{perpendicular} = \tfrac{1}{2}\omega\varepsilon''\varepsilon_0 EE^* V_s = \tfrac{1}{2}\omega\varepsilon''\varepsilon_0 E_0^2 V_s \frac{4}{(\varepsilon'+1)^2 + \varepsilon''^2}$$

Since water has a complex permittivity $\varepsilon^* \approx 79.9 - j9.2$ at 2.45 GHz [40,41], the power dissipated in the same water sample in the parallel configuration is larger by a factor of 1660 than in the perpendicular configuration.

Depolarisation is often overlooked when exciting samples at microwave frequencies and since many cavities used to deliver electromagnetic energy do not have simple field distributions, depolarisation is inevitable. In this work, the effects of depolarisation are minimized in the TM_{010} mode and the Split Post Dielectric Resonator (described in the subsequent chapter), which has a circularly polarised, non-depolarising E-field for sheet samples.

2.3.2 Cavity construction

Resonant techniques are most often used for measurement of medium to low loss samples. However, by reducing sample size it is possible to measure high loss samples effectively. A high quality factor and large dynamic range are necessary in order to extend the range of the cavity to samples with large losses. In search of a high Q-factor, we must account for the losses in the cavity. When the sample is inserted, the loaded Q-factor has contributions from other sources of loss such as resistive losses in the cavity walls and coupling losses. The contributing Q-factors are related as follows:

$$\frac{1}{Q_L} = \frac{1}{Q_{resistive}} + \frac{1}{Q_{coupling}} + \frac{1}{Q_{sample}} \qquad (10)$$

Coupling losses can be accounted for by measuring the cavity insertion loss, but resistive losses in the cavity walls must be minimised to achieve high Q. The walls must therefore be made of a highly conducting metal. Difficulties arise in construction when the mode of interest causes current flow over a join in the cavity walls, which can cause dramatic losses and a large reduction in Q. In the TM_{010} mode (and TM_{0n0} modes in general) the surface current flow is vertical (i.e. along the z axis) in the curved side-wall and radial on each of the two flat end-plates. A conventional cavity construction would consist of a hollow cylinder with two end-plates, but in the TM_{0n0} mode this yields current flow across the metal joins, with a possible suppression of Q factor. Attempts have been made to minimise losses from these boundaries, and such methods have included use of the TM_{020} mode, with the break in the cavity walls positioned at the *H*-field null point, where no currents flow on the metal surface [42]. In this work, the novel construction shown in Figure 2.9 results in surface current flow parallel to any joins preserving a high Q (here above 8000), but importantly the split configuration permits the continued use of TM_{0n0} modes even when the gap, *S*, becomes large. In subsequent sections it will be shown that for splits of up to 8mm, the Q factor remains high enough (>7000) to take measurements with less than 3.5% error based upon conventional measurements with no gap. This enables unprecedented access to samples under test in a highly uniform TM_{010} E-field, offering a simple method to combine other complementary measurement techniques or for stimulus by light or heat.

For an operating frequency of 2.5GHz, we have a = 4.6cm. This is chosen (as opposed to exactly 2.45 GHz) since the dielectric loading of the sample reduces the frequency slightly, so that the measurement is taken closer to 2.45 GHz. The height of the cavity, d, is such that the uniformity of the E-field is not compromised by the insertion hole and mode degeneracy is avoided by limiting d. The dimensions of the cavity also influence the Q-factor of the resonator. For resistive losses in the cavity walls

$$Q_{resistive} = \frac{\omega \iiint_V \mu_0 |H|^2 dV}{R_S \iint_S |H|^2 dS} \qquad \mathbf{(11)}$$

where V denotes integration over the entire volume for energy stored in the cavity and S denotes integration over the surfaces of resistance R_s, for power dissipated in the walls and end-plates. Analytic integration of equation **(11)** for the purely azimuthal magnetic field present within any of the TM_{0n0} modes yields

$$Q_{resistive} = \frac{a/\delta}{1 + a/d} \qquad (12)$$

where δ is the classical skin depth in the metal cavity walls at the resonant frequency.

Using equations (9) and (12), for fixed length d the maximum Q is attained when $a = d$, giving $Q_{max} = a/2\delta$. This is lower than the Q produced by some other modes (e.g. TE_{011} in particular), but this is not a major sacrifice given the highly uniform axial electric field generated. Figure 2.8 shows the effect of varying the radius and length of the cavity upon the Q-factor in the TM_{010} mode. The power dissipation ratio is linear since with increasing a, the ratio of end plate area to side wall area increases as a^2/a. For increasing length, the diminishing contribution from end-plate loss causes Q to plateau.

a)

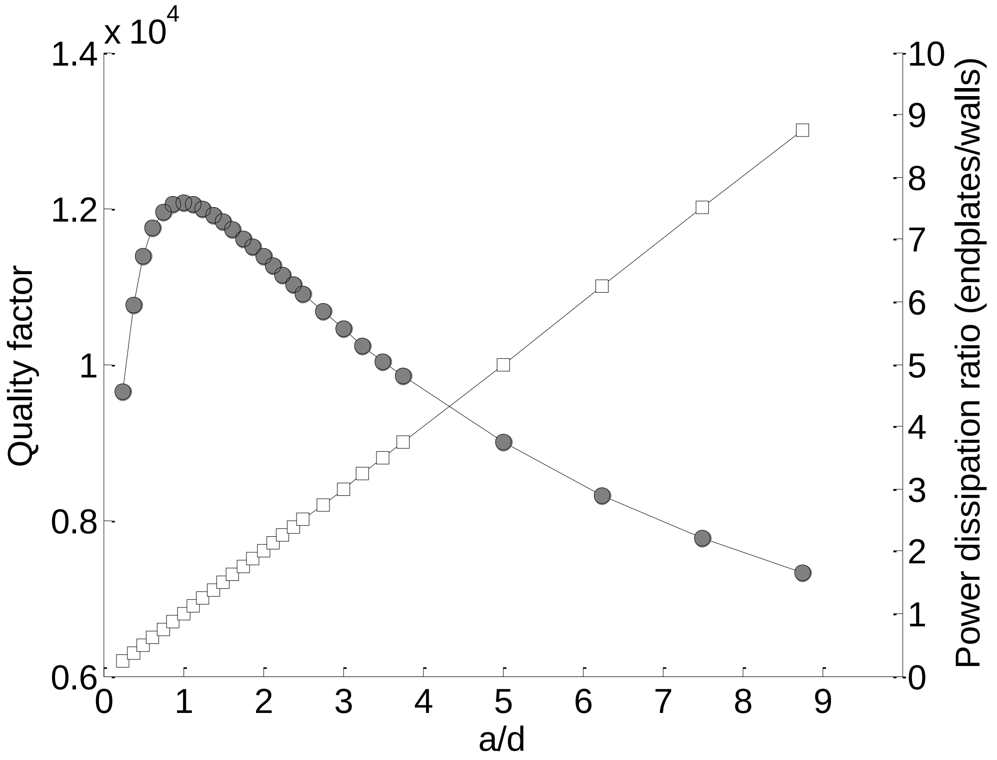

b)

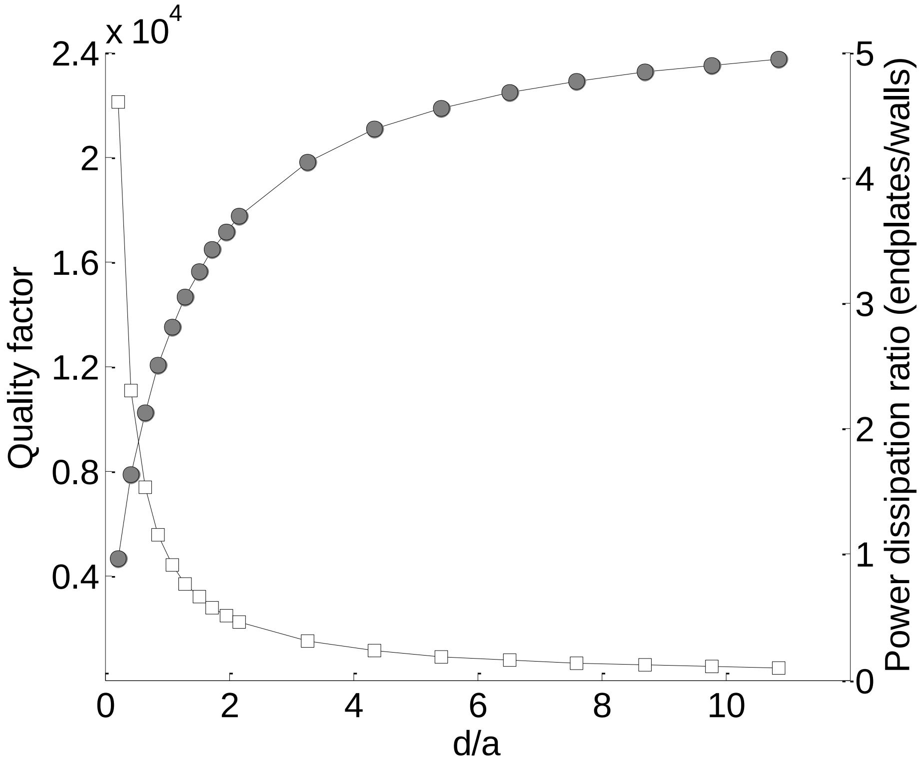

Figure 2.8 – Theoretical Quality factor (circles) and power dissipation ratio (squares) for a) increasing cavity radius and b) increasing cavity length. For an aluminium wall resistivity of 2.8×10^{-8} Ωm.

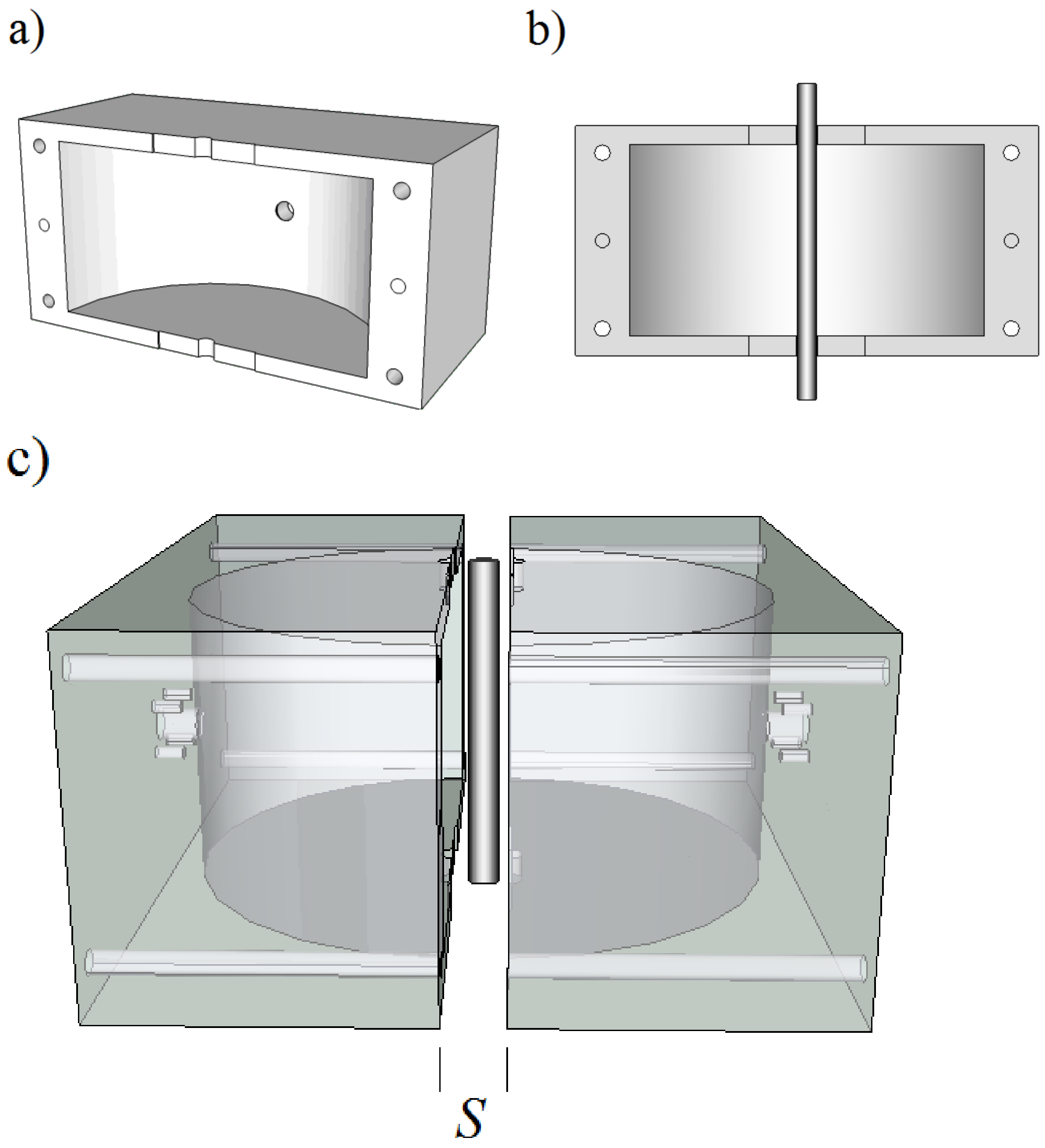

Figure 2.9 – a) Half of cavity construction formed by one aluminium block. In this configuration the wall currents avoid traversing any lossy boundaries. b) Plan view of cavity with cylindrical sample inserted axially. c) Transparent schematic of complete split cavity with split size S, and cylindrical sample inserted axially.

The cavity is constructed from two identical aluminium blocks. Into each is machined a half-cylinder that provides an uninterrupted surface for current-flow. A cutter program developed using a Delcam machining package is used to mill the half-cylinder from each block. Use of a 5mm Ball Nose cutter enables milling without creating any discontinuities in the cavity walls. The resulting cavity height is 4cm and the radius is 4.6cm. Capacitive coupling is realised using pin-terminated square SMA launchers, positioned diametrically opposite to each other. Symmetric coupling is attained by adjusting the pin lengths and measurements of S_{21} are performed in the frequency domain using an Agilent E5071B vector network analyzer.

The assumptions of perturbation theory allow the use of much simplified equations relating frequency and bandwidth shifts to the real and imaginary parts of the permittivity. As the sample size begins to grow, perturbation theory begins to break down and fields can no longer be considered to be within the small perturbation limit. In many configurations this makes the analytical approach intractable and an inversion based upon this method is no longer valid. In this case, computational modelling of the fields may permit the calculation of material properties for larger samples, where the distribution of cavity fields or the fields inside the sample itself may be considerably different. In the TM_{010} mode the simple field distribution within the cavity has enabled the derivation of analytical results for a rod inserted axially into a cylindrical cavity [26]. This, in theory, permits the analytical inversion of resonant measurements for samples of any size. In practise, once occupying a large proportion of the cavity, even low-loss samples will cause resonance to be significantly damped.

2.3.3 Measurement principles and Calibration

In order to measure the complex permittivity ε^*, of a sample, two independent parameters must be measured. Upon insertion of a sample, the change in resonant frequency and change in bandwidth can be related to the real and the imaginary parts of the permittivity respectively. Figure 2.10 shows the resonant curve of the empty cavity (blue) and the cavity with a sample inserted axially (red). When the dielectric sample is introduced into the high electric field of the TM_{010} mode, the frequency of resonance decreases, and the bandwidth increases.

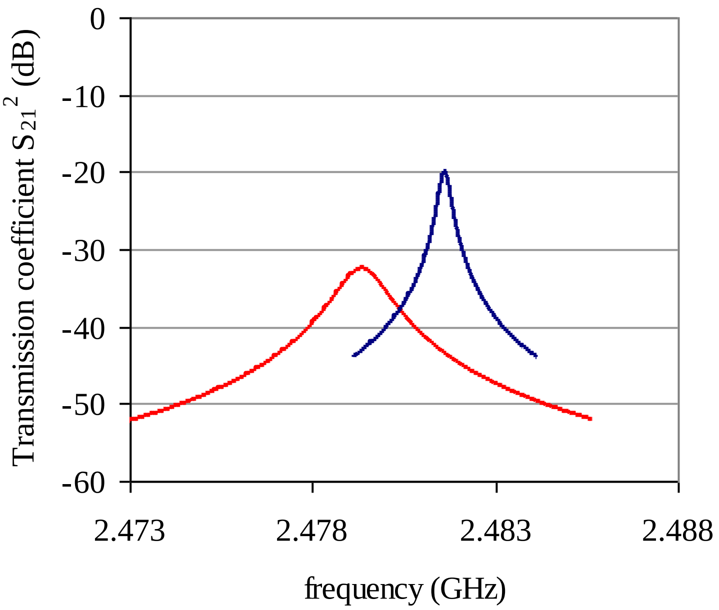

Figure 2.10 – Resonant curve of the TM_{010} cavity before (blue) and after (red) sample insertion.

It can be shown that for a sample in a polarizing field [33]

$$\frac{\Delta f}{f}=\frac{-\mathrm{Re}\left(pE_0^*\right)}{4U} \qquad \frac{\Delta BW}{f}=\frac{-\mathrm{Im}\left(pE_0^*\right)}{2U} \tag{13}$$

where p is the (complex) dipole moment created by the inserted sample, E_0 is the cavity electric field and U is the stored energy in the cavity.

Therefore we can relate the induced dipole moment to the fractional frequency shift and fractional bandwidth shift. The real part of the dipole moment relates to polarization in a sample and the imaginary part relates to losses. For any given sample, we can measure the complex dipole moment, simply by observing the shift in frequency and bandwidth upon insertion into the polarizing field. The dipole moment can then be used to infer material properties of the inserted sample.

Before testing samples in this manner, we must first calibrate the measurement. This calibration can be done using a sample of known permittivity, which will form a known dipole moment in the polarizing field. Here we use precision manufactured, vanadium coated steel spheres, which form well-defined dipole moments upon insertion. From this known dipole moment, we will calibrate the parameters of the measurement.

The dipole moment created by a metal sphere in a uniform electric field is $p = 4\pi\varepsilon_0 a^3 E_0$

Since

$$U = \frac{1}{2}\varepsilon_0 \int_{cav} E^2 dV \tag{14}$$

Substituting for dipole moment p, in equation (13) and using equation (14) we obtain, for a metal sphere

$$\frac{\Delta f}{f} = \frac{3}{2}\frac{V_s}{V_{eff}} \tag{15}$$

where V_s is the sample volume, and

$$V_{eff} = \int_{cav} \frac{E^2}{E_0^2} dV \tag{16}$$

Since the E-field in equation (16) is normalised to the peak field E_0, upon integration throughout the volume, the resulting V_{eff} will be some value less than the volume of the cavity and can be considered as an effective volume occupied by the cavity fields. The simple relation shown above can be applied to any sample under test, provided that the dipole moment can be solved. V_{eff} therefore becomes a universal constant for the cavity (within the small perturbation limit) that can be used for any further samples measured in the same configuration. For the TM_{010} mode it can be shown that $V_{\mathrm{eff}}/V_{\mathrm{cavity}} = J_1^2(p_{01}) = 0.267$. For the cavity considered here, with radius 4.6cm and height 4cm, this yields $V_{eff} = 71.6\mathrm{cm}^3$. For the case of metal spheres in equation (15) we now have the means to directly calculate the shift in frequency for a given sample volume.

Measurements are taken using an Agilent ENA 5071B Vector Network Analyser (VNA). The loading effect of the coupling arrangement on the measured bandwidth is removed using the measured insertion loss. Precision manufactured, vanadium coated steel spheres of increasing radius were inserted into the centre of the cavity E field and the shift in resonant frequency observed.

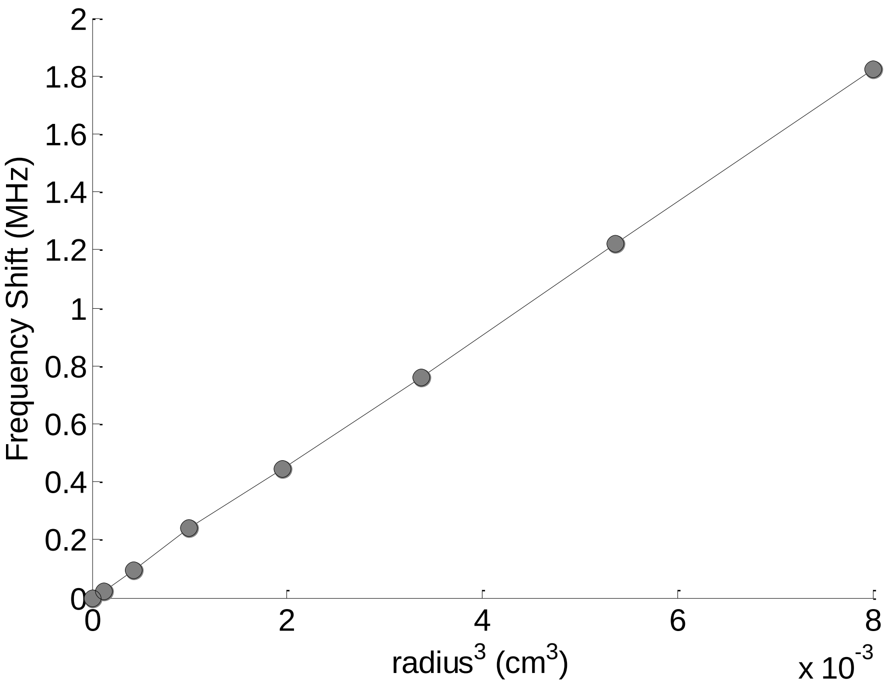

Figure 2.11 – Frequency shift plotted against a^3 for a series of metal spheres (i.e. vanadium coated steel balls) inserted into the cavity. The response is seen to be highly linear to within 1%, demonstrating the robustness of the approach. Any deviations from linearity are due to uncertainties in the size of the sphere rather than the frequency measurement.

Since, from (15) we have

$$\frac{\Delta f}{a^3} = \frac{2\pi f}{V_{eff}}$$

from the gradient of the line we establish V_{eff} = 69.7cm^3. The value obtained by integrating the electric field across the cavity volume is 71.6cm^3, which is remarkably close, but the small difference is associated with the modification of the electric field in the vicinity of the sample hole, corrections for which will be discussed in subsequent sections. The ability of this calibration technique to fully account for these fringing fields in one simple measurement will prove invaluable for a split cavity, in which the fringing fields at the split are substantial. The validity of split cavity calibrations shall be explored in subsequent sections.

By using this calibrated value for the effective volume, any sample for which the dipole moment can be solved can be measured. Equations (13) may be used to determine the relationship between the complex permittivity and the shift in either resonant frequency or bandwidth. For cylindrical samples passing completely through the cavity in a non-depolarising configuration, it can be shown that the dipole moment is $p = (\varepsilon_r - 1)\varepsilon_0 E_0 V_S$. From (13) and (14) we now have

$$\frac{\Delta f}{f} = -\frac{(\varepsilon' - 1)}{2}\frac{V_s}{V_{eff}} \qquad \frac{\Delta BW}{f} = \varepsilon'' \frac{V_s}{V_{eff}} \tag{17}$$

2.3.4 On calibration, corrections and uncertainty

For resonant perturbation measurements, the method of calibration is critically important for ensuring accurate results. Conventionally, perturbation measurements are inverted analytically, empirically, or numerically. The analytical approach is valid for simple structures in which the perturbation effect upon the electromagnetic fields of the presence of a sample can be solved. For cavity perturbation of the TM_{010} cylindrical mode, the analytical approach used in section 2.3.3 resulted in a value V_{eff} = 71.6cm^3. This value is valid for the inversion of measurements using equations (17), but is an idealised case. The analytical result for the inversion of measurements cannot account for fringing fields without some correction factor. Also, this approach cannot account for experimental errors in measurement, whereas empirical calibration methods can. In the previous section it was shown, using the known dipole moment of a metal sphere, that the experimental value of V_{eff} was 69.7cm^3. This is certainly a more reliable approach given the assumptions made by the analytical approach of a perfectly formed cylinder with no fringing fields and perfectly obeyed boundary conditions.

Empirical calibration by known materials is clearly the more desirable approach since it accounts for experimental errors that theoretical methods cannot. But comprehensively characterising complete inversion behaviour for samples of arbitrary complex permittivity is impractical and this ‘black-box’ approach tells us nothing of underlying causes and mechanisms.

Numerical approaches such as Finite Element Modelling (FEM) are suited to more complex structures for which field distributions cannot be solved analytically. In another ‘black-box’ approach, FEM may be used to establish inversion values for arbitrary complex permittivity, and a complex frequency may be obtained, which implicitly includes all higher order effects. This method is useful and helps one to understand the electromagnetic behaviour of the system, but once more we rely upon a predetermined inversion ‘look-up’ table and the results are only as accurate as the model used. Use of a look-up table is not a problem per se, and indeed, for conventional cavity measurements, this FEM type inversion has become popular [43], but for investigations where a split is present, empirical calibration is certainly the most dynamic approach.

When the cavity split is present, the analytical approach is flawed and any attempts to model the fields at the split become cumbersome; modelling evanescent fields is often impractical in a non-trivial geometry. For conventional cavity configurations the geometry is far simpler and methods to correct for evanescent field at the sample insertion hole have been relatively successful. Mode matching is carried out at the insertion hole and integrating the cavity fields at the interface enables simple matching to the evanescent TM_{01} field which decays rapidly outside of the cavity. For the split cavity, mode matching at each of the four interfaces of the split leads inevitably to vast assumptions about the forms taken by the matched fields. For example, matching the TM_{010} mode E-field at the top and bottom end-plates of the resonator requires approximating the axially symmetric field in rectangular coordinates; this is shown schematically in Figure 2.12a) and quickly becomes inaccurate as the cavity is split. Numerical approaches to modelling the fringing fields as shown in Figure 2.12b) are much better.

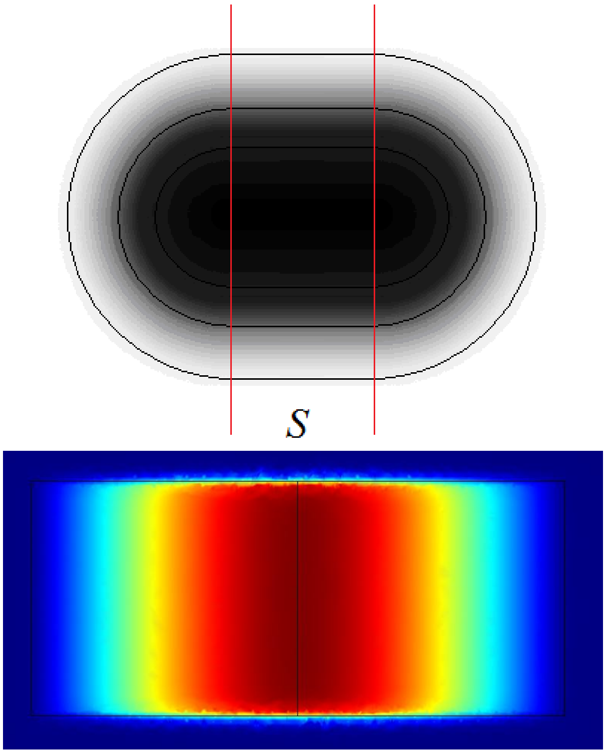

Figure 2.12 – a) Plan view of a schematic approximation of TM010 cavity E-field strength (dark is high). As the two halves of the cavity are separated by the split, S, this approximation breaks down. b) Side view of FEM model of fringing E-field at the cavity split (red denotes high field).

As we shall see, it may be impractical to use a numerical inversion such as that obtained from finite element modelling when a cavity split is present. One of the greatest sources of error is the limited accuracy of FEM models, which is acceptable for enclosed, precision machined cavities, but for a cavity with an arbitrary split width, we must use some form of empirical calibration.

To calibrate the measurement at each split width we may use a sample of known complex permittivity, but it is simply easier to use the universal approach described in section 2.3.3. Prescribing a set split width at which to measure a sample introduces experimental errors in the setup. This is because even minor errors in the width of the split make the theoretical model irrelevant. But in accordance with the dynamic calibration using a metal sphere described above an accurate experimental value of V_{eff} is obtained for the inversion. Any significant errors in measurements at large split widths subsequent to this quick and easy calibration are not directly due to errors in the cavity setup.

At this point we note the more general limitations of the perturbation approach. This approach is a simplification of the real situation. It relies upon a model of the resonant system, by which *small* perturbations to the electric field yield meaningful data. The unperturbed and perturbed fields are considered to have the same field distribution. This is evident in equation (16), where integration of the perturbed field, normalized by the unperturbed field leads to a value which enables our inversion based upon approximations of linear relationships between a) real permittivity and frequency shift and b) imaginary permittivity and bandwidth shift. This exposes the limitations of the perturbation technique, since there is not a linear relationship between these parameters at high values of real or imaginary permittivity and neither are the perturbed and unperturbed fields the same. We conclude that these higher order effects are irrelevant if we remain within the limits of perturbation theory, but it is possible to account for all of the non-linear effects encountered if calibration is carried out using samples of known complex permittivity. A non-linear function of complex permittivity may be obtained which is related to the shift in complex frequency

$$\Delta\tilde{f} = \Delta f - j\frac{1}{2}\Delta BW = m(\varepsilon', \varepsilon'')$$

where the imaginary part is the shift in frequency and the real part describes the shift in bandwidth. The complex frequency describes the function *m*, which is dependent upon the real permittivity ε' and the imaginary permittivity ε" of the sample.

But as discussed above, use of the complex frequency would require full characterization of the complex space of interest. This is no good for the split cavity since the largest source of error would be the accuracy to which we could define the split (and model it accordingly). The empirical method of the metal spheres enables a quick and dynamic calibration of the split cavity, which does not require knowledge of the split width.

One particular limitation of the perturbation approach, which is resolved by using the complex frequency is a higher-order effect exposed by considering the response of a lossless sample with finite real permittivity. The Q factor, upon insertion of a lossy sample is reduced (i.e. bandwidth is increased since Q = *f* / BW), but since we have

$$Q = 2\pi \frac{E_{stored}}{E_{diss}}$$

where E_{stored} is energy stored in the system and E_{diss} is the average energy dissipated in the system over one cycle, for a sample with negligible imaginary permittivity (loss) and finite real permittivity (storage), we may observe an *increase* in Q. This is not adequately described by the perturbation theory, but we may assume that for such a low-loss sample is beyond the range of measurement of this system regardless.

For conventional cavity perturbation measurements, correction factors have been developed for the analytical approach to data inversion. Firstly, the influence of the sample hole was corrected analytically based upon mode matching methods at the holes [23]. This method is useful provided that we are within acceptable limits for the analytical approach. More recently, the ‘rigorous analysis’ used by Kawabata et al. [43] has been used to develop correction charts to account for inconsistencies in the perturbation formulation. However, this approach uses the Ritz-Galerkin method, which describes a family of methods for discretising problems, and of which the finite element method is a member. Therefore, this amounts to nothing more than solving the problem numerically and using look-up tables. The corrections to perturbation theory described by Kawashima et al. [44] are superfluous.

2.3.5 Investigation of the effects of the cavity split

2.3.5.1 Quality factor in the split cavity

The split cavity method relies upon the existence of a pronounced resonance, which is to be perturbed by the sample under test. As discussed in previous sections, the Quality factor describes the ‘sharpness’ of the resonance and can be related to the bandwidth by

$$Q = \frac{f_0}{BW}$$

For the resonant perturbation technique, a high quality factor is required for high accuracy measurements. As the Q factor is reduced, the uncertainty in the measurement is increased. How then does the Q factor behave in the split cavity? As the cavity is split from the conventional enclosed configuration, many modes previously present will be destroyed as wall currents cannot traverse the split. These include TE modes of interest such as the TE_{011} mode used in the already established split cavity, which forms Japanese Industrial Standard, JIS-R-1641 [45]. Modes that survive the presence of the split do so because their wall currents run parallel to the join. This also means that modes such as the TM_{210} mode which has some rotational degeneracy, becomes fixed in orientation. Such control over the orientation of such modes can be achieved by positioning the coupling points in desired regions of high electric or magnetic field, but the presence of the split comprehensively destroys other orientations in modes such as the TM_{210}.

The split cavity described in this chapter is initially positioned with a split of 0mm. By using an Agilent ENA 5071B Vector Network Analyser (VNA), the frequency of resonance and bandwidth are recorded. This is repeated at split widths of 2mm, 4mm, 6mm, and 8mm. The cavity has locating rods on which it slides (see Figure 2.9) positioned in each corner to maintain the orientation of each section. The cavity split is extended using a micrometer to achieve an accurate position.

From the measured results for frequency and bandwidth of the resonant TM_{010} mode, we calculate the quality factor (unloaded using measured insertion loss values).

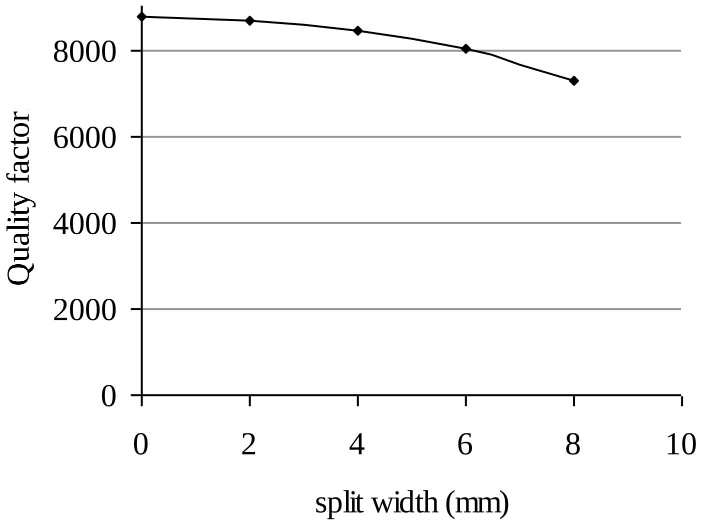

Figure 2.13 – Quality factor of the TM_{010} mode at increasing split widths

Figure 2.13 shows the unloaded quality factor of the cavity as the split width is increased. The quality factor remains remarkably high and for widths of up to 8mm is still above 7000. This suggests that accurate measurements may still be taken using the TM_{010} mode at large split widths. As we shall see in subsequent sections, for a given cavity configuration, measurements remain highly repeatable.

2.3.5.2 V_{eff} in the split cavity

Method

In order to investigate the effects of the presence of the cavity split, we first establish the calibration characteristics at increasing split widths. Using the system described in section 2.3.3, metal spheres are suspended at the point of maximum E-field. From the known dipole moment induced by the sphere, an effective volume occupied by the cavity fields is obtained. With increasing split width, the evanescent fringing fields protrude further from the sides of the cavity causing V_{eff} to increase. The nature of this increase exposes the level to which this dynamic calibration technique compensates for the altered cavity configuration. Subsequent investigation will then test the validity of measurements at large split widths calibrated in this way.

The split cavity described in section 2.3.2 is initially positioned with a split of 0mm. By using an Agilent ENA 5071B Vector Network Analyser (VNA), the frequency of resonance is recorded with the sample holder in place. In this case the sample holder is simply a low-loss PET tube. A 2.5mm diameter, precision manufactured vanadium coated steel sphere is suspended in the centre of the cavity and the resonant frequency is measured once more. From equation (15) we obtain V_{eff} for the cavity in its current configuration. This is repeated three times at split widths of 2mm, 4mm, 6mm, and 8mm. The cavity has locating rods on which it slides (see Figure 2.9) positioned in each corner to maintain the orientation of each section. The cavity split is extended using a micrometer to achieve an accurate position.

Results and discussion

The mean and standard deviation of the calibration measurement raw data are shown in Table 2. From the values in Table 2, V_{eff} is determined for each split width.

Split (mm)	f_0 (GHz)	σ_0 (kHz)	f_s (GHz)	σ_s (kHz)
0	2.49487	1.51	2.49441	1.75
2	2.46102	231	2.46058	241
4	2.43050	5.46	2.43010	8.43
6	2.40395	8.72	2.40357	14.1
8	2.37498	11.9	2.37462	12.2

Table 2 – Table of raw measurement data for calibration using 2.5mm diameter metal spheres, f_0 denotes the empty cavity and f_s denotes the cavity with sphere in position.

Figure 2.14 shows the effective volume V_{eff} occupied by the cavity E-field in cm^3 at split widths of 0mm, 2mm, 4mm, 6mm, and 8mm. The volume increases as expected and is linear in nature.

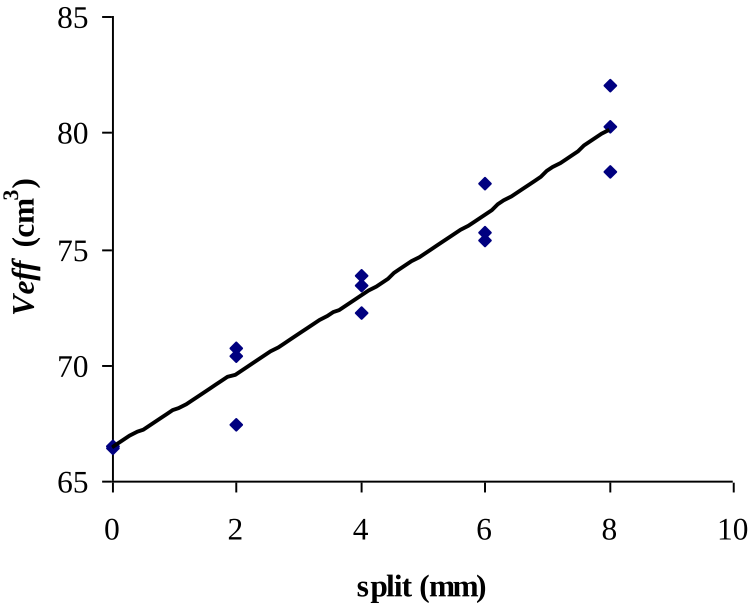

Figure 2.14 – V_{eff} in cm^3 for increasing split width S.

V_{eff} increases as the fringing fields at the split protrude further out of the cavity and the E-field occupies a greater volume. The data were obtained for this calibration by re-setting the split width for each measurement taken. This was in order to test the robustness of V_{eff} when positioning the cavity split using a micrometer. The results indicate that for no split width, the calibration is highly repeatable, with the standard deviation σ, of frequency measurements less than 2 kHz. For measurements taken with a split present, σ is increased. This result indicates that the dominant source of error is the imprecise width of the split. If the width of the split is 0.5mm out, it could cause an error of almost 1cm^3 in V_{eff}. We shall see that this does not matter for sample measurements, because it is not necessary to correlate split widths, we simply need to calibrate the cavity at the arbitrary width being used; what the width of the split happens to be is irrelevant. This dynamic, empirical calibration therefore has a great advantage over numerical or analytical inversion techniques since the accuracy of such techniques is dependent upon having accurate knowledge of the cavity dimensions, which is impractical for a split cavity such as this.

Split (mm)	V_{eff} (cm^3)	σ_{eff} (cm^3)	$\Delta\varepsilon'(\sigma_{\mathrm{eff}})$	$\Delta\varepsilon''(\sigma_{\mathrm{eff}})$
0	66.502	0.0363	1.245×10^{-3}	3.321×10^{-4}
2	69.498	1.4804	1.271×10^{-3}	3.391×10^{-4}
4	73.195	0.6919	1.257×10^{-3}	3.352×10^{-4}
6	76.294	1.0828	1.264×10^{-3}	3.371×10^{-4}
8	80.207	1.4981	1.272×10^{-3}	3.392×10^{-4}

Table 3 – Mean V_{eff} and standard deviation σ_{eff} from measurement data of Table 2. The final two columns show the change in real and imaginary permittivity if the calibration value V_{eff} deviates by one standard deviation.

The calibrated values for V_{eff} and the standard deviation are shown in Table 3 for the different split widths. We note that the standard deviation σ_{eff} increases as the split width is increased. Since the dominant source of error is the imprecise measurement of split width, we conclude that this source of error is exacerbated at larger widths when measurements are taken with a micrometer. But, as discussed above, this source of error is irrelevant when taking sample measurements and we do not require a more accurate method of defining the cavity split width.

The final two columns in Table 3 show the change in real permittivity $\Delta\varepsilon'(\sigma_{\mathrm{eff}})$, and the change in imaginary permittivity $\Delta\varepsilon''(\sigma_{\mathrm{eff}})$ for one standard deviation in the calibration value of V_{eff}. That is to say, if the calibration of the cavity at any given split width was off by one standard deviation, what would the resulting error in measured permittivity values be? These calculated values are based upon a cylindrical sample of diameter 1.36mm, with complex permittivity $\varepsilon^* = 4 - j0.4$, and with initial $V_{\mathrm{eff}} = 70\mathrm{cm}^3$. We observe that both $\Delta\varepsilon'(\sigma_{\mathrm{eff}})$ and $\Delta\varepsilon''(\sigma_{\mathrm{eff}})$ increase with increasing split width, but the magnitude of the changes is very small. This indicates that the influence of the calibration quantity upon the final inverted permittivity values is small, which is good news for a cavity with arbitrary and imprecise split widths. In the next section, we measure cylindrical dielectric samples and we note that any significant sources of error are unlikely to be due to errors in the calibration of V_{eff}.

2.3.6 Cavity Measurements

As a demonstration of the application of this work, the cylindrical dielectric samples used to investigate aspects of the measurement technique consist of powders of micron-sized transparent conducting oxide (TCO) coated mica flakes. The structure of these conducting particles is described in detail in chapter 3, but for the purposes of these investigations we note simply that these high-frequency techniques are capable of measuring powders, as well as sheets, liquids, plasmas and indeed dielectric and magnetic materials in any form.

2.3.6.1 Dielectric measurements at increased split widths

Method

To investigate cavity perturbation measurements at increasing split widths, a cylindrical dielectric sample is measured in the enclosed cavity and the same sample is then measured at different split widths. Results are compared for agreement and sources of error are investigated.

Once again the split cavity is initially positioned with a split of 0mm. A quick calibration measurement is carried out using the metal sphere method described above. With V_{eff} calibrated, we proceed to measure the sample. Using an Agilent ENA 5071B Vector Network Analyser (VNA), the frequency of resonance and bandwidth are recorded with an empty sample tube in place. For these measurements the sample tube is a quartz-glass tube with inner diameter 1.36mm. A filled tube is then placed axially in the centre of the cavity and the frequency of resonance and bandwidth are once again recorded. From equations (17) and using the calibrated V_{eff} value for the cavity configuration (i.e. 0mm split width) we obtain values of real permittivity ε', and imaginary permittivity ε" for the sample. This is repeated three times at split widths of 2mm, 4mm, 6mm, and 8mm. The cavity has locating rods on which it slides (see Figure 2.9) positioned in each corner to maintain the orientation of each section. The cavity split is extended using a micrometer to achieve an accurate position.

Results

The shift in resonant frequency Δ*f*, and the shift in bandwidth ΔBW upon insertion of the sample are shown for each split width in Table 4a). Corresponding values of real and imaginary permittivity are shown in Table 4b).

Split (mm)	Δf (MHz)	σ_f (kHz)	ΔBW (MHz)	σ_{BW} (kHz)
0	4.5002	35.0348	1.4204	5.6945
2	4.2198	41.0927	1.3308	2.7837
4	3.9375	61.5440	1.2328	11.8017
6	3.6469	11.8094	1.1538	1.2233
8	3.3987	26.0865	1.0774	5.9057

Split (mm)	ε'	$\sigma_{\varepsilon'}$	ε''	$\sigma_{\varepsilon''}$
0	3.9945	0.0224	0.4717	0.0020
2	3.9752	0.0911	0.4691	0.0109
4	3.9597	0.0585	0.4633	0.0074
6	3.8881	0.0339	0.4569	0.0066
8	3.8637	0.0580	0.4539	0.0076

Table 4 – a) Shift in frequency and bandwidth and standard deviation, upon insertion of a cylindrical dielectric sample at varying split widths and b) corresponding values of complex permittivity and standard deviation at varying split widths.

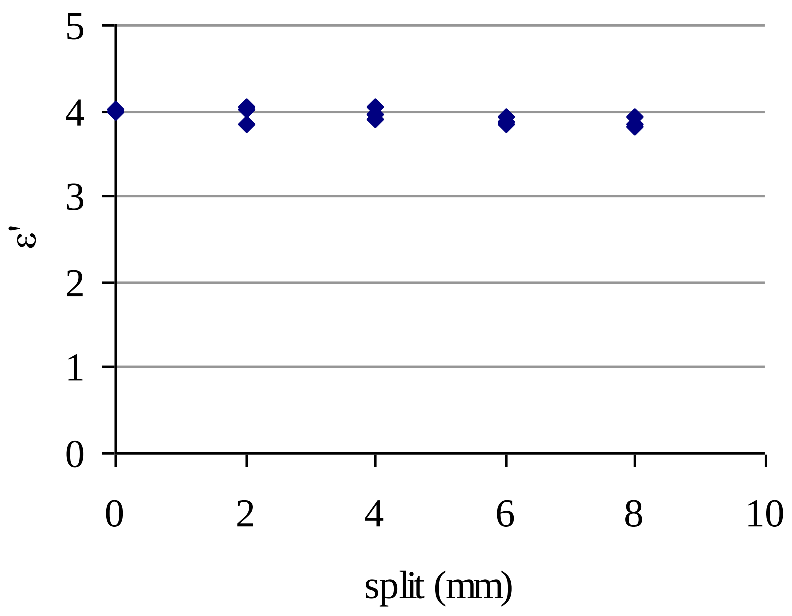

Figure 2.15 – Measured values of real permittivity for cylindrical sample at varying split widths. There is good agreement even for a split width of 8mm.

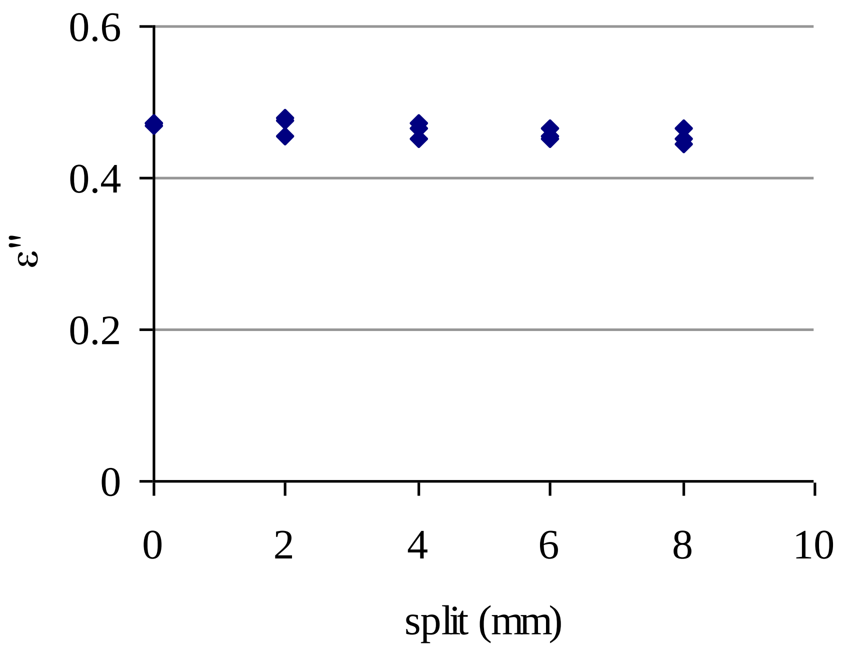

Figure 2.16 – Measured values of imaginary permittivity for cylindrical sample at varying split widths. We observe similar results for the real permittivity: there is good agreement though there is a tendency to underestimate the permittivity value at larger split widths.

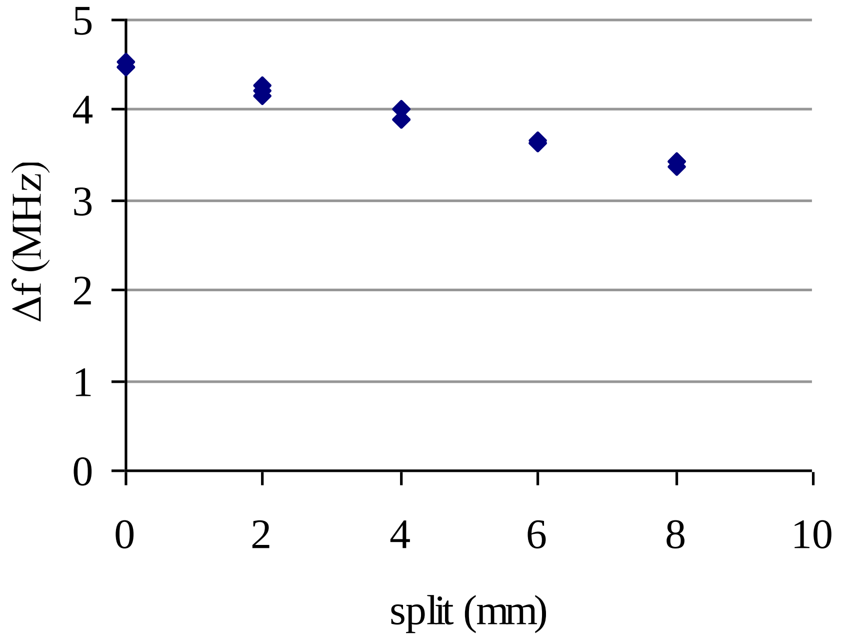

Figure 2.17 – Measured shift in resonant frequency upon insertion of the cylindrical dielectric sample. The effects of the presence of the sample are diminished at larger split widths.

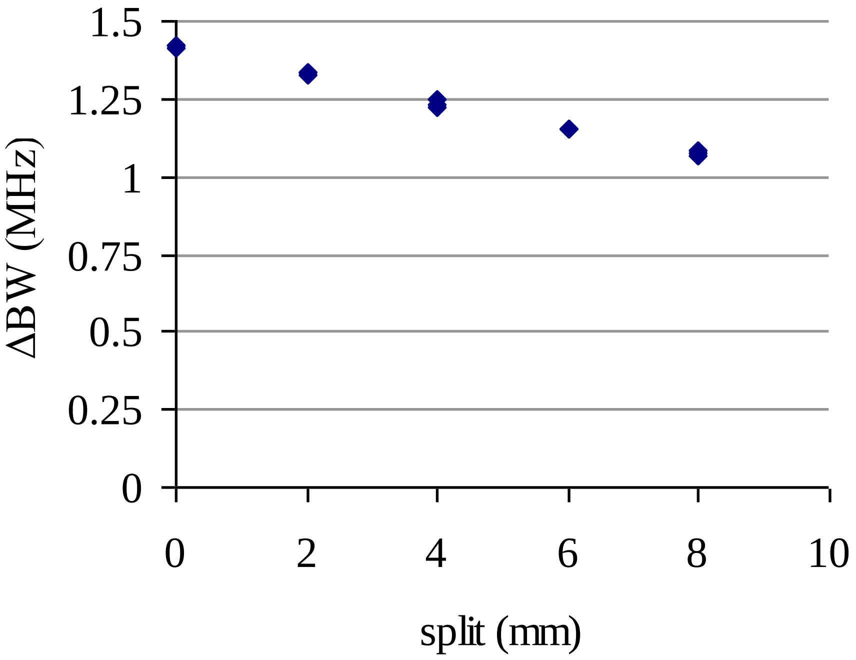

Figure 2.18 – Measured shift in resonance bandwidth upon insertion of the cylindrical dielectric sample into the cavity. The effects of the presence of the sample are again diminished at larger split widths.

Discussion

Figure 2.15 and Figure 2.16 show that dielectric measurements in the split cavity remain highly consistent, even for split widths up to 8mm in size. Measurements of the same sample taken in a cavity with a large split agree well with measurements taken in an enclosed configuration. Shown in Table 5 below are the percentage errors based upon the mean values measured in the enclosed cavity. The errors in real and imaginary permittivity are around 0.5% for a 2mm split and are well below 4% even for widths of 8mm.

Split (mm)	0	2	4	6	8
ε'	3.9945	3.9752	3.9597	3.8881	3.8637
% error	-	0.48	0.87	2.66	3.27
ε''	0.4281	0.4691	0.4633	0.4569	0.4539
% error	-	0.55	1.78	3.13	3.77

Table 5 – Percentage error of measured sample values at varying split width.

The shift in resonant frequency Δf, and the shift in bandwidth ΔBW, are shown in Figure 2.17 and Figure 2.18. We note that as the cavity split widens, the measurable shift in resonant frequency and bandwidth is reduced. This is an important feature of the split cavity, since the ability to measure sensitively the complex permittivity of samples relies upon a measurable shift in f and BW. We therefore lose some sensitivity in the split configuration, but also to a lesser degree some resolution is lost. This also contributes to errors at large split widths and we would observe a similar error in the calibration measurements shown in Figure 2.14 if experimental error was not dominated by uncertainty in the width of the split. In these sample measurements however, precise knowledge (indeed, any knowledge) of the split width is not necessary if the calibration is carried out in the cavity configuration used for measurement.

The results of sample measurements at larger widths agree well, but begin to underestimate the real and imaginary parts of the permittivity. This disparity is exhibited in Table 5, Figure 2.15 and Figure 2.16. We can further investigate the disparity by considering equations (17), which are stated in previous sections, and are as follows

$$\frac{\Delta f}{f} = \frac{(\varepsilon' - 1)}{2}\frac{V_s}{V_{eff}} \qquad \frac{\Delta BW}{f} = \varepsilon''\frac{V_s}{V_{eff}}$$

We know from Figure 2.17 and Figure 2.18 that at larger widths, the shift in frequency and bandwidth upon insertion of the sample are reduced. This is of course offset when measuring at larger widths by the calibration of V_{eff}, which adjusts accordingly. In fact, considering only the first of the above equations, we can see that the only variables to change at large widths are Δf, f and V_{eff}. Therefore to maintain an accurate measurement we must have

$$\frac{\Delta f}{f} = \frac{A}{V_{eff}}$$

where A is a constant. So as $\Delta f / f$ decreases, $1 / V_{\mathrm{eff}}$ must decrease proportionally. Figure 2.19 shows normalised values of $\Delta \mathrm{f} / \mathrm{f}$ and $1 / \mathrm{V}_{\mathrm{eff}}$ as the split width is increased. There is a clear disparity present, which must either be caused by an underestimated value of $\Delta f / f$, or an underestimated value of V_{eff} (that is, an overestimated value of $1 / V_{\mathrm{eff}}$), or of course, both.

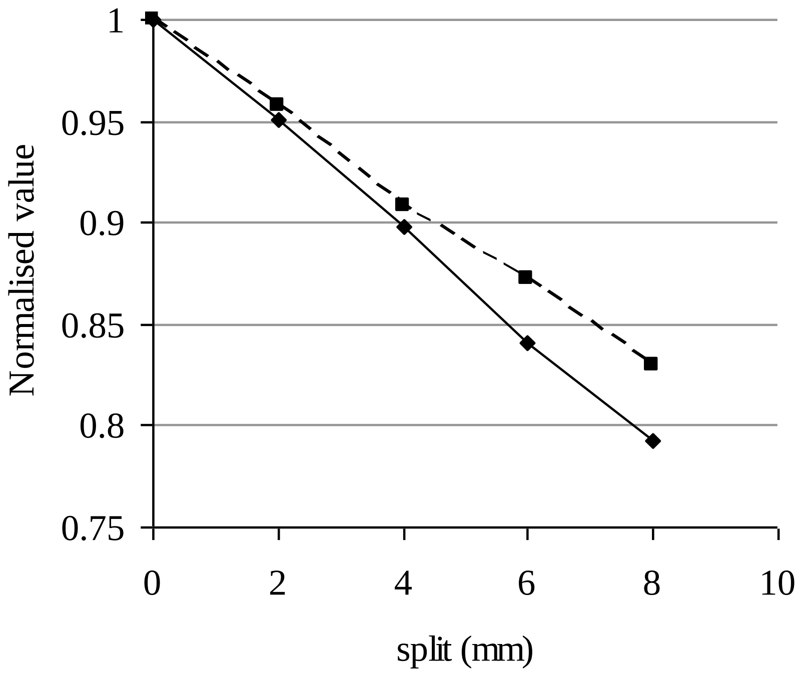

Figure 2.19 – Normalised values of $\Delta f\,/\,f$ (solid line) and 1 / V_{eff} (dashed line) for varying split width.

But how does the presence of the split lead to the apparent underestimation of $\Delta f\,/\,f$, and/or V_{eff}? Firstly, we note that it is not possible to 'underestimate' $\Delta f\,/\,f$ simply by virtue of the inversion; it is the measured quantity. But, can V_{eff} be entirely to blame for the underestimated complex permittivity at large split widths? The value V_{eff} is a convenient and intuitive variable, formed when the dipole moment is substituted into (13). V_{eff} then becomes (16), and if the perturbed E-field E, is considered to be the same as the unperturbed E-field E_0, then the $E^2/E_0^2 = 1$ is integrated over the volume of the cavity.

$$V_{eff} = \int_{cav} \frac{E^2}{E_0^2} dV$$

The resulting value is an effective volume occupied by the cavity E-field, and is some value less than the actual volume of the cavity.

But *can* we assert that the value V_{eff} remains valid for the cavity at increased split widths? The perturbation equations (13), are valid for any resonant system in the small perturbation limit. But, the assumption made that the unperturbed and perturbed fields are the same in equation (16) is less valid than in the enclosed cavity; even though the perturbing sample is the same in each case.

The error may be interpreted as fundamental nonlinearities in the dipole moment p. The dipole moment of a long cylinder in a parallel, uniform E-field is

$$p = (\varepsilon_r - 1)\varepsilon_0 E_0 V_s$$

V_{eff} appears in the final equation (17) because the dipole moment is a function of E_0, which will always be the case and therefore some version of V_{eff} remains in any corrected formulation. But this is where the nonlinearity occurs. The assumptions made in the formulation of the dipole moment itself become flawed at large split widths, principally because the dipole is based upon a uniform polarising field, which is no longer the case at the cavity split. In this sense, the calibrated value for V_{eff} using the metal spheres is perhaps more accurate because the field at the centre of the cavity where the sphere is placed remains relatively uniform.

A correction to the measurement discrepancy at large split widths would therefore involve a modification to the dipole moment of the cylinder to represent the reduction in the induced dipole due to non-uniform fields at the cavity split.

Such non-uniformity in the fields would be accounted for if calibrations were carried out using a cylindrical sample of known permittivity, but even when this is done, the non-uniformity of the fields is a function of both split width and sample permittivity. The non-uniformity of the field becomes a non-linearity in the measurement when samples with finite (>1) permittivity are introduced. The already non-uniform fields become even less uniform at the split in the presence of a high permittivity sample. In an enclosed cavity this does not pose a problem, since the fields remain relatively uniform because of the overriding influence of the cavity walls.

In summary, there are two compounding factors contributing to the error. 1) The non-uniform fields at the cavity split leading to a reduced dipole moment and 2) The presence of a sample in these non-uniform fields leads to further non-uniformity of the field. The dipole moment is a non-linear function of permittivity and split width S; we have dipole moment $p(\varepsilon^*, S, E_0, V_s)$. This manifests itself in the inversion equations in the form of a non-linear V_{eff}, which is a function of split width and sample permittivity. We have for a cylindrical sample

$$\frac{\Delta f}{f} = \frac{(\varepsilon' - 1)}{2} \frac{V_s}{V_{eff}(S, \varepsilon^*)} \qquad \frac{\Delta BW}{f} = \varepsilon'' \frac{V_s}{V_{eff}(S, \varepsilon^*)}$$

Here we encounter a situation where non-linearities in the measurement make numerical approaches unavoidable. For the system used here, using the cavity with a split present becomes a trade-off between split width and the level of accuracy required. The alternative of course is to take the complex frequency approach, with a numerical inversion accounting for all non-linearities, but in this case we lose the freedom associated with the arbitrary split width. The split cavity developed in this work has the useful feature of easy and comprehensive access to the sample under test, plus with the novelty of the presence of a uniform, axially directed E-field and a simple, quick calibration technique for arbitrary split width. It is clear that the width of the cavity is limited by our accuracy requirements, but the system performs well, with less than 1% error in the real permittivity for split widths up to 4mm. If our accuracy requirements are not met at the prescribed split width, a complex frequency inversion based upon a numerical approach must be used.

Another method of circumventing the loss of accuracy at large split widths is to use samples in the form of pellets. The dipole moment of pellet geometries can be solved analytically and an inversion is trivial for known sample size. In this way, the sample is unaffected by non-uniform fields at the cavity split. At very large split widths the error is therefore reduced. Using pellets to perturb the cavity removes issues of field uniformity and the dynamic calibration of metal spheres for arbitrary split widths may still be used. The sample is in a highly depolarising configuration when in pellet form, a consequence of which is that Δf is less for any given measurement and so resolution is lost, but errors associated with the cavity split are significantly reduced and measurements of pellet samples are more robust at larger split widths. Highly depolarising measurements such as these become very sensitive to parameters such as sample volume.

2.3.6.2 Higher order modes

Many modes exist simultaneously in the cylindrical cavity. We have thus far exploited the TM_{010} mode because of the useful, highly uniform electric field at its centre and its robustness to measurements with a split cavity. But there are also many opportunities to use these higher-order modes and innovative approaches may be taken to exploit the unique properties of each. In this section, a brief account is given of some of the more interesting higher order modes and the possibilities for their use in dielectric measurements are discussed.

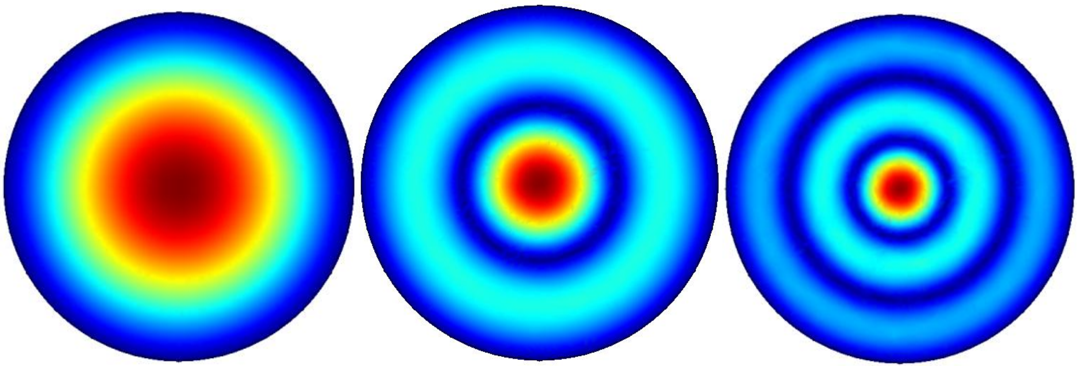

a) TM_{010} Electric-field   b) TM_{020} Electric-field   c) TM_{030} Electric-field

Figure 2.20 – The electric field distributions for TM_{0n0} modes in the cylindrical cavity. The frequency of these modes depends only upon the radius of the cavity. For a cavity with radius of 4.6cm, we have: a) TM_{010}, f = 2.4946 GHz, b) TM_{020}, f = 5.7258 GHz, a) TM_{010}, f = 8.9766 GHz.

The TM_{010} mode described in this work has a family of modes associated with it, which exhibit many of the same useful properties. The frequency of resonance for TM_{0n0} modes depends only upon the radius of the cavity. The electric currents associated with these modes all run along the walls of the cavity from the centre of one end-plate, the centre of the other. This means that in the split cavity, currents run parallel to the split and the modes survive even large split widths.

We shall see that most other modes are destroyed by the presence of the split in this configuration, but TM_{0n0} modes remain robust. Each of the modes maintains the high *E*-field at the centre of the cavity and the high field uniformity exhibited by the TM_{010} mode. We also note that the high field point is more localised in the TM_{020} mode. At first glance, this might suggest that for a given sample placed in the centre of the cavity, we would achieve a greater filling factor (i.e. ratio of field in the sample to field outside of the sample), leading to increased sensitivity. This is easily investigated by taking the ratio of the total electric energy at the centre of the cavity to the total electric energy outside of the centre. Considering the 'centre' of the cavity in this case to be a cylinder of 1cm radius, spanning the entire height of the cavity, we take the following ratio of volume integrals for the TM_{010} and TM_{020} modes.

$$\frac{\int_0^l \int_0^{2\pi} \int_0^c \varepsilon_0 \left|\overline{E}(\rho,\phi,z)\right|^2 \rho d\rho d\phi dz}{\int_0^l \int_0^{2\pi} \int_c^a \varepsilon_0 \left|\overline{E}(\rho,\phi,z)\right|^2 \rho d\rho d\phi dz} \tag{18}$$

where cavity radius a = 4.6cm, centre boundary c = 1cm, and length of the cavity l = 4cm. Since only the radial component of the *E*-field, $E(\rho)$ is different, this rather cumbersome integral cancels down to become

$$\frac{\int_{\rho=0}^{c} J_0\left(\frac{p_{0n}}{a}\rho\right)^2 \rho d\rho}{\int_{\rho=c}^{a} J_0\left(\frac{p_{0n}}{a}\rho\right)^2 \rho d\rho} \tag{19}$$

since the radial component of the cavity *E*-field is

$$E(\rho) = E_0 J_0\left(\frac{p_{0n}}{a}\rho\right)$$

where E_0 is the *E*-field magnitude, J_0 is the zero order Bessel function of the first kind, n indicates the mode of the TM_{0n0} field and p_{0n} denotes the nth root of Bessel function J_0.

The results of this integration show that for the TM_{010} mode, 19% of the total electric energy is present in the region of radius 1cm in the centre of the cavity and the remaining 81% is in the surrounding, outer region. In the TM_{020} mode, the same integration reveals that only 8% of the electric energy is present in the centre region. We therefore obtain a much greater filling factor for the TM_{010} mode than for higher order modes.

These higher order modes can be used to measure dielectric samples in precisely the same way as the TM_{010} mode, and being able to take measurements at different frequencies allows us to measure frequency dependent behaviour of any samples under test to a high degree of accuracy.

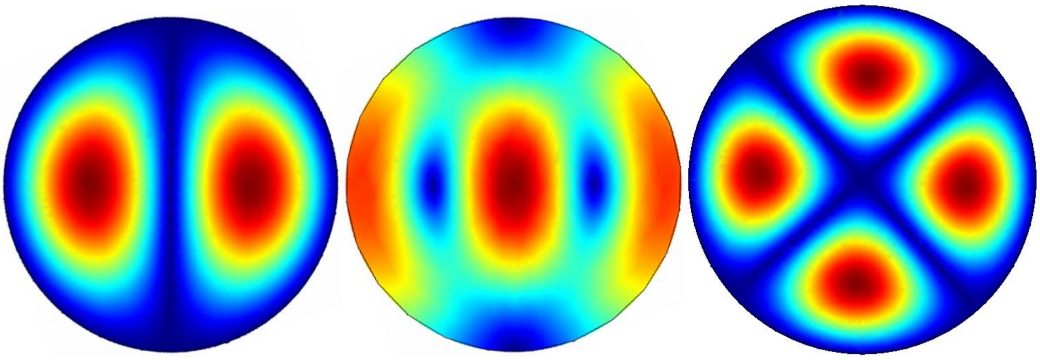

a) TM_{110} Electric-field

b) TM_{110} Magnetic-field

c) TM_{210} Electric-field

Figure 2.21 – Finite Element Model solutions for the distributions of a) the TM_{110} electric field and b) the TM_{110} magnetic field, both of which are at f = 3.9748 GHz, and c) the TM_{210} mode electric field in the cylindrical cavity, which occurs at f = 5.327 GHz.

In Figure 2.21a) and b) is shown the electric and magnetic fields of the TM_{110} mode respectively. This mode has a relatively good field separation and at its centre is a magnetic field maximum and an electric field null. This mode is well-suited to measurements of magnetic samples or measurement using the excitation of eddy currents.

2.3.6.3 The TM_{210} mode as a reference

In Figure 2.21c), is shown the electric field of the TM_{210} mode. This mode has no *E*-field at its centre, and as a result it has many useful applications as a reference.

When samples are inserted into the cavity axially, the TM_{210} mode remains unperturbed, even for samples of extremely high permittivity. Taking the same approach used above, we can determine the fraction of the total electric energy present in the centre region of the cavity and relate this directly to the sensitivity of the mode to perturbation by dielectric samples.

We no longer have rotational symmetry since the circular component of the *E*-field in TM_{mn0} modes (where m > 0) is sinusoidal in form. The *E*-field now becomes

$$E_z(\phi,\rho) = E_0 \sin(m\phi) J_0\left(\frac{p_{0n}}{a}\rho\right)$$

which is integrated according to equation (18).

The fraction of electric energy in the sample region of the cavity normalised to the TM_{010} mode is shown for higher order modes of interest in Figure 2.22. The electric energy present in the sample region is over six orders of magnitude less for the TM_{210} mode than for the TM_{010} mode, demonstrating the independence of the TM_{210} mode from the influence of the sample under test.

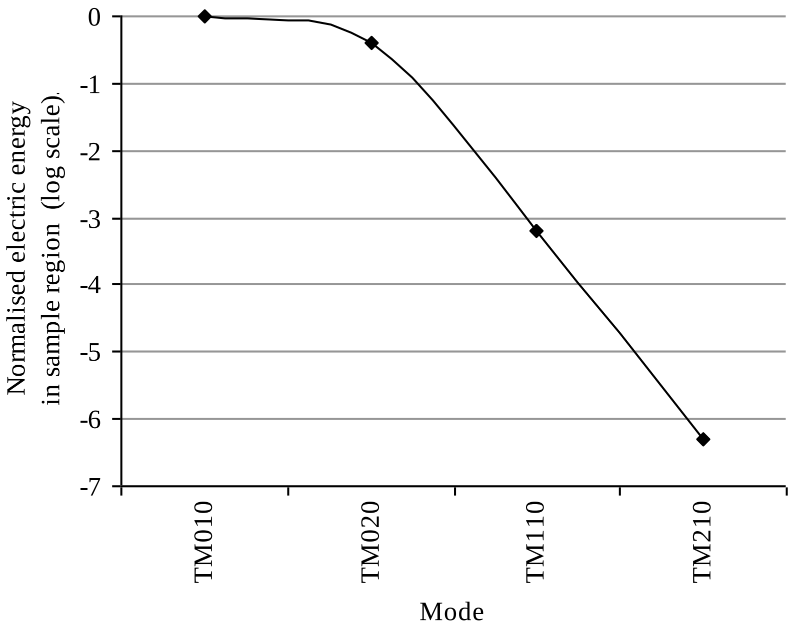

Figure 2.22 - The fraction of electric energy in the sample region (cylinder of radius 0.68mm) of the cavity normalised to the TM_{010} mode, for modes TM_{010}, TM_{020}, TM_{110} and TM_{210}.

From Figure 2.22, we see that the TM_{020} mode is marginally less influenced by the presence of the sample, whilst the central null-point of the TM_{110} mode shown in Figure 2.21a) causes a reduction by a factor of 1000. The TM_{210} mode as shown in Figure 2.21c) is clearly even less influenced by the presence of the sample.

This independence of the TM_{210} mode may be tested experimentally by measuring the frequency shift when a sample of high permittivity is placed into the centre.

f_0 (GHz)	σ_{f0} (Hz)	f (GHz)	σ_f (Hz)	Δf (Hz)
5.33217	1186	5.33216	1530	8165.248
BW_0 (kHz)	σ_{BW0} (Hz)	BW (kHz)	σ_{BW} (Hz)	ΔBW (Hz)
507.7	986	508.2	758	456

Table 6 – Mean resonant frequency and bandwidth of the TM_{210} mode with (f, BW), and without (f_0, BW_0) a sample in place.

Using the same cylindrical sample used in the dielectric measurement investigations of previous sections ($\varepsilon^* = 3.99 - j0.47$, radius 0.68mm), measurements were taken of the resonant frequency and bandwidth of the TM_{210} mode with and without the sample in place. Each measurement was repeated ten times.

Table 6 shows the mean and standard deviation σ, of measured values. Upon insertion of the sample, we observe a shift in frequency Δf and bandwidth ΔBW of 8165 and 465 Hz respectively. Such a small change in values cannot be interpreted as a shift due to the presence of the dielectric since the standard deviation in all measurements taken is of the order of 1 kHz. We therefore conclude that for samples of permittivity $\varepsilon^* = 3.99 - j0.47$ and radius 0.68mm, no measurable shift occurs.

As a reference point this mode is invaluable, no sample, regardless of dielectric strength will influence the mode in this configuration. Any effects upon the mode are attributable to the cavity alone.

Having established the robustness of the TM_{210} mode, we now turn to its applications. Since the resonant frequency of the TM_{010} mode and the TM_{210} mode are inherently linked, we may use measurement of one to learn about the other. When standard cavity perturbation measurements are taken, the resonant frequency and bandwidth of the cavity are noted for the unperturbed fields; the sample is then inserted and the frequency and bandwidth are noted once more. By using the fixed relationship between the TM_{010} mode and the TM_{210} mode, we can establish an unperturbed frequency for the TM_{010} resonance without having to observe sample-free measurement at all. This is an advantageous extension of the cavity perturbation technique in terms of general convenience, but importantly, enables measurements to be taken over time without having to disturb the sample under test.

For both the TM_{010} and the TM_{020} modes the frequency of resonance depends only upon the radius of the cavity. Given this identical and exclusive dependence, the ratio of frequencies is fixed. We have

$$\frac{f_{010}}{f_{210}} = \frac{p_{01}}{p_{21}} = 0.468263711$$

In order to validate the approach we once again consider measurements of the cylindrical sample, with permittivity $\varepsilon^* = 3.99 - j0.47$ and radius 0.68mm and use the TM_{210} mode as a reference.

There is necessarily some systematic offset of the frequency ratio from theory to the actual values due to the nature of the split in the cavity, since the TM_{010} mode has rotational symmetry and the TM_{020} does not. But this offset itself is fixed and can easily be calibrated when the TM_{010} mode is unperturbed.

	f_{010}/f_{210}	f_{010} (GHz) sample	$\sigma_{010,s}$ (kHz)	f_{010} (GHz) inferred from TM_{210}	$\sigma_{010,0}$ (kHz)	ε'	Error (based upon TM_{010})
Theory	0.46826	2.48581	45.07	2.49685870	0.716	1.952	51.12%
Calibrated	0.46704	2.48581	45.07	2.49032544	0.714	4.067	1.82%

Table 7 – Resulting permittivity values and associated errors of measurements taken of a sample of known permittivity (ε' = 3.9945, measured using the TM_{010} mode in section 2.3.6), using the TM_{210} mode as a reference and inferring unperturbed frequency value from theoretical and from experimental values of f_{010}/f_{210}.

In Table 7 we observe the results of cavity perturbation measurements taken using the TM_{210} mode as a reference. Clearly, the systematic offset in the theoretical frequency ratio of the TM_{010} and TM_{210} modes causes a significant error of 51% in the resulting permittivity value. This is easily accounted for by calibrating the ratio. This calibration need only be carried out once, since though subsequent measurements exhibit a small error of 1.82%, the standard deviation in the resulting permittivity values, $\sigma_{\varepsilon'} = 0.0308$, compares favourably with that of the measurements taken using the conventional TM_{010} method, $\sigma_{\varepsilon'} = 0.0224$ (see section 2.3.6). We conclude that using the TM_{210} mode to infer unperturbed frequencies is indeed a viable method for measuring the permittivity of dielectric samples. We also note that the standard deviation in measured frequencies mirrors the behaviour of results with and without the sample present, even though the sample is present for all measurements presented here.

The robustness of the TM_{210} mode as a substitute for unperturbed TM_{010} frequencies seems evident, and it relies upon the mode being unaffected by the presence of the sample. In order to further test the limits of the TM_{210} mode, a silver-coated copper wire of diameter 1mm is placed in the sample position and the frequency shift is measured. Then an alloy steel rod of diameter 2.39mm is placed in the sample position and the frequency shift is measured once again. In other, similar TM modes the presence of a metal on the cylinder axis would destroy any resonance, since the parallel *E*-field cannot exist at the metal surface of the wire. For the TM_{210} mode this does not occur. Instead of the resonance being destroyed, or there being no perturbation as for dielectric samples, we observe the following

	f_0 (GHz)	σ_{f0} (Hz)	f (GHz)	σ_f (Hz)	Δf (Hz)
Dielectric	5.33217	1186	5.33216	1530	8165
Wire	5.33710	1759	5.33712	9918	-17120
Rod	5.33710	1738	5.33724	6264	-137549

Table 8 – Mean resonant frequency of the TM_{210} mode with (f), and without (f_0) a sample in place for a dielectric sample and a metal wire of diameter 1mm.

The resonance of the cavity actually *increases* in frequency (adopting the convention of a downward shift in frequency being positive). This raises the question of whether the TM_{210} mode is as robust as we first thought. In order to explain such behaviour we must look to the *H*-field in the TM_{210} mode.

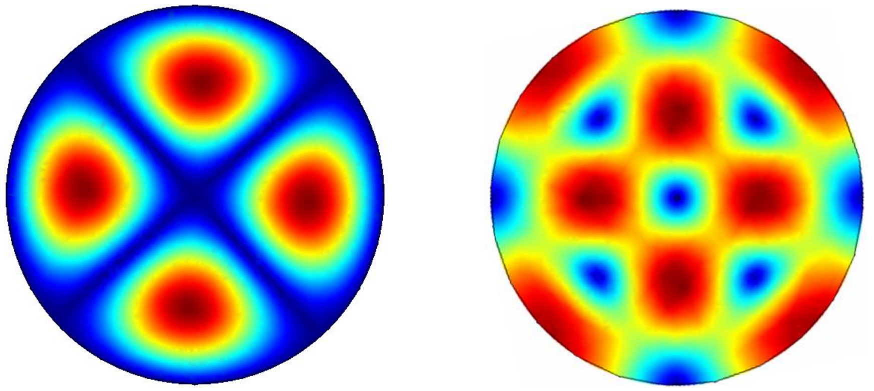

a) TM_{210} Electric field

b) TM_{210} Magnetic field

Figure 2.23 – a) the Electric field distribution of the TM_{210} mode and b) the magnetic field distribution of the TM_{210} mode.

The electric and magnetic field distributions of the TM_{210} mode are shown in Figure 2.23. At first glance it may seem that both fields have a null at their centre, and as before we should see no perturbation from samples inserted axially. To further investigate the magnetic field at the centre of the cavity, we use equation (18) once more to assess the fraction of magnetic energy present at the centre.

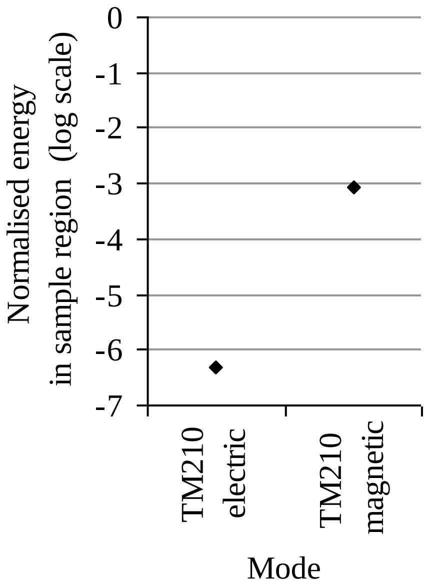

Figure 2.24 - The fraction of energy in the sample region (cylinder of radius 0.68mm) of the cavity normalised to the TM_{010} mode electric energy, for TM_{210} electric energy and TM_{210} magnetic energy. The Magnetic energy present is greater by a factor of 1000.

The magnetic energy in the sample region is more than 1000 times that of the electric energy. Values in Figure 2.24 are once again normalised to the electric energy value present in the sample region of the TM_{010} mode, which is larger still (see Figure 2.22), but the *H*-field is strong enough in the TM_{210} mode to be influenced by the presence of the sample. The magnitudes of electric and magnetic energies in a given region of the cavity are commensurable because in resonant systems the total electric and magnetic energies are equal.

Samples of high permittivity may be measured using the TM_{210} reference without difficulty, but for highly conducting samples, or samples with finite magnetic permeability, perturbation of the *H*-field leads to a shift in frequency which is not experienced by the TM_{010} mode. This perturbation is due to induced eddy currents in the conducting material. The TM_{210} mode can adequately perform its role as a reference for highly conducting samples, but only if samples of small radius are measured. The extent to which metallic samples affect the TM_{210} mode is easily checked before measurements are carried out.

The presence of the magnetic field can be used in order to measure the magnetic properties of samples with finite (>1) magnetic permeability, but is also an important method of measuring the conductivity of samples. Often in dielectric measurements we consider losses due to finite conductivity, which are easily interpreted when this is the dominant cause of loss. But using *H*-field measurements of induced eddy currents allows us to separate the contributions of conductive loss and dielectric loss, giving a definitive answer to the question of whether conduction mechanisms are present in the sample [46,47]. However, though the TM_{210} mode has a suitable magnetic field for such measurements, the easily accessible magnetic field of the TM_{110} mode may be a better candidate.

2.3.6.4 Environmental corrections

The ability of the TM_{210} mode to act as a reference for TM_{010} dielectric measurements enables measurements to be taken without disturbing the sample under test. This is of great benefit for measurements taken over time. Not simply in terms of automation and convenience, but the TM_{210} mode is a reference for the unperturbed cavity itself. This means that any environmental changes experienced may be tracked by this mode and corrected for, comprehensively separating effects of sample and cavity.

Over the duration of any cavity measurement the ambient temperature may drift, the result of which is a thermal expansion in the cavity itself. We have the temperature dependent resonant frequency, for TM_{mn0} modes,

$$f(T) = \frac{cp_{mn}}{2\pi a(T)} \tag{20}$$

where, c is the speed of light in free space, and p_{mn} is the nth root of the m order Bessel function of the first kind. $a(T)$ is the temperature dependent radius of the cavity, given by

$$a(T) = a_0(1 + \alpha(T))\Delta T$$

$\alpha(T)$ is the fractional increase in length per Kelvin change in temperature, and is called the linear thermal expansion coefficient, given by

$$\alpha(T) = \frac{1}{a}\frac{\partial a}{\partial T}$$

After substituting for $a(T)$ in equation (20), the fractional frequency shift reduces to

$$\frac{\Delta f}{f} = \alpha(T)\Delta T$$

So the fractional frequency shift is independent of which TM_{mn0} mode is being considered and for each 1 Kelvin rise in temperature, the fractional frequency increases by $\alpha(T)$, which for aluminium is $\alpha(T) = 22.2 \times 10^{-6}\ \mathrm{K}^{-1}$. For example, at a frequency of 2.4946 GHz (TM_{010} mode), a 1 Kelvin change in temperature will cause a 55.4 kHz shift in frequency. At a frequency of 5.327 GHz (TM_{210} mode), a 1

Kelvin change in temperature will cause a 118.26 kHz shift in frequency, but both modes will have an identical fractional frequency shift.

A correction for changes in ambient conditions is easily implemented. Since the TM_{210} mode isolates the effects of the cavity and excludes any effects of the sample, the measurement includes such a correction inherently and becomes invariant with temperature. This is a useful feature for measurements in general and is essential for measurements of samples being investigated under the influence of heating. Such is the accuracy of this method of temperature correction that the method may itself find use tracking temperature changes. Using a standard VNA we can measure frequency shifts to kHz accuracy with confidence. We are therefore able to track changes in frequency to around a 20mK resolution for the TM_{010} mode, 10mK resolution for the TM_{210} mode, and even higher resolution for higher order modes. This method therefore offers hyper-accurate tracking of temperature changes, in dielectric measurements, but also one of the highest resolutions currently available for temperature measurement in general.

The resonant frequency of the TM_{010} and TM_{210} modes were measured over a period of 12 hours. The resonator was left overnight and the frequency shift recorded as the ambient temperature follows the diurnal variation of the laboratory.

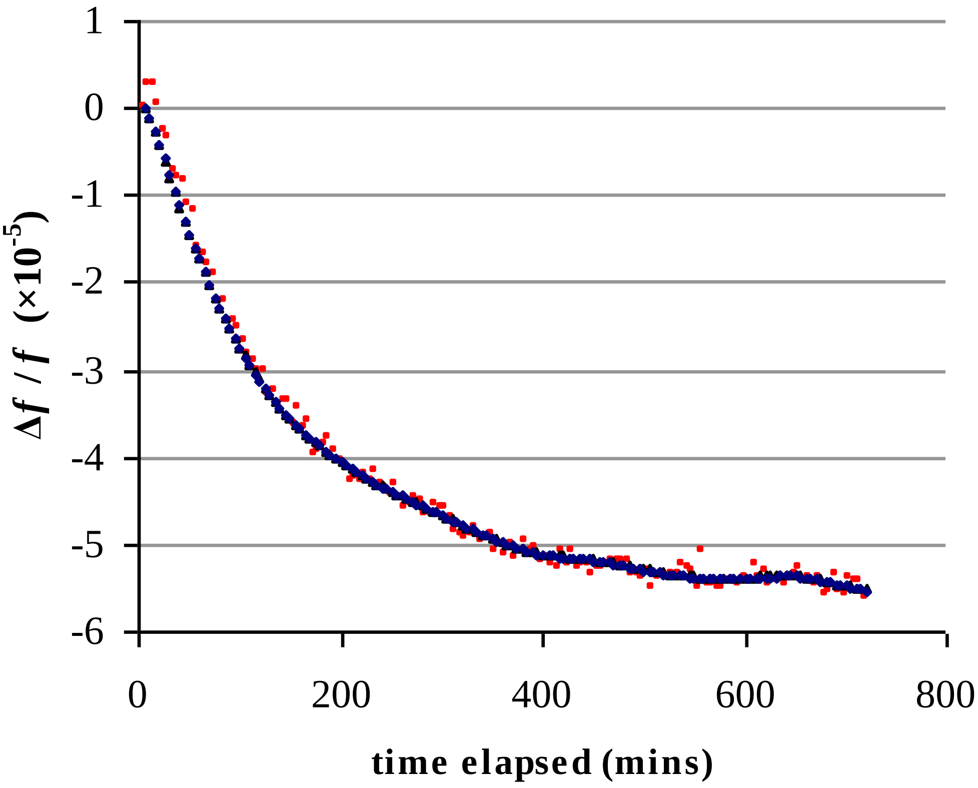

Figure 2.25 – Fractional frequency shift of the TM_{010} (blue), TM_{110} (red) and TM_{210} (black) modes over a period of 12 hours.

The fractional frequency shift of the TM_{010}, TM_{110} and TM_{210} modes is shown in Figure 2.25. Over the 12 hour period, the TM_{210} mode tracks the TM_{010} mode almost identically, but the uncertainty in the TM_{110} mode is larger. This is quantified by the mean absolute error (from the TM_{010} mode) shown in Table 9.

	TM_{110}	TM_{210}
Mean Absolute Error (×10^{-5}) of fractional frequency shift (from TM_{010} mode)	0.104	0.009

Table 9 – Mean Absolute Error (MAE) from the TM_{010} mode fractional frequency shift of the TM_{110} mode and the TM_{210} mode.

The TM_{210} mode is clearly the more accurate reference to the TM_{010} mode and has a very small error in fractional frequency shift of less than 0.2%.

Though the mean absolute error of the TM_{210} mode is 0.009×10^{-5}, the mean error is 0.006×10^{-5}. This suggests that there is some small systematic offset present. The systematic offset is the same effect that was described above and is due to the nature of the split in the cavity, since the TM_{010} mode has rotational symmetry and the TM_{020} does not. This offset however, is clearly minute and can be corrected since it is a fixed relationship between the two modes.

Since we have the relationship

$$\frac{\Delta f}{f} = \alpha(T)\Delta T$$

the maximum fractional frequency shift observed of $-5.52349\ \times10^{-5}$ is simply divided by $\alpha(T)$ to give a temperature change of -2.488K.

Stimulus of samples in the split cavity

The split cavity described in this work offers a uniform, axially polarised *E*-field for measurements at arbitrary split widths. We therefore have unprecedented access for samples under test in a uniform TM_{010} *E*-field. Such quick and easy access enables the straightforward implementation of countless experiments. As a demonstration, the following investigations test the photoactivity of powders and sheets of transparent conducting oxides.

Mica platelets approximately 20-30μm in length and up to 1μm in thickness coated with a layer of antimony-doped tin oxide (ATO) were placed into the cavity on a low-loss PTFE platform. With a split of arbitrary (1-2cm) width, an ultraviolet lamp of centre wavelength 254nm was suspended above the powder sample.

Results and discussion

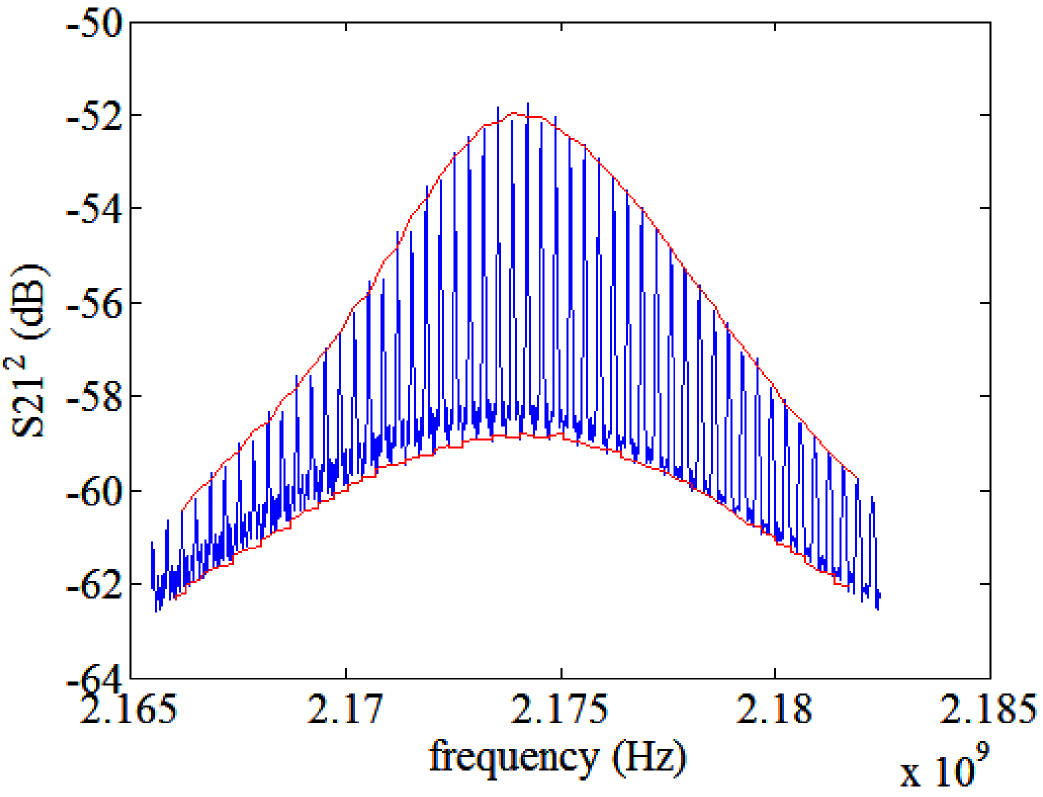

Figure 2.26 – Trace of the TM_{010} mode power transmission coefficient, taken from the Agilent ENA5701B Vector Network Analyser for the TCO powder sample under UV irradiation (blue) and the Lorentzian curves fitted to the excited and unexcited states.

The resonance of the TM_{010} mode of the split cavity is shown under UV stimulation in Figure 2.26. The ‘spiked’ trace shows the Vector Network Analyser (VNA) sweep of the TCO sample under the influence of the UV lamp. The UV strip light is mains operated at a frequency of 50Hz. The observed spikes therefore correspond to excitation of electrons into the conduction band as the 254nm wavelength light oscillates with a period of 20ms. The relaxation time of the excited electrons is much shorter than the VNA or UV lamp responses and the periods of excitation are associated with mains fluctuations above some ‘switch-on’ threshold. In fact, the spikes present in the trace correspond to the ‘off’ state, where no UV light falls upon the sample. This occurs twice for each cycle and therefore 100 peaks are exhibited per second as the VNA samples the resonant peak. As described in section 2.2.3, the cavity resonator response is Lorentzian in form, so by fitting a Lorentzian curve to the excited and unexcited states of the sample it is possible to extract the resonant frequency and bandwidth of the states. This result shows the unique ability of the split cavity to investigate the dielectric and conductive properties of powders.

In order to refine this approach, powders may be formed into pellets so that sample volumes and macroscopic dipole moments are more easily calculated. A further step may be to use a sheet sample of conducting particles dispersed in a low-loss dielectric lacquer as described in chapter 3 of this work. In this way, sample volumes are more easily calculated plus the level of UV excitation is quantifiable since the sample can be irradiated from both sides and is fully penetrated by the UV light. The AC driven UV source used here serves to expose the dynamic nature of the measurement technique and provides further questions regarding relaxation of the excited state. This is may have some further use in the interpretation of excitation mechanisms, but using a DC UV source will isolate the ‘steady’ excited state for clearer analysis.

2.4 Conclusions

The cavity resonator measurement technique is well established as a useful and accurate method for assessing the complex dielectric and magnetic properties of samples. The method can be tailored to measure bulk dielectrics, metals, powders, liquids, gases and plasmas. These may be anything from biological tissue to inorganic electronic materials. The method has even been used to investigate the fundamental physics of materials such as the quantum hall effect. Cavity perturbation methods have found use in industry, for example in the measurement of ceramic plates using a split cavity, which forms Japanese Industrial Standard JIS-R-1641.

In this work, a new experimental scheme is developed in which a cylindrical resonant cavity is constructed with a split orthogonal to the plane of the split described in JIS-R-1641 (i.e. in the plane of the cylinder axis). In the TM_{010} mode, this cavity operates effectively, with no associated wall currents having to traverse joints in the cavity construction. We therefore maintain a high quality factor

(>8000), enabling the accurate measurement of dielectric samples. By integration of the purely azimuthal *H*-fields at the surfaces of the cavity walls and end plates it is determined that the optimum Q factor is obtained when the cavity radius a is equal to the cavity height, and that the maximum obtainable Q for the TM_{010} mode is therefore equal to $a/2\delta$, where δ is the skin depth of the electromagnetic fields at the cavity walls. The TM_{010} mode has a highly uniform electric field at its centre in which a cylindrical sample inserted axially will experience minimal depolarisation, enabling highly accurate measurements. Such depolarisation is shown, for a cylinder of water, to result in a decrease in dissipated power of a factor of over 1600. A simple and dynamic calibration technique is described, which uses metal spheres of known electric dipole moment to characterize the cavity configuration. This means that measurements may be taken with the cavity split at arbitrary widths simply by taking a measurement of the metal sphere first.

The merits of different methods of calibration are discussed, in particular, the ability of empirical methods of calibration to account for systematic experimental error rather than the idealised approaches of analytical or numerical approaches. Analytical and numerical approaches are useful in conventional measurements, but for complex structures with evanescent fields, which are difficult to model, empirical approaches are invaluable.

Limitations of the perturbation method were discussed and the complex frequency was introduced as a method of overcoming the assumptions made by perturbation theory. But for the split cavity, we conclude that the complex frequency approach is not dynamic enough to avoid experimental errors. The calibration must be empirical and since use of the complex frequency would require full characterization of the complex space of interest, it is impractical for arbitrary split widths.

Correction factors were discussed as a means to account for non-linear effects beyond the assumptions of perturbation theory. One example of such analytical corrections is introduced in section 2.3.4, and uses mode matching techniques to account for the presence of the sample insertion hole. The more recent ‘rigorous’ approaches which use Ritz-Galerkin methods may indeed be called corrections, but serve no practical purpose, since they are simply concerned with numerically producing inversion charts. This may of course be a valid approach and may even expose sources of non-linearity, but it is not a correction factor in the analytical sense and is certainly not appropriate for practical measurements in the split cavity at arbitrary split width.

The cavity resonator was investigated with the split present, up to 8mm in width. The Q factor remains >7000 for large split widths indicating that accurate and highly repeatable measurements may be taken. The value used in the inversion, V_{eff} describes an effective volume occupied by the cavity fields and in the linear perturbation equations used in this work functions as a calibration variable. For the split cavity, the behaviour of the effective volume occupied by the cavity *E*-field is investigated for widths of up to 8mm. The increase in effective volume is linear in nature and the dominant source of error is the setting of the split width. Each time that V_{eff} is measured the split is repositioned, and the standard deviation in measured V_{eff} is over $1\mathrm{cm}^3$ for larger split widths. Two main conclusions are drawn regarding this result, firstly that for a cylindrical sample of diameter 1.36mm, with complex permittivity $\varepsilon^* = 4 - j0.4$, and with initial $V_{\mathrm{eff}} = 70\mathrm{cm}^3$, the change in resulting permittivity caused by variations in V_{eff} of one standard deviation are negligible (this is not the case for less robust configurations of the cavity measurement such as in depolarising samples). And secondly, though inadequate knowledge of the split width is the dominant source of uncertainty here, no such error exists in cavity measurements, since the inversion does not require any knowledge of the split width; the value of V_{eff} is calibrated for any given arbitrary width.

Sample measurements were carried out in the split cavity at widths once again up to 8mm. Using a cylindrical dielectric sample consisting of powders of micron-sized transparent conducting oxide (TCO) coated mica flakes, the width of the split is increased and measurements were compared with established results from the enclosed cavity (i.e. no split). The measurements remain consistent, with the errors in real and imaginary permittivity around 0.5% for a 2mm split and well below 4% even for widths of 8mm. We also note that as the cavity split widens the measurable shift in resonant frequency and bandwidth is reduced. This is an important feature of the split cavity, since the ability to measure sensitively the complex permittivity of samples relies upon a measurable shift in f and BW. We therefore lose some sensitivity in the split configuration, but also to a lesser degree some resolution is lost.

The causes of the error introduced at large split widths are investigated and it is concluded that non-uniform fields at the cavity split cause a reduced dipole moment, but the presence of a sample with finite (>1) permittivity compounds this effect. The value of V_{eff} becomes a non-linear function of split width and permittivity.

Non-linearities in the measurement make numerical approaches unavoidable at very large split widths. For cylindrical samples, using the cavity with a split present is a trade-off between split width and the level of accuracy required. The alternative of course is to take the complex frequency approach, with a numerical inversion accounting for all non-linearities, but in this case we lose the freedom associated with the arbitrary split width. The split cavity developed in this work has the useful feature of easy and comprehensive access to the sample under test, and with the novelty of the presence of a uniform, axially directed *E*-field and a simple, quick calibration technique for arbitrary split width. It is clear that the width of the cavity is limited by our accuracy requirements, but the system performs well, with less than 1% error in the real permittivity for split widths up to 4mm. If our accuracy requirements are not met at the prescribed split width, a complex frequency inversion based upon a numerical approach must be used. Furthermore, we conclude that this nonlinearity in the measurement is present only for samples present at the cavity split; pellet samples would not experience the same errors.

Higher order modes were investigated and their potential uses discussed. Analytical integration of the cavity fields shows that for the TM_{010} mode, 19% of the total electric energy is present in the region of radius 1cm in the centre of the cavity and the remaining 81% is in the surrounding, outer region. In the TM_{020} mode, the same integration reveals that only 8% of the electric energy is present in the centre region. We therefore obtain a much greater filling factor for the TM_{010} mode than for higher order modes.

Carrying out the integration throughout the sample region shows that for the TM_{210} mode, the electric energy present is over six orders of magnitude less than for the

TM_{010} mode. The TM_{210} mode is therefore unaffected by the presence of dielectric samples in the centre of the cavity. This is proven experimentally, results showing that the presence of a sample of permittivity $\varepsilon^* = 3.99 - j0.47$ and radius 0.68mm affects the mode negligibly. As a reference point this mode is invaluable, no dielectric sample, regardless of dielectric strength will influence the mode in this configuration. Any effects upon the mode are attributable to the cavity alone.

The TM_{210} mode was used as a reference for measurement of the TM_{010} mode. Normally such a measurement would require an unperturbed cavity measurement first, but by using the fixed relationship between the TM_{010} mode and the TM_{210} mode, we can establish an unperturbed frequency for the TM_{010} resonance without having to observe sample-free measurement at all. This is an advantageous extension of the cavity perturbation technique in terms of general convenience, but importantly, enables measurements to be taken over time without having to disturb the sample under test.

The temperature dependence of TM_{mn0} modes was established and it was determined that the fractional frequency shift for a given temperature change is identical in all such modes. Over a period of twelve hours, as the ambient temperature of the laboratory fluctuates diurnally, the TM_{210} mode is shown experimentally to track the fractional frequency shift of the TM_{010} mode to a mean absolute error as small as 0.009. The shift in frequency depends only upon the radius of the cavity and it is shown that temperature changes may be tracked to around a 20mK resolution for the TM_{010} mode, 10mK resolution for the TM_{210} mode, and even higher resolution for higher order modes.

Finally, as a demonstration of the benefits of the split cavity, the photoactivity of powders and sheets of transparent conducting oxides is tested. Lorentzian curves are obtained of the real-time excitation of charge carriers into the conduction band as UV light stimulates the sample. This remarkable result shows the versatility of the split cavity for testing stimulated samples in any form.

3 COMPOSITES OF CONDUCTING PARTICLES AND TCOS AT MICROWAVE FREQUENCIES

3.1 INTRODUCTION

The high frequency electromagnetic properties of composite materials are of key importance in applications such as metamaterials, microwave heating, electromagnetic screening, radar absorption and plasmonic light trapping. Knowledge of the parameters influencing electromagnetic absorption at these frequencies is of particular interest and enables the effective design of composites to better perform their function, whether it is to create perfect lenses [48,49,50], cause targeted heating in substances [51], selectively absorb parts of the electromagnetic spectrum [52,53], or increase the efficiency of light absorption in solar cells [54].

In these areas of research it is desirable to characterize the electrical properties of composites of conducting particles. However, measuring the conductivity, carrier mobility and carrier density of conducting and semiconducting particles is a challenge. DC measurements of composites are not possible below the percolation threshold since a macroscopic current cannot flow through samples without complete conduction pathways. At microwave frequencies however, it is possible to measure the effective complex permittivity of samples and infer the electrical properties of constituent materials. Microwave measurement techniques are widely used to measure the high frequency properties of bulk dielectrics and provide a fast, non-invasive way to assess the complex permittivity of materials. In homogeneous samples, the measured loss can be directly related to the effective conductivity at the frequency of measurement. A recent review of microwave measurement techniques applied to polar liquids was carried out by Gregory et al. [55]. In this work, the onset of DC conduction and the associated low frequency dispersion is investigated using broadband frequency measurements as the concentration of conducting particles approaches and exceeds the percolation threshold. Theoretical examinations of percolative behaviour are carried out using Lorentz models and time domain analysis, and random resistor-capacitor networks are used to identify possible ‘emergent’ behaviour in composites of conducting particles.

In composites of conducting particles there is a complex relationship between the frequency response of the system and the structure and properties of its constituent materials. This relationship is further complicated if the particles themselves are inhomogeneous. Modelling of dilute composites consisting of layered; conducting particles reveals a frequency dependent electromagnetic absorption that peaks at a characteristic frequency associated with structural and material parameters. Approaches to modelling the frequency dependent permittivity of mixtures suggest that for spherical particles with a non-conducting core and a conducting outer shell, this frequency of relaxation is proportional to the ratio of core volume to total volume (see Figure 3.8) and the conductivity of the shell [3,4].

Models of the frequency response of composites indicate that increasing the conductivity of the particle causes an increase in the frequency of maximum absorption [3,4]. In this work, it is shown that this is inadequate for the case of degenerately doped semiconductors. Using the simple Drude model of the degenerate electron gas it is demonstrated that increasing the conductivity does indeed increase the frequency of the absorption peak but importantly, for semiconductors, increasing the mobility (and therefore the DC conductivity) of the particle beyond a critical value leads to a decrease in the frequency of the absorption peak. Furthermore, the effect is present in both layered and homogeneous particles, though it is observed at lower frequencies for layered particles such as those measured in this work. The analysis in this work is entirely equivalent to the widely used Rayleigh formulation [56], demonstrating the wide impact of this result.

In this work, the effect is measured in composites of layered, degenerately doped semiconducting particles and it is observed that by annealing we may increase the mobilities of the particles such that there is a reduction in the absorption peak frequency.

A broadband (100MHz-8.5GHz) coaxial reflectance probe [57], is used to measure the loss of a dilute composite of mica particles approximately 40μm in length, coated with antimony-doped tin oxide (ATO). The transparent conducting oxide (TCO) layer is degenerately doped and is of moderate conductivity. A series of samples is annealed at temperatures from 650°C to 900°C. It is shown that there is a measurable shift in the absorption peak frequency corresponding to the increasing electron mobility in the TCO layer.

3.2 BACKGROUND

In this work, Mica platelets approximately 20-30μm in length and up to 1 μm in thickness were coated with a layer of antimony-doped tin oxide. The degenerately doped layer was deposited by a sol-gel process giving rise to a uniform coating of ~40nm thickness. A 100nm non-conducting silica (SiO_2) layer was deposited as a diffusion barrier before the final <20nm layer of titania (TiO_2) was deposited to prevent agglomeration of the particles. The non-conducting outer layers also serve to prevent percolation of charge-carriers through the composite, though samples in this work are below the percolation threshold and are considered to be electromagnetically ‘dilute’ and non-interacting. Scanning electron microscope images are of the resulting particles are shown in Figure 3.0.

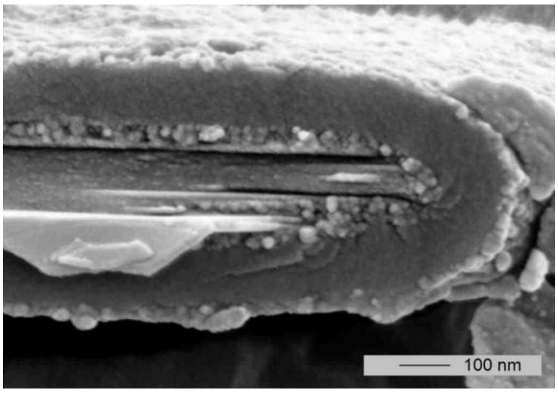

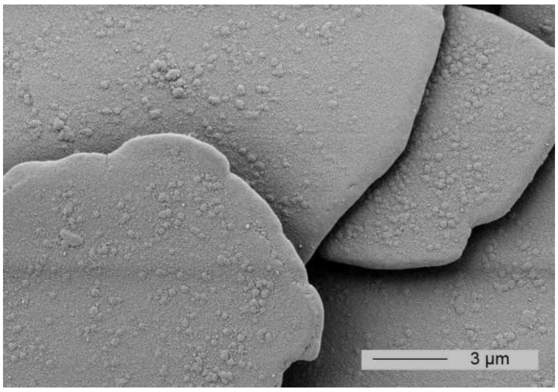

Figure 3.0 – Conducting ATO coated mica platelets, with SiO_2 diffusion barrier and TiO_2 outer layer.

3.2.1 Mixing Laws and Complex Dielectric Materials

3.2.1.1 Introduction to Mixing Laws

Predicting the effective electrical properties of complex heterostructures is not a trivial task. Many mechanisms contribute to the overall polarisation of a composite and though many theories exist to predict the overall response to an electric field, large differences are evident when compared to measurement.

This section begins with a general discussion of composites and their effective response to electromagnetic fields. From first principles, some of the more common theoretical approaches to predicting effective electrical properties are derived.

Investigation of the effective permittivity of random heterogeneous media such as conducting particles randomly placed in a dielectric matrix must start from the simplest case. Our understanding of the electrodynamic response of the composite may then be systematically extended to more complex scenarios such as anisotropic geometries or intrinsically anisotropic materials. Approaching the discussion of composite media in this way allows us to highlight deficiencies in mixing theories and modelling and enables us to seek improved methods for predicting the effective properties of these materials.

This section therefore begins with the simple model of spherical conducting particles in a dielectric matrix and proceeds to derive the most fundamental of all mixing laws, the Maxwell Garnett mixing formula. This thorough derivation will allow us to assess the weaknesses of the formula and others like it.

3.2.1.2 The Maxwell Garnett mixing formula

The spheres in Figure 3.1 are given permittivity ε_i. We term this the *inclusion* phase, which can be said to occupy a fraction f of the total volume. The dielectric background in which the spheres reside is given a permittivity ε_e, and it follows that this *host* phase occupies a volume-fraction $1 - f$.

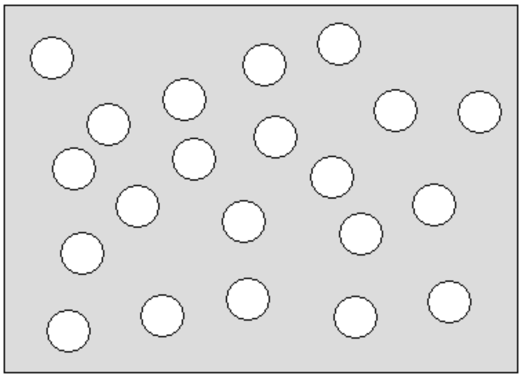

Figure 3.1 – Distribution of spherical particles in host phase

The effective permittivity of this mixture can be considered via the constitutive relation of the volume-averaged electric field ***E*** and electric flux density ***D***.

$$\langle D \rangle = \varepsilon_{eff} \langle E \rangle \tag{21}$$

The averaged fields can now be considered as the sum of averaged fields in the respective phases weighted by the volume fractions.

$$\langle D \rangle = f\varepsilon_i E_e + (1-f)\varepsilon_e E_e \tag{22}$$

$$\langle E \rangle = fE_e + (1-f)E_e \tag{23}$$

Now for the effective permittivity

$$\varepsilon_{eff} = \frac{f\varepsilon_i\left(\frac{E_i}{E_e}\right) + \varepsilon_e(1-f)}{f\left(\frac{E_i}{E_e}\right) + (1-f)} \qquad (24)$$

The key to solving for effective permittivity is therefore to have a method of relating the internal and external electric fields for particles in the composite. This is achieved by considering the case of a single dielectric sphere placed in the host dielectric matrix and subjected to a uniform polarising field $\boldsymbol{E_0}$. The initially uniform field is deformed by the presence of the inhomogeneity, the effect of which can be modelled by a dipole centred at the origin. The field inside the sphere becomes a uniform depolarising field, and is in the opposite direction to $\boldsymbol{E_0}$.

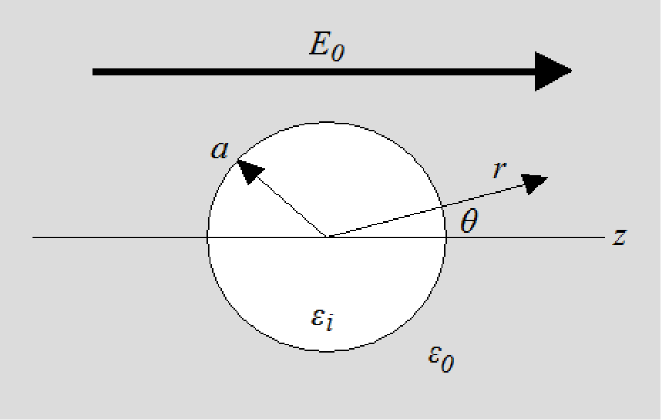

Figure 3.2 – Sphere in uniform field $\mathbf{E_0}$

The uniform field acts along the axis *z*, the sphere has radius *a*. As before, the sphere has permittivity ε_i, and the host matrix has permittivity ε_o. The problem can be solved by taking the Laplace equation with the appropriate boundary conditions at $r = a$. The solution to $\nabla^2\Phi = 0$ is unique and the problem is formulated in spherical coordinates to simplify the application of boundary conditions. After separating variables, using Legendre polynomials we can expect the solution to be of the form

$$\Phi_{in} = \sum_{l=0}^{\infty} A_l r^l P_l(\cos\theta) \qquad (25)$$

inside the sphere,

$$\Phi_{out} = \sum_{l=0}^{\infty}\left[B_l r^l + C_l r^{-(l+1)}\right]P_l(\cos\theta) \qquad (26) \qquad \text{outside the sphere.}$$

Outside the sphere contributions can be seen from the polarising electric field and from the induced dipole which distorts the uniform field around the sphere. These are quasistatic approximations that work well in practice [58]. At infinity $\Phi = -E_0 r\cos\theta$ and the boundary condition causes the only non-vanishing term in the expansion (26) to be $B_1 = -E_0$. The remaining coefficients in equations (25) and (26) can be obtained at *r* = *a* by using the following boundary conditions.

For ***E*** tangential to surface

$$-\frac{1}{a}\frac{\partial\Phi_{in}}{\partial\theta}\bigg|_{r=a} = -\frac{1}{a}\frac{\partial\Phi_{out}}{\partial\theta}\bigg|_{r=a} \qquad (27)$$

For ***D*** normal to surface

$$-\varepsilon_i\frac{\partial\Phi_{in}}{\partial r}\bigg|_{r=a} = -\varepsilon_o\frac{\partial\Phi_{out}}{\partial r}\bigg|_{r=a} \qquad (28)$$

In each series above, after imposing the boundary conditions, the resulting equations can be satisfied only if subsequent terms after *l* = 1 vanish [4], leading to

From (27)

$$A_1 = -E_0 + \frac{C_1}{a^3} \qquad (29)$$

and from (28)

$$\varepsilon_i A_1 = \varepsilon_e\left(-E_0 - \frac{2C_1}{a^3}\right) \qquad (30)$$

Solving simultaneously we have,

$$A_1 = \frac{-3E_0\varepsilon_e}{\varepsilon_i + 2\varepsilon_e} \qquad (31)$$

$$C_1 = E_0 a^3\left(1 - \frac{3\varepsilon_e}{\varepsilon_i + 2\varepsilon_e}\right) \qquad (32)$$

Substituting in the coefficients gives

$$\Phi_{in} = -\left(\frac{3\varepsilon_e}{\varepsilon_i + 2\varepsilon_e}\right)E_0 r\cos\theta \qquad (33)$$

$$\Phi_{out} = -E_0 r\cos\theta + \left(1 - \frac{3\varepsilon_e}{\varepsilon_i + 2\varepsilon_e}\right)E_0\frac{a^3}{r^2}\cos\theta \qquad (34)$$

We can now state from equation (33) that since Φ_{in} describes a constant electric field parallel to the applied field $E_{in} < E_o$ as follows:

$$\left|\Phi_{in}\right| = \frac{3\varepsilon_e}{\varepsilon_i + 2\varepsilon_e}E_0 z \qquad (35)$$

leading to

$$\left(\frac{E_i}{E_e}\right) = \frac{3\varepsilon_e}{\left(\varepsilon_i + 2\varepsilon_e\right)} \qquad (36)$$

Returning to equation (24) and substituting we arrive finally at

$$\boxed{\varepsilon_{eff} = \varepsilon_e + 3f\varepsilon_e\frac{\varepsilon_i - \varepsilon_e}{\varepsilon_i + 2\varepsilon_e - f\left(\varepsilon_i - \varepsilon_e\right)}} \qquad (37)$$

Equation (37) is the Maxwell Garnett (MG) mixing formula. This seminal formula is the starting point for many approaches to analysing mixtures. Thorough analysis of the MG formula derivation as shown above is of fundamental importance when studying mixing formulas of this type and serves to expose the limitations of the approach. An example of the behaviour of the MG mixing formula over all volume fractions is given below for ε_i =10 and ε_e =1.

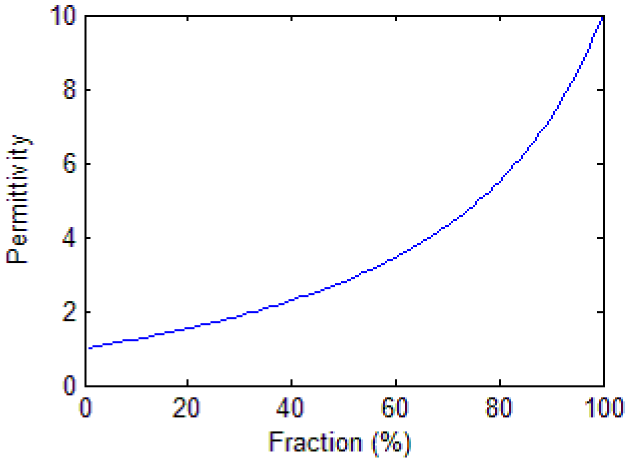

Figure 3.3 – Behaviour of the Maxwell Garnett mixing model for ε_i =10 and ε_e =1

3.2.1.3 Mixing law limitations and the Clausius-Mossotti formula

The above analysis based upon single perturbing particles can now be applied to a distribution of many particles in a background medium. The MG formula takes the polarising field to be uniform, and independent of other perturbing particles. However, the Clausius-Mossotti (CM) formula considers the polarisability of each particle as a dipole and sets the particles in a background of averaged polarisation densities. This must surely be an improvement on the MG external field, which remains ignorant of its guests in the host medium? This question may be resolved by examining briefly the origins of the CM formula.

Note that the CM method describes the effective permittivity of a composite as a function of the polarisabilities and the MG formula replaces the polarisabilities with material parameters of the mixture. The CM formulation contains explicit detail of the nature of polarisation of the individual particles, but the MG formula uses only permittivity values and volume fractions whilst assuming spherical shape.

The dipole moment $\boldsymbol{p}$ is linearly related to the polarising field as

$$p = \alpha E_e \tag{38}$$

where the coefficient of proportionality ***α*** represents the polarisability. The dipole moment is proportional to the internal field within the particle, its volume, and the dielectric contrast between the permittivities.

$$p = \int (\varepsilon_i - \varepsilon_e) E_i dV \tag{39}$$

Using the result (36) obtained earlier for E_i we may write

$$p = (\varepsilon_i - \varepsilon_e)\frac{3\varepsilon_e}{(\varepsilon_i + 2\varepsilon_e)} E_e V = 4\pi a^3 \varepsilon_e \frac{\varepsilon_i - \varepsilon_e}{\varepsilon_i + 2\varepsilon_e} E_e \tag{40}$$

and so the polarisability can be written

$$\alpha = V(\varepsilon_i - \varepsilon_e)\frac{3\varepsilon_e}{\varepsilon_i + 2\varepsilon_e} \tag{41}$$

which appears in the final CM formula for the effective medium.

The average electric polarisation density is given by

$$\langle P \rangle = np_{mix} \tag{42}$$

where n is the number density of dipoles, which are all assumed by nature of the averaging to be of equal strength. p_{mix} is the dipole moment of a single particle in the mixture and is different from the previously calculated dipole moment. Since polarisability remains constant, the local field $\boldsymbol{E_L}$ around the particle must also change and is given by

$$p_{mix} = \alpha E_L \tag{43}$$

Combining equations (42) and (43),

$$\langle P \rangle = n\alpha E_L \tag{44}$$

The classical approach to the external electric field is to consider that it is a uniform field in which the particle is placed. In reality, the external field is distorted due to the polarisation of the particle and the local field is increased. The contribution of this polarisation to the local field (also known as the Lorentz field) can be calculated as follows

$$E_L = \langle E \rangle + \frac{1}{3\varepsilon_e}\langle P \rangle \tag{45}$$

This equation is governed by the shape of the particle and features the 'depolarisation factor' 1/3, which is characteristic of a sphere. Substituting for <*P*> in equation (45) and rearranging for $\boldsymbol{E_L}$ yields

$$E_L = \frac{\langle E \rangle}{1 - \frac{n\alpha}{3\varepsilon_e}} \tag{46}$$

Since

$$\langle D \rangle = \varepsilon_{eff}\langle E \rangle = \varepsilon_e\langle E \rangle + \langle P \rangle \tag{47}$$

we can substitute for <*P*> followed by $\boldsymbol{E_L}$, and rearrange for ε_{eff} to obtain

$$\varepsilon_{eff} = \varepsilon_e + \frac{n\alpha}{1 - \frac{n\alpha}{3\varepsilon_e}} \tag{48}$$

which is the Clausius-Mossotti mixing formula.

3.2.1.4 Review of the classical approach

The Maxwell Garnett formula is the basis for many variations that are applied in wide-ranging settings. It can be manipulated to apply to more complicated mixtures such as anisotropic materials or geometrical anisotropy caused by arbitrarily shaped inclusions, and even lossy materials. The MG formula can be effectively applied to lossy materials by the conventional approach of using a complex permittivity,
Where

$$\varepsilon = \varepsilon' - j\varepsilon'' = \varepsilon' - \frac{j\sigma}{\varepsilon_0 \omega} \qquad (49)$$

Where σ is the conductivity, ε_0 is the permittivity of free space, and ω is the angular frequency. We must also note at high frequencies that the MG formula is only valid in the quasi-static limit (the wavelength is much greater than particle dimensions).

Uncertainties

The derivation started by analysing the response of a single particle in a uniform field. This was then adapted to account for other particles in a homogenised background medium, with local fields perturbed by the Lorentz contribution. This provides a solid theoretical base that at first glance may be considered to model well the behaviour of composites. It is the case however, that this analysis is based upon averages and homogenised fields. Real composites are not averages, and in a random medium whose electrical response is influenced by its microstructure, the precise results produced cannot provide the exact answer. It is of course not possible to have absolute knowledge of such a microstructure, and so we must accept some form of statistical approach. But having accepted this, we note that it is necessary to accommodate uncertainties in the structure and set about characterising them. In subsequent sections we shall introduce bounds as a method of quantifying the uncertainty of these results.

Weaknesses

Apart from the inherent uncertainties brought about by averaging, there are a number of fundamental factors that cause differences between MG predictions and reality. The common feature of these is that they stem from the idealised model in which the MG system is conceived. A factor in the geometrical dependence of the electrical response is the interaction between the particles. The CM formula accounts for the Lorentz field of each particle, but the stimulus for this contribution to the local field from polarisation is simply an averaged field and cannot account for the cumulative effect of neighbouring Lorentz contributions. In order to do so, we would have to completely describe the many-body problem of interacting particles.

Differences can also be caused by mechanisms such as percolation. When the concentration of conducting inclusions reaches the percolation threshold the electrical response of the composite changes considerably. Conducting pathways form across the length of the sample and current flows. It is also the case that in real composites clustering occurs and particles are no longer individual spheres but clustered conductors of random shape.

3.2.1.5 Bounds on effective permittivity values

As discussed in the previous section, we cannot have complete knowledge of a sample microstructure. Variations in the structure can alter the effective electrical properties of the medium and so a level of uncertainty must be accepted. In order to quantify these uncertainties we can produce upper and lower bounds on the possible values of permittivity and assert that the actual value must lie somewhere therein. To begin this brief look at bounds on the effective permittivity, we first examine the most basic limits and then discuss how, by considering more information about the medium, we can further narrow the allowable values.

In a two-phase mixture we might expect the effective permittivity of the medium to fall somewhere between the permittivity values of each constituent material. This seems to be a reasonable assumption, but the effective permittivity of lossy materials can actually exceed the value of both constituents [2]. Here we treat only lossless dielectrics for which the assumption will hold. To state stricter bounds than this a two-phase mixture is considered with arbitrary volume fraction, but with the inclusions aligned firstly with the direction of flux and then perpendicular to the flux.

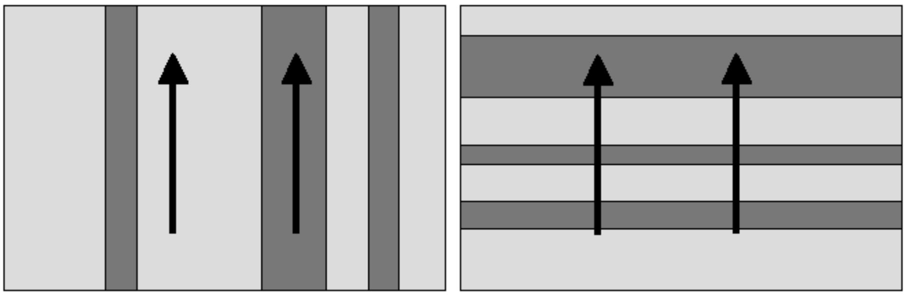

Figure 3.4 – Inclusions aligned with the electric flux and perpendicular to the electric flux form limits of possible effective permittivity values for the medium

The effective permittivities for the two cases are

$$\varepsilon_{eff,\max} = f\varepsilon_i + (1-f)\varepsilon_e \tag{50}$$

$$\varepsilon_{eff,\min} = \frac{\varepsilon_i \varepsilon_e}{f\varepsilon_e + (1-f)\varepsilon_i} \tag{51}$$

Each case corresponds to capacitors either connected in series or parallel in a circuit. These two simple limits are known as Wiener bounds. Stricter bounds exist such as those developed by Hashin and Shtrikman, who used a variational method to develop bounds for the effective permeability of a mixture, though the results are analogous. A functional is written for the electrostatic energy in the medium, which is a volume integral of the fields and polarisation densities. The stationary value of this volume integral can be shown to be the correct total energy value. Exploiting the stationary value by using various trial distributions upper and lower bounds can be formed, leading to the following Hashin-Shtrikman bounds [59]

$$\varepsilon_{eff,ext1} = \varepsilon_e + \frac{f}{\dfrac{1}{\varepsilon_i - \varepsilon_e} + \dfrac{1-f}{3\varepsilon_e}} \tag{52}$$

$$\varepsilon_{eff,ext2} = \varepsilon_i + \frac{1-f}{\dfrac{1}{\varepsilon_e - \varepsilon_i} + \dfrac{f}{3\varepsilon_i}} \tag{53}$$

Figure 3.5 shows the possible values of a composite with inclusions of permittivity in a host matrix of permittivity 1. The Hashin-Shtrikman bounds are seen to be significantly stricter than the Wiener bounds.

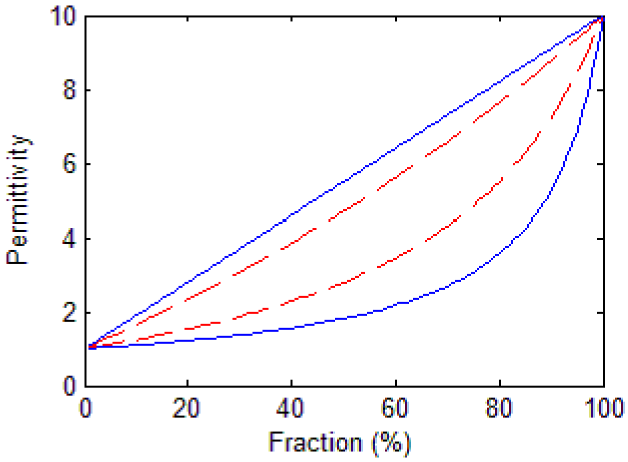

Figure 3.5 – Wiener (blue) and Hashin-Shtrikman bounds (red dash) for ε_i =10, ε_e =1

Higher-order bounds exist which take into account correlation functions of the structure (such as radial distribution functions and orientational distribution functions) in order to characterise the microstructure and classify the material into still stricter bounds [60].

3.2.2 An Introduction to Relaxation in Core-Shell Structured Particles

This section provides an introduction to the concepts of relaxation in small particles, which are further explored in subsequent sections. We consider the polarization behaviour of small conducting particles and explore frequency dependent behaviour. Small conducting particles exhibit interesting electrodynamic properties which vary dramatically with size, distribution, conductivity, shape and structure. Small *homogeneous* metallic particles often display loss peaks in the optical frequency range that are associated with resonance absorption and scattering effects. By adjusting the properties of conducting particles it is possible to observe a shift in frequency of such loss-peaks to the microwave region. In this section, the nature and cause of this frequency shift will be considered theoretically.

Microwave absorbing materials find use in areas such as medical research, telecommunications and microwave heating applications. Composite materials containing particles with conductive coatings provide a means to tailor dielectric relaxation at microwave frequencies. A thin-film related reduction in conductivity can be considered to contribute to the reduced-frequency relaxation effect. The relationship between coating conductivity and relaxation frequency is the subject of current research, and the literature [61] provides various examples of investigations of particles with conductive coatings. In Youngs et al. (2006) it states in relation to shifting relaxation to microwave frequencies that, "This could be achieved by using a filler with reduced conductivity, but there is no continuum of conductivity in naturally occurring materials to allow engineers to readily achieve this aim or to have complete design freedom." However, in this work the use of degenerately doped conducting oxides does indeed allow the investigation of relaxation effects via a continuum of coating conductivities.

3.2.2.1 Interpretations

Typical dielectric relaxation of Debye form is shown in Figure 3.6. In its simplest interpretation, the polarisation observed is considered to be due to a gathering of charge at the interfaces between constituent materials. This is the so-called Maxwell-Wagner effect and from this starting-point we can begin to unravel the subtleties of dielectric relaxation in complex heterogeneous materials.

Considering the bulk properties of a material with reversible polarisation, we may define a complex dielectric permittivity such that

$$\varepsilon^*(\omega) = \varepsilon_\infty + \frac{\varepsilon_s - \varepsilon_\infty}{1 + j\omega\tau} \tag{54}$$

where,

$$\varepsilon^*(\omega) = \varepsilon'(\omega) - j\varepsilon''(\omega) \tag{55}$$

The real and imaginary permittivities may be given as follows

$$\varepsilon'(\omega) = \varepsilon_\infty + \frac{\varepsilon_s - \varepsilon_\infty}{1 + \omega^2 \tau^2} \tag{56}$$

$$\varepsilon''(\omega) = \left(\varepsilon_s - \varepsilon_\infty\right) \frac{\omega\tau}{1 + \omega^2 \tau^2} \tag{57}$$

This well-known classical treatment of Debye [62] presents a general approach to time-dependent dielectric polarisation based upon τ, the relaxation time. The angular frequency is represented by ω, and the bulk permittivity values are split into the contribution from static permittivity, ε_S, and the contribution from electronic polarisation, ε_∞, which is considered to be instantaneous in the microwave region and is responsible for the optical refractive index of the material.

3.2.2.2 Loss-peaks and the relaxation time

Debye behaviour is plotted in Figure 3.6. The most striking feature is a frequency dependent loss, which has a peak that is characteristic of the material. To fully grasp the physical origin of Debye behaviour, we consider the basic model of a single electric dipole influenced by a time-dependent electric field.

The polarisation of a system will cause loss. We observe the peak loss value at a frequency which maximises the polarisation per unit energy applied. This frequency gives the characteristic relaxation time associated with the dominant polarisation mechanism, and since the polarisation mechanism in this system is due to charge transport, it could tell us something about intrinsic conduction properties of the material such as electron mobility.

Practical materials are not expected to follow Debye behaviour closely. Broadening of the loss-peak occurs and often a material with Debye processes may only weakly exhibit the classical response, or indeed exhibit no loss-peak at all in the frequency region of interest as is the case for percolative conducting materials.

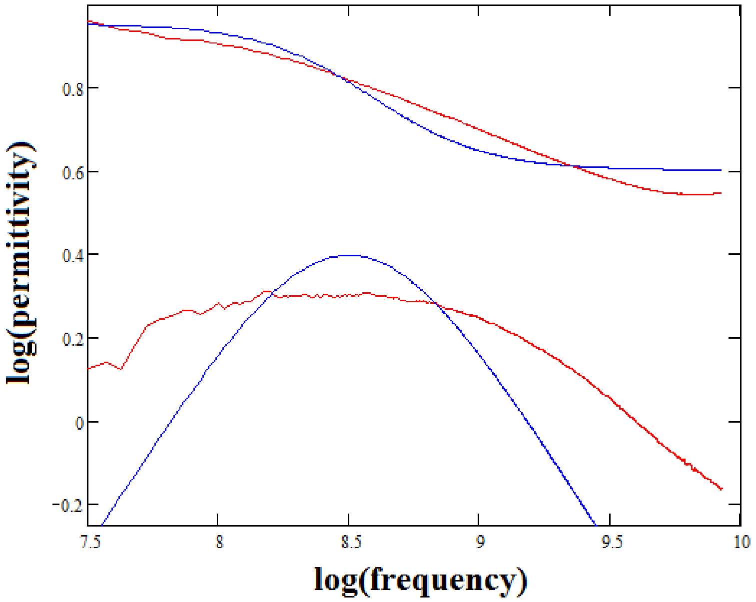

Figure 3.6 – Composite sample relaxation (red) plotted against the ideal Debye response (blue). See section 3.3.3 for sample details.

Figure 3.6 shows the real and imaginary permittivity in the for the ideal Debye response (blue) and example results (red) for Merck KGaA conducting pigments investigated in later sections of this work. For the Debye response, we have $\varepsilon_\infty = 4$, $\varepsilon_S = 9$, and the relaxation time τ, is taken as 0.5ns. The Debye model was derived for molecular polarisation and represents a system with a single relaxation time. Clearly, in a larger system, many reversible polarisations take place, all with different physical parameters. A real system will therefore have many relaxation times, which may contribute to a deviation from the Debye behaviour [63]. One might expect this behaviour in the system under test because of distributions in particle size, coating thickness, coating conductivity and variation in the spatial distribution of the particles themselves.

As mentioned above, more than one relaxation mechanism will be present and multiple relaxation times will contribute to the bulk material response. This is a common interpretation of dielectric polarisation; however, at high dipole densities this approach is not rigorous. It may be useful and instructive to characterise a response by distributions of relaxation times, but this makes the assumption that all contributing mechanisms are Debye-like polarisations. Dipoles present will interact with each other mutually and with increasing cooperative influence, this becomes an intractable multi-polar, many-body problem not adequately represented by relaxation times. We must be aware that values of τ in these cases may not simply be attributed to identifiable dipoles, but require a higher-order interpretation. However, in dilute systems with little or no interaction, the distribution of relaxation times approach may be considered a good approximation.

3.2.2.3 Multi-layered particles – A closer look

It is possible to tune dielectric relaxation to a given frequency by appropriate choice of physical parameters; most notably by choosing conductivity or those properties that affect charge transport.

The Clausius-Mossotti (CM) approach can be used to demonstrate the effect that a reduction in conductivity of the particles has on the frequency response. The CM model considers the polarisability of each particle as a dipole and sets the particles in a background of averaged polarisation densities.

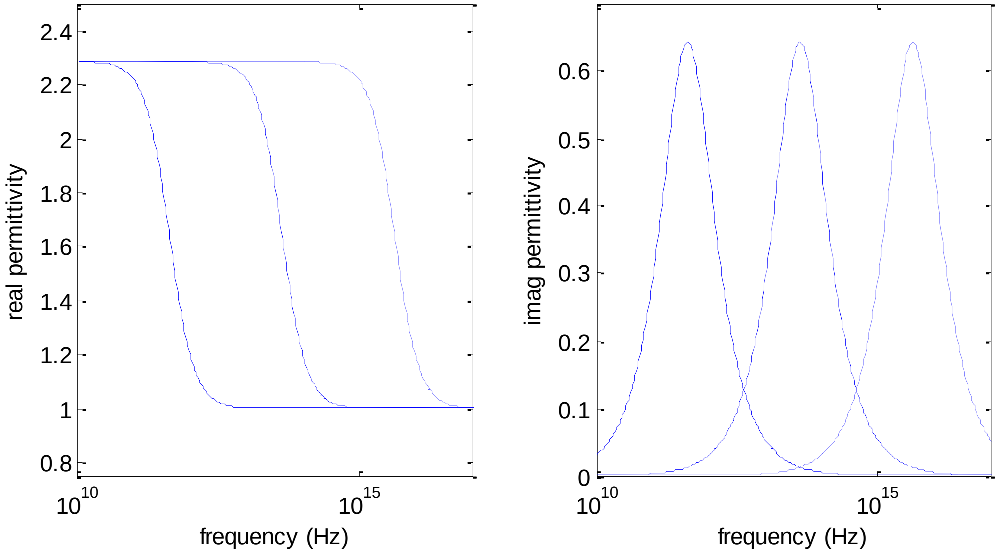

Figure 3.7 - The effect of conductivity on relaxation frequency

Figure 3.7 uses the CM model and shows the real and imaginary permittivities for solid particles of radius 10μm and at a volume concentration of 0.3. The three relaxation peaks correspond to conductivities of 10^2 S/m (solid line), 10^4 S/m (dashed line) and 10^6 S/m (dotted line). The reduced conductivity brings the frequency of relaxation down considerably, though to observe relaxation at microwave frequencies would require a conductivity of around 1 S/m.

It is possible instead, to use a dielectric particle with a conductive coating to bring relaxation down to microwave frequencies. To investigate this it is possible to extend the CM model to layered particles. The CM formula is as follows

$$\varepsilon_{eff} = \varepsilon_e + \frac{n\alpha}{1 - \frac{n\alpha}{3\varepsilon_e}} \tag{58}$$

where ε_{eff} is the effective permittivity of the sample, ε_e is the permittivity of the background medium, n is the number density of dipoles and α is the polarisability. Note that the 1/3 coefficient in the denominator of the CM equation is the depolarisation factor and is a result of the shape of the particle. It is instructive here to use spherical inclusions.

The solution for the polarisability of the layered spherical particle in Figure 3.8 is formed in the same manner as for the homogeneous particle. The electromagnetic plane-wave incident upon the sphere induces a secondary field inside and outside of the body. The resultant field is then the vector sum of the primary and secondary fields [64]. The induced secondary field for the layered sphere is constructed in three parts, one for each of the regions defined in Figure 3.8. Each part is written as an expansion that is identical to those for the single-sphere problem, but the amplitude coefficients will have different values determined by the different boundary conditions [65]. This approach is similar to that used by Mie [66], though only the absorption is included in the expansion and scattering terms are neglected, with the assumption that we are within the long-wavelength limit (i.e. the wavelength is much greater than the dimensions of the particle).

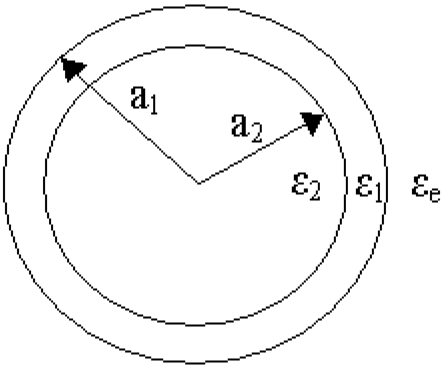

Figure 3.8 - The layered spherical particle

In the long-wavelength limit, the solution for the polarisability of the layered sphere in Figure 3.8 is as follows

$$\alpha = 3\varepsilon_e V \frac{(\varepsilon_1 - \varepsilon_e)(\varepsilon_2 + 2\varepsilon_1) + \dfrac{a_2^3}{a_1^3}(2\varepsilon_1 + \varepsilon_e)(\varepsilon_2 - \varepsilon_1)}{(\varepsilon_1 - 2\varepsilon_e)(\varepsilon_2 + 2\varepsilon_1) + 2\dfrac{a_2^3}{a_1^3}(\varepsilon_1 - \varepsilon_e)(\varepsilon_2 - \varepsilon_1)} \tag{59}$$

The analytical solution for structures such as this can be extended to multi-layered spheres regardless of the number of layers. In equation (60), for N layers the extension ends with the terms a_N^3/a_1^3 in the numerator and a_N^3/a_{N-1}^3 in the denominator [2].

$$\alpha = 3\varepsilon_e V \frac{(\varepsilon_1 - \varepsilon_e) + (2\varepsilon_1 + \varepsilon_e)\dfrac{(\varepsilon_2 - \varepsilon_1)\,a_2^3/a_1^3 + (2\varepsilon_2 + \varepsilon_1)\dfrac{(\varepsilon_3 - \varepsilon_2)\,a_3^3/a_1^3 + \cdots}{(\varepsilon_3 + 2\varepsilon_2) + \cdots}}{(\varepsilon_2 + 2\varepsilon_1) + 2(\varepsilon_2 - \varepsilon_1)\dfrac{(\varepsilon_3 - \varepsilon_2)\,a_3^3/a_2^3 + \cdots}{(\varepsilon_3 + 2\varepsilon_2) + \cdots}}}{(\varepsilon_1 + 2\varepsilon_e) + (2\varepsilon_1 - \varepsilon_e)\dfrac{(\varepsilon_2 - \varepsilon_1)\,a_2^3/a_1^3 + (2\varepsilon_2 + \varepsilon_1)\dfrac{(\varepsilon_3 - \varepsilon_2)\,a_3^3/a_1^3 + \cdots}{(\varepsilon_3 + 2\varepsilon_2) + \cdots}}{(\varepsilon_2 + 2\varepsilon_1) + 2(\varepsilon_2 - \varepsilon_1)\dfrac{(\varepsilon_3 - \varepsilon_2)\,a_3^3/a_2^3 + \cdots}{(\varepsilon_3 + 2\varepsilon_2) + \cdots}}} \tag{60}$$

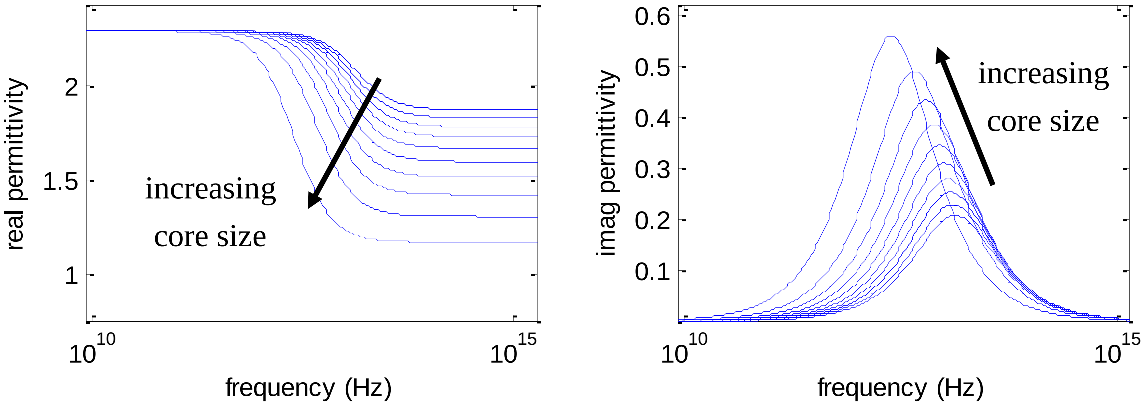

Figure 3.9 - Frequency response for increasing core:layer ratio of layered spherical particle. The core is air and the outer layer has conductivity of 10^4 S/m

Using the CM formulation, Figure 3.9 maps the transition from a solid conducting particle to a conducting layer with a dielectric (air) inner core. The particle has a diameter of 10 microns and as the size of the air core is increased linearly by volume a number of effects become apparent. The loss peak grows and reaches a maximum as the ratio a_2^3/a_1^3 converges towards 1. The influence upon frequency is also seen to increase dramatically as the shell thickness is reduced. The real permittivity in the low-frequency region remains unaffected by the particle structure. This is because the core is highly screened by the conducting outer layer and the contribution to polarisation by the core can only be seen at higher frequencies, where the shell begins to act more like a dielectric. The asymptotic real permittivity value at high frequency is therefore seen to decrease as the influence of the low-permittivity core increases.

The effects of changing the conductivity and layer thickness upon the frequency response of the layered particle are significant. It is apparent that the CM formulation models the behaviour of the layered structure well given the assumptions discussed above such as non-interaction with other particles. In subsequent sections, this approach will be extended to layered ellipsoidal particles. We shall discover that the particles under test in this work exhibit a relaxation frequency which is reduced to the microwave region by virtue of their core-shell structure and lower conductivity. However, a further reduction in conductivity may be associated with thin-film effects.

Size effects and surface scattering can have a significant influence upon charge transport and as noted above, shifts in conductivity will certainly lead to a shift in relaxation frequency. Very thin conductive coatings exhibit conductivities much lower than that of the bulk material caused by factors such as reduction in the mean-free-path and surface roughness [4]. The contribution of surface scattering becomes appreciable in the size range below 100nm; certainly greater than the thickness of layers in the samples under test here. Discontinuities in such coatings can also have a dramatic effect upon scattering [67,68]. These combined effects will cause the frequency to be reduced still further.

There is a conceptual subtlety in the polarisation of particles where screening is observed. The effects contributing to the imaginary permittivity of the depolarising particle will contribute to the real permittivity at low frequencies i.e. macroscopic energy storage occurs via the very mechanism that is the dominant cause of loss. This is one example of the intrinsic link between the real and imaginary parts of the permittivity. Indeed the imaginary part of the permittivity is often linked with the conductivity of the sample. If this conductivity is complex, then the imaginary part (i.e. conventionally the reactance), contributes to energy storage in an equivalent, capacitive sense.

Another revealing result is observed when the core permittivity is larger than that of the outer layer. When the core of the particle is not subject to a large depolarising field, the polarisation due to the real permittivity of the core causes a second relaxation peak [69]. This double relaxation peak emerges when the loss-peaks of two separate polarisation mechanisms are allowed to contribute to the overall response.

3.2.3 Mixtures At High Concentrations

3.2.3.1 Introduction to percolation

In the context of this work, the volume fraction of ATO coated mica particles dictates whether macroscopic percolation of conduction current can take place. At concentrations of around 6% by weight in lacquer, these composites begin to percolate. In this section, a short introduction to the important subject of percolation theory is described. Subsequently, percolation investigations of Merck composites are presented.

A non-conducting dielectric matrix, with conducting (or semiconducting) inclusions can be considered as a large lattice of conducting pathways. However, if the concentration of inclusions is low, pathways become broken or isolated and will form clusters. If we call p the probability of a path being occupied, then in an N^2 two-dimensional lattice as shown in Figure 3.10, $p2N(N-1)$ pathways will be occupied. This perspective of percolation is called bond-percolation as opposed to site-percolation, where occupied or vacant adjacent sites determine percolation rather than the connecting bonds.

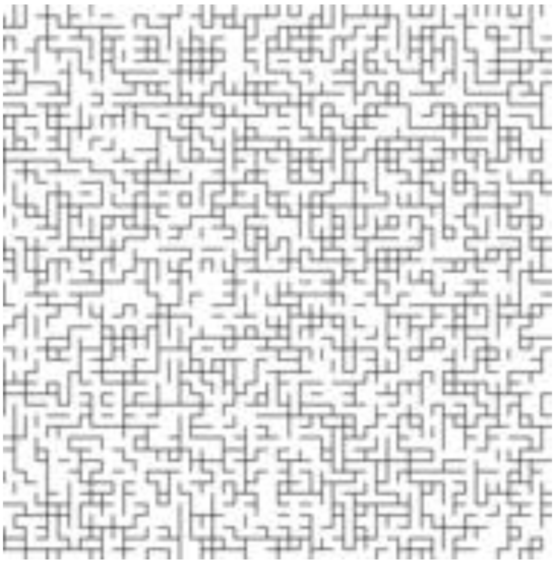

Figure 3.10 - Lattice exhibiting bond percolation

As the concentration of inclusions is increased, clusters will grow until eventually one will stretch across the entire lattice becoming an infinite cluster, it is now said to percolate through the system. The probability p_c, at which this occurs, is called the percolation threshold or the critical threshold. Peculiar phenomena are observed at this threshold, and do not necessarily translate to larger lattices. It is at this threshold that one first observes percolation across the lattice and in the terminology of phase transitions we see a ‘critical slowing down’. For example, in a conductor-insulator composite, newly formed conducting pathways will have greatly varying values of resistance. On an infinite scale, these varying values at the phase transition aggregate to an 'emergent' trend. These features are called critical phenomena and are described by scaling theory. The study of critical phenomena has applications in many fields e.g. analysing the advancement of forest fires or idealised models of oil fields to determine the probability of oil reservoirs being present [70]. Basic scaling theory examines the structure of a cluster as a representative of the entire lattice i.e. its nature on many length scales.

Taking a very small sample of the lattice in Figure 3.10, can properties such as average cluster size or proportion of occupied bonds of our sample be considered truly representative? To answer this question we consider a bond placed in the largest cluster of a percolating material with $p > p_c$. Placing a frame of size $S \times S$ around this point and counting the number of bonds belonging to the cluster $f(S)$, we see that within the cluster $f(S)$ grows linearly with S^2. However, around the percolation threshold, the cluster may have holes or include other clusters. $f(S)$ will no longer grow linearly with S^2, but instead grows linearly with S^d, where d may be 1.9 or some value below the initial dimension. We now have $f(S) \propto S^d$, where d is the fractal dimension of the lattice. Relating this to the case of conducting inclusions in a dielectric matrix, if $f(S)$ grows with $S^{1.9}$, the average density of conducting pathways can be considered to decay as $S^{-0.1}$. Therefore, for a sample of size 10cm the average density of conducting pathways will be $(10^4)^{-0.1} \approx 0.4$ that of a sample of 10μm.

Scaling behaviour such as this must be taken into consideration when modelling cells of dielectric materials. The applicability of the model to the generalised or 'infinite' case must be carefully scrutinised. However, the density of conducting pathways becomes uniform when considering length scales of sufficient size, ξ, which is called the correlation length. For our example, we can now say that $f(S)$ is proportional to $S^{1.9}$ below the correlation length and proportional to S^2 above it. The correlation length may be considered to be a measure of the largest hole in the largest cluster and a sample larger than this length should be used in order to model larger structures accurately.

3.2.3.2 Time domain analysis and the Lorentz model

The overall electromagnetic frequency response of any composite sample can fundamentally be divided into two contributions: the first from current percolation between particles; the second from the polarization of particles. In order to model the behaviour of such samples, we examine the form of the contribution from each individually and combine them in the final model, attributing appropriate critical behaviour to the percolative contribution as a function of particle volume concentration.

Starting in the time domain, the polarization of a particle is described and is related to frequency domain behaviour. In this way we are able to directly relate the frequency response to the many material and geometrical factors influencing polarization. Initially, non-percolating, polarizing particles are modelled using a Debye-type formulation. This instructive approach highlights the factors influencing the frequency response. We then look in more detail at the influence of the structure of the polarizing particles. Percolation of conduction current will then be examined using the Drude model to explain the low frequency dispersion present in percolating samples. Again, this approach will be further developed to look in more detail at the material and structural influences present. We then obtain a comprehensive final model, which combines the percolative, Drude-like behaviour and the polarising Debye-like behaviour.

THE POLARIZING PARTICLE AND THE LORENTZ MODEL

The familiar form of Debye-type relaxation can be understood by considering the response of a polarizing particle in the time domain. Upon application of the polarizing electric field, the bound charge distribution immediately begins to move, until there is a saturation of polarization. This is demonstrated by the susceptibility kernel

$$\chi(t)=\Theta(t)Ae^{-t/\tau} \tag{61}$$

where Θ is the Heaviside function, which is unity for all positive values and zero otherwise, *A* is a constant and τ is the relaxation time. This exponential decay in the time domain is observed in Figure 3.11a) , the Fourier transform of which leads us directly to the common form for Debye polarization in Figure 3.11b).

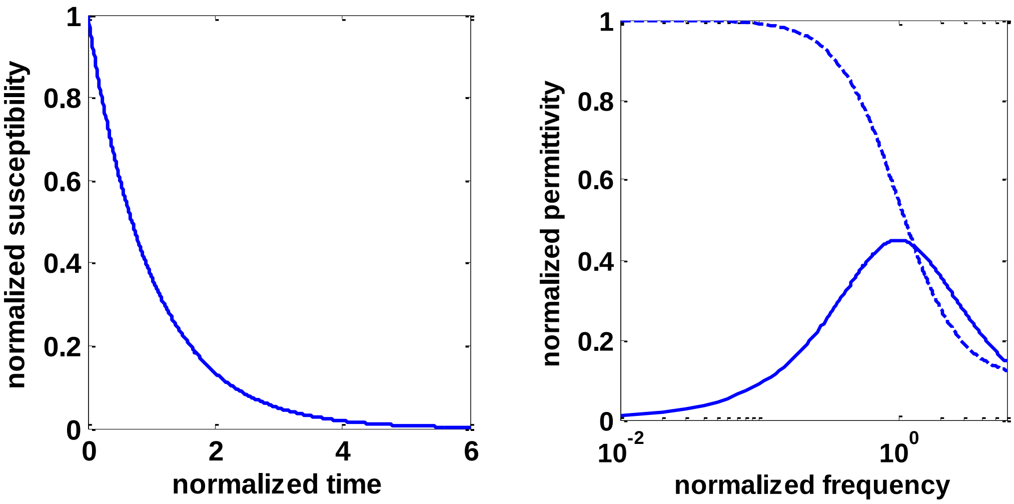

Figure 3.11 – a) Susceptibility kernel for Debye polarization in the time domain and b) real (dotted line) and imaginary permittivity frequency response for the Debye model.

The frequency behaviour shown in Figure 3.11b) can be described by the Lorentz model of an oscillating system. This model is often used to describe plasmonic resonances observed at optical frequencies and accounts for the resonance absorption responsible for the brilliant colours in optical pigments. The Lorentz equation describes the frequency dependent complex permittivity as follows:

$$\varepsilon(\omega)=\varepsilon_\infty+\varepsilon_0\frac{\omega_p^2}{\omega_0^2-\omega^2+j\omega v} \tag{62}$$

where ε_∞ is the high frequency permittivity, ε_0 is the static permittivity, ω_p is the plasma frequency, ω_0 is the resonance frequency and *v* is the damping amplitude.

We now examine the relationship of this phenomenon to the dielectric relaxation observed in Merck pigments (further described in subsequent sections) in order to cast light upon the nature of contributing mechanisms. We then further extend the model to describe the behaviour of percolating pigments observed in section 3.3. The form of dielectric relaxation observed in conducting pigments may be viewed as an overdamped resonance in the Lorentz-type system. The effect of the increased damping is to cause a reduction in both frequency and magnitude of the imaginary permittivity.

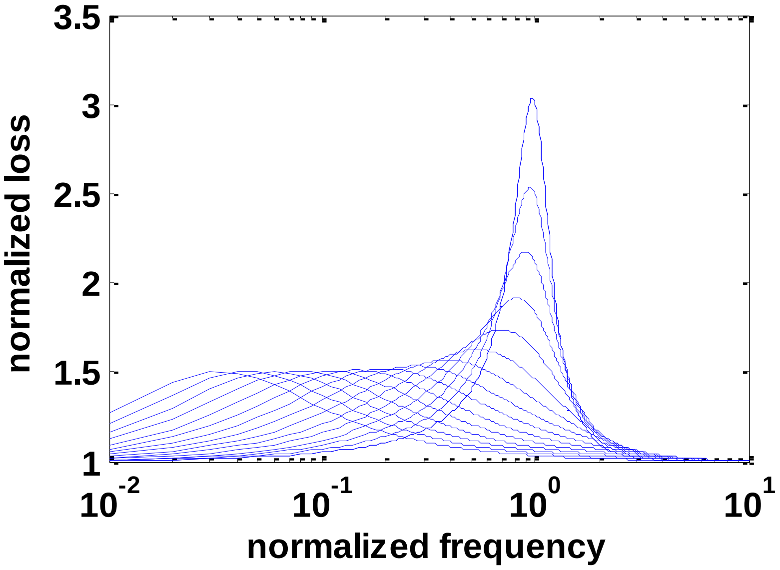

Figure 3.12 – Imaginary permittivity of the Lorentz system under increased damping. The system moves away from resonance and the loss magnitude becomes stable at some lower value.

Figure 3.12 shows the imaginary permittivity of a Lorentz system under increased damping. The loss peak reduces in frequency and magnitude, and takes the form of the Debye-type response observed in Merck pigments as the damping amplitude v is increased. This revealing approach suggests that a deeper understanding of the causes of observed frequency behaviour may be obtained by directly relating charge transport mechanisms in the ATO layer to damping effects in the oscillating system. That is to say, such effects as surface scattering and scattering due to the polycrystalline nature of the ATO layer, which are issues of electron mobility, may be distinguishable from factors of carrier density.

THE PERCOLATING LORENTZ MODEL

We now look at the application of the Lorentz model to percolating samples, before combining percolating and non-percolating conditions within the framework of polarizing pigments.

Using the Lorentz model, we have determined that the damping amplitude affects the location and form of the loss-peak in the frequency domain. Damping has a substantial effect upon the response of percolating samples also, but to explore the fundamental differences we return to the time domain. Upon application of the polarizing electric field, the charge (which is no longer bound as in the non-percolating case) begins to move, but there is no saturation of polarization. The charge continues to move as the current percolates through the network of touching particles. This is described by the susceptibility kernel (see Figure 3.13a) below)

$$\chi(t) = \varepsilon_0 \Theta(t) \frac{\omega_p^2}{v} \left(1 - e^{-tv}\right) \tag{63}$$

where Θ is the Heaviside function, ε_0 is the permittivity of free space, ω_p is the plasma frequency and v is the damping coefficient.

The freedom of charge carriers is reflected in the continued response of Figure 3.13a), the Fourier transform of which reveals in Figure 3.13b), the low frequency dispersion familiar to percolating materials.

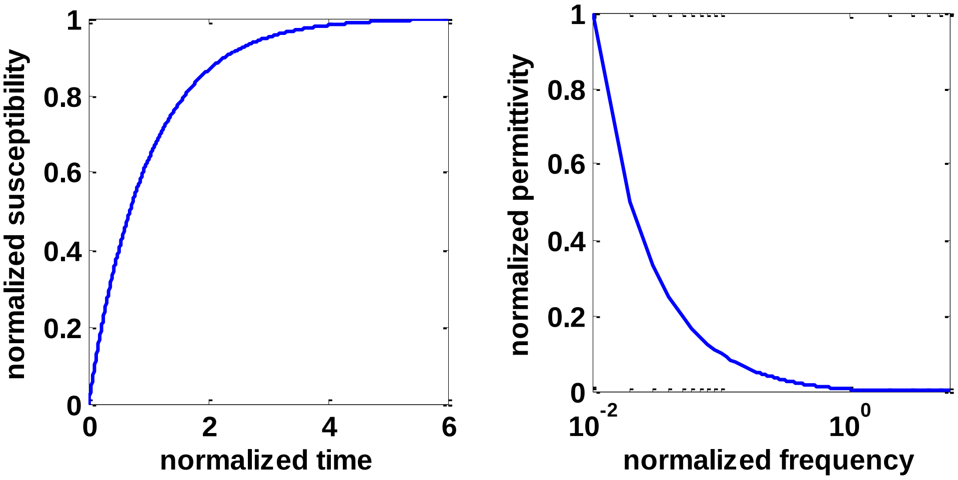

Figure 3.13 – a) Susceptibility kernel for the Drude model of current percolation in the time domain and b) imaginary permittivity frequency response for the Drude model.

The percolating and non-percolating models differ a great deal in the time domain and consequently in their frequency response. The fundamental difference is simply that the non-percolating particles exhibit interfacial polarization, whereas in percolating samples charge does not necessarily accumulate at such interfaces, but will continue through neighbouring conducting layers.

In the Lorentz system of equation (62) this may be modelled by setting $\omega_0 = 0$, giving

$$\varepsilon(\omega) = \varepsilon_\infty + \varepsilon_0 \frac{\omega_p^2}{-\omega^2 + j\omega\nu} \qquad (64)$$

which is shown in Figure 3.13b). This is the Drude model for frequency dependent permittivity.

THE INDEPENDENCE OF RELAXATION TIMES FOR DRUDE AND DEBYE-TYPE RESPONSES

It is clear that low-frequency dispersion associated with percolation is present in samples above the percolation threshold. The fully conducting sample would therefore have a monotonically decreasing imaginary permittivity as frequency increases. But how should this emerge? At a frequency of 0 Hz, the direct current cannot flow until the percolation threshold is reached, at which point we observe a first order critical transition to the conducting state. However, for alternating current the transition between such states behaves differently depending upon the frequency of observation and the position in the frequency domain relative to the relaxation frequency of the medium. It is clear that the time domain behaviours exhibited in Figure 3.11a) and Figure 3.13a) are related by the charge transport properties of the medium, but to determine to what extent, we must examine the structure of the sample further. Given the frequency behaviour of fully percolating i.e. conducting samples, we might expect the lower 'leg' of the relaxation frequency response to rise as the percolation threshold is reached.

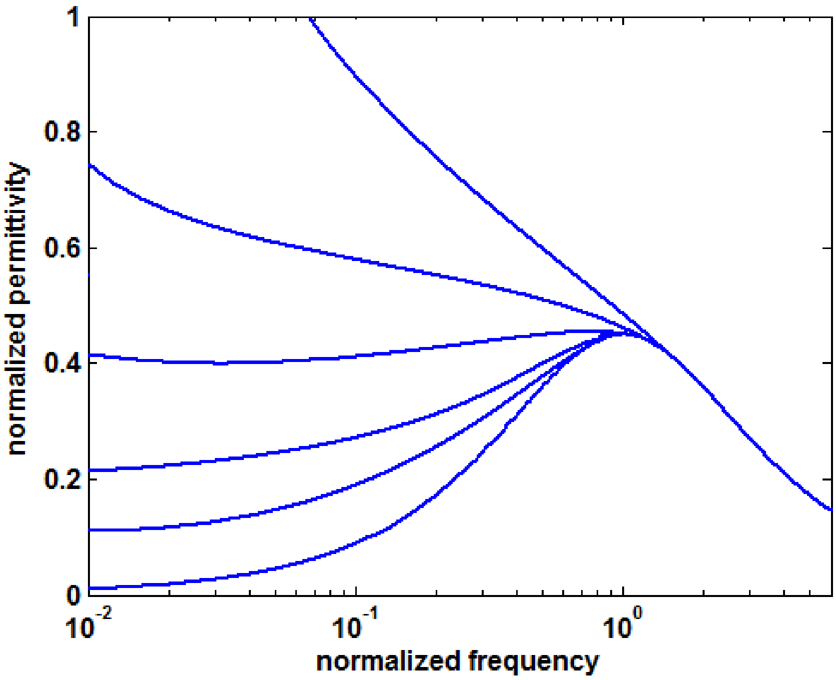

Figure 3.14 – Schematic rise of the lower 'leg' of the imaginary permittivity as percolation begins.

In Figure 3.14 the expected development of low frequency dispersion as the percolation threshold is traversed is shown schematically. The Drude-type response present in percolating systems develops from the relaxation peak of the non-percolating system. Such a system shall be investigated experimentally in section 3.3.3.

3.2.4 The Broadband Coaxial Probe

3.2.4.1 Principles

The high frequency measurement of composites has been carried out using cavity resonance methods, providing accurate results at fixed resonant frequencies. Broadband measurements, however, can provide yet more information about a material. Broadband reflectance probes are used through microwave frequencies (typically 0.1 – 10GHz) to yield signature complex plots of electrical characteristics for composites under test. The greatest advantage of the coaxial probe over other open-ended electromagnetic sensors is its effectiveness in non-destructive measurements over a broad frequency band, exposing polarisation phenomena and electrical behaviour across a large spectral range.

The coaxial reflectance probe operates on the basis that the echo signal produced at the end of a coaxial cable is characteristic of the material terminating it. The fringing electromagnetic fields at the end of the probe interact with the sample; knowledge of this behaviour and the fields around the aperture lead us to the apparent aperture admittance.

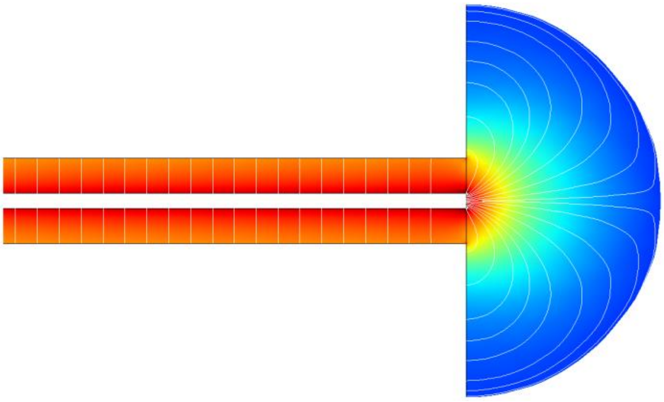

Figure 3.15 - The coaxial probe electric field distribution

Figure 3.15 shows a COMSOL finite element model of the coaxial probe used in this investigation. The coaxial cable is connected to a broadband signal source, in this case a Vector Network Analyser (VNA) and the probe end is left as an open circuit. Signals generated by the VNA are partially reflected back from the interface and the VNA yields a complex reflection coefficient, ρ.

When the open end is simply air-terminated, the electromagnetic fields at the end of the probe are evanescent, negligible power is transmitted and the reflection coefficient, $|\rho| \approx 1$. The end of the probe effectively acts as an air-spaced capacitor. If instead of the air termination a dielectric is placed at the coaxial aperture, the phase and magnitude of ρ are affected greatly by the complex permittivity ε^*, of the material. Where

$$\varepsilon^* = \varepsilon' - j\varepsilon'' \tag{65}$$

ε’ is the storage term and can be attributed to the polarisation, and ε” is the loss term. The permittivity of the terminating material influences the fringing fields of the probe. In this way it is possible to generate characteristic plots of the dielectric properties of materials across broad frequencies [71].

Figure 3.16 below shows the raw data taken from the VNA. It shows a plot of the S_{11} parameters taken from 300kHz to 8.5GHz.

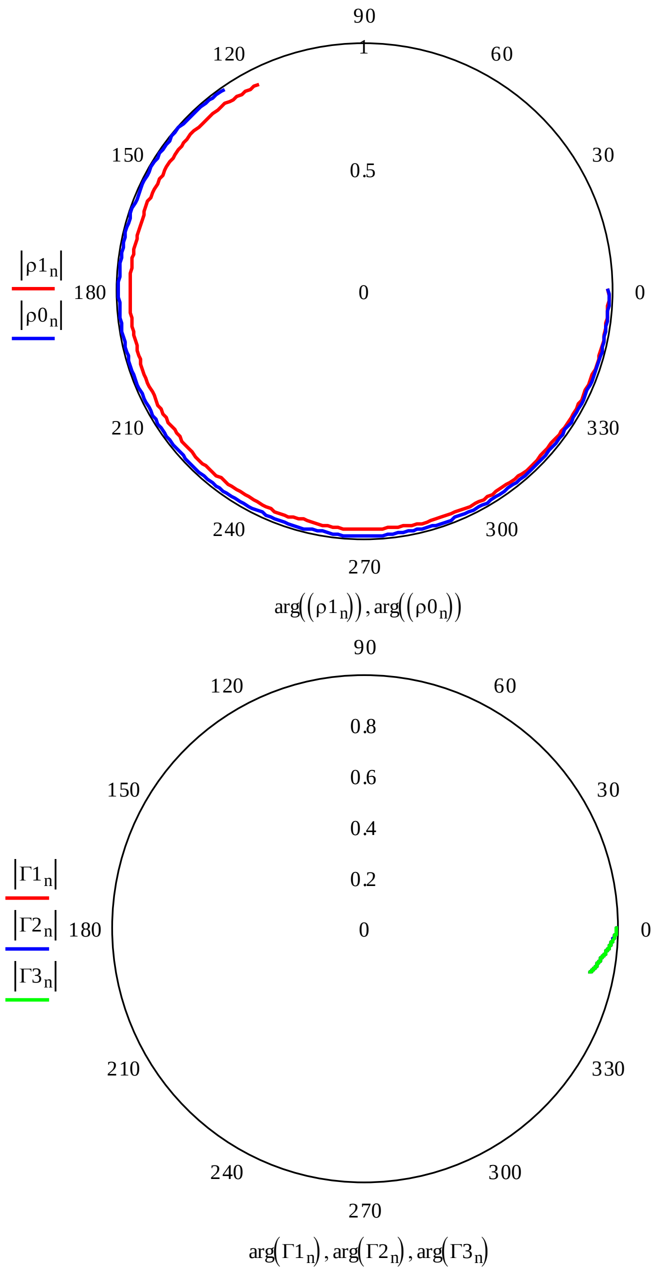

Figure 3.16 - Raw data obtained from VNA

Plot *ρ0* in Figure 3.16 is for the air terminated probe. Starting at the point 1+j0, it can be seen that as the frequency increases, the phase θ, of the reflection coefficient also increases. However, the losses remain negligible even up to 8.5GHz and the magnitude is still around 1. Plot *ρ1* shows the S_{11} parameter for the dielectric sample Minatec Gold TAT21/05, provided by Merck KGaA, which clearly exhibits a significant phase change and loss. The right hand chart in Figure 3.16 shows the ratios of ρ1 and ρ2 for three different measurements.

3.2.4.2 Inversion

The reflection coefficient, ρ, is given by

$$\rho = \frac{Z_L - Z_0}{Z_L + Z_0} \tag{66}$$

where Z_L is the impedance of the load and Z_0 is the characteristic impedance of the source (50Ω).

Considering load admittance and the associated phase of the reflection, we have

$$\rho = \frac{1 - Z_0 Y_L}{1 + Z_0 Y_L} e^{j\theta} \tag{67}$$

The phase information included in this reflection coefficient is frequency dependent, but it will also include an additional phase change due to the electrical length of the probe itself, here denoted by $e^{j\theta}$. The VNA is only calibrated to the plane of the port, so to account for the difference in electrical length we eliminate the $e^{j\theta}$ term by dividing ρ by the reference measurement, ρ_{air}, which has the same phase change. Thus

$$\frac{\rho}{\rho_{air}} = \frac{1 - Z_0 Y_L}{1 + Z_0 Y_L} \frac{1 + Z_0 Y_{L,air}}{1 - Z_0 Y_{L,air}} \tag{68}$$

If the aperture admittance of the air terminated probe is known, it becomes trivial to extract the aperture admittance of the sample under test, Y_L. It is at this point that a model is required relating the aperture admittance to the material properties. This will enable us firstly to determine the aperture admittance of air (as the material properties of air are well documented), allowing us to extract Y_L from equation (68), and secondly, it will enable us to relate the newly extracted Y_L, to the effective permittivity of the sample.

A discussion of the approach to modelling aperture admittance follows in subsequent sections. The model used in this work, reduces finally to

$$Y_L = jA\omega\varepsilon + jB\omega^3\varepsilon^2 + C\omega^4\varepsilon^{5/2} + O(\omega^5\varepsilon^3) \qquad (69)$$

where the coefficients *A*, *B* and *C* are determined by the geometry of the aperture. However, subsequent terms in this series expansion tend to zero with the assumption that the aperture of the probe remains electrically small and radiation is negligible, giving

$$Y_L = jA\omega\varepsilon \qquad (70)$$

The coefficient *A* can now be determined experimentally or analytically for the geometry of the probe in use. For the probe in this work, *A* was determined by measuring dielectrics of known permittivity, yielding a result of 8.2 ± 0.5 × 10^{-15} Ω^{-1}s. This may be interpreted as quantifying the fringing field entering the material from the end of the probe.

In practice, this technique requires a calibration measurement to be taken for each set of measurements, but measurements take seconds to complete and the calibration is carried out by simply removing the sample from the probe and exposing it to the air. The inversion is then completed automatically.

The procedure does require that a good contact is made between the aperture and the material, but using a simple clamping mechanism the procedure is effective and robust.

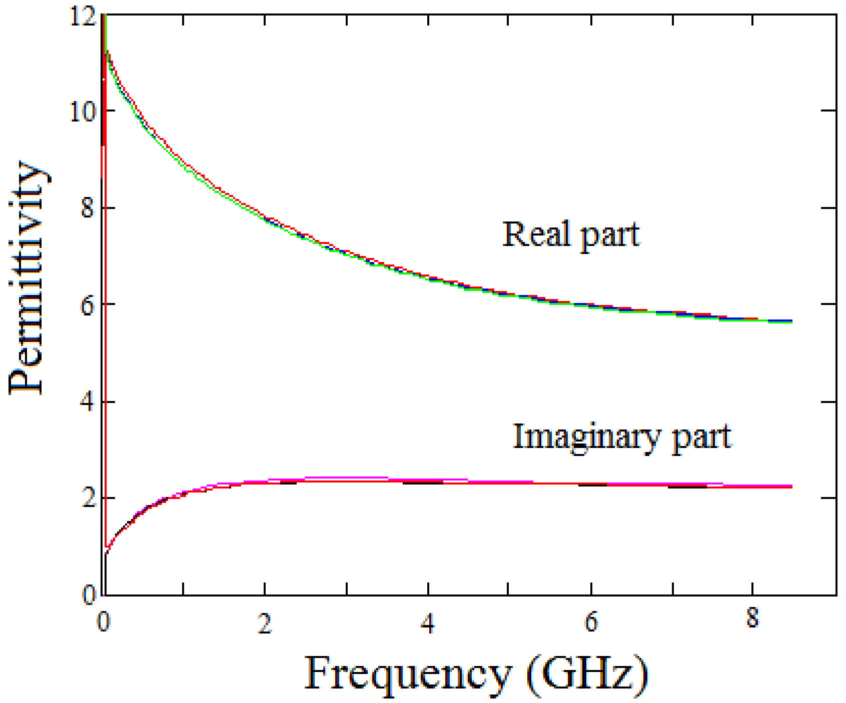

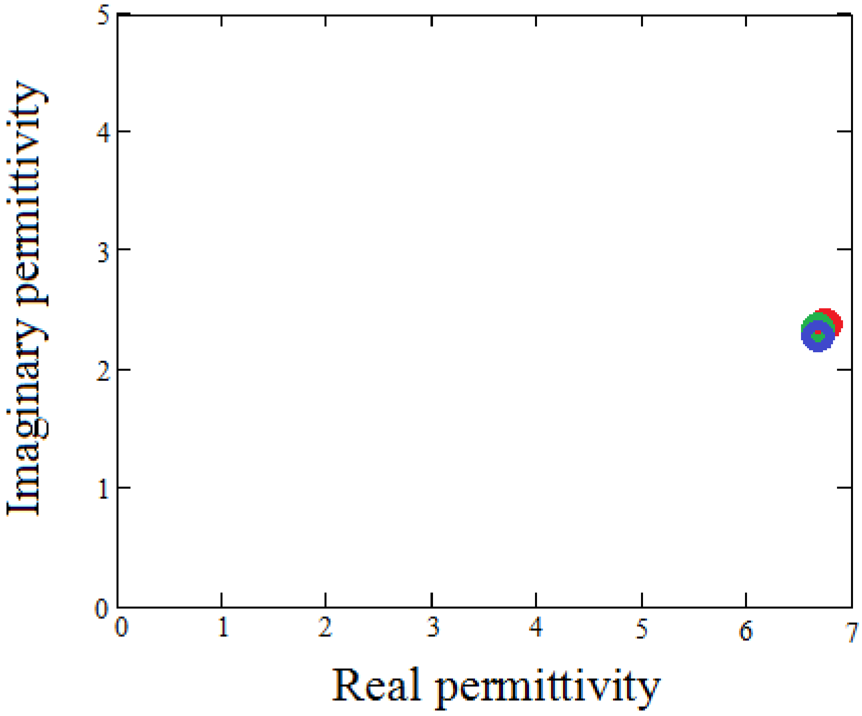

Figure 3.17 - Minatec Gold TA-T 21/05 broadband measurements

Figure 3.17 shows measurements of the sample Minatec Gold TAT 21/05 taken at the same position on the sheet sample. The top graph plots the real and imaginary permittivity components against frequency and the bottom graph plots the real against the imaginary parts at a frequency of 2.737GHz. The technique is shown to be repeatable and accurate and a clear frequency dependence emerges for both polarisation and loss terms of the permittivity. The reflectometric coaxial probe technique is useful in characterising solid dielectrics, but it also has uses in characterising liquids. If the probe is simply dipped into a liquid, the same measurement can be performed with ease, and with greater accuracy. There is no longer an issue caused by poor contact between the probe and the material.

3.2.4.3 Modelling the probe

In order to extract the permittivity from measurements of aperture admittance, the electromagnetic fields at the end of the probe must be modelled. Modelling of open-ended coaxial lines can be traced back to the work of Levine and Papas [72,73] who derived variational expressions based on integral equations for the aperture electric and magnetic fields. These expressions assume an infinite conducting flange and that the field distribution is of the dominant TEM mode and is proportional to $1/\rho$. More recent formulations for determining aperture admittances also make this assumption and although this is acceptable at lower frequencies, at higher microwave frequencies the aperture is not electrically small and excites higher order modes that must be accounted for in analysis, the extent to which they must be accounted for has been investigated with conflicting conclusions [57].

It has become common for researchers to use simpler expressions of the aperture admittance that yield satisfactory results for a range of frequencies and permittivities. One such expression was derived by Misra [74,75], basing the analysis of the aperture on a model of two capacitors and a conductance. One capacitor represents the fringe field in the line and the other represents the field in the material. The conductance represents the power radiated from the end of the line. By making a quasi-static approximation to the integrand in a variational expression for the aperture admittance we obtain

$$Y_L = \frac{j2k^2}{\omega\mu_0\left[\ln\left(\frac{b}{a}\right)\right]^2}\int_a^b\int_a^b\int_0^\pi \frac{\cos(\phi')e^{-jkr}}{r}d\rho d\rho' d\phi' \tag{71}$$

using a cylindrical coordinate system (*ρ, φ, z*) where primed coordinates represent source points and unprimed represent field points, *a* and *b* are the inner and outer conductor radii respectively, *k* is the wavenumber in the material and

$$r = \left[\rho^2 + \rho'^2 - 2\rho\rho'\cos(\phi')\right]^{1/2} \tag{72}$$

As described above, the solution to this elliptic integral reduces to equation (70), allowing the inversion to effective permittivity values of the sample.

3.2.5 The Split Post Dielectric Resonator

3.2.5.1 Principles

The split post dielectric resonator (SPDR) provides an accurate technique for measuring the complex permittivity of dielectric sheets and thin films at a given frequency [76,77] and will be used in subsequent sections to determine the sheet resistance of composite samples. This is a resonant perturbation method similar to those in chapter 2, but is included here because it is well-suited to the measurement of sheet samples and thin-films. This is because of the non-depolarising TE_{011} field into which samples are inserted. The SPDR consists of a high permittivity, low-loss dielectric post, which is encased in a metal cavity to prevent radiation losses. If the dielectric post is formed of two cylindrical pieces with a small gap between them, the electric fields of the TE_{011} resonant mode behave as if the gap were not there. Sheet samples may be inserted into the split in order to perturb the fields and make measurements in the same way as in the cavity perturbation methods of chapter 2.

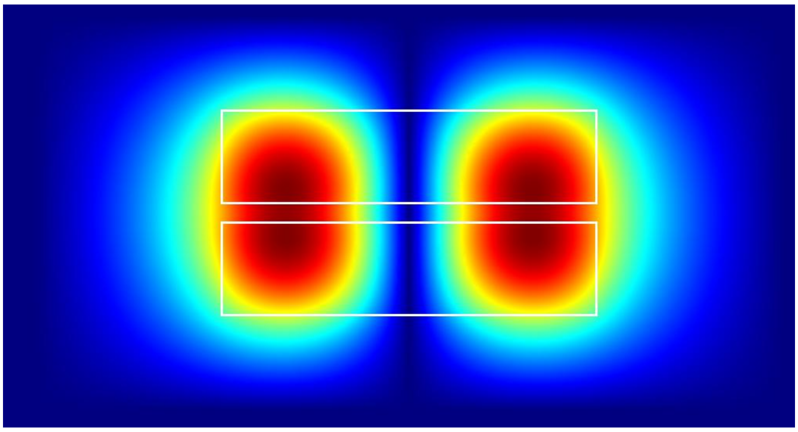

Figure 3.18 – Cross section of the TE_{011} mode *E*-fields in the split post dielectric resonator

Figure 3.18 shows a finite element model of the SPDR electric fields. The Electric field is mostly contained in the high permittivity dielectric regions. The 'ring' of high electric field formed at the gap is the location at which the sample is being measured. The sample must therefore be larger than radius of the dielectric resonator, but thinner than the gap in order to fit into the high *E*-field region. Practically the dielectric resonator is held in position by a low-loss PTFE casing. For a $(Zn,Sn)TiO_4$ resonator of radius r = 1cm and with aluminium housing, we achieve a quality factor in excess of 8000. The circularly polarized *E*-field of the TE_{011} mode is parallel to the inserted sample and since minimal depolarisation occurs, the sample is fully penetrated by the interrogating field.

No special sample preparation is needed and so this non-contact, non-destructive, highly sensitive technique offers the most accurate high frequency dielectric measurements for sheets and thin-films available.

Using the same approach to resonant measurements as in chapter 2, we take

$$\frac{\Delta f}{f} = A(\varepsilon' - 1)t \qquad\qquad \frac{\Delta BW}{f} = 2A\varepsilon'' t$$

where A is a constant which depends upon the resonator geometry and t is the sample thickness.

In subsequent sections, this technique will be used to measure the sheet resistance of composite samples containing conducting particles. When measuring sheet resistance, the measurement becomes invariant with sample thickness since

$$\frac{\Delta BW}{f} = 2A\varepsilon'' t\,, \qquad \text{if} \qquad \varepsilon'' = \frac{\sigma}{\varepsilon_0 \omega}\,,$$

we have

$$\Delta BW = \left(\frac{A}{\pi\varepsilon_0}\right)\sigma t = \left(\frac{A}{\pi\varepsilon_0}\right)\frac{1}{R_{sq}}$$

3.3 ELECTROMAGNETIC ABSORPTION THROUGH THE PERCOLATION THRESHOLD

3.3.1 Random Resistor Capacitor Networks, Emergent and Universal Properties

Very large networks of random resistors and capacitors can be used to model the heterostructures of random media. Two-phase conductor-insulator materials are represented by lattices of lumped components, which can be simulated across a range of frequencies to investigate the many phenomena observed in composite materials.

Conducting inclusions within a dielectric matrix alter the field distribution across the material and provide regions for charge storage, increasing the effective capacitance of the structure. Above the percolation threshold, these inclusions form conducting pathways with associated resistances, but also associated with the inclusions are capacitive effects brought about by the geometry of the heterostructure.

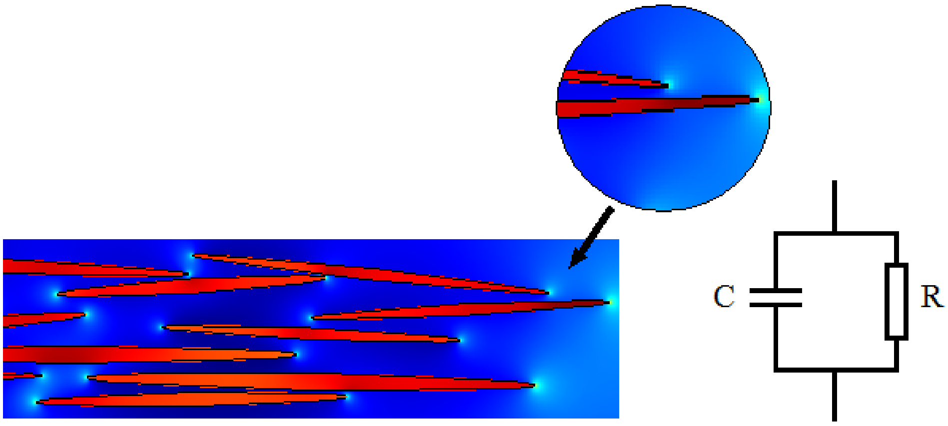

Figure 3.19 - The capacitive nature of heterostructures

It can be seen in Figure 3.19, that as conducting inclusions overlap and make contact with each other, they form resistive and capacitive cells. In the material under test, these capacitive properties manifest themselves as a frequency dependence leading to a complex admittance for bulk material properties. Investigations of these structures may be carried out by constructing random networks of lumped capacitors and resistors in parallel, then reducing the network to an equivalent admittance over a range of frequencies.

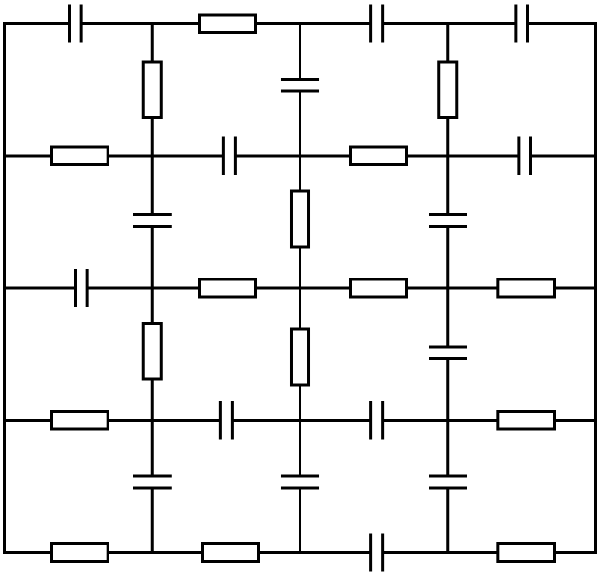

Figure 3.20 - The random RC network (n = 5)

The model is constructed in the MathWorks software Matlab. At random, components are allocated positions in the lattice until all positions are filled to a preset proportion (e.g. 60% capacitors, 40% resistors) as shown in Figure 3.20 for a square lattice of width n = 5. Capacitors and resistors are then given values of 1nF and 1kΩ respectively.

To reduce the network to an equivalent complex admittance, an algorithm derived by Frank and Lobb [78] is used. This is based upon star-delta transforms throughout the lattice, which take the admittance of each bond and iteratively reduce the mesh to a single admittance. This process can then be carried out across a range of frequencies and be repeated for many random configurations of the constituent components, to obtain distributions of frequency responses.

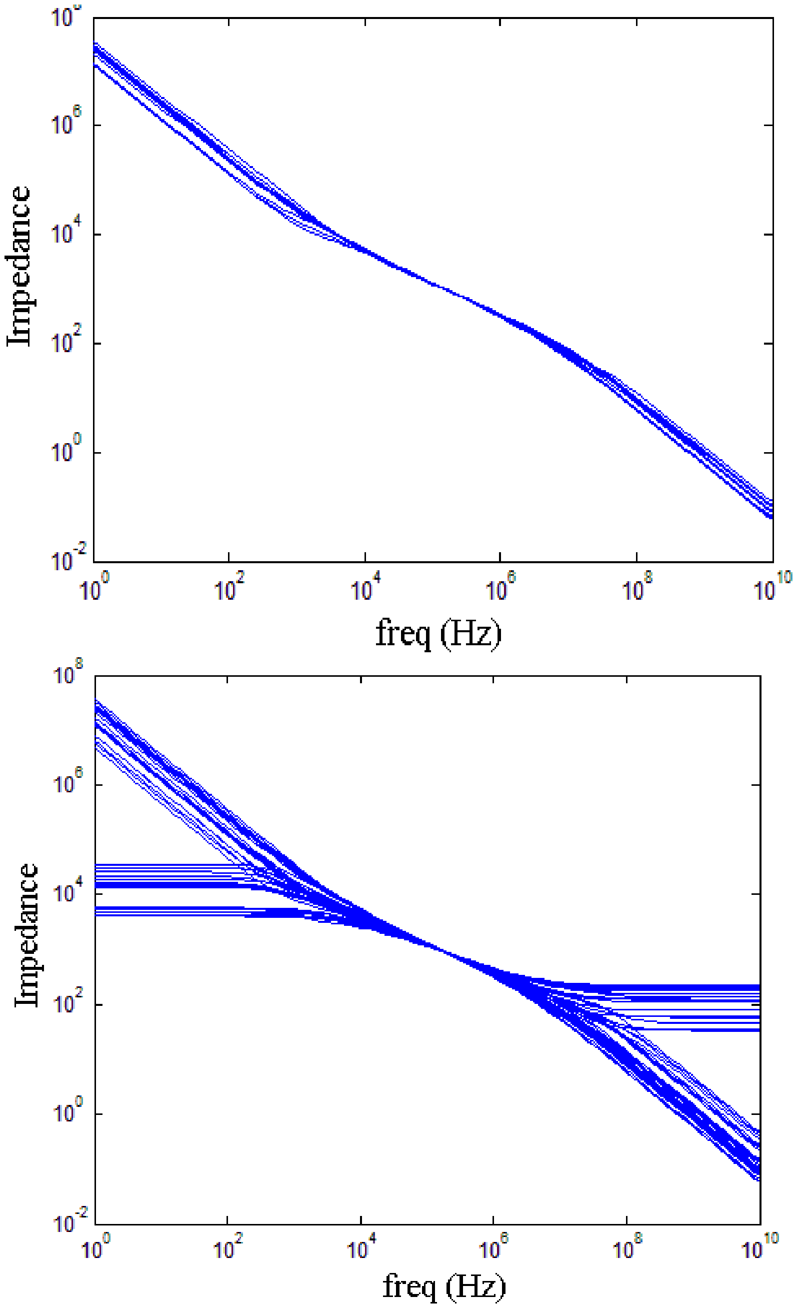

Figure 3.21 - Frequency response of RC networks showing percolative behaviour, firstly with an R:C ratio of 40:60, then with a ratio of 50:50. In each case values of 1nF and 1kΩ are used.

The top graph of Figure 3.21 shows results generated by the simulation at a lattice size of n = 20 (722 components) and at a proportion of 40% resistors (the remaining 60% are capacitors). It has been shown mathematically that the percolation threshold for 2D resistor-capacitor networks is 50% [70]. The graph shows the outcome of 60 randomly generated lattice configurations. Clearly, as the proportion of resistors is below the percolation threshold, at low frequencies the equivalent impedance of the network is extremely high, since at DC capacitors are effectively open circuit. As the frequency increases to the microwave region, the impedance of the percolating capacitors is dominant and the effective impedance of the network becomes very small. In the lower graph of Figure 3.21, the lattice size is again n = 20 (722 components), but 50% of components are now resistors (and the other 50% capacitors). At the percolation threshold, we now observe randomly generated cases of both resistor percolation and capacitor percolation.

The graphs of Figure 3.21 highlight an interesting result of the simulation. In the central frequency region there appears a fractional power law behaviour, which it has been suggested [79], directly relates to the composition of the lattice.

The existence of anomalous power law frequency dependence in dielectric materials has been a longstanding problem [80,81,82]. It was proposed that the power law behaviour exhibited by many materials could be linked to the permittivity and conductivity response of two-phase conductor-insulator networks and equivalently, RC networks [83,84,85]. Almond et al. showed that the electrical response of conductor-insulator composites could be predicted by a simple phenomenological logarithmic mixing rule known as Lichtenecker’s rule [86], based on the discovery that large RC networks exhibit properties that conform to these expressions [87]. This power law behaviour has been described as an ‘emergent’ property of the networks [85], which is ‘universal’ in relaxation processes [63]. The complex conductivity of a network is given as [85]

$$\sigma^* = \left(j\omega C\right)^x \left(\frac{1}{R}\right)^{1-x} \tag{73}$$

where x is the proportion of the network occupied by capacitors. We have, for the real part of σ^*, $\mathrm{Re}(\sigma^*) = \sigma$

$$\sigma = C^x R^{x-1} \cos\left(\frac{x\pi}{2}\right)\omega^x \tag{74}$$

and for the imaginary part of σ^*, $\mathrm{Im}(\sigma^*) = j\omega C$, which is the admittance of the network

$$C = C^x R^{x-1} \sin\left(\frac{x\pi}{2}\right)\omega^{x-1} \tag{75}$$

Figure 3.22 shows the conductivity of networks with an RC ratio of 50:50, where *R* = 1kΩ and *C* = 1nF. For a lattice size of n = 10 (162 components), the power law behaviour spans two decades in frequency and is centred around a characteristic frequency given by 1 / (2π*RC*). But if we increase the size of the lattice to n = 40 (3042 components), the power law region expands to cover more of the frequency range.

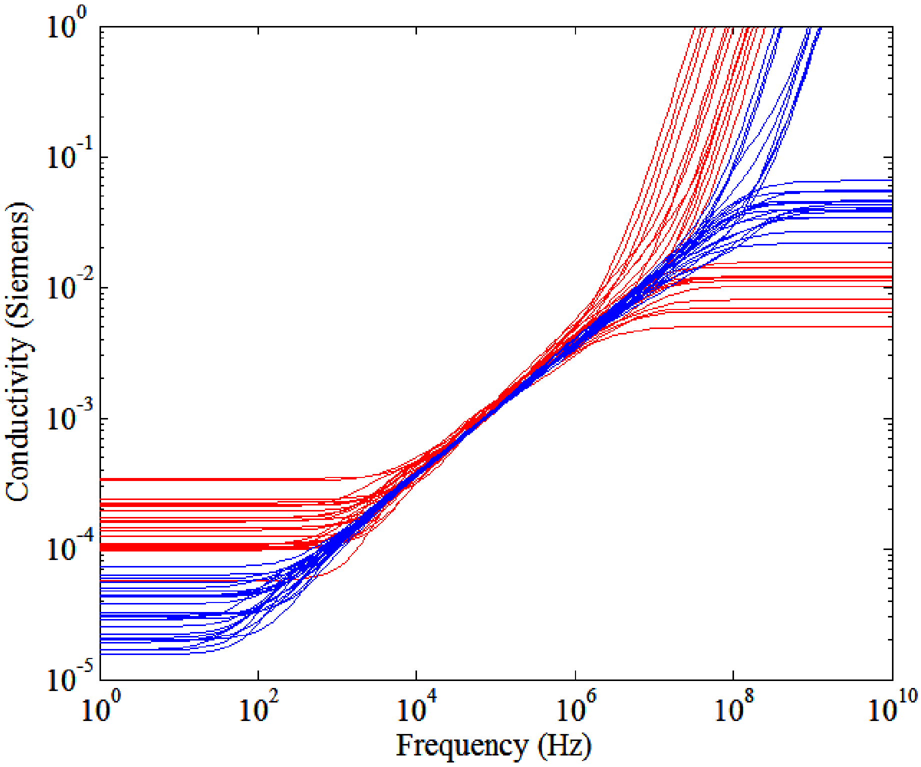

Figure 3.22 – Frequency dependent conductivity of RC networks with an RC ratio of 50:50, for 30 permutations each of n = 10 (162 components) (red), and n = 40 (3042 components) (blue).

As the lattice size increases, the computational intensity increases exponentially, but in real composites, the effective lattice size is much larger than computationally achievable in RC network models and the power law region must span a very much larger frequency band. At low frequencies, we may expect the conductivity to asymptotically approach some DC value. But at what frequency might we expect this asymptotic behaviour to cause a deviation from the power law? A number of factors influence the extent of the power law region at low frequencies. In the context of a random RC network, we note that the higher the proportion of resistors, the higher the DC conductivity and from Figure 3.22 we also see that as the size of the lattice becomes larger, the DC conductivity is decreased. This is easily explained since in the former case, the extra resistors are placed in parallel pathways replacing the capacitors, but in the latter case, proportionally the same number of parallel pathways exist, but more resistors in series results in a lower conductivity. It is proposed that the power law behaviour itself is related to the composition of the lattice, and for a lattice composed 40% of capacitors, we obtain a slope of 0.4 [88].

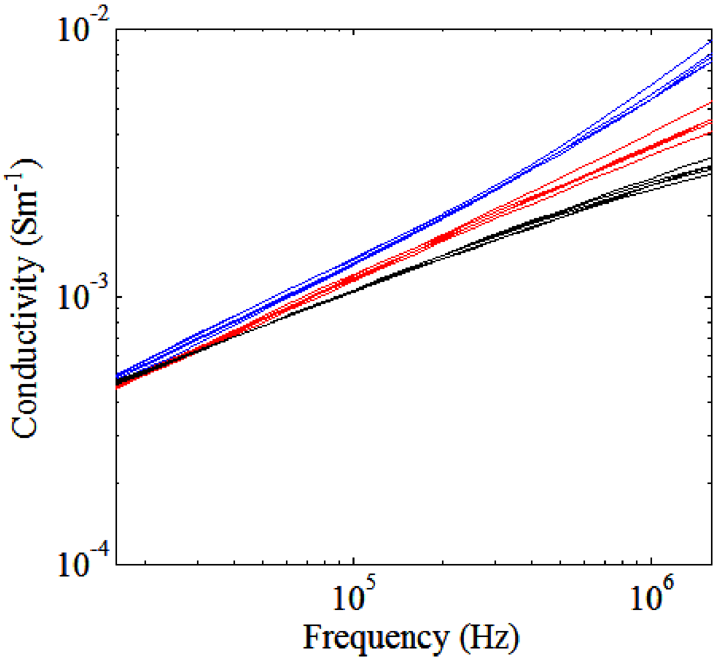

Figure 3.23 – Power law behaviour of *R* = 0.4 (blue), *R* = 0.5 (red) and *R* = 0.6 (black), for n = 40 (3042 components) with 5 iterations each. Based upon the component values, the characteristic frequency is 1.5915×10^5 Hz

Figure 3.23 shows the conductivity slopes at the characteristic frequency for 10 permutations of the lattice with RC ratio 40:60 (blue), 10 permutations of 50:50 (red), and 10 permutations of 60:40 (black) and each with n = 40 (3042 components), where $R = 1\text{k}\Omega$ and $C = 1\text{nF}$. We observe the following results

RC ratio	40:60 (blue trace)	50:50 (red trace)	60:40 (black trace)
Gradient	0.571	0.495	0.419

Table 10 – Gradients in the ‘emergent’ anomalous power law dispersion region for different RC ratios.

As shown in the literature, the slopes correspond to the proportion of capacitors present in the lattice. But how does this correspond to real composite materials? In Almond et al. 2006 [88], results are given for 3D network simulations which exhibit the same power law behaviour as in the 2D networks, this suggests that the 2D results may be applicable to real percolating structures. Almond goes on to present results for a lead zirconium titanate (PZT) powder, sintered to form a low-density pellet. Water was infused into the porous pellet to form the conducting phase. In this case the slopes for the measured samples matched the porosity of the PZT pellet, corresponding to the proportion on insulating (capacitive) phase present. Clearly this indicates that the same power laws govern the resistor-capacitor networks and the water-PZT samples, and are dependent upon the proportion of capacitive and conductive phases. We now investigate to what extent these principles apply to the composites of conducting particles examined in this work.

Experimental

Mica platelets approximately 20-30μm in length and up to 1 μm in thickness were coated with a layer of antimony-doped tin oxide. The degenerately doped layer was deposited by a sol-gel process giving rise to a uniform coating of ~40nm thickness. The platelet particles were annealed in air for 30 minutes 700°C. The coated platelets were then dispersed in a solvent based lacquer, based on a polyacrylate and nitrocellulose mixture. Ten samples were prepared for measurement by dispersing the coated particles in the lacquer at concentrations (by weight) of 1% to 10%, and then applying a layer of the mixture around 50 μm thick, to 100 μm thick PET sheets (of low dielectric loss). The resulting sheet samples were then cured prior to measurement, giving dry particle volume concentrations of 2.6%, 4.8%, 6.8%, 8.6%, 10.2%, 11.6%, 12.8%, 14.0%, 15.1% and 16.0%.

The coaxial probe technique as discussed in section 3.2.4 is used to measure the broadband (200MHz-8.5GHz) conductivity of the samples. A schematic diagram of the novel miniaturised coaxial probe used in this work is shown in Figure 3.24, based on an Anritsu K-connector (here K102F), which has an inherent bandwidth from DC up to 40 GHz. The connector’s glass bead provides a convenient coaxial aperture, which can be ground flat and then polished using fine emery paper. The probe's inner and outer radii are $a = 0.15$mm and $b = 0.80$mm, respectively. Hence the aperture remains electrically small (i.e. wavelength much larger than $b - a$) over the full range of measurement frequencies (up to 8.5 GHz).

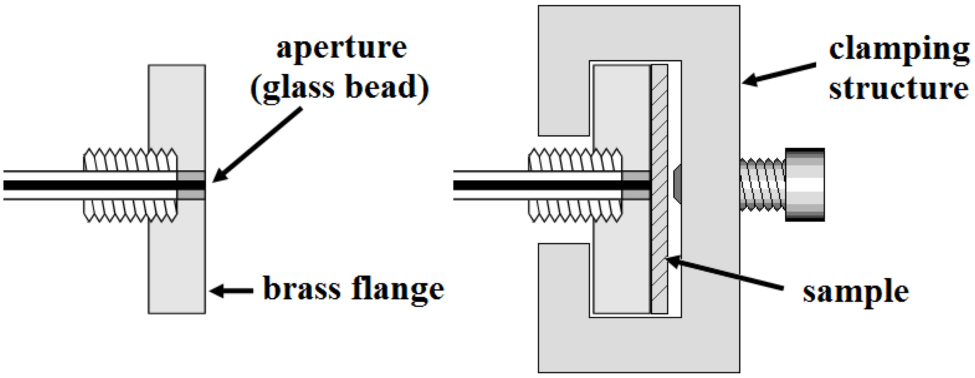

Figure 3.24 – Schematic diagram of the coaxial probe and sample fixture.

The thick film samples were placed against the aperture of the coaxial reflectance probe. With the sample flat and in intimate contact with the aperture, measurements of the voltage reflection coefficient S_{11} were taken in the range 100MHz to 8.5GHz using an Agilent ENA 5071B Vector Network Analyser (VNA). The calibration plane is shifted to the aperture plane by first measuring the probe without the sample and then using this to normalize the sample data. The complex permittivity of the sample was calculated using the simple inversion process based on a capacitive aperture admittance model described in previous sections.

Results and discussion

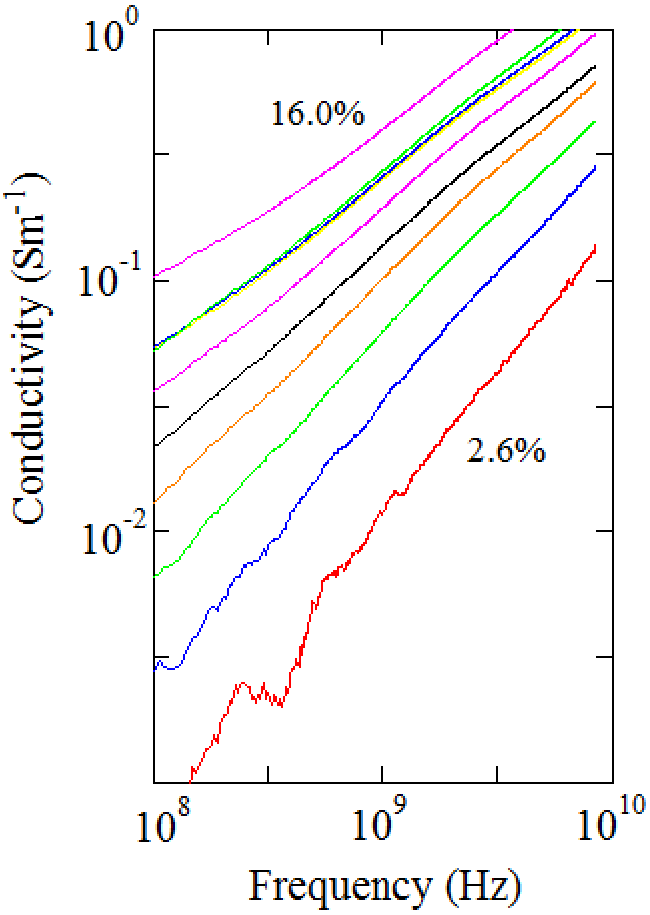

Figure 3.25 – Broadband measurement of the frequency dependent conductivity of conductor-insulator composites at volume concentrations of 2.6% (bottom trace) through to 16.0% (top trace).

PVC (%)	**2.6**	**4.8**	**6.8**	**8.6**	**10.2**	**11.6**	**12.8**	**14.0**	**15.1**	**16.0**
Gradient	0.932	0.929	0.886	0.810	0.787	0.726	0.705	0.716	0.745	0.735

Table 11 - Gradients in the 'emergent' anomalous power law dispersion region for different particle volume concentrations (PVC).

The frequency dependent conductivity of the ten samples is shown in Figure 3.25 and their gradients are shown in Table 11.

In Figure 3.25 the frequency dependent conductivities show the characteristic change in gradients, with low frequency dispersion present for the higher concentration, percolating samples. We assume the higher frequencies measured to be above the low frequency dispersion regime and in the anomalous power law dispersion regime. All gradients are therefore taken from this region.

From Table 11 we see that the gradient decreases as the proportion of the capacitive phase decreases, just as in our RC network interpretation. Indeed, with 97.4% capacitive phase by volume (2.6% PVC), we have a gradient of 0.93, which overestimates the role of the conductive phase somewhat. This trend of overestimation by the experimental results continues, until at 84% capacitive phase by volume (16% PVC), we have a gradient of 0.73.

The conductor-insulator composite system here deviates from the predicted behaviour of the power law, though emergent behaviour is present. We can learn about conductor-insulator composites by this perspective, but the application of the anomalous power law is only valid for particular systems. The RC networks have lumped element resistors and capacitors; in a real composite the equivalent resistances and capacitances are distributed. But for equivalence, the regions occupied by the distributed resistances and capacitances should have the same aspect ratios. Since

$$\frac{1}{R} = \frac{\sigma A}{l} \qquad\qquad C = \frac{\varepsilon\varepsilon_0 A'}{l'} \tag{76}$$

From [88], when $\frac{A}{l} = \frac{A'}{l'}$, and by using equations (76) in equation (74), we have

$$\sigma = (\varepsilon\varepsilon_0)^x \sigma^{1-x} \cos\left(\frac{x\pi}{2}\right)\omega^x \tag{77}$$

Equation (77) is useful for predicting the power law response of samples that behave like RC network, i.e. they satisfy the scaling condition $\frac{A}{l} = \frac{A'}{l'}$. In the PZT pellet used by Almond et al., the water (conductive) phase and the PZT (capacitive) phase make a good approximation to this condition. A real material satisfying the aspect ratio condition might be a packed cubic arrangement of conducting and insulating cubes.

In the conducting composite measured in this work however, this scaling condition is not satisfied. The conductive phase is in the form of platelets, which may diminish any capacitive effects. Certainly this is what is suggested by the experimental results, since for composites obeying equation (77), the gradients would be higher and so, in the power law interpretation, the capacitive effect may be suppressed relative to the PZT case.

3.3.2 Direct Current Versus High Frequency

3.3.2.1 Experimental

Current research into the nature of percolation and the percolation threshold is almost always in a static (0Hz) regime. This stems from the use of critical phenomena such as percolation to study such things as the advancement of forest fires or idealised models of oil fields to determine the probability of oil reservoirs being present. Scaling theories were developed in order to service these real world application areas. Following this pattern, in the literature, the approach to investigating the percolation threshold electrically is inevitably, also at DC, since the fundamental mechanisms of current percolation are inherently DC phenomena. In a conductor-insulator composite, as the concentration of conducting inclusions is increased and the percolation threshold is approached, a critical phase transition is observed and the DC resistance of the macroscopic sample reduces dramatically as the bulk sample becomes conducting. Practically, below the percolation threshold conventional Ohmmeters and high voltage Ohmmeters reach a maximum resistance, beyond which meaningful measurement cannot be taken.

At high frequencies, measurements of the conductive properties of the particles in the composite may be taken below the percolation threshold. Even though no full conducting pathways exist, there is now a contribution from the displacement current, the mechanism of which in conducting particles is still conventional charge transport. In this way, a high frequency sheet resistance can be obtained and compared with the DC sheet resistance above and below the percolation threshold.

To investigate the effects of high frequency conduction through the percolation threshold, samples were prepared with conducting particles dispersed in a polymer matrix. Each sample has an increasing concentration of conducting particles in order to observe the electrical properties as we approach the percolation threshold.

For the percolating particles, as in the previous section, mica platelets approximately 20-30μm in length and up to 1 μm in thickness were coated with a layer of antimony-doped tin oxide. The degenerately doped layer was deposited by a sol-gel process giving rise to a uniform coating of around 40nm thickness. After drying and annealing at 700°C, the particles are distributed in a lacquer at concentrations of 1% to 10% by weight and applied to PET sheets.

For DC measurements a conventional digital multimeter (DMM) is used for sheet resistance above the percolation threshold, but for below the percolation threshold, a high voltage (HV) METRISO 5000D-PI [89] Ohmmeter is employed .

High frequency measurements are carried out using a split post dielectric resonator (SPDR) operating at 2.8 GHz. The principles of operation of the SPDR are similar to those of the cavity resonator in chapter 1, but the SPDR is optimised for sheet measurements (see section 3.2.5 for details of the split post dielectric resonator).

3.3.2.2 Results and discussion

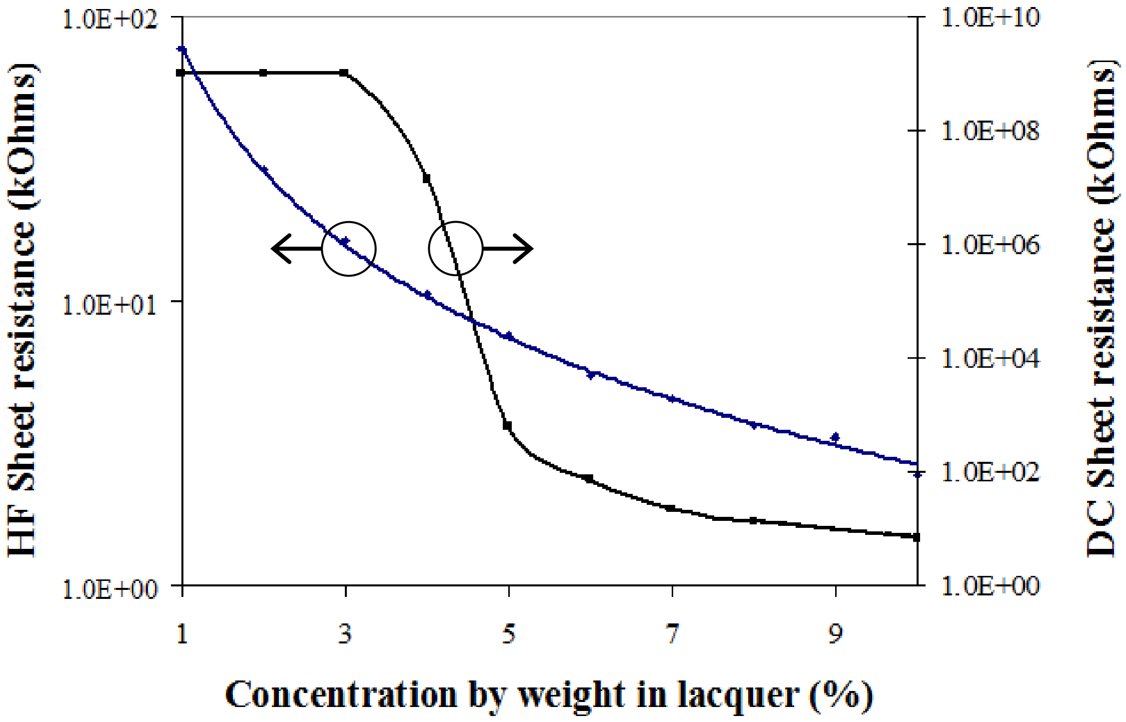

Figure 3.26 – High frequency and Direct Current measured sheet resistance of composites of conducting particles at concentrations through the percolation threshold.

The onset on percolation is clear in the DC sheet resistance measurements at between 4% and 5% particle concentration by weight in lacquer (i.e. before the sample is cured). Far below the percolation threshold a limiting value is produced by the HV Ohmmeter since no current can flow at all. Above 3%, it is clear that a small level of percolation is achieved, bringing the DC sheet resistance down to GigaOhm values. The decrease is sharp and characteristic of a first order critical phase transition.

The high frequency measurements of sheet resistance have no limiting values at concentrations far below the percolation threshold because at microwave frequencies we are able to detect the presence of the low concentration particles and their associated displacement current. Indeed, the percolation threshold itself remains invisible to the microwave measurement and we simply observe a smooth curve describing the increasing quantity of conducting particles in the sample. This approach is clearly advantageous and measurements of conducting particles may be made irrespective of their concentration. In the following section, we investigate percolation at a broad range of frequencies and determine over what frequency range such measurements transcend the effects of percolation as in the case of Figure 3.26.

3.3.3 Broadband Investigations

3.3.3.1 Experimental

In order to systematically investigate the shift from non-percolating to percolating composites it is necessary to isolate the mechanism of percolation in a controlled experiment. To achieve this, factors affecting the electromagnetic frequency response such as the bulk polarisation density must remain unchanged.

As discussed in section 3.2.3, if we take $\varepsilon^* = \varepsilon' - j\varepsilon''$, the imaginary permittivity may be related to the conductivity of the sample by $\varepsilon'' = \sigma/\omega\varepsilon_0$. In section 3.2.3, the onset of percolation was described by an increase in low frequency conduction of the macroscopic sample, corresponding to growth in cluster size as the conducting particles begin to touch. Low frequency dispersion is observed in percolating samples, but by simply increasing the concentration of conducting particles to reach the percolation threshold, we increase the number of polarising particles and also the quantity of conducting material. This would significantly alter the frequency response of the samples. To maintain uniformity in frequency response whilst exposing the effects of current percolation, samples were constructed of mixtures containing percolating (conducting outer layer) and non-percolating (non-conducting outer layer) particles. Both types of layered particle have the same structure (but additional, non-conducting layers are added to the latter) and should therefore have the same inherent frequency response.

For the percolating particles, as in the previous section, mica platelets approximately 20-30μm in length and up to 1 μm in thickness were coated with a layer of antimony-doped tin oxide. The degenerately doped layer was deposited by a sol-gel process giving rise to a uniform coating of ~40nm thickness. For the non-percolating particles, A 100nm non-conducting silica (SiO_2) layer was deposited as a diffusion barrier before the final <20nm layer of titania (TiO_2) was deposited to prevent agglomeration of the particles. These non-conducting outer layers serve to prevent percolation of charge-carriers through the composite.

Eleven samples were made; the two pigment types were mixed together in varying proportions at volume concentrations above the percolation threshold. The mixture is varied in 10% steps by number density of particles from 100% non-percolating pigment to 100% percolating pigment. Notably, the mixture is varied by number density of polarising particles in order to maintain a consistent electrical response and enable a systematic investigation of the effects of percolation in isolation from other effects.

The particles were mixed in powder form, by weight, before being distributed in a lacquer based upon a polyacrylate and nitrocellulose mixture and applied to a PET sheet before being cured. All samples have a particle concentration of 10% by weight in the lacquer before curing, corresponding to a dried particle volume-concentration of 16% (which is above the percolation threshold if all particles are conducting).

The non-percolating particles are larger than the percolating particles since they have two extra layers. So to obtain the same number density of particles in all samples we take the density ratio of percolating to non-percolating particles as 1:1.9. As an example, to achieve a 60:40 (percolating:non-percolating) ratio by number density of particles, we take (60:40)×(1:1.9) = (60:76), which as a percentage by weight is 44:56. Enough mixture in powder form is then dispersed in lacquer to achieve the prescribed 10% particle concentration by weight. Finally, the imaginary permittivity (i.e. loss) of the samples is measured using the broadband coaxial probe described in section 3.2.4.

3.3.3.2 Results and discussion

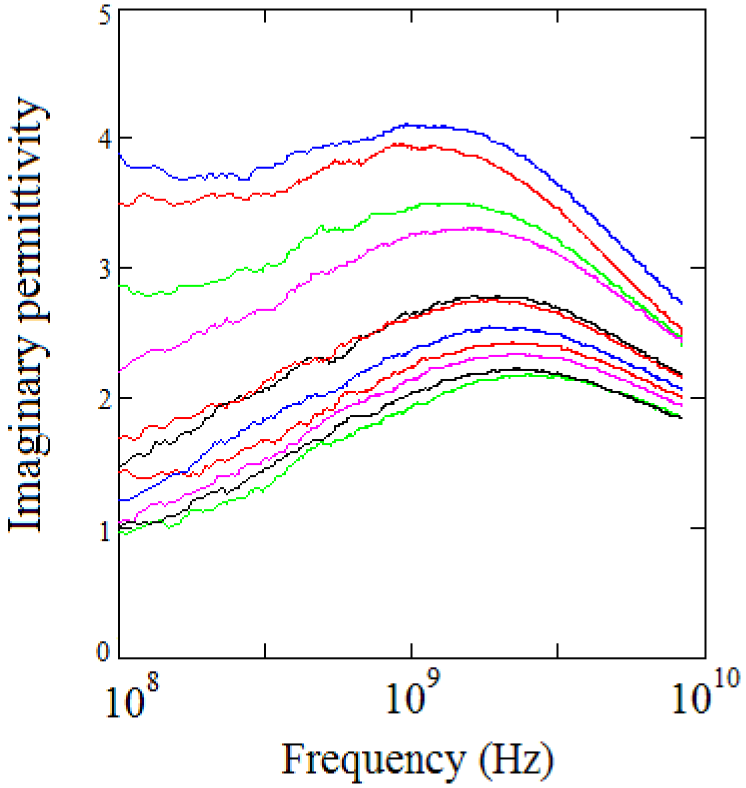

Figure 3.27 – Mixtures of percolating and non-percolating particles in ratios from 0:100 to 100:0 in 10% steps. Low frequency dispersion is exhibited as percolation increases.

Clearly the mixture in Figure 3.27 begins to percolate as the composition changes, but the relaxation peak is also present. We might expect this since the mixture contains non-percolating particles as well as percolating particles, but we find the relaxation peak present even for a mixture of 100% percolating particles. The frequency location of the loss peaks has remained the same for each sample, but the magnitude of the loss is increasing as the proportion of conducting particles increases. This cannot be due to the effect of percolation itself since it is present at frequencies above the frequency of relaxation. But it may be due to errors in the density ratios, leading to increased numbers of polarizing particles for the given weight of dispersed particles.

The presence of both the Drude-type low-frequency current conduction and the

Debye-type relaxation for an apparently fully percolating sample suggests that the two types of response must have some independence and percolation does not simply emerge from the relaxation peak as described in Figure 3.14 of section 3.2.3. Both forms are caused by charge transport in the conducting ATO layers of the sample, which remain the same. The only difference between the two types of response in these samples is the path taken by the moving charge. In fact, as charge accumulates at the interfacial boundaries in non-percolating samples the form of the polarization in the frequency domain is dictated by the mechanisms of charge transport. The differences may therefore arise due to the differences in scattering of an electron passing through the relatively uniform ATO layer of the non-percolating particles and the increased scattering experienced by an electron tunnelling through the network of irregular connecting sites on the surface of percolating particles. The result is that we observe different relaxation times for percolating and non-percolating samples. In the high frequency region above the low frequency dispersion, the non-percolating response dominates and we observe the absorption peak emerging from the monotonic percolation response.

Conventionally, percolation in conducting composites is examined using DC measurements. When the composite is below the percolation threshold and the conducting particles are not in contact with each other, conduction current cannot percolate between particles. Simple measurements of resistance show that negligible DC current can flow through the macroscopic sample and therefore the properties of the conducting inclusions cannot be interrogated. Measurements of percolating and non-percolating samples at microwave frequencies do not require complete conducting pathways and measurements of the electrical properties of the composite are possible regardless of percolation. This assumption is not however universal. If we take a measurement at the spot frequency of 5 GHz, at this frequency we observe that non-percolating phenomena dominate the response. A change in the electrical properties of the sample may be measured at this frequency irrespective of the level of percolation in the material. But at frequencies below this level such as at 100 MHz in Figure 3.27 it is clear that percolation significantly affects the level of loss. Measurements at this spot frequency are not able to decouple the effects of changes in the electrical properties of inclusions and the effects of current percolation. When using the highly accurate methods of resonant microwave techniques for the investigation of conducting composites, measurements are taken at spot frequencies. It is therefore extremely important that broadband knowledge of the behaviour of the composites near the percolation threshold is obtained if measurements are to be taken of percolating samples. Together, the complementary use of resonant and broadband microwave measurement techniques is a powerful tool for the interrogation of conducting composites.

3.4 BROADBAND ELECTROMAGNETIC ABSORPTION IN CONDUCTIVE, LAYERED ELLIPSOIDAL PARTICLES

In this section, we investigate experimentally and theoretically the absorption peaks of composites of TCO coated mica platelets. We begin by discussing generally the behaviour of absorption peaks in materials and conventional approaches to modelling composites, and then extend this to layered and ellipsoidal particles. Dilute composites of TCO coated particles are measured experimentally using a broadband coaxial probe and we observe absorption peaks at dramatically lower frequencies than predicted for homogeneous particles because of the layered structure. Samples are annealed at increasing temperatures in order to affect the carrier mobility in the transparent conducting oxide layer. We observe that the absorption peaks of each sample increase in frequency with increasing annealing temperature as expected from the associated carrier mobility increase, but at high annealing temperatures, the frequency of the absorption peak begins to *decrease*. This is contrary to conventional theory, which describes the absorption peak frequency as proportional to the DC conductivity.

In order to investigate this behaviour theoretically, the simple Drude model of the degenerate electron gas is used to describe the frequency dependent conduction properties of the degenerately doped TCO layer. Combined with a theoretical model of polarization in layered particles we determine a possible cause of the contrary behaviour at high mobilities and show that it may be a result of the mobility rising above a critical value, beyond which further increases cause a reduction in the absorption peak frequency.

3.4.1 A Framework for Modelling the Effective Permittivity

The effective permittivity $\varepsilon_{eff}(\omega)$ of a composite is dependent upon a complex relationship between the material parameters of its constituents and structural factors. We begin constructing a model for the effective permittivity of a composite by considering the polarizability of a single particle. This approach does not consider the higher order interaction effects of mixing, but highlights the fundamental parameters affecting frequency dependent electromagnetic absorption in composites. For a quasi-static analysis it is required that the system is in the long wavelength limit, where for particle radius a and free space wavelength λ, we have $\lambda >> a$. A second requirement is that for thickness t of the conducting layer and skin depth δ, we have $\delta >> t$, where in this work the minimum skin depth $\delta_{\min} = \sqrt{1/\sigma\mu_0 2\pi f} > 1\text{mm}$ at $f_{\max} = 8.5\text{GHz}$ and $\sigma_{\max} \approx 0.16$ S/m (based upon $n_{\max} = 1\times10^{20}\text{cm}^{-3}$ and $\mu_{\max} = 50\text{cm}^2\text{V}^{-1}\text{s}^{-1}$), with $t \approx 40\text{nm}$. Where f is the frequency, $\sigma = n\mu e$ is the DC conductivity, e is the unit charge of an electron, n is the electron density and μ is the electron mobility, which is distinct from μ_0, the permeability of free space.

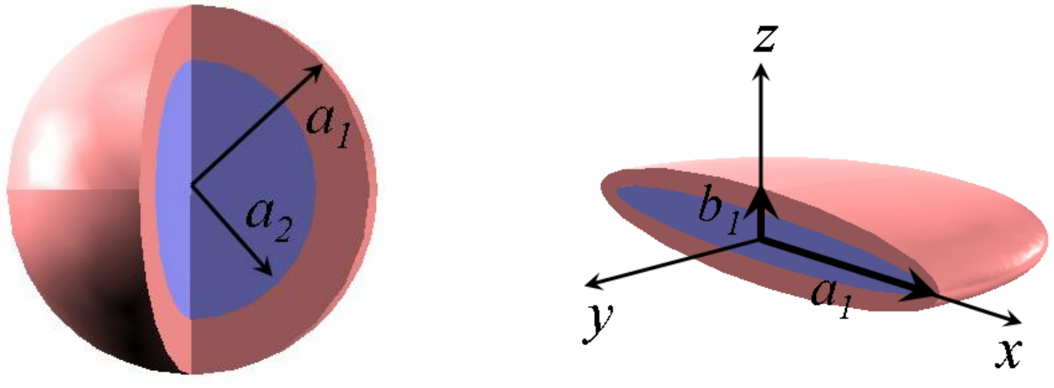

Figure 3.28 – Dimensions and coordinate system for a) layered sphere, b) layered oblate spheroid (*x* aligned).

For a homogeneous dielectric sphere in a uniform polarizing field in the x direction, we solve the Laplace equation with the appropriate boundary conditions. The uniform internal electric field and the axial symmetry of the problem lead to the internal to external field ratio [58]

$$\frac{E_{in}}{E_0} = \frac{\varepsilon_e}{\varepsilon_e + N_x(\varepsilon_1 - \varepsilon_e)} \tag{78}$$

where E_{in} is the internal electric field strength, E_0 is the polarizing field strength, N_x is the x-directed depolarization factor (1/3 for spherical inclusions) and ε_e and ε_1 are the complex permittivities of the background medium and the sphere respectively. The polarizability α is simply the electric field ratio multiplied by the volume V of the particle and the permittivity contrast.

$$\alpha = V(\varepsilon_1 - \varepsilon_e)\frac{\varepsilon_e}{\varepsilon_e + N_x(\varepsilon_1 - \varepsilon_e)} \tag{79}$$

The local field E_L at an inclusion is the sum of contributions from the average macroscopic field $\langle E \rangle$ and the average polarization $\langle P \rangle$ of other dipoles in the sample.

$$E_L = \langle E \rangle + \frac{N_x}{\varepsilon_e}\langle P \rangle \tag{80}$$

For a non-percolating, dilute mixture obeying the Lorentz relation (80), direct substitution of the particle polarizability into the Clausius-Mossotti formula [90] leads to an effective permittivity, ε_{eff} for the system.

$$\varepsilon_{eff} = \varepsilon_e + \frac{\varepsilon_e n\alpha}{\varepsilon_e - N_x n\alpha} \tag{81}$$

where n is the number density of particles and N_x describes the depolarization effect associated with the Lorentz field contribution.

For dielectric spheres, we obtain the Maxwell-Garnett mixing equation [91], which is equivalent to the Rayleigh mixing formula, but at low frequencies scattering effects may be neglected and absorption dominates.

The Maxwell-Garnett and Rayleigh formulas contain no information about individual scatterers. The composites in this work contain inclusions that are layered and are ellipsoidal and a more detailed treatment of the polarizability is therefore needed. We shall see that the effect of this altered polarizability is to reduce the frequency of associated absorption peaks and reduce the extent to which the high mobility effects described in this work influence the absorption peak.

3.4.2 Layered and Ellipsoidal Particles

The polarizability of layered particles cannot be solved in the same way as for the homogeneous sphere since layered particles do not have a uniform internal field. Here we use the approach developed by Sihvola et al. [92], in which the fields in homogeneous regions of mutilayered particles are calculated by interpreting static field components as travelling waves and exploiting propagation matrices. The polarizability of a single layered sphere as shown in Figure 3.28a) is given by

$$\alpha = 3\varepsilon_e V \frac{(\varepsilon_1 - \varepsilon_e)(\varepsilon_2 + 2\varepsilon_1) + R(2\varepsilon_1 + \varepsilon_e)(\varepsilon_2 - \varepsilon_1)}{(\varepsilon_1 - 2\varepsilon_e)(\varepsilon_2 + 2\varepsilon_1) + 2R(\varepsilon_1 - \varepsilon_e)(\varepsilon_2 - \varepsilon_1)} \tag{82}$$

where R is simply the volume ratio of the core to the total volume.

A model of the effective permittivity must also consider the ellipsoidal nature of the inclusions. The effects of the ellipsoidal shape of the polarized particle can be introduced by the depolarization factor $N_{x,y,z}$. In homogeneous particles, as seen above the depolarization factor directly influences the polarizability of the inclusion and the effective permittivity of the mixture in equations (79) and (81) respectively.

In this work we approximate the particles as oblate spheroids, since for spheroids we may write a closed form solution for the depolarization factor. Depolarization factors for inclusions of arbitrary shape must be solved numerically. For spheres, $N = 1/3$, but oblate spheroids are anisotropic, having $N_x = N_y \neq N_z$ [93]. For simplicity, we consider all particles to be aligned to the x axis as shown in Figure 3.28b) with a uniform polarizing field in the x-direction. We have

$$N_x = \frac{1}{2}\left(1 - \frac{1+e^2}{e^3}\left(1 - \tan^{-1} e\right)\right) < \frac{1}{3} \tag{83}$$

$$e = \sqrt{\frac{a_1^2}{b_1^2} - 1}$$

where e is the eccentricity of the oblate spheroid.

The approach of Sihvola et al. [92] cannot be applied directly in the case of uniformly layered ellipsoids, since the static solution in each homogeneous layer is not solvable using the Laplace equation. A solution to the Laplace equation for layered ellipsoids by separation of variables is possible only if the boundaries between the layers are confocal [94]. Giving, for the oblate spheroid, the x-directed polarizability

$$\alpha_x = \varepsilon_e V \frac{(\varepsilon_1 - \varepsilon_e)\lfloor\varepsilon_1 + N_{x,2}(\varepsilon_2 - \varepsilon_1)\rfloor + R(\varepsilon_2 - \varepsilon_1)\lfloor\varepsilon_1 + N_{x,1}(\varepsilon_e - \varepsilon_1)\rfloor}{\lfloor\varepsilon_e + N_{x,1}(\varepsilon_1 - \varepsilon_e)\rfloor\lfloor\varepsilon_1 + N_{x,2}(\varepsilon_2 - \varepsilon_1)\rfloor + RN_{x,1}(1 - N_{x,1})(\varepsilon_1 - \varepsilon_e)(\varepsilon_2 - \varepsilon_1)} \tag{84}$$

where $N_{x,1}$ is the x-directed depolarization factor of ellipsoid 1 (outer) and $N_{x,2}$ is the x-directed depolarization factor of ellipsoid 2 (inner) as shown in Figure 3.28b) and R is again the volume ratio of the core to the total volume. For confocal ellipsoids we have $N_{x,1} > N_{x,2}$. Substituting the polarizability expression (84) into (81) leads us to an equation describing the x-component of the effective permittivity of a mixture containing aligned, confocally layered oblate spheroids.

3.4.3 Experimental

3.4.3.1 Sample manufacture and measurement

Once again, Mica platelets approximately 20-30μm in length and up to 1 μm in thickness were coated with a layer of antimony-doped tin oxide. The degenerately doped layer was deposited by a sol-gel process giving rise to a uniform coating of ~40nm thickness. A 100nm non-conducting silica (SiO_2) layer was deposited as a diffusion barrier before the final <20nm layer of titania (TiO_2) was deposited to prevent agglomeration of the particles. The non-conducting outer layers also serve to prevent percolation of charge-carriers through the composite, though samples in this work are below the percolation threshold and are considered to be electromagnetically ‘dilute’ and non-interacting. Scanning electron microscope images are of the resulting particles are shown in Figure 3.29.

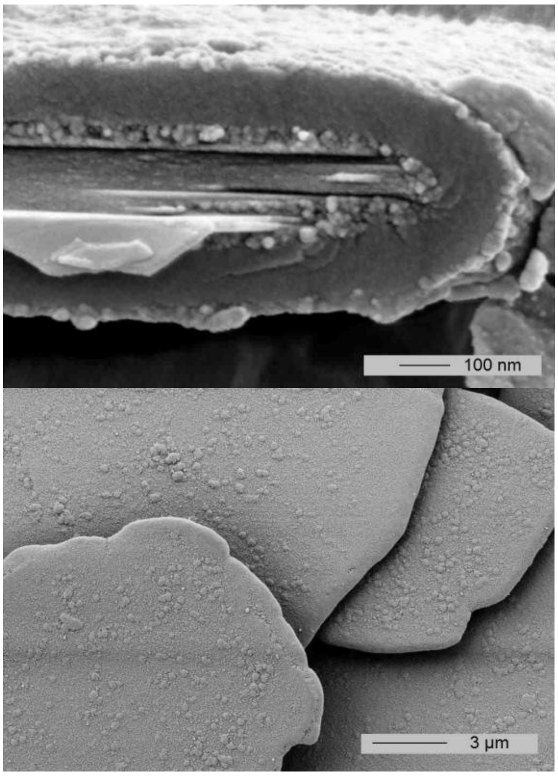

Figure 3.29 – Conducting ATO coated mica platelets, with SiO_2 diffusion barrier and TiO_2 outer layer.

A series of the platelet particles were first annealed in air for 30 minutes at 650°C, 700°C, 750°C, 800°C, 850°C and 900°C. The coated platelets were then dispersed in a solvent based lacquer, based on a polyacrylate and nitrocellulose mixture. The samples were prepared for measurement by dispersing the coated particles in the lacquer at a volume concentration of 3.3%, and then applying a layer of the mixture around 50 µm thick, to 100 µm thick PET sheets (of low dielectric loss). The resulting sheet samples were then cured prior to measurement of the imaginary permittivity (i.e. loss) of the samples using the broadband coaxial probe described in section 3.2.4.

3.4.4 Results

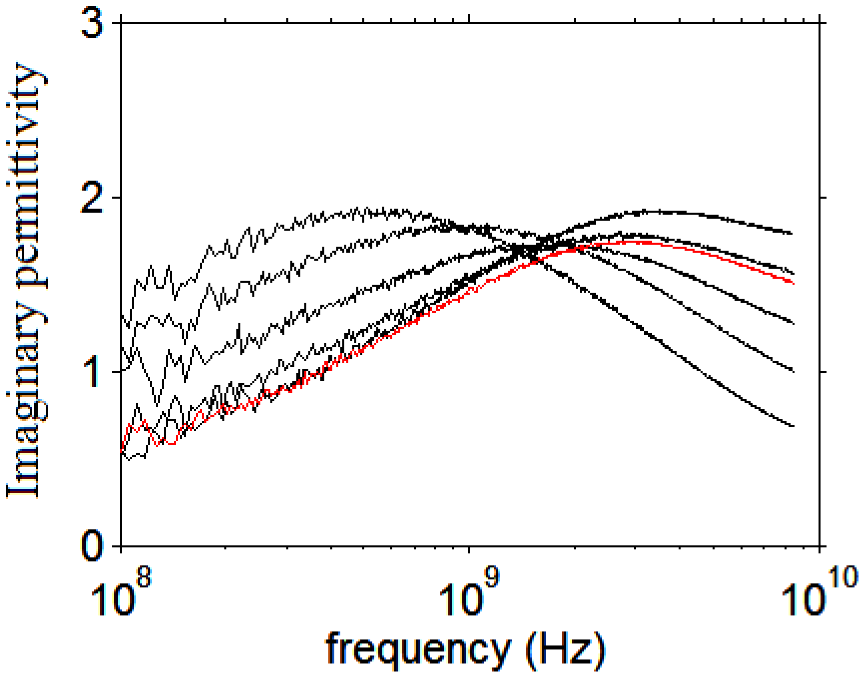

Figure 3.30 – Broadband imaginary permittivity (loss) of annealed samples of TCO coated platelets. The frequency of the absorption peak increases with annealing temperature, but reduces beyond 900°C (red trace).

The absorption peaks of the annealed composites are shown in Figure 3.30. As the annealing temperature is increased, the mobility of the TCO layer is increased and the frequency of the absorption peak rises as predicted by conventional theory for increasing conductivity. When the annealing temperature reaches 900°C, the frequency of the absorption peak begins to decrease. This behaviour is contrary to conventional understanding if we consider the mobility to be increasing with higher annealing temperatures.

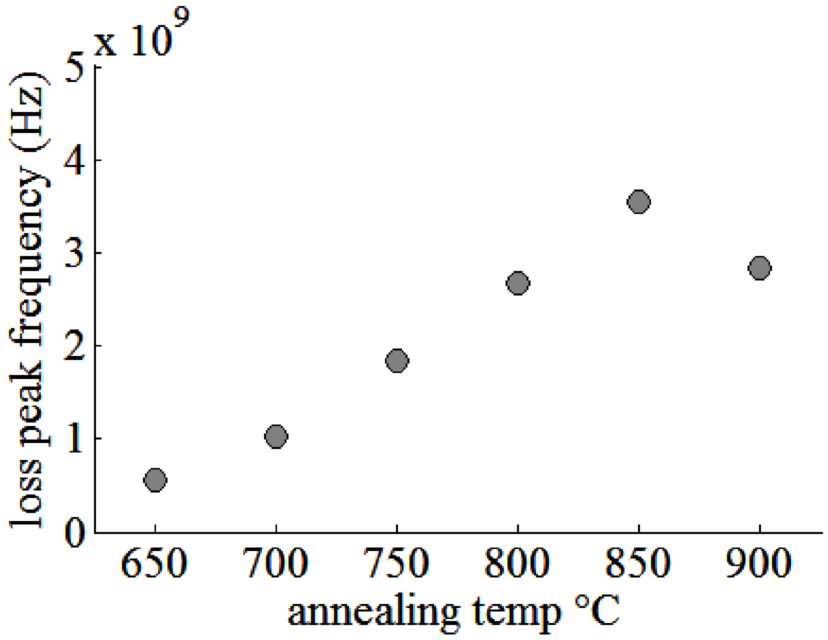

Figure 3.31 – Absorption peak frequency for of TCO coated platelets annealed at increasing temperatures.

A clear absorption peak is visible at microwave frequencies for each of the annealed samples. The frequency of absorption peaks is dramatically reduced by the layered structure of the particles [95], but we shall see in the next section that, though the thickness and conductivity of the coating are fundamental parameters influencing the location of the absorption peak in the frequency domain, we must look more closely at the conduction properties of the coating to predict the frequency behaviour shown in Figure 3.31.

3.4.5 Calculations and Discussion

The frequency of relaxation f_{rel} for composites of conducting particles is a function of the bulk conductivity of the inclusions. In this work, the frequency dependence of the absorption peak is directly related to the frequency dependence of the imaginary polarizability through its introduction into the Maxwell Garnett mixing equation; an approach entirely equivalent to the Rayleigh formulation. Such a formulation is conventionally considered to predict that $f_{\mathrm{rel}} \propto \sigma_{\mathrm{dc}}$ [3,4], where σ_{dc} is the bulk DC electrical conductivity. But we observe that in the case of degenerate semiconductors such as those in Figure 3.31, the increase of f_{rel} with σ_{dc} is not monotonic.

The electrical properties of ITO thin films above the Mott critical density [96] are discussed in Porch *et al.* [97], within the framework of the simple Drude model where the parabolic conduction band is considered to be partially filled by a degenerate free electron gas. There is a strong frequency dependence of the scattering time τ for Fermi surface electrons [98], though if we consider only microwave frequencies (0.1GHz – 10GHz), τ is assumed to be approximately constant. The Drude form of the complex permittivity is $\varepsilon^* = \varepsilon' - j\varepsilon''$ [99], thus giving

$$\varepsilon' = \varepsilon_\infty - \frac{\omega_p^2 \tau^2}{1+\omega^2\tau^2} \tag{85}$$

$$\varepsilon'' = \frac{1}{\omega} \frac{\omega_p^2 \tau}{1+\omega^2\tau^2} \tag{86}$$

where $\omega_p^2 = ne^2 / \varepsilon_0 m^*$, ε_∞ is the high frequency relative permittivity and m^* is the electron effective mass. In order to examine the electrical behaviour of the transparent conducting layer, from the literature we take typical values for Drude parameters in TCO thin films $\varepsilon_\infty \approx 4.0$, $m^* \approx 0.35 m_e$ and $\tau \approx 3.3 \times 10^{-15}$ s [97]. Minor scaling of these values does not affect our general conclusions.

Well above the plasma frequency of a conducting material we have $\varepsilon' = \varepsilon_\infty$. Below ω_p, we have $\varepsilon' < 0$, but at microwave frequencies, for Drude-like materials, $|\varepsilon'| << |\varepsilon''|$. For the purposes of this study we therefore make the approximation $\varepsilon^* = 1 - j\varepsilon''$.

Figure 3.32 shows full numerical solutions for the absorption peak frequency for a composite of aligned, layered ellipsoids as in Figure 3.28b), from equations (84) and (81), where the volume fraction $f = nV = 0.05$. Here the simple Drude model of electrical properties above the Mott critical density is used with $\mu = e\tau / m^*$ and $\varepsilon_2 = \varepsilon_e = 1$. The conducting layer is 40nm at its widest point, $a_1 = 40.001\mu$m, $a_2 = 40\mu$m,

b_2 = 1μm, and so for confocality we have b_1 = 1.039μm. This corresponds to $N_{x,1}$ = 0.0197 and $N_{x,2}$ = 0.019.

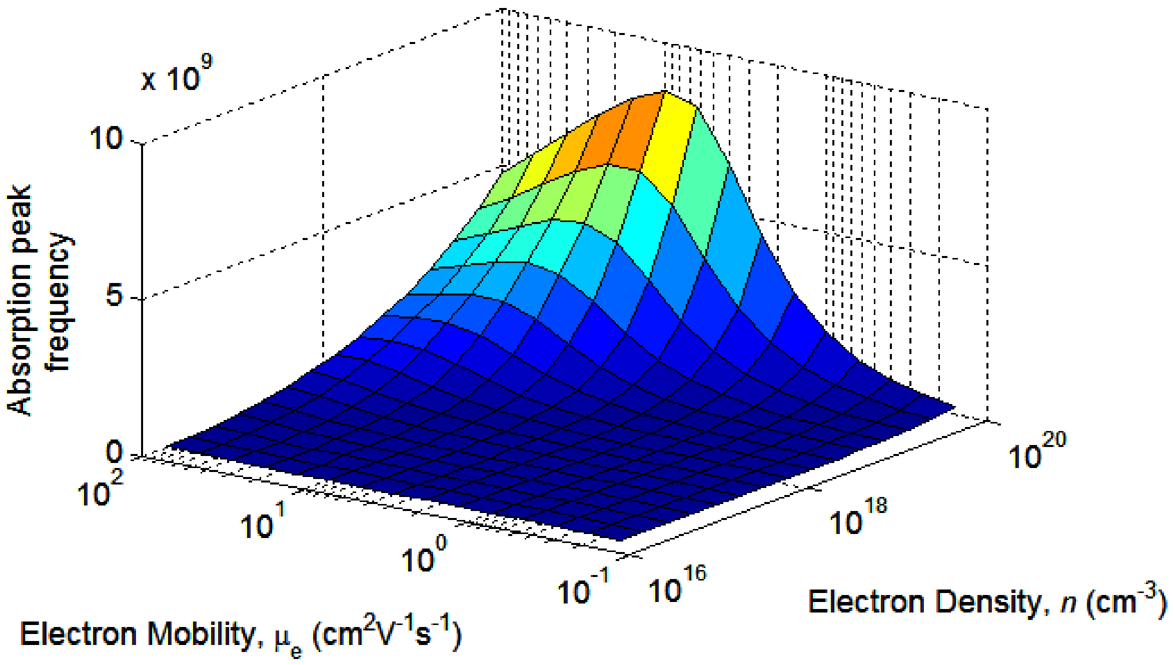

Figure 3.32 – Calculated absorption peak frequency for layered oblate spheroids with conducting outer layer.

We observe that with increasing mobility μ, the absorption peak frequency increases. But importantly, for increasing carrier density the increase in absorption peak frequency is not monotonic. There exists a carrier density for which f_{rel} is a maximum. It is clear that this previously unobserved behaviour may be masked by associated increases in n, and that to exhibit a decrease in absorption peak frequency, we must have $|\partial\mu| >> |\partial n|$ since above the critical mobility value, at high mobilities

$$\left|\frac{\partial f_{rel}}{\partial \mu}\right| < \left|\frac{\partial f_{rel}}{\partial n}\right| \qquad (87)$$

Immediately above the critical mobility value, the general assumption $f_{\mathrm{rel}} \propto \sigma_{\mathrm{dc}}$ is not valid.

To further examine this behaviour we consider the frequency dependent absorption of a single, layered, spherical particle. The absorption peak exhibited by the mixture corresponds to the imaginary part of the polarizability of the individual particle as described in equation (79). For homogeneous, spherical particles with ε_e = 1, the imaginary polarizability peaks when the frequency dependent imaginary permittivity $\varepsilon''_{pk}(\omega) = 3$, which is independent of particle size. For particles with a conducting layer we observe that the frequency of the absorption peak is reduced. Considering equation (82), it can be shown that the imaginary part of the complex polarizability (i.e. the absorption) of a layered, spherical particle, will reach a maximum when we have

$$\varepsilon''(\omega) = -\frac{3}{2\sqrt{2}} \frac{\sqrt{(4R + 5 + 3\sqrt{8R+1})}}{R-1} \qquad (88)$$

which means that for any coating with a given frequency dependent imaginary permittivity, the absorption peak frequency depends upon R alone, where R is the volume ratio of the core to the total volume. We note that equation (88) reduces to the value 3 for homogeneous particles (R = 0) as expected.

As an example, shown in Figure 3.33 is the frequency dependent imaginary permittivity for increasing levels of electron mobility based upon the Drude model of the free electron gas. Marked on the graph are the levels $\varepsilon''_{pk}(\omega) = 3$, and $\varepsilon''_{pk}(\omega) = 150$.

An individual conducting sphere exhibits an absorption peak (a peak in the imaginary part of the polarizability) at the frequency that ε'' reaches the value set by equation (88). For homogeneous spheres (R = 0), this value is $\varepsilon''_{pk}(\omega) = 3$. And for a 1μm core with a 10nm conducting shell (R = 0.9703), this value is $\varepsilon''_{pk}(\omega) \approx 150$.

The absorption peak occurs at a far lower frequency for the layered particle than for homogeneous conducting particles. We observe that for the ratio R = 0.97, which is typical of the particles in this work, the frequency of the absorption peak is dramatically reduced to microwave frequencies, as we have observed experimentally in Figure 3.30.

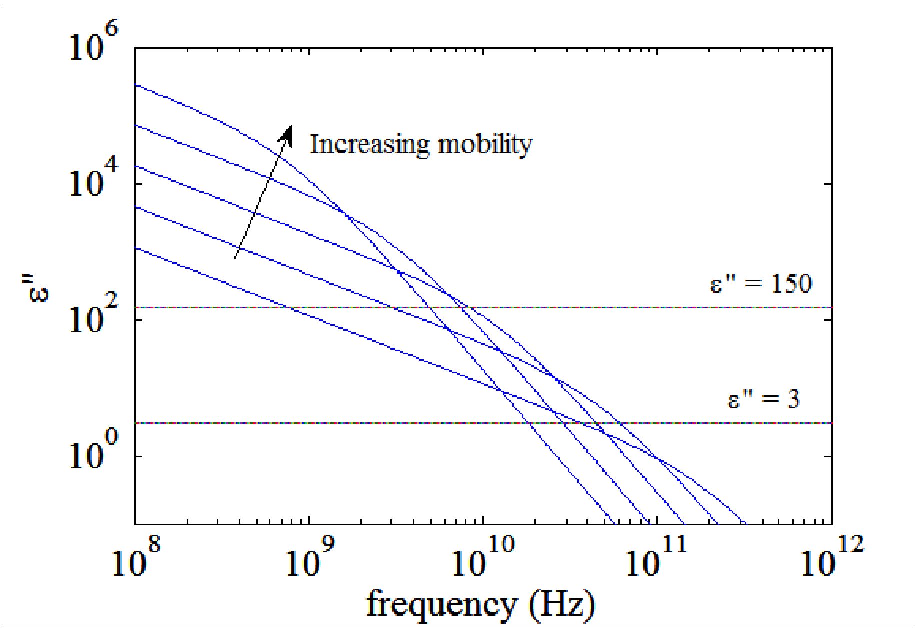

Figure 3.33 – Drude imaginary permittivity of conducting material (blue traces) vs frequency, for increasing values of mobility. Absorption peaks for individual particles occur when *ε”* = 3 for homogeneous spheres and *ε”* ≈ 150 for layered sphere with *R* = 0.97. The absorption peak is at a lower frequency in layered particles.

Figure 3.33 illustrates the frequency domain behaviour of the absorption peaks observed in Figure 3.31 and Figure 3.32. The frequency dependent, Drude imaginary permittivity (blue traces) of the conducting material for an increasing mobility from 0.1 to 100 $cm^2V^{-1}s^{-1}$ in logarithmic steps and for an electron density $n = 1\times10^{20}cm^{-3}$ is shown; corresponding to values used for the layered ellipsoid in Figure 3.32.

The absorption peak is observed at a significantly lower frequency for layered particles, but the high mobility effects leading to $\partial f_{rel} / \partial \mu < 0$ are somewhat suppressed. In Figure 3.33 we observe that at the lower line (ε'' = 3), as the mobility increases, the absorption frequency begins to reduce. At the upper line (ε'' = 150), the same mobility increase does not immediately have the same effect.

We conclude that theoretical evidence strongly suggests that the frequency behaviour of the absorption peak at high carrier mobilities is a result of the mobility rising above a critical value, beyond which further increases cause a reduction in the absorption peak frequency; though a subject of future work must be to rule out any possible contribution of material degradation.

3.5 CONCLUSION

This chapter investigated the electromagnetic behaviour of composites of conducting particles and layered conducting particles at high frequencies. Mixing laws for composites and classical mixing formulas were introduced and their limitations discussed.

We cannot have complete knowledge of a sample microstructure and variations in the structure can alter the effective electrical properties of the medium, therefore a level of uncertainty must be accepted. In order to quantify these uncertainties upper and lower bounds on the possible values of permittivity were presented.

Classical interpretations of frequency dependent loss were discussed via the Debye model of dielectric relaxation. A general approach to the analysis of loss-peaks in terms of the relaxation time is deemed inadequate and we take a closer look at the polarization of multi-layered particles, by using the Clausius-Mossoti approach.

The Clausius-Mossotti (CM) approach was used to demonstrate the effect that a reduction in conductivity of the particles has on the frequency response. The CM model considers the polarizability of each particle as a dipole and sets the particles in a background of averaged polarization densities. The reduced conductivity brings the frequency of relaxation down considerably, though to observe relaxation at microwave frequencies would require a conductivity of around 1 S/m. We conclude that the dominant effect upon absorption peak frequency is from conductivity of the particle material, but that layered particles have a dramatically reduced frequency of absorption peak. It is also noted that there may be a small contribution to the frequency dependence from thin-film effects causing decreased mobility in the conducting layer.

The coupled effects of real and imaginary permittivity are exposed in this work since there is a conceptual subtlety in the polarization of particles where screening is observed. The effects contributing to the imaginary permittivity of the depolarizing particle will contribute to the real permittivity at low frequencies i.e. macroscopic energy storage occurs via the very mechanism that is the dominant cause of loss. This is one example of the intrinsic link between the real and imaginary parts of the permittivity. Indeed the imaginary part of the permittivity is often linked with the conductivity of the sample. If this conductivity is complex, then the imaginary part (i.e. conventionally the reactance), contributes to energy storage in an equivalent, capacitive sense. Another revealing result is observed in the case that the core permittivity is larger than that of the outer layer. When the core of the particle is not subject to a large depolarising field, the polarisation due to the real permittivity of the core causes a second relaxation peak. The double relaxation peak emerges when the loss-peaks of two separate polarisation mechanisms are allowed to contribute to the overall response.

Critical phenomena and the scaling of percolative behaviour in general are discussed and the polarization of particles in the time domain is reviewed.

Debye-type relaxation is explored by considering the response of a polarizing particle in the time domain. Upon application of the polarizing electric field, the bound charge distribution immediately begins to move, until there is a saturation of polarization. Using the Lorentz form of the Debye model we observe that for high damping amplitudes, the damping is responsible for a large reduction in loss-peak frequency. We next look at percolative behaviour, where in the time domain there is no saturation of polarization since the charge is no longer bound. Once again the Lorentz form is used, but with the resonance frequency set to zero, we obtain the Drude model of unbound charge.

A combination of both Debye-type polarization and Drude-type conduction is used to describe a percolating composite exhibiting both a relaxation peak, and low-frequency dispersion.

The percolation threshold is then investigated using random resistor-capacitor networks. Very large networks of random resistors and capacitors were used to model the heterostructures of random media. Two-phase conductor-insulator materials are represented by lattices of lumped components, which were simulated across a range of frequencies to investigate the many phenomena observed in composite materials.

In the resulting frequency dependent admittance, the central frequency region exhibits a fractional power law behaviour, which directly relates to the composition of the lattice. The gradient observed in the fractional power law region corresponds to the proportion of the lattice occupied by capacitive components.

It is observed that as the size of the network is increased power law region expands to cover more of the frequency range, with the conclusion that for real materials, this behaviour dominates all frequencies, subject to limiting low and high frequency values. It is verified that the value of the gradient in the anomalous power law region of the frequency dependent conductivity depends upon the proportion of capacitive components present in the lattice and results are shown from literature supporting the application of this to real materials.

The broadband coaxial probe technique is used to measure the frequency dependent conductivity of the TCO based composites used in this work.

Measured results indicate that the gradient decreases as the proportion of the capacitive phase decreases, just as in our RC network interpretation. Indeed, with 97.4% capacitive phase by volume (2.6% particle concentration by volume), we have a gradient of 0.93, which overestimates the role of the conductive phase somewhat. This trend of overestimation by the experimental results continues, until at 84% capacitive phase by volume (16% PVC), we have a gradient of 0.73. The conductor-insulator composite system here deviates from the predicted behaviour of the power law, though emergent behaviour is present. This deviation comes about because scaling behaviour is not satisfied in the composite material measured in this work. RC networks have lumped element resistors and capacitors; in a real composite the equivalent resistances and capacitances are distributed. But for equivalence, the regions occupied by the distributed resistances and capacitances should have the same aspect ratios.

We conclude that since the conductive phase here is in the form of platelets, any capacitive effects may be diminished. Certainly this is what is suggested by the experimental results, since for composites conforming to the behaviour shown by resistor-capacitor networks, the gradients would be higher and so, in the power law interpretation the capacitive effect are suppressed relative to network models and real material that satisfy the scaling law.

In order to investigate the critical behaviour of the percolation threshold, the split post dielectric resonator technique is used to measure the sheet resistance of percolating and non-percolating samples at high frequencies and results are compared to DC measurements of the same samples.

As the concentration of conducting particles is increased, DC measurements show the sharp phase transition as the percolation threshold is reached. Below the percolation threshold, the DC measurements show that the sheet resistance is too high to be measured. At high frequencies, measurements of sheet resistance below the percolation threshold do not default to some large ‘open-circuit’ value because using microwave frequencies we are able to detect the presence of the low concentration particles and their associated displacement current. Indeed, the percolation threshold itself remains invisible to the microwave measurement and we simply observe a smooth curve describing the increasing quantity of conducting particles in the sample. This approach is clearly advantageous and measurements of conducting particles may be made irrespective of their concentration. The question of whether this is true at all frequencies is answered by examining the broadband emergence of percolative behaviour.

Systematic broadband investigations of the shift from non-percolating to percolating composites are carried out. To isolate the effects of percolation, we attempt to fix other factors affecting the electromagnetic frequency response such as the bulk polarization density.

Samples were constructed of mixtures containing percolating (conducting outer layer) and non-percolating (non-conducting outer layer) particles and the concentration of the particles was maintained at some value above the percolation threshold. As the make-up of the mixture is varied from 100% non-conducting to 100% conducting particles, low-frequency dispersion emerges from the loss-peak. However, at the onset of low frequency dispersion, the ‘lower leg’ of the frequency response does not simply rise and engulf the relaxation behaviour of the particles. In fact, with 100% percolating particles, we still observe a small relaxation peak, which emerges from the low frequency dispersion that is characteristic of percolation. We can conclude that the relaxation times of percolative and polarization effects are independent and dissimilar.

We also conclude that high frequency measurements may be taken of composites of conducting particles and are insensitive to the level of percolation present, but at frequencies below the characteristic loss-peak frequency, low-frequency dispersion is present and percolation must be accounted for in measurements.

In the final section the absorption peaks of composites of TCO coated mica platelets were investigated experimentally and theoretically. The behaviour of absorption peaks in materials and conventional approaches to modelling composites were discussed generally which was then extended to layered and ellipsoidal particles.

Dilute composites of TCO coated particles were measured experimentally using a broadband coaxial probe and absorption peaks were observed at dramatically lower frequencies than predicted for homogeneous particles because of the layered structure. Samples were annealed at increasing temperatures in order to affect the carrier mobility in the transparent conducting oxide layer. The absorption peaks of each sample increased in frequency with increasing annealing temperature as expected from the associated carrier mobility increase, but at high annealing temperatures, the frequency of the absorption peak was *decreased*. This is contrary to conventional theory, which describes the absorption peak frequency as proportional to the DC conductivity.

In order to investigate this behaviour theoretically, the simple Drude model of the degenerate electron gas was used to describe the frequency dependent conduction properties of the degenerately doped TCO layer. Combined with a full theoretical model of polarization in layered spheroidal particles it was shown numerically that a possible cause of the contrary behaviour at high mobilities may be the mobility rising above a critical value, beyond which further increases cause a reduction in the absorption peak frequency.

It was shown that for any layered spherical particle, the absorption peak frequency occurs at an imaginary permittivity set by R alone, where R is the volume ratio of inner core to the entire particle. For homogeneous conducting particles ($R = 0$) we have an imaginary permittivity at which the absorption peak occurs of $\varepsilon''_{pk}(\omega) = 3$. And for typical particles used in this work ($R = 0.9703$), this value is $\varepsilon''_{pk}(\omega) \approx 150$. The Drude model of the frequency dependent imaginary permittivity shows that $\varepsilon''(\omega)$ reaches a value of around 150 at much lower frequencies than it reaches a value of 3. Indeed, as observed experimentally in this work, the layered particle absorption peaks are reduced to microwave frequencies.

As the carrier mobility in the Drude model of electron transport is increased, the frequency dependent behaviour is changed and the frequency at which $\varepsilon''(\omega)$ reaches either the value 3 or 150 is also changed. The absorption peak frequency increases with increasing mobility until some critical value at which the frequency begins to decrease, just as was observed in the experimental results.

This significant experimental result exhibits a behaviour that is previously unobserved in composite materials and the decrease in absorption peak frequency as the carrier mobility of the conducting material is increased has been comprehensively demonstrated theoretically. But the experimental result however, needs verification, since at high annealing temperatures mica particles may experience material degradation.

We conclude that theoretical evidence strongly suggests that the frequency behaviour of the absorption peak at high carrier mobilities is a result of the mobility rising above a critical value, beyond which further increases cause a reduction in the absorption peak frequency; though a subject of future work must be to rule out any possible contribution of material degradation.

4 MICROWAVE ABSORPTION IN COMPOSITES OF SMALL CONDUCTING PARTICLES

4.1 INTRODUCTION

The use of microwaves in materials processing is widespread and microwave heating is now a standard processing tool for the industrial chemist [100,101,102,103]. The ability of microwaves to facilitate fast, efficient volumetric heating is complemented by targeted and selective heating techniques [104]. Knowledge of the interaction of microwaves with conducting particles is important in many interdisciplinary applications; these include the enhancement of chemical and biological reactions [105], microwave absorbing screens and coatings [106] and fundamental studies involving the electronic characterisation of the particles themselves. Furthermore, microwave interaction with small conducting particles is important in other innovative applications such as the full sintering of metal particles [107] and targeted stimulus of biological functions [108].

Small conducting particles often feature as additives to act as catalysts or to simply augment the microwave heating characteristics of a material. It is desirable therefore to have a robust model of electromagnetic absorption in small conducting particles from which we may develop a scheme for the optimisation of heating processes.

In this work, analytic solutions for the electric and magnetic dipole absorption of small conducting spheres (i.e. of particle radii much less than the wavelength of the incident radiation) with isotropic electrical conductivity are developed and applied to the specific example of absorption in response to microwave irradiation, at the ISM (i.e. industrial, scientific and medical) standard frequency of 2.45 GHz.

The increasing use of single mode applicators for the efficient microwave heating of materials leads to high electric and magnetic field separation. Electric and magnetic absorption mechanisms are evaluated separately and power dissipation in each is assessed. A direct comparison of electric and magnetic absorption exposes the conditions under which each is preferable.

Ongoing experimental work in the literature is concerned with the heating effects of small conducting particles for the applications discussed above. The conclusions drawn analytically in this work are validated experimentally in countless studies. As an example, one such study is Fujiwara et al. 2010 [109], in which stainless steel powders of different compositions are heated in a 500W, single mode applicator. Figure 4.1 shows the relationship between powder size and highest temperature achieved in a magnetic field for two non-magnetic and two magnetic samples.

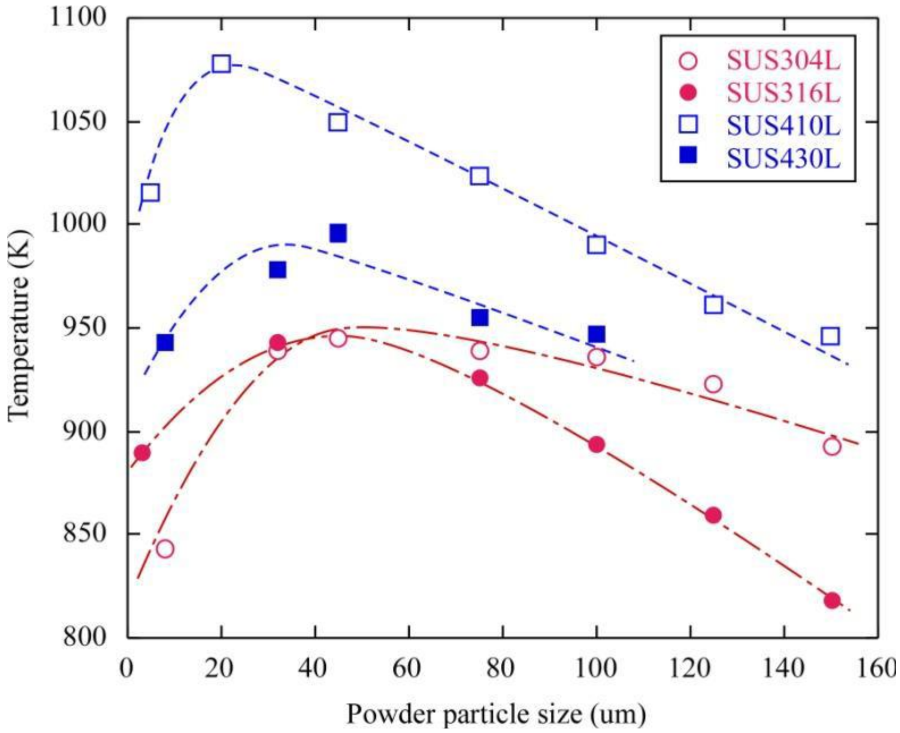

Figure 4.1 – The relationship of temperature reached to particle size upon heating by magnetic field, for non-magnetic stainless steel samples SUS304L and SUS316L (red) and magnetic stainless steel samples SUS410L and SUS430L (blue). Taken from reference [109].

As we shall see in subsequent sections, for non-magnetic particles, the maximum magnetic absorption point is a function of particle size for a given conductivity set by the ratio of radius *a* to skin depth δ, where $a = 2.41\delta$. For a material with a magnetic component, magnetic absorption is increased and the maximum absorption point occurs at smaller particle sizes.

In other studies, experimental results have been given for the heating of conducting particles and theoretical explanations have been presented based upon effective medium approximations [110,111,112,113]. In this work, we do not take a statistical or effective medium approach, since by examining the polarisation behaviour of single particles we may develop a clearer picture of electromagnetic absorption in dilute materials. Should the effects of particle interaction become significant, corrections to the general behaviour may be made.

By consideration of a full electromagnetic model of dipole absorption in conducting particles we account for the relationship of electric and magnetic dipole heating to the particle size, conductivity and magnetic properties. We establish simple principles for the optimisation of microwave absorption in conducting particles:

1) Magnetic absorption dominates electric absorption over a wide range of particle radii.
2) Optimum magnetic absorption is set by the ratio of mean particle radius a to the skin depth δ (specifically, by the condition $a = 2.41\delta$. Computational studies in the literature estimate this value as $a \approx 2.5\delta$ [114]).
3) For weakly conducting samples, electric dipole absorption dominates, and is maximised when the conductivity is approximately $\sigma \approx 3\omega\varepsilon_0 \approx 0.4$ S/m, independent of particle radius.
4) The absorption of sub-micron particles is small in both magnetic and electric fields. However, if the particles are magnetic, then magnetic dipole losses are dramatically enhanced compared to their values for non-magnetic particles below the Curie point.

It will be shown that magnetic absorption, or induction heating caused by eddy currents in the conducting particle is far more effective than electric absorption for a large range of particle radii and that this range is extended by the use of magnetic particles. For non-magnetic particles, optimum absorption is achieved when

$a = 2.41\delta$. This means that for particles of any conductivity, optimised magnetic absorption (and hence microwave heating by magnetic induction) can be achieved by simple selection of the mean particle size.

In weakly conducting samples, dominant absorption is by the electric field and electric dipole heating can be as effective as magnetic dipole heating for a powder sample of the same volume. But since the optimum absorption occurs at a specific conductivity and is independent of particle radius, it is harder to achieve maximum absorption at a given frequency. Finally, we see that since for sub-micron particles both electric and magnetic dipole absorption are small, the use of magnetic particles dramatically increases heating. An interesting application of this is the use of very small magnetic particles for the selective microwave heating of biological samples.

4.2 MODELLING ELECTROMAGNETIC ABSORPTION

If the applied magnetic field H_0 is that of a transverse electromagnetic wave then it is linked to the associated electric field E_0 by $H_0 = E_0 / \eta_0$, where $\eta_0 = 376.7\Omega$ is the wave impedance of free space. The same relationship holds for the electric and magnetic field magnitudes at their respective antinodes within a cavity resonator, often used to drive heating in conducting powder samples. Therefore, electric and magnetic power absorptions can be compared in both of these field configurations.

Power absorption will be calculated initially assuming that the spherical conducting particles are all of equal radius. The effects of including a distribution of particle radii will be considered once this simpler case has been dealt with. Results for the time averaged power absorption will be expressed per unit volume (i.e. 1 m^3) of conducting material, for an applied electric field of magnitude 1 V/m or an applied magnetic field of magnitude 0.002654 A/m. Assuming a linear electromagnetic response, the absorption at other field levels can be found by simply scaling the results here by the squares of the field magnitudes. It will also be assumed that the conducting spheres are dispersed with a low volume filling fraction (i.e. 0.01 or less) within a vacuum (approximating a low permittivity, low loss host material), thus removing the need to apply local field corrections. Hence, each particle (if they are of the same radius) will absorb equally and the total absorption is simply the sum of that due to the individual particles. Results will be presented as a function of varying particle radius, assuming that the overall volume (and volume filling fraction) of the sample is kept constant.

4.2.1 Electric Dipole Absorption in conducting particles

A conducting sphere (of radius a) will develop an electric dipole moment $\underline{p}$ in response to a uniform, applied electric field $\underline{E}_0$. Electromagnetic scattering can be neglected if the particle is electrically small, i.e. $a << \lambda_0$, where $\lambda_0 = 2\pi c / \omega$ is the free space wavelength and ω the angular frequency of the applied electric field. The analytic solution for $\underline{p}$ for a spherical conducting particle (of isotropic conductivity) in this limit is derived in appendix A [115].

$$\underline{p} = 2\pi a^3 \varepsilon_0 \underline{E}_0 \left(\frac{(2\varepsilon + 1)(1 - ka \cot ka) - (ka)^2}{(\varepsilon - 1)(1 - ka \cot ka) + (ka)^2} \right) \tag{89}$$

where $k = \omega\sqrt{\varepsilon\mu} / c$ is the wavenumber within the particle, $\varepsilon = \varepsilon_1 - i\varepsilon_2$ is the complex permittivity and $\mu = \mu_1 + i\mu_2$ is the complex permeability of the particle. Using equation (89), the time-averaged power dissipation per unit volume $\langle P_{\mathrm{E}} \rangle$ associated with electric dipole absorption of a spherical conducting particle is

$$\langle P_{\mathrm{E}} \rangle = -\frac{3\omega}{8\pi a^3} \operatorname{Im}\left(\underline{p} \cdot \underline{E}_0^*\right) = -\frac{3}{4} \omega \varepsilon_0 E_0^2 \ \operatorname{Im}\left(\frac{(2\varepsilon + 1)(1 - ka \cot ka) - (ka)^2}{(\varepsilon - 1)(1 - ka \cot ka) + (ka)^2} \right) \tag{90}$$

where E_0 is the amplitude (i.e. peak value) of the applied electric field.

For a non-magnetic, highly conducting particle (such as gold) at microwave frequencies then $\varepsilon \approx -i\sigma/\omega\varepsilon_0$ and $\mu = 1$, where σ is the bulk electrical conductivity. For a weakly conducting particle then a more appropriate form for the permittivity is $\varepsilon \approx \varepsilon_1 - i\sigma/\omega\varepsilon_0$, but for the purposes of this study it is assumed that $\varepsilon = 1 - i\sigma/\omega\varepsilon_0$ over a wide range of σ.

There are two limiting forms for equation (90), set by the ratio of the particle radius a to the skin depth $\delta = -1/\mathrm{Im}(k) = (2/\omega\mu_0\sigma)^{1/2}$. In the large skin depth limit (i.e. when $a/\delta \ll 1$), equation (90) reduces to the usual, quasi-static result for a lossy dielectric sphere in a uniform electric field

$$\lim_{a/\delta \to 0} \langle P_{\mathrm{E}} \rangle = -\frac{3}{2}\omega\varepsilon_0 E_0^2 \ \mathrm{Im}\left(\frac{\varepsilon - 1}{\varepsilon + 2}\right) \tag{91}$$

with a uniform internal electric field of magnitude $E_i = 3E_0/(\varepsilon + 2)$, i.e. it is unaffected by the classical skin effect, although for moderate to high conductivity (i.e. when $\sigma > \omega\varepsilon_0$) the internal field is screened significantly by the presence of the conductor.

Equation (91) itself also has two limiting forms, depending on the size of the ratio $\sigma/\omega\varepsilon_0$. When $\sigma/\omega\varepsilon_0 \ll 1$ then $\langle P_{\mathrm{E}} \rangle \approx 9\sigma E_0^2/2$, i.e. proportional to conductivity; when $\sigma/\omega\varepsilon_0 \gg 1$ then $\langle P_{\mathrm{E}} \rangle \approx 9\omega^2\varepsilon_0^2 E_0^2/2\sigma$, i.e. inversely proportional to conductivity. Hence, on varying the conductivity of the particle $\langle P_{\mathrm{E}} \rangle$ attains a maximum value of $\langle P_{\mathrm{E}} \rangle_{\max} = 3\omega\varepsilon_0 E_0^2/4$ when $\sigma = 3\omega\varepsilon_0$. In fact, in the limit $a/\delta \ll 1$ the electric dipole absorption within a particle of any shape within which the external electric field is screened is at a maximum when the particle conductivity is chosen such that $\sigma \approx \omega\varepsilon_0$. Once the conductivity exceeds this maximum value the internal electric field within the particle is reduced by screening, and so $\langle P_{\mathrm{E}} \rangle$ reduces accordingly.

In the small skin depth limit (i.e. when $a/\delta >> 1$)

$$\lim_{a/\delta\to\infty}\left\langle P_{\mathrm{E}}\right\rangle = \frac{9\omega^2\varepsilon_0^2}{4\sigma}\frac{a}{\delta}E_0^2 \propto a\sqrt{\frac{\omega^5}{\sigma}} \qquad (92)$$

Although the electric dipole absorption is enhanced in this limit, it is of little practical importance since the power dissipation is already negligibly small once this limit is reached.

(a)

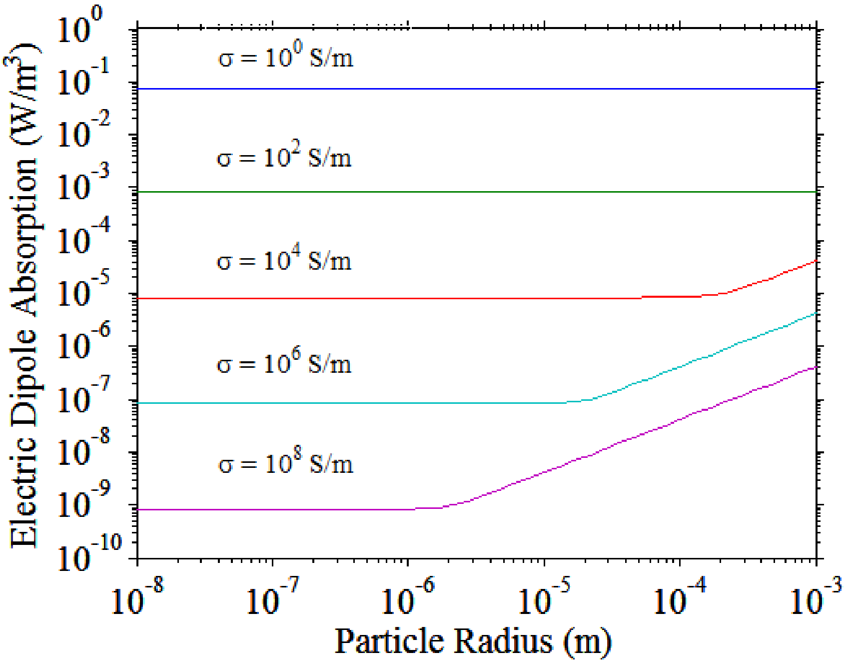

(b)

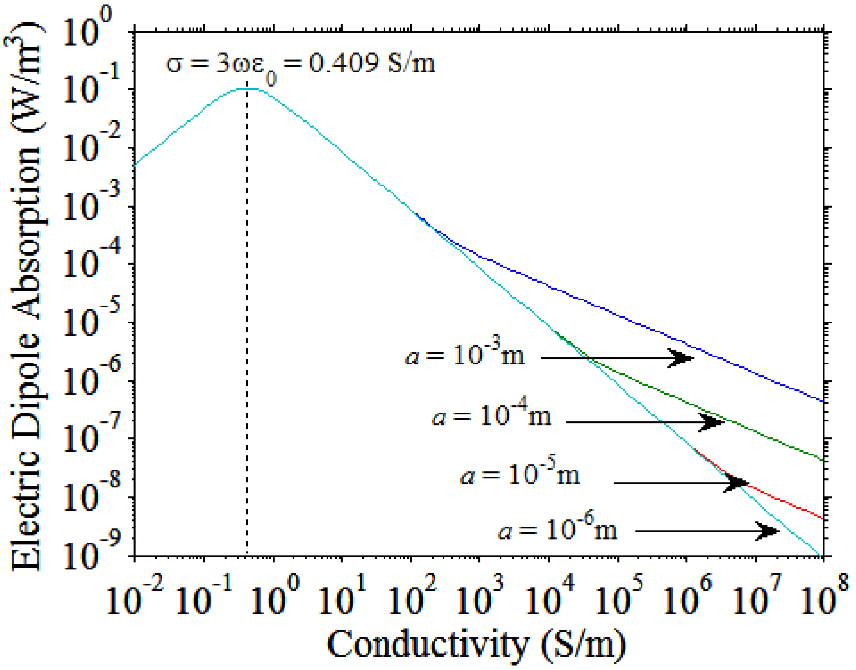

Figure 4.2 - The electric dipole absorption (in units of W/m^3) at a peak applied electric field of 1 V/m oscillating at a frequency of 2.45 GHz (a) as a function of particle radius for various values of conductivity, and (b) as a function of conductivity for various values of particle radius. There is an optimum absorption, which is set solely by the frequency and conductivity (via $\sigma \approx \omega\varepsilon_0$) and is independent of particle radius.

Results for the full calculation of $\langle P_\mathrm{E} \rangle$ (i.e. based on equation (90)) as a function of particle radius and conductivity are shown in Figure 4.2, illustrating the limiting functional forms and general features discussed above. Importantly, $\langle P_\mathrm{E} \rangle$ is independent of particle radius in the large skin depth limit ($a/\delta << 1$), meaning that it is insensitive to a finite particle size distribution, provided that the particles are well-dispersed so that local field corrections may be neglected. Hence, the contribution to the absorption of a single particle of 1 μm radius is 1000 times that of a particle of 100 nm radius, so to estimate the overall absorption for a sample consisting of a range of particle radii one needs only to know the overall volume of conducting material.

4.2.2 Magnetic dipole absorption in conducting particles

A conducting sphere will develop a magnetic dipole moment $\underline{m}$ in response to a uniform, applied magnetic field $\underline{H}_0$. Scattering can once more be neglected if the particle is electrically small, i.e. $a << \lambda_0$. The analytic solution for $\underline{m}$ in a spherical conducting particle (again of isotropic conductivity) in this limit is derived in appendix B [115]. We note the equivalent forms of the electric and magnetic dipoles given by equations (89) and (93).

$$\underline{m} = 2\pi a^3 \underline{H}_0 \left(\frac{(\mu+2)(1-ka\cot ka)-\mu(ka)^2}{(\mu-1)(1-ka\cot ka)-\mu(ka)^2} \right) \tag{93}$$

where again $k = \omega\sqrt{\varepsilon\mu}/c$ is the wavenumber within the particle, $\varepsilon = \varepsilon_1 - i\varepsilon_2$ is the complex permittivity and $\mu = \mu_1 + i\mu_2$ is the complex permeability of the particle. The time averaged power dissipation per unit volume $\langle P_\mathrm{M} \rangle$ associated with magnetic dipole absorption of a spherical conducting particle is

$$\langle P_{\mathrm{M}}\rangle = \frac{3\omega\mu_0}{8\pi a^3}\ \mathrm{Im}\left(\underline{m}\cdot\underline{H}_0^*\right) = \frac{3}{4}\omega\mu_0 H_0^2\ \mathrm{Im}\left(\frac{(\mu+2)(1-ka\cot ka)-\mu(ka)^2}{(\mu-1)(1-ka\cot ka)-\mu(ka)^2}\right) \tag{94}$$

where H_0 is the amplitude (i.e. peak value) of the applied magnetic field. The origin of this dissipation is associated with electromagnetic induction by the changing applied magnetic field, so one would expect it to be a sensitive function of the particle size. For a non-magnetic, conducting particle $\varepsilon = 1 - i\sigma/\omega\varepsilon_0$ and $\mu = 1$, so that equation (94) reduces to

$$\langle P_{\mathrm{M}}\rangle = \frac{3}{4}\omega\mu_0 H_0^2\ \mathrm{Im}\left(1+\frac{3\cot ka}{ka}-\frac{3}{(ka)^2}\right) \tag{95}$$

There are again two limiting forms for the magnetic dipole absorption set by the ratio a/δ. In the large skin depth limit (i.e. $a/\delta << 1$, appropriate for small particles of low conductivity at low frequency), equation (95) reduces to

$$\lim_{a/\delta\to 0}\langle P_{\mathrm{M}}\rangle = \frac{1}{20}\omega^2\mu_0^2 a^2\sigma H_0^2\ \propto \omega^2 a^2\sigma \tag{96}$$

which is that of a uniform applied internal magnetic field (in this case equal to the applied magnetic field since it is assumed that $\mu = 1$). In the small skin depth limit (i.e. $a/\delta >> 1$, appropriate for large particles of high conductivity at high frequency), equation (95) reduces to

$$\lim_{a/\delta\to\infty}\langle P_{\mathrm{M}}\rangle = \frac{9}{4}\frac{R_{\mathrm{s}}}{a}H_0^2\ \propto \frac{1}{a}\sqrt{\frac{\omega}{\sigma}} \tag{97}$$

where $R_{\mathrm{s}} = (\omega\mu_0/2\sigma)^{1/2}$ is the surface resistance of the conducting material.

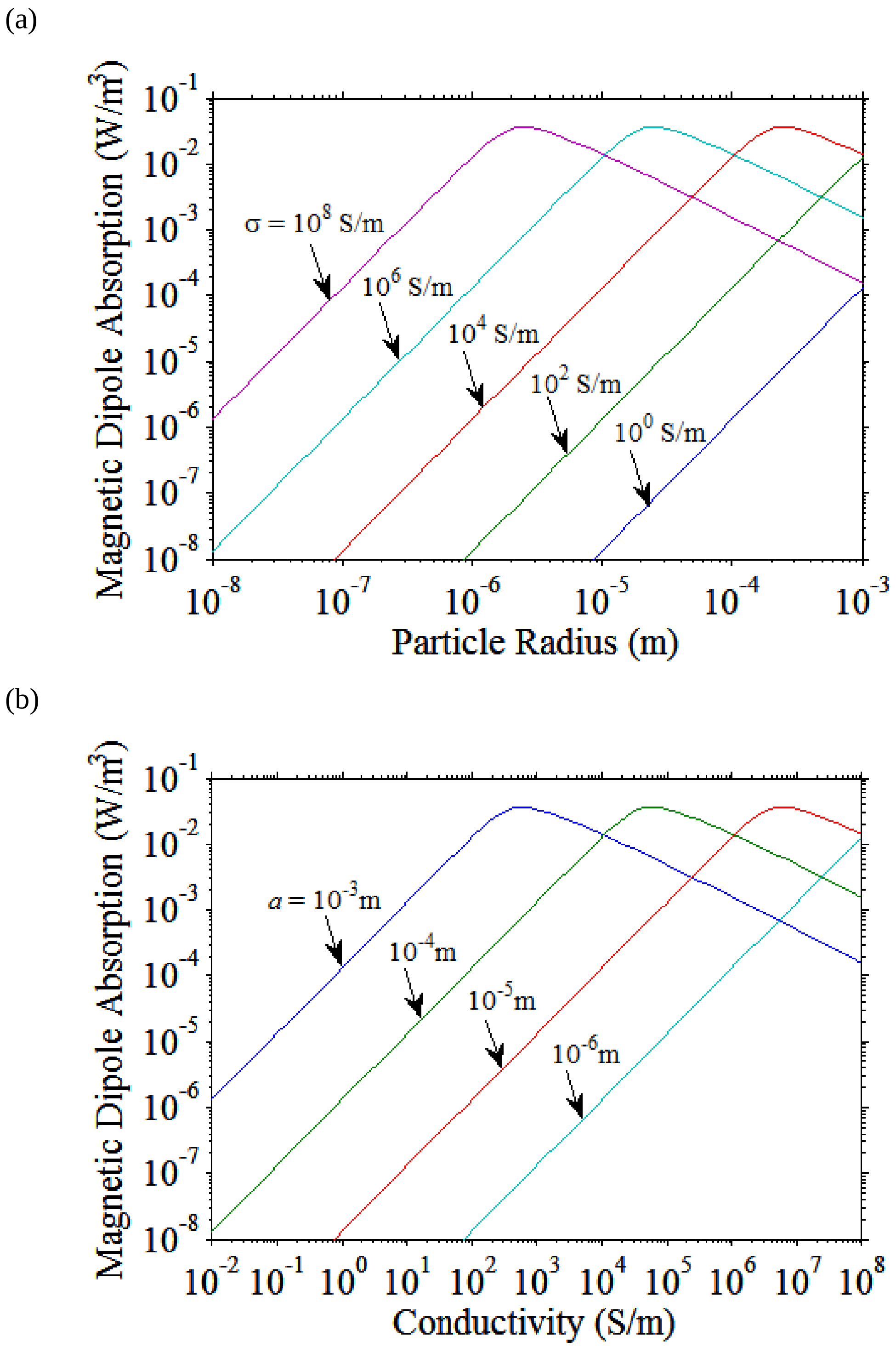

Figure 4.3 - The magnetic dipole absorption (in units of W/m^3) at a peak applied magnetic field of 0.002654 A/m (corresponding to a peak, free space electric field of 1 V/m) oscillating at a frequency of 2.45 GHz (a) as a function of particle radius for various values of conductivity, and (b) as a function of conductivity for various values of particle radius. This time the optimum is set by the frequency, conductivity and particle size via the relationship $a \approx 2.41\delta$, where δ is the skin depth.

Results for the full calculation of $\langle P_\mathrm{M} \rangle$ (based on equation (95)) as a function of particle radius and conductivity are shown in Figure 4.3, illustrating the limiting functional forms and general features discussed above. The different dependences of magnetic absorption on both conductivity and particle radius in either limit suggest that the magnetic dipole absorption (like electric dipole absorption) has a maximum value; from equation (95), it is found that for non-magnetic particles the maximum magnetic absorption occurs when $a \approx 2.41\delta$, where δ is the skin depth. Computational studies in the literature estimate this value as $a \approx 2.5\delta$ [114]. Comparing Figure 4.1 and Figure 4.3a) we see that the experimental results have the same form as predicted here and exhibit a maximum absorption corresponding to the condition $a \approx 2.41\,\delta$ for non-magnetic particles.

For $a \approx 2.41\,\delta$, we have

$$\langle P_\mathrm{M} \rangle_\mathrm{max} \approx 0.266\,\omega\mu_0 H_0^2 \tag{98}$$

Thus, the maximum electric dipole absorption exceeds the maximum magnetic dipole absorption by a factor of 2.82 (assuming that $\mu_0 H_0^2 = \varepsilon_0 E_0^2$, as discussed above), but occurs for a fixed value of conductivity set by $\sigma \approx 3\omega\varepsilon_0$. This is rather low if the frequency is restricted to microwave frequencies (e.g. around 0.4 S/m at 2.45 GHz) and is independent of particle radius. If magnetic absorption is used instead, there is much more flexibility in attaining the condition of maximum absorption since both particle radius and conductivity can be changed whilst maintaining the condition $a \approx 2.41\,\delta$. For example, gold particles of conductivity $\sigma = 4.00 \times 10^7\,\mathrm{S/m}$ have a skin depth of $\delta = 1.61\,\mu\mathrm{m}$ at 2.45 GHz, so maximum magnetic absorption occurs for particles of radii $a = 3.88\,\mu\mathrm{m}$. If particles of lower conductivity are chosen, then at a fixed frequency the maximum magnetic absorption can be obtained by an appropriate increase of the particle radius.

4.2.3 Comparison of Magnetic and Electric Power Dissipation

To emphasise the comparison between magnetic and electric absorption, the ratio $R = \langle P_{\mathrm{M}} \rangle / \langle P_{\mathrm{E}} \rangle$ is plotted as a function of particle radius and conductivity at 2.45 GHz in Figure 4.3. For particles of a highly conducting metal like gold, $R >> 1$ for all particle radii of practical significance, and in excess of 10^7 when $a = 2.41\delta = 3.88\,\mu\mathrm{m}$. The strong dependence of magnetic induction on particle radius means that for sub-micron particles of a highly conducting metal, the magnetic absorption is small (recall from equation (96) that $\langle P_{\mathrm{M}} \rangle \propto a^2$), but it is still much larger than the associated electric absorption. It will be seen in the next section that to enhance the magnetic absorption of highly conducting particles of sub-micron sizes, all that is required is to make them magnetic, with an associated complex (i.e. lossy) permeability.

For conducting particles, clearly magnetic power dissipation dominates for all practical particle sizes. In Yoshikawa et al. (2006) [113], experimental results are shown for the case of NiO particles with radius 3.5μm. The NiO is first placed in the *E*-field and then the *H*-field of a single mode microwave applicator, but heating only takes place in the high *E*-field. Since NiO has $\sigma < 1\times10^{-8}$ S/m, basic knowledge of the behaviour of insulators in electromagnetic fields suggests these different heating characteristics, but Figure 4.4 shows the extent of the difference and that the power dissipated in the *E*-field is almost 10 orders of magnitude larger than in the *H*-field.

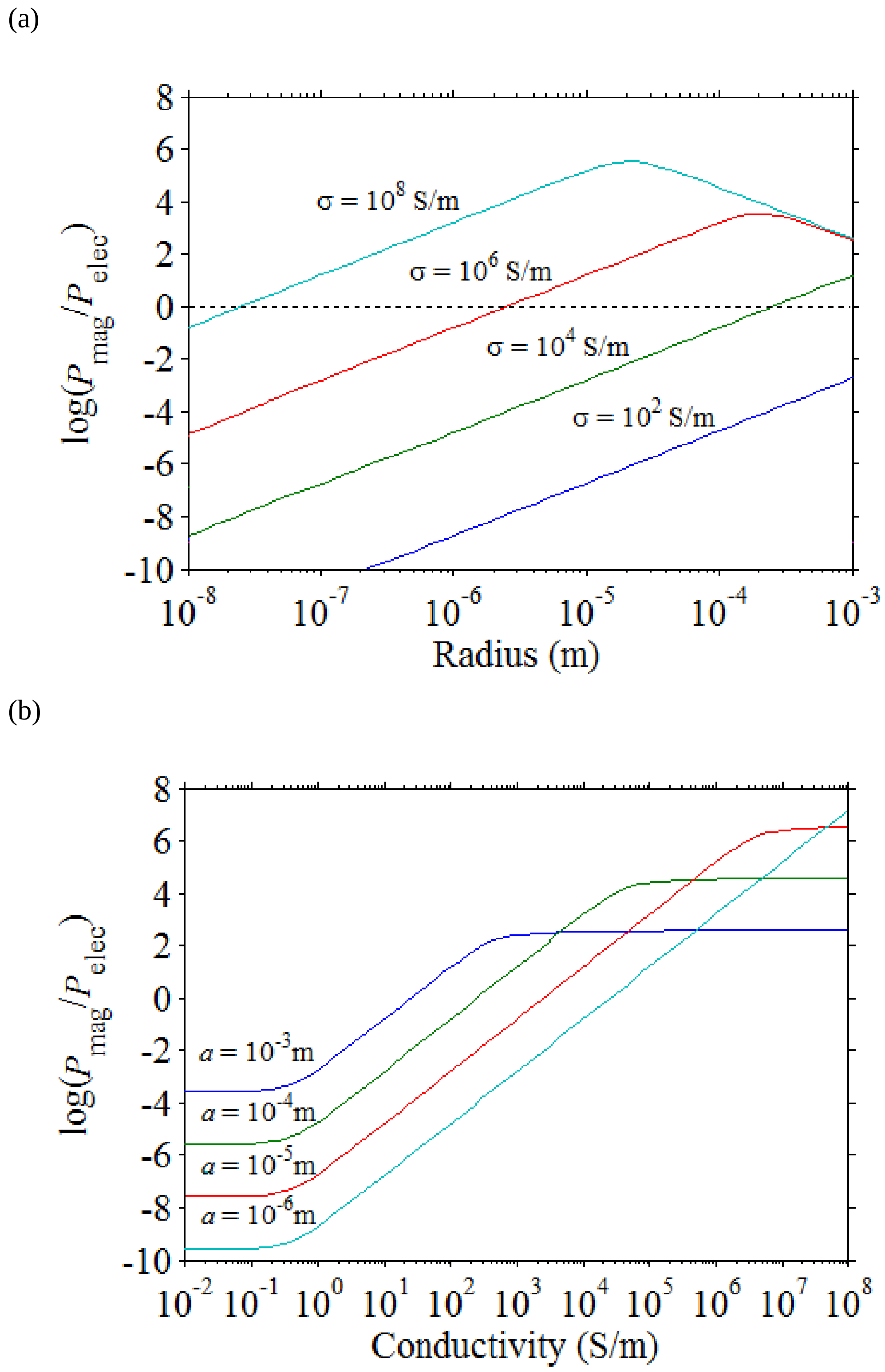

Figure 4.4 - The ratio of magnetic to electric dipole absorption for peak applied fields satisfying the relationship $E_0 = \eta_0 H_0$ oscillating at a frequency of 2.45 GHz (a) as a function of particle radius for various values of conductivity, and (b) as a function of conductivity for various values of particle radius. For metallic (i.e. highly conducting) particles the magnetic dipole absorption is the larger of the two for particle radii commonly met in practice.

The effect of including a distribution of particle radii is more important for the case of magnetic absorption than for electric absorption, particularly in the large skin depth limit. In this limit, (96) is modified to

$$\langle P_{\mathrm{M}} \rangle \approx \frac{1}{20} \omega^2 \mu_0^2 \sigma H_0^2 \, a_{\mathrm{eff}}^2 , \qquad a_{\mathrm{eff}}^2 \equiv \int_0^\infty r^5 f(r) dr \Big/ \int_0^\infty r^3 f(r) dr \tag{99}$$

where $f(r)$ is the particle radius distribution. For any reasonable form for $f(r)$ then $a_{\mathrm{eff}} > a$, and the magnetic absorption could be dominated by relatively few, much larger particles, though not too large as to be in the small skin depth limit. A general feature is that in the small skin depth limit $\langle P_{\mathrm{M}} \rangle$ is enhanced by up to 1 or 2 orders of magnitude compared to the situation of magnetic absorption in a sample of particles of the same radii.

4.2.4 Magnetic dipole absorption in magnetic particles

Finally, the magnetic dipole absorption in small magnetic particles will be considered. Introducing magnetic loss into a particle via a complex permeability $\mu = \mu_1 + i\mu_2$ enhances the magnetic absorption in the large skin depth regime. This is seen by re-evaluating equation (94) in the limit when $a << \delta$, giving the resulting limiting form for $\langle P_{\mathrm{M}} \rangle$

$$\lim_{a/\delta \to 0} \langle P_{\mathrm{M}} \rangle = \frac{3}{4} \omega \mu_0 H_0^2 \ \mathrm{Im}\left(\frac{\mu - 1}{2\mu + 1} \right) \approx \frac{9 \omega \mu_2 \mu_0 H_0^2}{2(2\mu_1 + 1)^2} \tag{100}$$

where for simplicity it is assumed that $\mu_2 << \mu_1$. The inclusion of a finite magnetic loss μ_2 thus removes the sensitivity of the magnetic absorption on particle radius and conductivity. For any particle in the large skin depth limit, a magnetic absorption within an order of magnitude of the maximum value for a non-magnetic particle is attained for values of μ_2 as small as 0.1. Results of the full calculation (based on equation (94)) for the example of $\mu = 1.5 + 0.1i$ are shown in Figure 4.5, which should be compared with the data of Figure 4.3 and Figure 4.4, particularly in the large skin depth region. Unlike that for magnetic dipole absorption, the effect of introducing magnetic loss has very little effect on the electric dipole absorption.

(a)

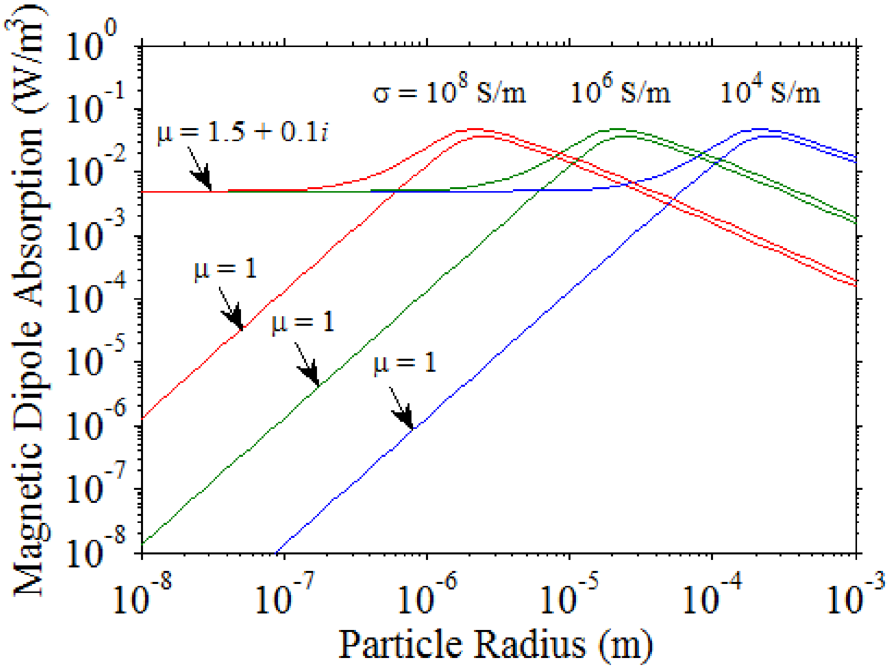

(b)

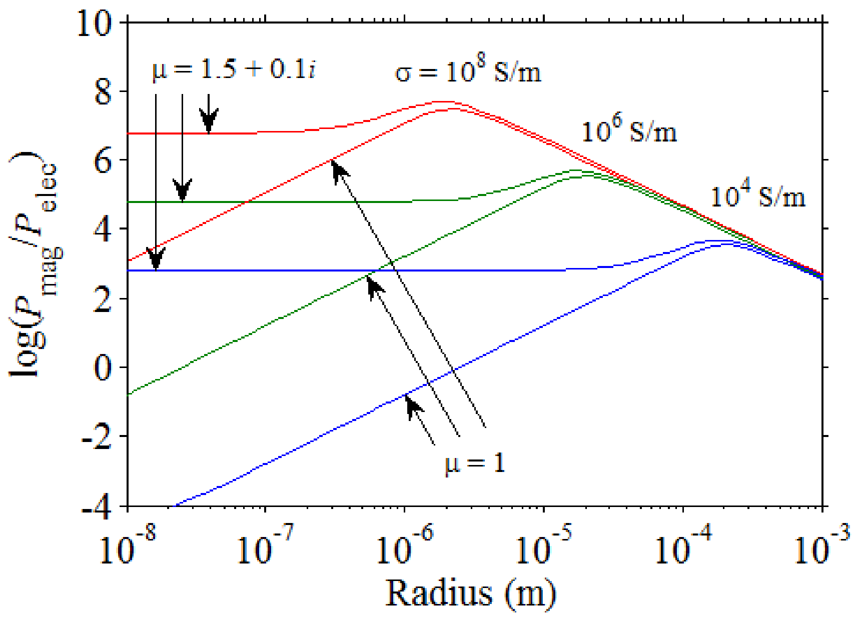

Figure 4.5 - The effect of introducing finite magnetic loss at 2.45 GHz on (a) the magnetic dipole absorption (conditions the same as for Figure 4.3), and (b) the ratio of magnetic to electric dipole absorption, both as a function of particle radius for various conductivities. Magnetic loss enhances magnetic dipole absorption in the large skin depth region, whilst the electric dipole absorption is almost unaffected over the whole range of particle radii studied here.

4.3 DISCUSSION, CONCLUSIONS AND SUMMARY

There is a common misconception that small, highly conducting particles heat profusely when placed in a large microwave electric field. However, it is clear from the results of Figure 4.2 that this is not the case, with the simple physical explanation that the electric field (which drives the heating) within a highly conducting particle is highly screened. Instead, it is the magnetic absorption associated with induction that accounts for the large experimental heating rates observed for small metal particles.

The presence of small metal particles may cause heating in their surroundings and therefore higher electric field absorption, but this is due to the reconfiguration of the electric field in the space outside of the particles. High fields develop at the surface of the particles and at sites of close contact between particles hot-spots can occur. This is the same mechanism that at sufficiently high electric field strengths can cause dielectric breakdown leading to arcing. In any case, the enhanced absorption is much smaller than can be achieved by magnetic absorption alone.

In the case of a dispersed metal powder bathed by microwave radiation, it is clear from Figure 4.4 that the dominant absorption is magnetic in origin. In the case of a metal powder sample placed in a microwave cavity at an apparent electric field antinode (i.e. at a magnetic field node), it would be expected that the only mechanism for heating would be via electric dipole absorption. This would indeed be the case for a very small powder sample, which can be placed at the exact antinode of the electric field, but for an extended powder sample placed within a microwave oven (where the distance between antinodes of the electric and magnetic fields at 2.45 GHz is around $\lambda_0/4 \approx 3\mathrm{cm}$) there must also be a significant magnetic field present. Under such conditions the microwave heating is predominantly via magnetic dipole absorption.

Enhancement of magnetic absorption (and thus heating) within sub-micron particles is best accomplished by making the particles from lossy magnetic materials. The magnetic dissipation exceeds the electric dissipation in these particles by many orders of magnitude for highly conducting particles, as can be seen from Figure 4.5. This has important implications for the selective heating of biological tissue using microwave radiation, into which has been embedded sub-micron magnetic particles. The surrounding tissue will be unaffected by an applied microwave magnetic field, while the embedded particles will heat strongly due to magnetic dipole absorption. Magnetic nanoparticles used in this way are being investigated for the treatment of cancer [116,117]. Attempting the same experiment using an applied microwave electric field will result in an efficient heating of the biological tissue (if water based) and an inefficient heating of the embedded particles, quite the opposite to the desired effect.

To summarise, analytic results for the electromagnetic absorption within electrically small, conducting particles for otherwise arbitrary values of conductivity and radii have yielded some important results for microwave heating applications.

A summary of limiting factors for electric and magnetic absorption is given in Table 12.

	Electric field	Magnetic field	
Particle	Non-magnetic	Non-magnetic	Magnetic
Dominant limitation	Screening	Skin effect	Skin effect
Notes	Max absorption when $\sigma \approx \omega\varepsilon_0$. The skin effect has no practical impact upon absorption in this regime.	Max absorption when $a = 2.41\delta$.	Absorption in sub-micron particles is significantly increased below Curie point.

where σ *is the conductivity,* ω *is the angular frequency,* ε_0 *is the permittivity of free space,* a *is the particle radius and* δ *is the skin depth.*

Table 12 – Limiting factors for electric and magnetic absorption in small

conducting particles. Particles considered are in the range σ > 0.1 S/m and *a* = 1nm – 1mm.

For particles of low conductivity, absorption is predominantly due to electric dipole absorption (driven by a microwave electric field), which is maximised when the conductivity is approximately $\sigma \approx \omega\varepsilon_0$. For highly conducting particles, magnetic dipole absorption (driven by a microwave magnetic field) exceeds electric dipole absorption over the full range of particle radii, from < 10 nm to > 1 mm. The maximum magnetic dipole absorption is of the same order of magnitude as the maximum electric dipole absorption (for equivalent electric and magnetic fields satisfying the condition $H_0 = E_0 / \eta_0$) for powders of the same volume, except it occurs for particle radii of the order of the microwave skin depth. An exact condition for spherical, non-magnetic powders is $a = 2.41\delta$; this is a remarkable result, which means that for a metal of any given conductivity at a particular frequency, maximum magnetic absorption can be assured by simple selection of the mean particle radius.

5 DISCUSSION AND CONCLUSIONS

In this thesis we have comprehensively investigated electrical aspects of TCOs and composites. To enable the investigation we have employed high frequency measurement tools capable of accurately measuring conducting and non-conducting composites and powders, as well as bulk materials. These tools are used to determine the properties of TCO based composites provided by Merck KGaA. A number of high frequency techniques are considered in this work, including the split post dielectric resonator and the broadband coaxial probe, but the cavity perturbation method is used for its versatile, non depolarizing configuration. The conventional cylindrical cavity method is extended to include a split in the axial plane, which provides an accessible space occupied by highly uniform TM_{010} E-fields. This space may accommodate samples of arbitrary shape, but importantly the sample may be externally stimulated and measured simultaneously. For example, simultaneous measurement of multiple properties as some chemical reaction takes place provides the opportunity to link changes in the electrical properties of materials to the changes in other properties under test. Mutual measurements may be taken highlighting, for example changes in crystal structure whilst the cavity reveals concomitant electrical changes. Also, the highly accessible sample in the split may be excited by external stimulus as was demonstrated in chapter 2 of this thesis. A further extension of the cavity perturbation technique has allowed us to correct for ambient temperature changes in the measurement down to an accuracy of the order of milliKelvins. The method therefore has one of the highest resolutions in temperature measurement available and may have applications based upon this property alone.

In the TM_{010} mode, this cavity operates effectively with the split present, with no associated wall currents having to traverse joints in the cavity construction. We therefore maintain a high quality factor (>8000), enabling the accurate measurement of dielectric samples. It is determined that the optimum Q factor is obtained when the cavity radius a is equal to the cavity height, and that the maximum obtainable Q for the TM_{010} mode is therefore equal to $a/2\delta$, where δ is the skin depth of the electromagnetic fields at the cavity walls. A simple and dynamic calibration technique is used which means that measurements may be taken with the cavity split at arbitrary widths simply by taking a measurement of the metal sphere first.

Limitations of the perturbation method were discussed and the complex frequency was introduced as a method of overcoming the assumptions made by perturbation theory. But for the split cavity, we conclude that the complex frequency approach is not dynamic enough to avoid experimental errors. The calibration must be empirical and since use of the complex frequency would require full characterization of the complex space of interest, it is impractical for arbitrary split widths.

The cavity resonator was investigated with the split present, up to 8mm in width. The Q factor remains >7000 for large split widths indicating that accurate and highly repeatable measurements may be taken. The value used in the inversion, V_{eff} describes an effective volume occupied by the cavity fields and in the linear perturbation equations used in this work functions as a calibration variable. For the split cavity, the behaviour of the effective volume occupied by the cavity E-field is investigated for widths of up to 8mm. The increase in effective volume is linear in nature and the dominant source of error is the setting of the split width.

Sample measurements were carried out in the split cavity at widths once again up to 8mm. Using a cylindrical dielectric sample consisting of powders of micron-sized transparent conducting oxide (TCO) coated mica flakes, the width of the split is increased and measurements were compared with established results from the enclosed cavity (i.e. no split). The measurements remain consistent, with the errors in real and imaginary permittivity around 0.5% for a 2mm split and well below 4% even for widths of 8mm.

The causes of the error introduced at large split widths are investigated and it is concluded that non-uniform fields at the cavity split cause a reduced dipole moment, but the presence of a sample with finite (>1) permittivity compounds this effect. The value of V_{eff} becomes a non-linear function of split width and permittivity.

Non-linearities in the measurement make numerical approaches unavoidable at very large split widths. For cylindrical samples, using the cavity with a split present is a trade-off between split width and the level of accuracy required. Furthermore, we conclude that this nonlinearity in the measurement is present only for samples present at the cavity split; pellet samples would not experience the same errors.

Higher order modes were investigated and their potential uses discussed. Analytical integration of the cavity fields in the sample region shows that for the TM_{210} mode, the electric energy present is over six orders of magnitude less than for the TM_{010} mode. The TM_{210} mode is therefore unaffected by the presence of dielectric samples in the centre of the cavity. This is proven experimentally, results showing that the presence of dielectric samples affects the mode negligibly. As a reference point this mode is invaluable, no dielectric sample, regardless of dielectric strength will influence the mode in this configuration. Any effects upon the mode are attributable to the cavity alone.

The TM_{210} mode was used as a reference for measurement of the TM_{010} mode. Normally such a measurement would require an unperturbed cavity measurement first, but by using the fixed relationship between the TM_{010} mode and the TM_{210} mode, we can establish an unperturbed frequency for the TM_{010} resonance without having to observe sample-free measurement at all. This is an advantageous extension of the cavity perturbation technique in terms of general convenience, but importantly, enables measurements to be taken over time without having to disturb the sample under test.

The temperature dependence of TM_{mn0} modes was established and it was determined that the fractional frequency shift for a given temperature change is identical in all such modes.The shift in frequency depends only upon the radius of the cavity and it is shown that temperature changes may be tracked to around a 20mK resolution for the TM_{010} mode, 10mK resolution for the TM_{210} mode, and even higher resolution for higher order modes.

Finally, as a demonstration of the benefits of the split cavity, the photoactivity of powders and sheets of transparent conducting oxides is tested. Lorentzian curves are obtained of the real-time excitation of charge carriers into the conduction band as

UV light stimulates the sample. This remarkable result shows the versatility of the split cavity for testing stimulated samples in any form.

Following the investigations of microwave measurement techniques, a study of the Merck particles themselves was conducted in which we relate the high frequency behaviour of these composite to theoretical descriptions of structural and material properties.

The behaviour of composites of conducting particles was investigated theoretically and experimentally at microwave frequencies. Merck KGaA samples of micron-sized mica particles coated with a transparent conducting oxide were measured over broadband microwave frequencies in an effort to learn more about the electrical behaviour of the composite. Results reveal absorption peaks in the microwave frequency range, and low frequency dispersion in percolative samples. Such a low frequency absorption peak is caused by the core-shell structure of the particle. When the mobility of the TCO shell is increased by raising annealing temperatures we observe experimentally an increase in the frequency of the absorption peak that is proportional to the increase in DC conductivity as predicted in the literature [3,4]. However, at higher levels of mobility we begin to see a *decrease* in the absorption peak frequency. This is a result that has not been predicted, or observed in the literature. A comprehensive electromagnetic model of representative layered conducting oblate spheroids was developed and by using the simple Drude model of the degenerate electron gas, we confirm theoretically the origin of this anomalous behaviour. There is a critical value of mobility beyond which the absorption peak frequency begins to decrease. This result may have a wide ranging impact as the field of semiconducting composites grows.

Mixing laws for composites and classical mixing formulas were introduced and their limitations were discussed. We conclude that significant limitations exist at high concentrations where electromagnetic interaction between particles becomes a notable. Since we cannot have complete knowledge of a sample microstructure and variations in the structure can alter the effective electrical properties of the medium a level of uncertainty must be accepted, though for micron sized particles interrogated by wavelengths of the order of centimetres, averaging effects are implicit.

Classical interpretations of frequency dependent loss were discussed via the Debye model of dielectric relaxation. A general approach to the analysis of loss-peaks in terms of the relaxation time is deemed inadequate and we take a closer look at the polarization of multi-layered particles, by using the Clausius-Mossoti approach.

Critical phenomena and the scaling of percolative behaviour in general were discussed and the polarization of particles in the time domain is reviewed. A combination of both Debye-type polarization and Drude-type conduction is used to describe a percolating composite exhibiting both a relaxation peak, and low-frequency dispersion.

The percolation threshold was investigated using random resistor-capacitor networks. In the resulting frequency dependent admittance, the central frequency region exhibits a fractional power law behaviour, which directly relates to the composition of the lattice. The gradient observed in the fractional power law region corresponds to the proportion of the lattice occupied by capacitive components.

It is observed that as the size of the network is increased power law region expands to cover more of the frequency range, with the conclusion that for real materials, this behaviour dominates all frequencies, subject to limiting low and high frequency values. It is verified that the value of the gradient in the anomalous power law region of the frequency dependent conductivity depends upon the proportion of capacitive components present in the lattice and results are shown from literature supporting the application of this to real materials.

The broadband coaxial probe technique is used to measure the frequency dependent conductivity of the TCO based composites used in this work. Measured results indicate that the gradient decreases as the proportion of the capacitive phase decreases, just as in our RC network interpretation. But results underestimate the role of the capacitive phase somewhat and the gradient is less than the predicted behaviour of the power law, though emergent behaviour is present. We conclude that this deviation comes about because scaling behaviour is not satisfied in the composite material measured in this work since the conductive phase here is in the form of platelets. This model is not therefore suited to composite systems such as this.

In order to investigate the critical behaviour of the percolation threshold, the split post dielectric resonator technique is used to measure the sheet resistance of percolating and non-percolating samples at high frequencies and results are compared to DC measurements of the same samples. The percolation threshold remains invisible to the microwave measurement and we simply observe a smooth curve describing the increasing quantity of conducting particles in the sample. At DC we see the expected critical phase transition from the non-conducting to the conducting state. This approach is clearly advantageous and measurements of conducting particles may be made irrespective of their concentration.

Systematic broadband investigations of the shift from non-percolating to percolating composites are carried out. As the composite begins to percolate low-frequency dispersion emerges from the loss-peak. However, at the onset of low frequency dispersion, the ‘lower leg’ of the frequency response does not simply rise and engulf the relaxation behaviour of the particles. In fact, well above the percolation threshold we still observe a small relaxation peak, which emerges from the low frequency dispersion that is characteristic of percolation. We can conclude that the relaxation times of percolative and polarization effects in this system are independent and dissimilar. We also conclude that high frequency measurements may be taken of composites of conducting particles and are insensitive to percolation effects, but at frequencies below the characteristic loss-peak frequency, low-frequency dispersion is present and percolation must be accounted for in measurements.

Having established theoretical approaches to model the particle polarization and fundamental material properties, we extend the investigation of TCOs towards the high impact application of thin-film solar cells.

Models of the μ-n relationship in transparent conducting oxides were considered using combined electron scattering models which have been fitted to experimental data for ITO. Above the Mott critical density for the Insulator-Conductor Transition, ionized impurity scattering causes a large decrease in electron mobility. It is suggested that to achieve high mobilities for a given TCO system, we must manipulate the material to move closer to the Mott critical density.

The simple Drude model was used here to determine the electrical and optical properties of the TCO as a function of electron mobility and electron density. When the electron mobility is increased, the optical transparency is reduced because of the electromagnetic absorption associated with the concomitant reduced skin depth. It was been proposed that properties for any TCO material may be improved by increasing mobility in preference to electron density. It was shown that this is particularly important for devices such as thin-film solar cells, in which the TCO layer must be both highly transparent and highly conducting.

Power absorption coefficients for a TCO layer in a typical thin-film solar cell were calculated as functions of the mobilities and electron densities. Using experimental data for ITO, a direct observation was made of total power absorption in the layer for a real ITO system. It was shown that decreasing the electron density n from 2.6×10^{21} cm^{-3} to 2×10^{21} cm^{-3}, increases μ_e and decreases total power absorption in the layer by around 8% relative to the theoretical minimum value. This result has a large potential impact for producers of thin-film solar cells and producers of TCOs in general. And could lead to significantly improved efficiencies in all applications where a transparent conducting oxide is used.

Having modelled effectively the behaviour of composites and TCOs the spotlight is once more focussed upon the properties of conducting composites in general. Interest in their microwave absorbing properties is ubiquitous and knowledge of the interaction of microwaves with conducting particles is important in many interdisciplinary applications.

It was shown that though there may be a common misconception that small, highly conducting particles heat profusely when placed in a large microwave electric field, it is not the case. The simple physical explanation is that the electric field (which drives the heating) within a highly conducting particle is highly screened. We observe that the magnetic absorption associated with induction accounts for the large experimental heating rates observed for small metal particles. The presence of small metal particles may cause heating in their surroundings and therefore higher electric field absorption, but this is due to the reconfiguration of the electric field in the space outside of the particles.

For metal powders in microwave radiation, it was shown that the dominant absorption is magnetic in origin.

Enhancement of magnetic absorption (and thus heating) within sub-micron particles is best accomplished by making the particles from lossy magnetic materials. The magnetic dissipation exceeds the electric dissipation in these particles by many orders of magnitude for highly conducting particles. This has important implications for the selective heating of biological tissue using microwave radiation, into which has been embedded sub-micron magnetic particles. Conventionally, in this case microwaves would heat biological tissue, but the surrounding tissue will be unaffected by an applied microwave *magnetic* field, while the embedded particles will heat strongly due to magnetic dipole absorption. Magnetic nanoparticles used in this way are being investigated for the treatment of cancer [116,117].

General principles were developed for efficient microwave absorption by small conducting particles. For particles of low conductivity, absorption is predominantly due to electric dipole absorption (driven by a microwave electric field), which is maximised when the conductivity is approximately $\sigma \approx \omega\varepsilon_0$. For highly conducting particles, magnetic dipole absorption (driven by a microwave magnetic field) exceeds electric dipole absorption over the full range of particle radii, from < 10 nm to > 1 mm. The maximum magnetic dipole absorption is of the same order of magnitude as the maximum electric dipole absorption (for equivalent electric and magnetic fields satisfying the condition $H_0 = E_0 / \eta_0$) for powders of the same volume, except it occurs for particle radii of the order of the microwave skin depth. An exact condition for spherical, non-magnetic powders is $a = 2.41\delta$; this is a remarkable result, which means that for a metal of any given conductivity at a particular frequency, maximum magnetic absorption can be assured by simple selection of the mean particle radius.

6 ANNEX A: TCOs in Thin-Film Solar Cells

The production of high-performance transparent conducting oxides (TCO) is of critical importance to thin-film solar cells. The remarkable properties of both high conductivity and high transparency are however only achievable within certain limits. As dopant density is increased, a natural competition between these two critical performance indicators emerges. The challenge facing producers of TCOs is therefore to achieve high dopant densities for high conductivity, but low dopant densities for high transparency. Producers of TCOs must search closer to the Mott conductor-insulator transition for high-performance materials, where the low carrier density but high mobility is well suited to use in thin-film solar devices. As thin-film solar cells emerge as a possible alternative to silicon wafer based technology, the optimization of TCOs remains essential for the further proliferation of thin-film photovoltaics. This article considers the power absorption of an indium tin oxide layer in such a thin-film device and pursues optimal performance close to the Mott transition.

The performance of thin-film solar cells is critically dependent upon the effective operation of transparent conducting oxide (TCO) layers, which play a significant role in both optical and electrical power transmission through these photovoltaic devices. In this article, we model the optical and electrical power transmission through TCO layers in thin-film solar cells as a function of both the electron carrier density, n, and its mobility, μ. The electrical and optical properties of the TCO layer are described by the simple Drude model of the degenerate free electron gas and the concomitant electromagnetic absorption due to skin-depth effects is thereby calculated. Above the critical carrier density for the composition-induced Mott Insulator-Conductor Transition, TCOs exhibit metallic-type conduction. However, with increasing electron (carrier) density above the transition, the optical transparency of the layer is significantly decreased. Importantly, in order to achieve high electrical conductivity whilst preserving high optical transparency of the TCO layer, electron mobilities need to be increased in preference to increasing electron densities. To reach higher carrier mobilities in any given TCO system, we propose that one should move the material close to the Mott transition. A model of ionized impurity scattering in indium tin oxide (ITO) at high carrier densities allows direct comparison of the μ-n relationship in real TCO layers to the total power absorption in such layers in thin-film solar devices. We determine that decreasing the electron density from 2.6×10^{21} cm^{-3} to 2×10^{21} cm^{-3} in such an ITO layer above the Mott critical density can decrease the total power absorption in the layer by a large amount (around 8% relative to the minimum theoretical absorption).

6.1 Introduction

Transparent conducting oxides (TCO) find widespread use as transparent electrodes in optoelectronic devices [118]. TCOs such as tin-doped indium oxide (ITO) and fluorine-doped tin oxide (FTO) are used as current collectors and form conducting layers in thin-film photovoltaic cells [119,120]. The TCO layer influences the performance of such solar cell devices in two respects. Firstly, by transmission of the optical power of incident light through the layer. Secondly, by transmission of electrical power through the layer by the transport of the optically-generated carriers. Consequently, it is very important that the TCO layer has both a low sheet resistance R_{sq} and high optical transparency in order to optimize the output power of the device. Unfortunately, as we will illustrate, these parameters are in natural conflict.

Since $R_{\mathrm{sq}} = 1/ne\mu_{\mathrm{e}}t$, to reduce the sheet resistance one might increase the carrier density n, the carrier mobility μ_{e}, or the film thickness t. However, increasing n and μ_{e} also affects the electromagnetic skin depth δ, which is associated with absorption of electromagnetic radiation. This ultimately determines the optical transparency of the film since the optical power transmission coefficient is approximately proportional to $\exp(-2t/\delta)$. For a given layer thickness, increasing the carrier density in any TCO system will therefore have the effect of increasing the conductivity, but also necessarily decreasing the transparency. In **Error! Reference source not found.** we show the effect of increasing the electron density, for a material at carrier densities above the Mott Insulator-Conductor Transition, upon the dc electrical conductivity and optical transparency of a typical TCO layer, calculated using the simple Drude model as discussed in the following sections.

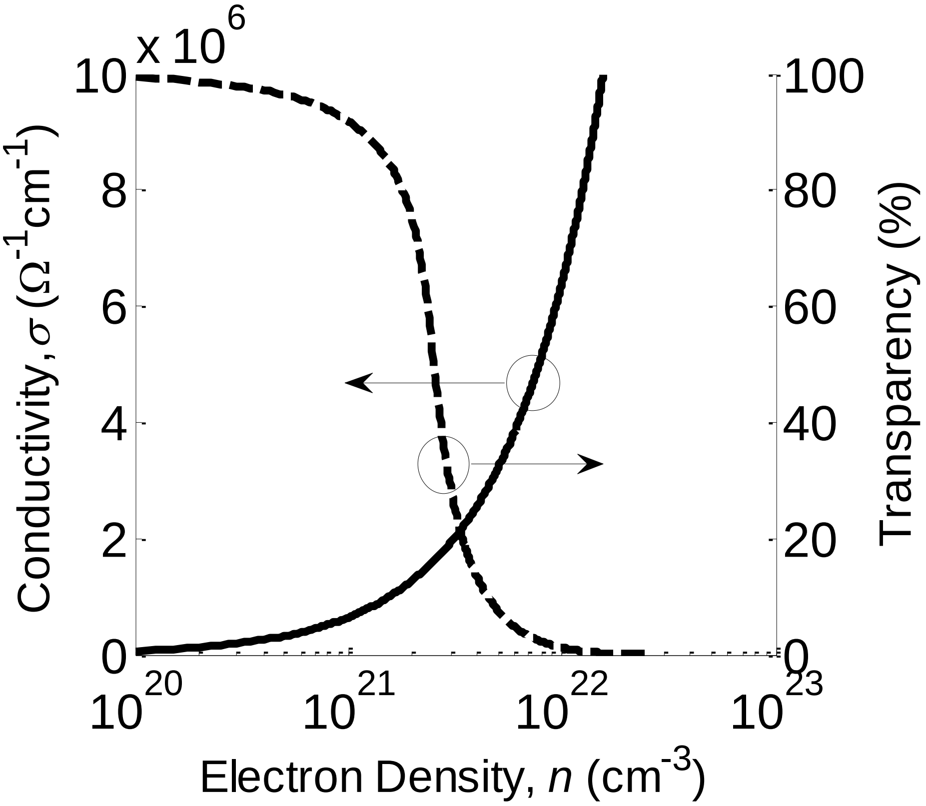

Figure 6.1 - The effect of increasing the electron density upon conductivity (solid line) and transparency (dashed line) in a TCO layer at carrier densities above the Mott Insulator-Conductor Transition. For normally incident light of wavelength 800nm, upon an ITO film of thickness 80nm.

Transparent conducting thin-films can therefore only be optimized for both low sheet resistance and high optical transparency by increasing the electron (carrier) mobility in preference to the carrier density [121]. In the following sections, this will be shown to have a major effect upon the power absorption of the transparent conducting layer in photovoltaic cells. In the relationship [122,123] between the mobility and carrier concentration shown in **Error! Reference source not found.**, we observe that higher mobilities may be achieved by moving the material closer to the Mott critical density, where reduced ionized-impurity scattering is exhibited at lower carrier densities. Then, for a given TCO system, this finding allows optimized values of both n and μ_e to be deduced for applications in solar energy devices. Photon absorption due to in-band states is ignored in this work under the assumption that this can be suppressed by appropriate materials processing.

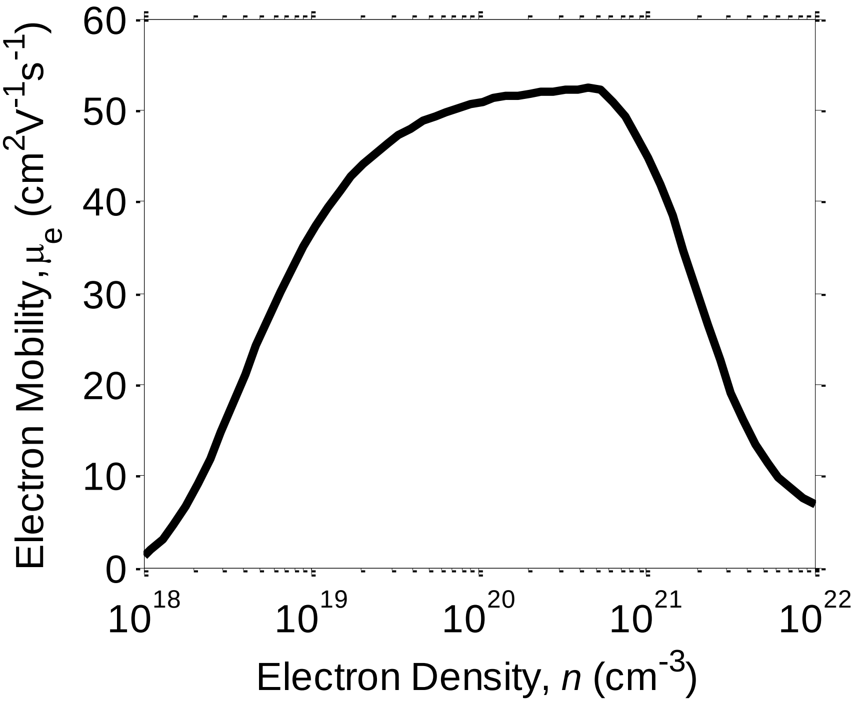

Figure 6.2 - μ_e**–**n **relationship using the combined model proposed by Ellmer et al. [**Error! Bookmark not defined.**] and fitted to empirical data for ITO.**

Plotting the empirical curve proposed by Masetti et al. [**Error! Bookmark not defined.**], for ionized impurity scattering in doped semiconductors and fitted to experimental values for ITO obtained by Ellmer et al. [124], an optimization in both parameters is demonstrated by comparison with power absorption curves for TCO photovoltaic device layers derived using the simple Drude model of optoelectronic properties above dopant levels set by the Mott criterion [96]. Importantly, a carrier density reduction from 2.6×10^{21} cm^{-3} to 2×10^{21} cm^{-3} is shown to result in an decrease in total power absorption in the TCO layer of around 8% relative to the theoretical minimum absorption of ITO.

6.2 The μ-n relationship and the Mott critical density

To investigate the μ-n relationship in TCOs and the effects of this relationship upon optical power absorption in a thin-film solar cell, we first consider empirical models of scattering mechanisms for TCOs and related doped semiconductor systems. The behaviour of such TCOs will, of course, vary greatly from material to material and with different preparation methods. However, the exact behaviour does not influence our conclusions since the principle of optimization remains valid for any given TCO system under the influence of ionized impurity scattering above the Mott critical density.

It is generally recognised that the dominant carrier scattering mechanism in ITO above $n \approx 3 \times 10^{21}$ cm^{-3} is due to ionized impurities [125] and with increasing carrier density, a decrease in carrier mobility is observed [**Error! Bookmark not defined.**]. This behaviour was modelled by Masetti et al. [**Error! Bookmark not defined.**] for carrier densities above the Mott critical density, and at densities of 1×10^{19} cm^{-3} by fitting experimental results for As, P and B doped Si to the empirical curve described by equation **Error! Reference source not found.**,

$$\mu_e = \mu_0 + \frac{\mu_{\max} - \mu_0}{1 + \left(n / C_r\right)^{\alpha}} - \frac{\mu_1}{1 + \left(C_s / n\right)^{\beta}} \qquad \textbf{(101)}$$

Here, $\mu_{\max}$ describes the carrier mobility at low carrier densities and $\mu_{\min}$ describes the mobility limited by ionized impurity scattering. The model was fitted to ITO experimental data by Ellmer et al.[7] yielding the parameters $\mu_{\max} = 210$ cm^2/Vs, $\mu_{\min} = 55$ cm^2/Vs, $\mu_1 = 50$ cm^2/Vs, $C_r = 15 \times 10^{17}$ cm^{-3}, $C_s = 20 \times 10^{20}$ cm^{-3}, $\alpha = 1$, $\beta = 2$.

Below the Mott critical density the decrease in mobility may have a number of contributing causes. Ellmer et al. [**Error! Bookmark not defined.**] include the influence of grain barrier limited transport at lower carrier densities in their model of polycrystalline ITO, and Leenheer et al. [**Error! Bookmark not defined.**] attribute similar behaviour in amorphous indium zinc oxide films to a hopping (or percolation) type carrier transport and lattice scattering. In **Error! Reference source not found.** we show the combined ionized and grain boundary model using the empirical parameters obtained for ITO [**Error! Bookmark not defined.**]. The electron mobility is limited above $n \approx 5 \times 10^{20}$ cm^{-3} by electron-ion impurity scattering modelled by equation **Error! Reference source not found.** as described above [**Error! Bookmark not defined.**], and below $n \approx 5 \times 10^{20}$ cm^{-3} scattering is described by the model proposed by Seto et al. [126], though carrier densities down to this order are not considered in this work.

6.3 Optical properties of the free electron gas

The optical properties of ITO thin films above the Mott critical density are discussed in Porch et al. [127], within the framework of the simple Drude model where a parabolic conduction band is considered to be partially filled by a degenerate free electron gas. There is a strong frequency dependence of the scattering time τ for Fermi surface electrons [98] in such a model, though if we consider only the visible part of the spectrum, τ is assumed to be approximately constant. The Drude form of the complex permittivity is $\varepsilon = \varepsilon_1 - j\varepsilon_2$ [99], thus giving

$$\varepsilon_1 = \varepsilon_\infty - \frac{\omega_N^2 \tau^2}{1+\omega^2\tau^2} \tag{102}$$

$$\varepsilon_2 = \frac{1}{\omega}\frac{\omega_N^2 \tau}{1+\omega^2\tau^2} \tag{103}$$

where $\omega_N^2 = ne^2/\varepsilon_0 m^*$, ε_∞ is the high frequency relative permittivity and m^* is the electron effective mass. Data collected by Porch et al. for ITO suggests that $\varepsilon_\infty \approx 4.0$, $m^* \approx 0.35m_e$ and $\tau \approx 3.3 \times 10^{-15}$ s. The plasma frequency ω_p of a conducting material is defined to be the frequency at which $\varepsilon_1 = 0$. At frequencies below the plasma frequency the conductor is highly reflective since $\varepsilon_1 < 0$. At high electron densities ($n > 1 \times 10^{21}$ cm^{-3}) and high electron mobilities ($\mu_e > 20$ cm^2/Vs) we have $\omega_N^2\tau^2/\varepsilon_\infty >> 1$ and $\omega_p \approx \omega_N/\varepsilon_\infty^{½} \propto n^{½}$. So for the conductor to be non-reflective to incident light in the visible spectrum (including red light of wavelength up to 780nm), we must have $n_{max} < 2.6 \times 10^{21}$ cm^{-3}.

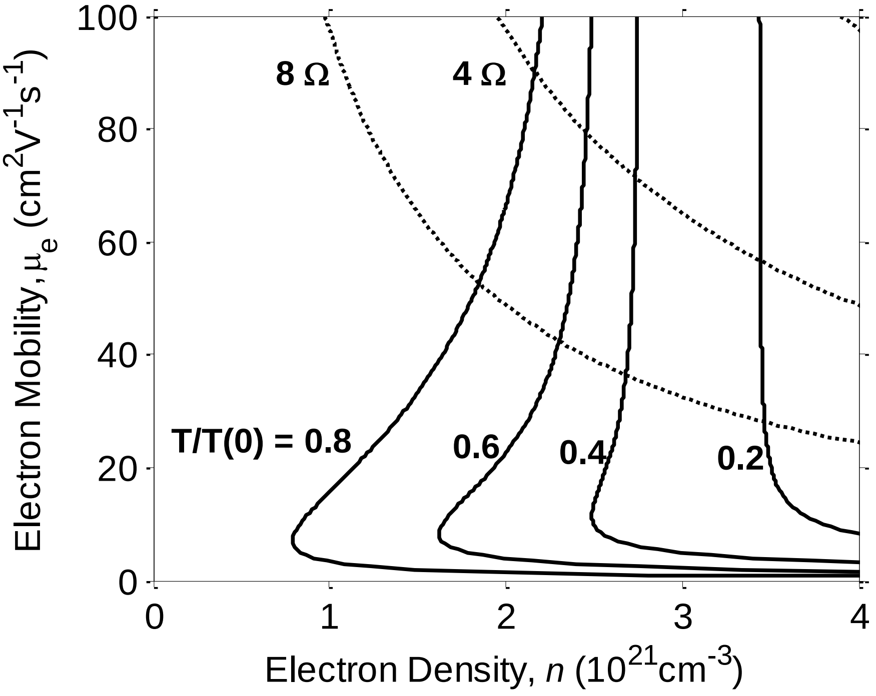

Figure 6.3 – Normalized optical power transmission coefficient T_{opt} (solid lines) as a function of electron density n and mobility μ_e for normally incident light of wavelength 800nm upon an ITO film of 80 nm thickness. Dotted lines are contours of constant sheet resistance $R_{sq} = 1/ne\mu_e t$ (units of Ω).

The skin depth and free electron absorption ultimately determine the transparency of sufficiently thick TCO layers. Calculations of the optical power transmission coefficient T can be carried out using the wavenumber $k = \omega\varepsilon^{1/2}/c$ and the plane wave impedance $Z = \omega\mu_0/k$. The skin depth is defined using the wavenumber k by $\delta = -1/\mathrm{Im}(k)$. This analysis gives

$$\delta = \frac{c}{\omega}\left(\frac{2}{\sqrt{\varepsilon_1^2 + \varepsilon_2^2} - \varepsilon_1}\right) \qquad \textbf{(104)}$$

which can be calculated using **Error! Reference source not found.** and **Error! Reference source not found.**. The skin depth δ and the optical power transmission coefficient T follow the same qualitative behaviour, since as a function of thickness $T(t) \approx T(0)\exp(-2t/\delta)$ for frequencies well above the plasma frequency ω_p.

In **Error! Reference source not found.** we show contours of normalized optical power transmission coefficient $T_{\mathrm{opt}} = T(t)/T(0)$ as a function of μ_{e} and n, for normally incident, incoherent light of free space wavelength λ_0 = 800nm and for an ITO film of thickness 80nm. The contours are normalized to the maximum theoretical optical power transmission, i.e. for $t = 0$, giving 100% transparency. For large values of n, the normalized optical power transmission coefficient becomes very small as the plasma frequency approaches the frequency of the incident light, since $\omega_{\mathrm{p}} \propto n^{½}$. The increased values of T_{opt} when $\mu_{\mathrm{e}} < 10\ \mathrm{cm}^2\mathrm{V}^{-1}\mathrm{s}^{-1}$ correspond to increased values of δ, and is the result of ω_{p} increasing with decreasing μ_{e} in this low mobility limit. Similar contours are obtained for both shorter wavelengths and decreased thicknesses, but increased values of T_{opt} are exhibited as we move further above ω_{p} and are less subject to skin depth effects as t is reduced.

6.4 Implications for thin-film photovoltaic devices

The power generated by a thin-film photovoltaic device is influenced by many layers and interfaces, but considering the TCO layer in isolation, and its optoelectronic performance, we can determine the total power absorption coefficient A_{T} calculated relative to the minimum theoretical value for the layer. The optical power passing through the TCO layer of a photovoltaic cell is subject to the effects of electromagnetic absorption. The same layer is responsible for conducting generated current towards a metal contact. The total power transmission of the TCO layer is therefore proportional to the factor [**Error! Bookmark not defined.**,128] $T_{\mathrm{T}} = T_{\mathrm{elec}} \times T_{\mathrm{opt}} = (n\mu_{\mathrm{e}}t) \times \exp(-2t/\ \delta)$, where the figure of merit $T_{\mathrm{elec}} = (n\mu_{\mathrm{e}}t)$ accounts for the increased spreading current as thickness t increases (assuming a rectangular contact geometry) and is the reciprocal of the sheet resistance. The term $T_{\mathrm{opt}} = \exp(-2t/\ \delta)$ accounts for the increased electromagnetic absorption due to the skin depth. For incident light entering the TCO layer, we define the power absorption coefficient $A_{\mathrm{T}} = 1 - T_{\mathrm{T}}$. This is normalized to the minimum theoretical absorption for the layer dictated by the intrinsic mobility limit for ITO established by Bellingham et al. [**Error! Bookmark not defined.**] at around $100\mathrm{cm}^2\mathrm{V}^{-1}\mathrm{s}^{-1}$.

In **Error! Reference source not found.** we show a schematic diagram of a typical thin-film solar module in superstrate configuration [**Error! Bookmark not defined.**]. The TCO layer spreads current between the rectangular contacts of each active cell in the solar module. The power absorption of the transparent conducting layer is decreased by increasing μ_e, but for varying n or t an optimum value exists which minimizes power absorption. This is demonstrated in **Error! Reference source not found.**, which plots normalized power absorption contours for normally incident incoherent light of free space wavelength λ_0 = 800nm and for an ITO film of thickness 80nm (appropriate for antireflection purposes). Each value of μ_e has a corresponding, optimized value of n, which lies on the locus shown in **Error! Reference source not found.** by a dashed line.

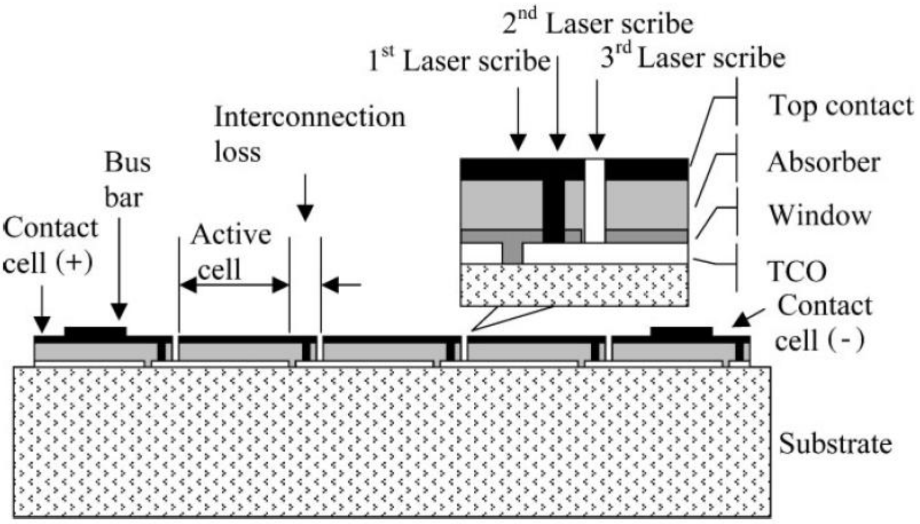

Figure 6.4 – Schematic diagram of a typical thin-film photovoltaic module (from Reference [Error! Bookmark not defined.**]).**

Plotting the empirical model described by equation **Error! Reference source not found.** with parameters obtained experimentally allows a direct analysis of the free carrier behaviour for a given TCO system. In **Error! Reference source not found.** the curve is plotted for an ITO system with empirical parameters obtained from reference [**Error! Bookmark not defined.**]. It is observed that following the ITO curve towards lower electron densities by moving closer to the Mott critical density minimizes the total power absorption of the photovoltaic device layer. For example, decreasing n from 2.6×10^{21} cm^{-3} to 2×10^{21} cm^{-3}, increases μ_e and decreases total power absorption by around 8%, a very significant result.

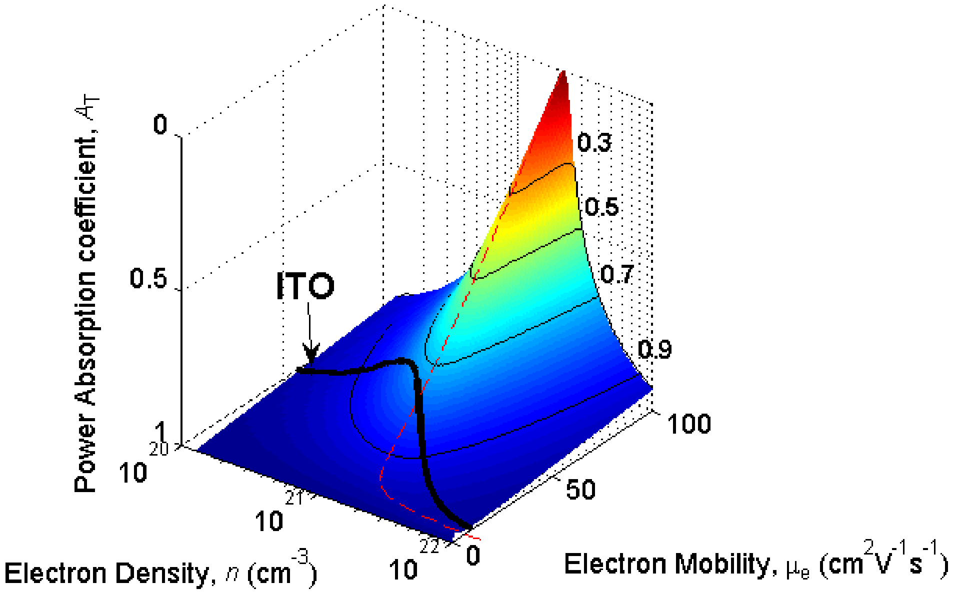

Figure 6.5 – Contours of power absorption coefficient A_T, normalized to the minimum theoretical value at μ_e = 100 cm^2/Vs for an ITO layer in a thin-film photovoltaic cell. The film thickness is 80nm and incident wavelength λ_0 = 800nm. Optimum carrier density for a given mobility is shown (red dashed line), which intersects the μ_e–n line describing ionized impurity scattering in ITO.

6.5 Summary and conclusions

Models of the μ-n relationship in transparent conducting oxides were considered using combined electron scattering models which have been fitted to experimental data for ITO. Above the Mott critical density for the Insulator-Conductor Transition, ionized impurity scattering causes a large decrease in electron mobility. It is suggested that to achieve high mobilities for a given TCO system, we must manipulate the material to move closer to the Mott critical density.

The simple Drude model was used here to determine the electrical and optical properties of the TCO as a function of electron mobility and electron density.

However, it is clear that these parameters are in natural conflict, since for increasing electron density, the conductivity is increased, but the optical transparency is reduced because of the electromagnetic absorption associated with the concomitant reduced skin depth. It has been proposed that properties for any TCO material may be improved by increasing mobility in preference to electron density. It was shown that this is particularly important for devices such as thin-film solar cells, in which the TCO layer must be both highly transparent and highly conducting.

Within the framework of the simple Drude model, power absorption coefficients for a TCO layer in a typical thin-film solar cell were calculated as functions of the mobilities and electron densities. Using the scattering model outlined above and fitted to experimental data for ITO, a direct observation was made of total power absorption in the layer for a real ITO system. It was shown that decreasing the electron density n from 2.6×10^{21} cm^{-3} to 2×10^{21} cm^{-3}, increases μ_e and decreases total power absorption in the layer by around 8% relative to the theoretical minimum value. We believe that this highly significant result will allow optimization of the performance of a given TCO material in thin-film solar cells.

7 APPENDICES

7.1 APPENDIX A: Spherical Particle within an Oscillating Electric Field

First consider the electric dipole developed by a spherical particle placed within in a uniform, oscillating electric field, and the subsequent electric dipole absorption. Electromagnetic scattering can be neglected if the sphere is electrically small, in which limit the electromagnetic fields are considered to be quasi-static; specifically, this occurs for a particle radius $a << \lambda_0$, where $\lambda_0 = 2\pi c / \omega$ is the free space wavelength and ω the angular frequency of the applied electric field.

Referring to the spherical polar co-ordinate system of Fig. A1, consider a uniform electric field of magnitude E_0 applied parallel to the *z*-axis. The sphere is considered to have isotropic relative permittivity ε and permeability μ, which can be complex quantities to allow for energy absorption.

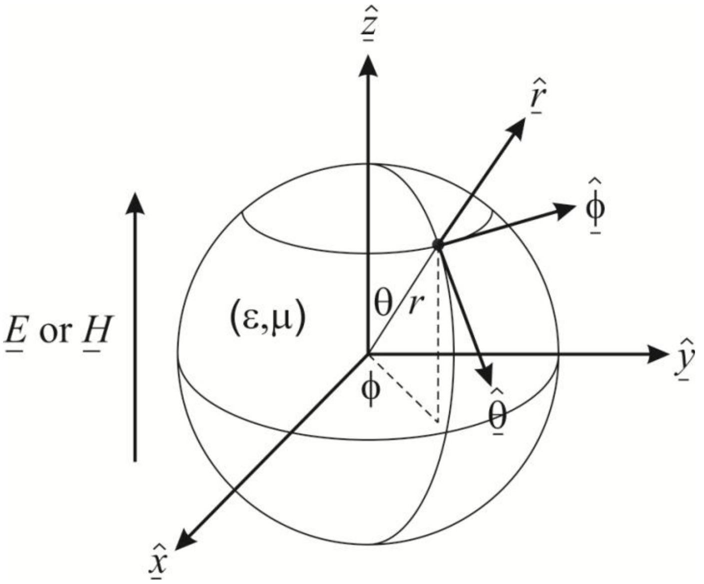

Figure A1: The spherical polar co-ordinate system used to solve the electromagnetic fields in and around a material sphere.

The quasi-static electric and magnetic field fields inside the sphere are of the form $\underline{E} = (E_r \cos\theta, -E_\theta \sin\theta, 0)e^{j\omega t}$ and $\underline{H} = (0, 0, H_\phi \sin\theta)e^{j\omega t}$, where E_r, E_θ and H_ϕ are scalar functions of radial position *r* only, and are proportional to the applied electric field magnitude E_0. This results in an electric dipole moment parallel to the applied electric field. Helmholtz's equation for the induced magnetic field within the sphere is then

$$\nabla^2 (H_\phi \sin\theta) + \left(k^2 - \frac{1}{r^2 \sin^2\theta} \right) H_\phi \sin\theta = 0$$

which reduces to

$$\frac{d}{dx}\left(x^2 \frac{dH_\phi}{dx} \right) + (x^2 - 2) H_\phi = 0 \qquad \text{(A1)}$$

Where $x = kr$. The wavenumber *k* is defined (in the usual manner) using $k = \omega\sqrt{\varepsilon\mu}/c$. The unique solution of Eqn.(A1) which remains finite as $x \to 0$ has the Bessel function form

$$H_\phi(x) \propto \frac{J_{3/2}(x)}{\sqrt{x}} = H_1 \frac{\sin x - x\cos x}{x^2}$$

where the magnetic field scaling factor H_1 is independent of radial position *r*. The corresponding electric field components within the sphere can now be calculated from Maxwell's displacement current density, i.e. $\underline{\nabla} \times \underline{H} = j\omega\varepsilon\varepsilon_0 \underline{E}$, resulting in

$$E_r(x) = E_1 \frac{\sin x - x\cos x}{x^3}, \quad E_\theta(x) = \frac{E_1}{2x}\left(\frac{\cos x}{x} - \frac{\sin x}{x^2} + \sin x \right)$$

(A2)

where the position-independent electric field scaling factor is $E_1 = 2H_1 k/(j\omega\varepsilon\varepsilon_0)$.

Outside of the sphere, the electric field is that of the original field (of magnitude E_0), perturbed by the dipole field associated with the presence of the sphere. The external electric field is again of the form $\underline{E} = (E_r \cos\theta, -E_\theta \sin\theta, 0)e^{j\omega t}$, and in terms of the sphere's induced electric dipole moment p

$$E_r = E_0 + \frac{p}{2\pi\varepsilon_0 r^3}, \qquad E_\theta = -E_0 + \frac{p}{4\pi\varepsilon_0 r^3}$$

(A3)

Applying the electric field boundary conditions at the sphere's surface for the field components of Eqns. (A2) and (A3) allows the electric dipole moment to be found, with the end result being

$$p = 2\pi\varepsilon_0 a^3 E_0 \frac{(2\varepsilon+1)(1-ka\cot ka)-(ka)^2}{(\varepsilon-1)(1-ka\cot ka)+(ka)^2} \qquad \text{(A4)}$$

In the low frequency limit (i.e. $ka << 1$), Eqn.(A4) reduces to the familiar result of the static electric dipole moment of a uniformly polarised dielectric sphere, namely

$$p_0 = 4\pi\varepsilon_0 a^3 E_0 \left(\frac{\varepsilon-1}{\varepsilon+2}\right)$$

7.2 APPENDIX B: Spherical Particle within an Oscillating Magnetic Field

Now consider the magnetic dipole developed by a spherical particle placed within a uniform, oscillating magnetic field, which can be developed in analogy with the treatment of the particle's electric dipole moment discussed in Appendix A. Assume that the sphere is again electrically small (i.e. $a << \lambda_0$) and has complex, isotropic relative permittivity ε and permeability μ. A uniform, oscillating magnetic field of magnitude H_0 applied parallel to the z-axis generates a magnetic dipole moment which is also parallel to the z-axis. The resulting electric and magnetic fields are then $\underline{H} = (H_r \cos\theta, -H_\theta \sin\theta, 0)e^{j\omega t}$ and $\underline{E} = (0, 0, E_\phi \sin\theta)e^{j\omega t}$, respectively. By the reduction of Helmholtz's equation applied to the azimuthal electric field component, it is found that E_ϕ satisfies

$$\frac{d}{dx}\left(x^2 \frac{dE_\phi}{dx} \right) + \left(x^2 - 2 \right) E_\phi = 0$$

which has the unique solution

$$E_\phi(x) \propto \frac{J_{3/2}(x)}{\sqrt{x}} = E_2 \frac{\sin x - x\cos x}{x^2}$$

which remains finite as $x \to 0$, where again $x = kr$ and $k = \omega\sqrt{\varepsilon\mu}/c$. The field scaling factor now is E_2, which differs from E_1 encountered in the treatment of the electric dipole moment. The corresponding magnetic field components can be generated using Faraday's law $\underline{\nabla} \times \underline{E} = -j\omega\mu\mu_0 \underline{H}$, resulting in

$$H_r(x) = H_2 \frac{\sin x - x\cos x}{x^3}, \quad H_\theta(x) = \frac{H_2}{2x}\left(\frac{\cos x}{x} - \frac{\sin x}{x^2} + \sin x \right)$$

(B1)

where the magnetic field scaling factor is defined by $H_2 = 2jE_2k/\omega\mu\mu_0$.

Outside of the sphere, the magnetic field is that of the original field (of magnitude H_0), perturbed by the dipole field associated with the presence of the sphere. The external magnetic field is again of the form $\underline{H} = (H_r \cos\theta, -H_\theta \sin\theta, 0)e^{j\omega t}$, and in terms of the sphere's induced magnetic dipole moment m

$$H_r = H_0 + \frac{m}{2\pi r^3}, \qquad H_\theta = -H_0 + \frac{m}{4\pi r^3}$$

(B2)

Applying the magnetic field boundary conditions at the sphere's surface for the field components of Eqns. (B1) and (B2) allows the magnetic dipole moment to be found, with the end result being

$$m = 2\pi a^3 H_0 \left(\frac{(2\mu + 1)(1 - ka\cot ka) - (ka)^2}{(\mu - 1)(1 - ka\cot ka) + (ka)^2} \right) \tag{B3}$$

In the low frequency limit (i.e. $ka << 1$), Eqn.(B3) reduces to the familiar result of the static magnetic dipole moment of a uniformly magnetised sphere, namely

$$m_0 = 4\pi a^3 H_0 \left(\frac{\mu - 1}{\mu + 2} \right)$$

8 REFERENCES

[1] Kobayashi Y. and Nakayama A., “Round robin test on a cavity resonance method to measure complex permittivity of dielectric plates at microwave frequency”, *IEEE Transactions on Dielectrics and Electrical Insulation,* 13 (2006), 751-759.

[2] Sihvola A., “Electromagnetic mixing formulas and applications”, *IEE Electromagnetic wave series* 47, Institution of Electrical Engineers. London, (1999).

[3] Pelster R. and Simon U., “Nanodispersions of conducting particles: preparation, microstructure and dielectric properties”, *Colloid Polym. Sci,* 277 (1999), 2-14.

[4] Bowler N., “Designing dielectric loss at microwave frequencies using multi-layered filler particles in a composite”, *IEEE Transactions on Dielectrics and Electrical Insulation* 13 (2006) 703-711.

[5] Almond D. P., “Composite dielectrics and conductors: simulation, characterization and design”, *J. Phys. D: Appl. Phys.,* 39 (2006) 1295-1304.

[6] Gerbec J. A., Magana D., Washington A. and Strouse G. F., “Microwave-Enhanced Reaction Rates for Nanoparticle Synthesis”, *J. Am. Chem. Soc.* 127 (2005), 15791-15800

[7] Kim S., Yoon Y. and Lee K., “Magnetic, dielectric, and microwave absorbing properties of iron particles dispersed in rubber matrix in gigahertz frequencies”, *Journal of Applied Physics* 97 (2005) 10F905 - 10F905-3

[8] Roy R., Agrawal D., Cheng J. and Gedevanishvilli S., “Full sintering of

powdered-metal bodies in a microwave field”, *Nature*, 399, (1999) 668–670

[9] Stanley S. A., Gagner J. E., Damanpour S., Yoshida M., Dordick J. S. and Friedman J. M., “Radio-Wave Heating of Iron Oxide Nanoparticles Can Regulate Plasma Glucose in Mice” *Science* 336, (2012) 604-608

[10] Suzuki M., Ignatenko M., Yamashiro M., Tanaka M. and Sato M., “Numerical Study of Microwave Heating of Micrometer Size Metal Particles”, *ISIJ International* 48 (2008) 681–684

[11] Buchelnikov V. D., “Heating of metallic powders by microwaves: Experiment and Theory”, *Journal of Applied Physics* 104, (2008) 113505

[12] Fujiwara H., Toyota S., Anggraini L., Ameyama K. and D. Agrawal, “Microwave Heating Behavior of Fine Stainless Steel Powders in H-Field At 2.45 GHz”, *Proc. International Microwave Power Institute's 44th Annual Symposium*, (2010), 79-82.

[13] Slocombe D., Porch A., Pepper M. and Edwards P. P., “The Mott transition and optimal performance of transparent conducting oxides in thin-film solar cells”, *Energy Environ. Sci.*, 5 (2012), 5387-5391

[14] Masetti G., Saveri M. and Solmi S., *IEEE Trans. Elec. Dev*., 30 (1983), 7.

[15] Pozar D. M., “Microwave engineering”, 3rd Ed., Wiley, US, (2005).

[16] Jin J., “The finite element method in electromagnetics”, 2nd Ed., Wiley, US, (2002).

[17] COMSOL Multiphysics, User’s Guide, COMSOL Ltd. UK, (2008).

[18] Porch A., “Resonator measurements”, Cardiff University, UK, (2008).

[19] Maclean W. R., “The reactance theorem for a resonator”, *Proceedings of the*

I.R.E., 33 (1945), 539-541.

[20] Maclean W. R., “A microwave dielectric loss measuring technique”, *Journal of Applied Physics*, 17 (1946), 558-566.

[21] Works, Dakin, and Boggs, *A.I.E.E. Tech. Pap*., (1944), 44-161

[22] Horner F., Taylor T. A., Dunsmuir R., Lamb J. and Jackson W., “Resonance methods of dielectric measurement at centimetre wavelengths”, *Journal of the Institution of Electrical Engineers*, 93 (1946), 53-68.

[23] Estin A. J. and Bussey H. E., “Errors in dielectric measurements due to a sample insertion hole in a cavity”, *IRE Transactions on Microwave Theory and Techniques,* 8 (1960) 650-653.

[24] Lukac P., “The determination of electron density by means of a cylindrical TM_{010} microwave cavity”, *Brit. J. Appl. Phys. (J. Phys. D),* 1 (1968) 1495-1499.

[25] Hooper G., “Microwave measurement of electron density in a plasma column contained in a dielectric tube”, *J. Phys. D: Appl. Phys*. 5 (1972), L47.

[26] Li S., “Precise calculations and measurements on the complex dielectric constant of lossy materials using TM010 cavity”, *IEEE Transactions On Microwave Theory And Techniques*, 29 (1981), 1041-1048.

[27] Kobayashi Y. and Nakayama A., “Round robin test on a cavity resonance method to measure complex permittivity of dielectric plates at microwave frequency”, *IEEE Transactions on Dielectrics and Electrical Insulation,* 13 (2006), 751-759.

[28] Krupka J., Gabelich S. A., Derzakowski K. and Pierce B. M., “Comparison of split post dielectric resonator and ferrite disc resonator techniques for microwave permittivity measurements of polycrystalline yttrium iron garnet”, *Meas. Sci.*

Technol. 10 (1999), 1004–1008.

[29] Kajfez D., Guillon P., “Dielectric resonators”, Artech House, Dedham, MA, (1986).

[30] Nishikawa, “Dielectric high-power bandpass filter using quarter-cut TE018 image resonator for cellular base stations’, *IEEE Transactions On Microwave Theory And Techniques*, 35 (1987), 12.

[31] Mansour R., “Novel configurations for dielectric loaded and conductor loaded cavity resonators with improved spurious performance”, *Proceedings of APMC, Taipei, Taiwan, R.O.C.* (2001) 741-746.

[32] Kent G., **“**An evanescent-mode tester for ceramic dielectric substrates”, *IEEE Trans. Microwave Theory Tech***.,** 36**,** (1988) 10.

[33] Klein O., Donovan S., Dressel M., Gruner G., “Microwave cavity perturbation technique: part I principles”, *International Journal of Infrared and Millimeter Waves*, 14 (1993), 2423-2457.

[34] Donovan S., Klein O., Dressel M., Holczer K., Gruner G., “Microwave cavity perturbation technique: part II: experimental scheme”, *International Journal of Infrared and Millimeter Waves*, 14 (1993), 2459-2487.

[35] Dressel M., Klein O., Donovan S., Gruner G., “Microwave cavity perturbation technique: part III: applications”, *International Journal of Infrared and Millimeter Waves*, 14 (1993), 2489-2517.

[36] Kawabata H., Kobayashi Y. and Kaneko S., “Analysis of cylindrical cavities to measure accurate relative permittivity and permeability of rod samples”, *Proceedings of Asia-Pacific Microwave Conference*, (2010).

[37] Tinga W. R., Edwards E. M., “Dielectric measurements using swept

frequency techniques", *J. Microwave Power,* 3 (1968), 144.

[38] Krasovitsky V., Terasawa D., Nakada K., Kozumi S., Sawada A. and Sato N., "Microwave cavity perturbation technique for measurements of the quantum Hall effect", *Cryogenics*, 44 (2004), 183–186.

[39] Jackson J. D., "Classical Electrodynamics", John Wiley & Sons, New York, (1975).

[40] Barthel J., Bachhuber K., Buchner R. and Hetzenauer H., "Dielectric spectra of some common solvents in the microwave region. Water and lower alcohols," *Chem. Phys. Lett..,* 165 (1990), 4.

[41] Santarelli V. A., MacDonald J. A., Pine C., "Overlapping dielectric dispersions in toluene," *J. Chem. Phys*., 46 (1967), 2367.

[42] Anderson J. C., "Dielectrics", Chapman and Hall, London, Science Paperbacks, Modern Electrical Studies, (1964).

[43] Kaneko S., Kawabata H. and Kobayashi Y., "Improved perturbation method of complex permittivity using correction charts for TM010 and TM020 modes of a circular cylindrical cavity", *Proceedings of Asia-Pacific Microwave Conference*, (2010)

[44] Kawabata H., Tanpo H. and Kobayashi Y., "A rigorous analysis of a TM010 mode cylindrical cavity to measure accurate complex permittivity of liquid", *Proceedings of the 33rd European Microwave Conference*, Munich, (2003).

[45] Kobayashi Y., "Standardization of measurement methods of low-loss dielectrics and high-temperature superconducting films", *IEICE Trans. Electron*., E87-C (2004), 652-656.

[46] Linhart J. G., Templeton I. M., Dunsmuir R., "A microwave resonant cavity

method for measuring the resistivity of semiconducting materials”, *Bnt. J. Appl. Phys*, 7 (1956) 36–37.

[47] Champlin K. S. and Krongard R. R., “The measurement of conductivity and permittivity of semiconductor spheres by an extension of the cavity perturbation method,” *IRE Transactions on Microwave Theory and Techniques*, (1961), 545-551.

[48] Liu J., Bowler N., “Analysis of losses in a double-negative metamaterial composed of magnetodielectric spheres embedded in a matrix”, *Microwave and Optical Technology Letters* 53 (2011), 1649-1652.

[49] Holloway C. L., Kuester E. F., Baker-Jarvis J. and Kabos P., “A double negative (DNG) composite medium composed of magnetodielectric spherical particles embedded in a matrix”, *IEEE Trans Antennas Propag* 51 (2003), 2596–2603.

[50] Pendry J. B., “Negative refraction makes a perfect lens”, *Phys Rev Lett* 85 (2000), 3966–3969.

[51] Meredith R. J., “Engineers' handbook of industrial microwave heating”, *IEE power series* 25, Institution of Electrical Engineers. London, (1998).

[52] Oh J. H., Oh K. S., Kim C. G. and Hong C. S., “Design of radar absorbing structures using glass/epoxy composite containing carbon black in X-band frequency ranges”, *Composites Part B: Engineering* 35 (2004), 49-56.

[53] Ohlan A., Singh K., Chandra A. and Dhawan S. K., “Microwave absorption properties of conducting polymer composite with barium ferrite nanoparticles in 12.4-18 GHz”, *Applied Physics Letters* 93 (2008), 053114.

[54] Catchpole K. R. and Polman A., “Plasmonic solar cells”, *Optics Express* 16 (2008), 21793-21800.

---

[55] Gregory A. P. and Clarke R. N., “A review of RF and microwave techniques for dielectric measurements on Polar Liquids”, *IEEE Transactions on Dielectrics and Electrical Insulation* 13 (2006) 727-743

[56] Rayleigh, “On the influence of obstacles arranged in a rectangular order upon the properties of a medium,” *Phil. Mag.*, 34 (1892), 481-502.

[57] Gregory A. P., Clarke R. N., “Dielectric metrology with coaxial sensors”, *Meas. Sci. Technol*., 18 (2007), 1372-1386

[58] Jackson J. D., “Classical Electrodynamics”, John Wiley & Sons, New York, (1975).

[59] Hashin Z. and Shtrikman S., “A variational approach to the theory of the effective magnetic permeability of multiphase materials”, *J. Appl. Phys*. 33 (1962), 3125.

[60] Torquato S., “Random heterogeneous materials: microstructure and macroscopic Properties”, Springer (2002).

[61] Youngs I. J., Bowler N. and Ugurlu O., “Dielectric relaxation in composites containing electrically isolated particles with thin semi-continuous metal coatings”, *J. Phys. D: Appl. Phys*. 39 (2006) 1312-1325.

[62] Debye P., *Ann. Phys.* (Leipz.) 30 (1909), 57.

[63] Jonscher A. K., “The universal dielectric response and its physical significance”, *IEEE Transactions on Electrical Insulation*, 27 (1992) 3.

[64] Stratton J. A., “Electromagnetic Theory”, *International Series in Pure and Applied Physics*, McGraw-Hill, London (1941).

[65] Aden A. and Kerker M., “Scattering of electromagnetic waves from two

concentric spheres", *J. Appl. Phys*., 22 (1951) 10.

[66] Mie G., *Ann. Phys*. (Leipz.) 25 (1908), 377.

[67] Liu H. D., Zhao Y. P., Ramanath G., Murarka S. P. and Wang G. C., "Thickness dependent electrical resistivity of ultrathin (< 40 nm) Cu films", *Thin Solid Films*, 384 (2001), 151 – 156.

[68] Perenboom J. A. A. J., Wyder P. and Meier F., "Electronic properties of small metallic particles", *Physics Reports* 78 (1981), 173-292.

[69] Bowler N., "Effects of lossy, layered filler particles on the bulk permittivity of a composite material", *J. Phys. D: Appl. Phys.*, 37 (2004), 326-333.

[70] Stauffer D. and Aharony A., "Introduction to Percolation Theory", Taylor & Francis,
London, 2nd edition, (1991).

[71] Pournaropoulos C. L. and Misra D. K, "The co-axial aperture electromagnetic sensor and its application in material characterization", *Meas. Sci. Technol.* 8 (1997), 1191–1202.

[72] Levine H. and Papas C. H., "Theory of the circular diffraction antenna", *J. Appl. Phys*. 22 (1951) 29–43.

[73] Papas C. H., "An application of Sommerfeld's complex order wave functions to antenna theory", *J. Math. Phys*. 33 (1954) 269–75.

[74] Pournaropoulos C. L. and Misra D., "A study on the coaxial aperture electromagnetic sensor and its application in material characterisation", *Trans. IEEE Trans. Instrum. Meas*.
43 (1994), 111–5.

---

[75] Misra D., “On the measurement of the complex permittivity of materials by an open-ended coaxial probe”, *IEEE Microwave and Guided Wave Letters*, 5 (1995), 161-164.

[76] Agilent Application Note: “Split post dielectric resonators for dielectric measurements of substrates”, Agilent Technologies Inc., USA (2006)

[77] Krupka J., Derzakowski K., Tobar M. E., Hartnett J. and Geyer R. G., “Complex permittivity of some ultralow loss dielectric crystals at cryogenic temperatures”, *Measurement Science and Technology*, 10 (1999), 387-392.

[78] Frank D. J. and Lobb C. J., “Highly efficient algorithm for percolative transport studies in two dimensions”, *Phys. Rev. B* 37 (1988) 302.

[79] Jonscher A. K. “The ‘universal’ dielectric response”, *Nature* 267 (1977), 673 – 679.

[80] Jonscher A. K., “A new model of dielectric loss in polymers”, *Colloids Polym. Sci.* 253 (1975) 231.

[81] Jonscher A. K., “Dielectric Relaxations in Solids”, Chelsea Dielectric Press, London (1983).

[82] Dyre J. C. and Schroder T. B., “Universality of ac conduction in disordered solids”, *Rev. Mod. Phys.*, 72 **(**2000), 873.

[83] Almond D. P. and Vainas B., “The dielectric properties of random RC networks”, *J. Phys.: Condens. Matter*, 11 (1999), 9081.

[84] Vainas B., Almond D. P., Lou J. and Stevens R., “An evaluation of random R-C networks for modelling the bulk ac electrical response of ionic conductors”, *Solid State Ion.*, 126 **(**1999**)** 65.

[85] Bouamrane R. and Almond D. P., “The ‘emergent scaling’ phenomenon and the dielectric properties of random resistor–capacitor networks”, *J. Phys.: Condens. Matter* 15 (2003), 4089.

[86] Lichtenecker K., “Die dielektrizitätskonstante natürlicher und künstlicher mischkörper”, *Z. Phys.* 27 (1926), 115.

[87] Almond D. P. and Bowen C. R., “Anomalous power law dispersions in ac conductivity and permittivity shown to be characteristics of microstructural electrical networks”, *Phys. Rev. Lett.* 92 (2004) 157601.

[88] Almond D. P., “Composite dielectrics and conductors: simulation, characterization and design”, *J. Phys. D: Appl. Phys.*, 39 (2006) 1295-1304.

[89] Gossen Metrawatt, METRISO 5000D-PI, 5000 V Digital Insulation Measuring Instrument, (http://www.gossenmetrawatt.com/english/produkte/metriso5000d-pi.htm) accessed 15-06-12.

[90] Kittel C., “Introduction to solid state physics”, 7th ed., John Wiley and Sons Inc., NY (1996).

[91] Maxwell Garnett J. C., “Colours in metal glasses and metallic films”, *Phil. Trans. R. Soc.* 203 (1904) 385.

[92] Sihvola A., “Transmission line analogy for calculating the effective permittivity of mixtures with spherical multilayer scatterers”, *Journal of Electromagnetic Waves and Applications*, 2 (1988), 741-756.

[93] Landau L. V., Lifshits E. M., Pitaevskii L. P., “Electrodynamics of Continuous
Media”, Pergamon, NewYork, (1984).

---

[94] Sihvola A., “Polarizability and effective permittivity of layered and continuously inhomogeneous dielectric ellipsoids”, *Journal of Electromagnetic Waves and Applications,* 4 (1990), 1 – 26.

[95] Youngs I. J., Bowler N., Lymer K. P. and Hussain S., “Dielectric relaxation in metal-coated particles: the dramatic role of nano-scale coatings”, *J. Phys. D: Appl. Phys.*, 38 (2005) 188–201.

[96] Edwards P. P. and Sienko M. J., “Universality aspects of the metal-nonmetal transition in condensed media”, *Phys. Rev. B,* 17 (1978), 2575.

[97] Edwards P. P., Porch A., Jones M. O., Morgan D. V. and Perks R. M., “Basic materials physics of transparent conducting oxides”, *Dalton Trans*., (2004), 2995-3002.

[98] Hamberg I. and Granqvist C. G., “Evaporated Sn-doped In_2O_3 films: basic optical properties and applications to energy-efficient windows”, *J. Appl. Phys*., 60 (1986), R123.

[99] Wooten F., “Optical Properties of Solids”, Academic Press, San Diego, (1972).

[100] Mingos D.M.P. and Baghurst D.R., “Applications of microwave dielectric heating effects to synthetic problems in chemistry”, *Chem. Soc. Rev.* 20 (1991) 1-47

[101] Zhang X., Hayard D.O. and Mingos D.M.P., “Effects of microwave dielectric heating on heterogeneous catalysis”, *Catalysis Letters* 88 (2003) 33–38

[102] Jones D.A., Lelyveld T.P., Mavrofidis S.D., Kingman S.W. and Miles N.J., “Microwave heating applications in environmental engineering – a review”, *Resources,. Conservation and Recycling* 34 (2002) 75–90.

---

[103] Thostenson E.T. and Chou T.W., “Microwave processing: fundamentals and applications”, *Composites Part A* 30 (1999) 1055–1071.

[104] Harutyunyan A. R., Pradhan B. K., Chang J., Chen G. and Eklund P. C., “ Purification of Single-Wall Carbon Nanotubes by Selective Microwave Heating of Catalyst Particles”, *J. Phys. Chem. B* 106 (2002), 8671-8675

[105] Gerbec J. A., Magana D., Washington A. and Strouse G. F., “Microwave-Enhanced Reaction Rates for Nanoparticle Synthesis”, *J. Am. Chem. Soc.* 127 (2005), 15791-15800

[106] Kim S., Yoon Y. and Lee K., “Magnetic, dielectric, and microwave absorbing properties of iron particles dispersed in rubber matrix in gigahertz frequencies”, *Journal of Applied Physics* 97 (2005) 10F905 - 10F905-3

[107] Roy R., Agrawal D., Cheng J. and Gedevanishvilli S., “Full sintering of powdered-metal bodies in a microwave field”, *Nature*, 399, (1999) 668–670

[108] Stanley S. A., Gagner J. E., Damanpour S., Yoshida M., Dordick J. S. and Friedman J. M., “Radio-Wave Heating of Iron Oxide Nanoparticles Can Regulate Plasma Glucose in Mice” *Science* 336, (2012) 604

[109] Fujiwara H., Toyota S., Anggraini L., Ameyama K. and D. Agrawal, “Microwave Heating Behavior of Fine Stainless Steel Powders in H-Field At 2.45 GHz”, *Proc. International Microwave Power Institute's 44th Annual Symposium*, (2010), pp. 79-82.

[110] Buchelnikov V. D., Louzguine-Luzgin D. V., Anzulevich A. P., Bychkov I. V., Yoshikawa N., Sato M. and Inoue A., “Modelling of microwave heating of metallic powders”, *Physica B* 403 (2008) 4053–4058

[111] Buchelnikov V. D., “Heating of metallic powders by microwaves: Experiment and Theory”, *Journal of Applied Physics* 104, (2008) 113505

[112] Cheng J., Roy R., Agrawal D., "Radically different effects on materials by separated microwave electric and magnetic fields", *Mat Res Innovat* 5 (2002) 170–177

[113] Yoshikawa N., Ishizuka E. and Taniguchi S., "Heating of Metal Particles in a single mode microwave applicator", *Materials transactions* 47 (2006) 898-902

[114] Suzuki M., Ignatenko M., Yamashiro M., Tanaka M. and Sato M., "Numerical Study of Microwave Heating of Micrometer Size Metal Particles", *ISIJ International* 48 (2008) 681–684

[115] Porch A., Private communication, March 2012.

[116] Hergt R., Dutz S., Muller R. and Zeisberger M., "Magnetic particle hyperthermia: nanoparticles magnetism and materials development for cancer therapy", *J. Phys.: Condens. Matter* 18 (2006) S2919–S2934

[117] Andra W., "Magnetic hyperthermia Magnetism in Medicine", Berlin: Wiley–VCH, (1998) 455–70

[118] Granqvist C. G. and Hultaker A., *Thin Solid Films*, 411 (2002), 1.

[119] Chopra K. L., Paulson P. D. and Dutta V., *Prog. Photovolt: Res. Appl.*, 12 (2004), 69-92.

[120] Grätzel M., *Inorg. Chem*, 44 (2005), 6841-6851.

[121] Edwards P. P., Porch A., M. O. Jones, D. V. Morgan and R. M. Perks, Dalton Trans., (2004), 2995-3002.

[122] Leenheer A. J., Perkins J. D., van Hest M. F. A. M., Berry J. J., O'Hayre R.

P. and Ginley D. S., *Phys. Rev. B*, 77(2008), 115215.

[123] Masetti G., Saveri M. and Solmi S., *IEEE Trans. Elec. Dev*., 30 (1983), 7.

[124] Ellmer K. and Mientus R., *Thin Solid Films*, 516 (2008),4620-4627.

[125] Bellingham J. R., Phillips W. A. and Adkins C. J, *J. Mater. Sci. Lett*., 11 (1992), 263-265.

[126] Seto J. Y. W., *J. Appl. Phys*., 46 (1975), 12.

[127] Porch A., Morgan D. V., Perks R. M., Jones M. O. and Edwards P. P., *J. Appl. Phys.,* 95 (2004), 9.

[128] Porch A., Morgan D. V., Perks R. M., Jones M. O. and Edwards P. P., *J. Appl. Phys*., 96 (2004), 8.